Acoustical Physics, Vol. 50, No. 6, 2004, pp. 623–640. Translated from Akusticheskiĭ Zhurnal, Vol. 50, No. 6, 2004, pp. 725–743.
Original Russian Text Copyright © 2004 by Brysev, Krutyansky, Pernod, Preobrazhensky.

Nonlinear Ultrasonic Phase-Conjugate Beams and Their Application in Ultrasonic Imaging

A. P. Brysev[1], L. M. Krutyansky[1], P. Pernod[2], and V. L. Preobrazhensky[1, 2]
[1] *Wave Research Center, Prokhorov General Physics Institute, Russian Academy of Sciences,*
ul. Vavilova 38, Moscow, 119991 Russia
e-mail: brysev@orc.ru
[2] *Institut d'Electronique, de Microelectronique, et de Nanotechnologies (IEMN-DOAE, UMR CNRS 8520),*
59651 Villeneuve d'Ascq, Cedex, France
e-mail: philippe.pernod@iemn.univ-lille1.fr

Received July 5, 2004

Abstract—The latest results of experimental and theoretical research into phase conjugation of nonlinear ultrasonic beams are generalized, and prospects for the development of nonlinear ultrasonic imaging are outlined. *© 2004 MAIK "Nauka/Interperiodica".*

Interest in the implementation of nonlinear wave phenomena in acoustic imaging systems for medical purposes and nondestructive testing has noticeably quickened in the last few years. For example, images of biological objects obtained using the second harmonic of an incident ultrasonic wave show a higher resolution due to the narrowing of the focal distribution of the second harmonic, as well as a reduction of the level of sidelobes and reverberation noise in comparison with the fundamental frequency wave [1–5]. An analysis of the harmonics of a nonlinearly propagating wave can be easily adapted to existing diagnostic systems. It is believed that "harmonic imaging" systems will soon become common to ultrasonic medical diagnostics. It is necessary to note that the use of the second harmonic in acoustic microscopy was apparently proposed for the first time more than quarter of a century ago [6]. Today, the methods of nonlinear acoustics are implemented more and more actively in ultrasonic nondestructive evaluation [7, 8].

Along with the aforementioned investigations, studies concerned with phase conjugation in acoustics have been progressing rapidly [9–14]. The interest in the application of phase conjugation in ultrasonic imaging is connected with the well-known capability of phase-conjugate waves to compensate for phase distortions introduced by a propagation medium. A compensation for phase distortions by phase conjugation was demonstrated experimentally in acoustic microscopy [13, 14]. At the same time, the possibility of an extension of the phase-conjugation technique to the case of nonlinear ultrasonic imaging is not *a priori* evident because of the partial violation of the invariance of nonlinear acoustic equations with respect to time reversal. The reasons for this violation can be, in particular, an anomalously strong sound attenuation at a shock wave front or a noncoincidence of the amplitudes of incident and phase-conjugate waves. The latter fact becomes especially important under the conditions of phase conjugation with amplification, which is of practical interest.

At ultrasonic frequencies, a giant amplification (over 80 dB) is practically implemented in the case of parametric phase conjugation beyond the threshold of the absolute instability of phonons in magnetoacoustic active media [15, 16]. Over-threshold (supercritical) phase-conjugating amplifiers, which are the sources of the stimulated radiation of phase-conjugate phonon pairs, are now one of the basic instruments for the experimental investigation of nonlinear wave processes in the case of ultrasound phase conjugation [17]. Nonlinear distortions of quasi-plane phase-conjugate sound beams generated by an over-threshold phase-conjugating amplifier were discovered and studied in [18]. In [19, 20], the space–time structure and harmonic composition of focused nonlinear phase-conjugate beams propagating in a homogeneous medium were studied. The compensation for phase distortions in the case of the retrofocusing of a nonlinear beam in an inhomogeneous medium was discovered in the process of imaging a test object with the help of the second harmonic of a phase-conjugate wave in an acoustic microscope [21]. The theoretical interpretation of the phenomenon on the basis of the nonlinear geometrical acoustics of inhomogeneous refractive media without dispersion is proposed in [21, 22]. An experimental study of the field structure of a parametrically amplified phase-conjugate wave for a focused beam transmitted through an aberration layer was reported in [23]. A high quality of autofocusing of both the second and higher harmonics in the focal region of an incident wave was demonstrated. Narrowband parametric amplification basically provides an opportunity to perform phase conjugation of

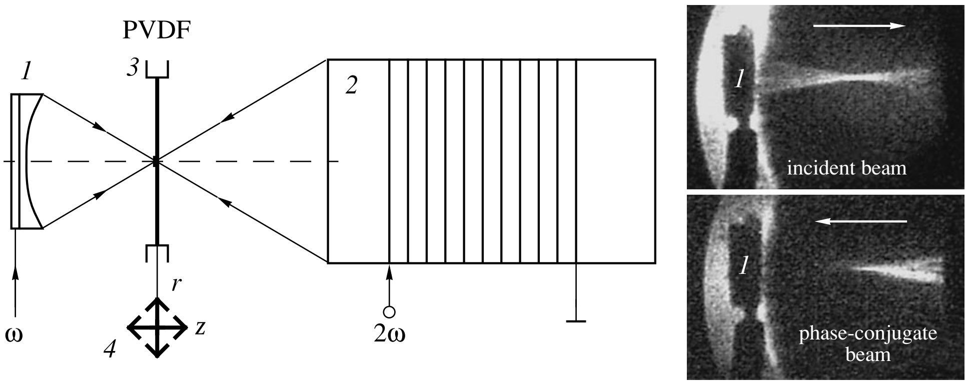

Fig. 1. Experimental scheme. Optical stroboscopic visualization of the incident and phase-conjugate beams is given on the right side [19].

the single harmonics of nonlinear acoustic beams. In this case, in particular, phase conjugation with amplification of the second harmonic of an incident wave leads (in the process of backward propagation) to the generation of the fourth and even higher (with respect to the spectrum of the incident wave) harmonics. Thus, it becomes possible to obtain acoustic images using higher harmonics without increasing the order of the nonlinearity of wave interaction in a medium. A similar frequency multiplication for imaging of a test object with the help of the fourth harmonic of the incident wave in a phase-conjugating microscope was demonstrated in [24]. In this case, the conservation of the property of compensation for phase aberrations was noted in the process of autofocusing under the conditions of the selective phase conjugation of the single harmonics of an incident wave.

The purpose of this review is to generalize the latest results of experimental and theoretical research into the phase conjugation of nonlinear ultrasonic beams and to outline prospects for the development of nonlinear phase-conjugation ultrasonic imaging.

1. FIELD STRUCTURE OF A NONLINEAR PHASE-CONJUGATE FOCUSED WAVE

Because of the high amplification provided by over-threshold parametric phase-conjugating amplifiers employing magnetostrictive ceramics, the intensity of ultrasonic phase-conjugate beams can be sufficiently high (over 1 W/cm^2) for an effective generation of harmonics on the path of the backward propagation of such beams to the source. As is well known, this leads to a nonlinear distortion of the initial sinusoidal time profile of a wave and, as a consequence, to the growth of its attenuation. In the case of focused beams, which are commonly used in ultrasonic imaging, nonlinear effects manifest themselves most strongly. Apart from distorting the time profile, the influence of nonlinearity manifests itself, in particular, in a shift of the amplitude maximum on the beam axis towards the source. Moreover, the shape of the wave front in a nonlinear beam that is inhomogeneous over its cross section is distorted in comparison with the linear case, which can lead to a nonlinear focusing and defocusing of the beam [25]. All of these factors can affect the quality of phase-conjugate focusing in a nonlinear medium and, therefore, they need special investigation and evaluation. In this section, we give the results of experimental and numerical simulation that were lately obtained [17–20] and reflect on the major specific features of the behavior of nonlinear focused phase-conjugate ultrasonic beams in a homogeneous medium.

A typical scheme for the experimental investigation of such beams is given in Fig. 1, where, on the right side, the optical visualization of fields of incident and phase-conjugate beams is shown as an illustration. An ultrasonic pulse with a frequency $f = 5.0$ MHz and a duration of 30 μs was radiated into water by a spherically focused Panametrics V307-SU transducer with a diameter of 27 mm and a focal distance of 84 mm. The pressure amplitude of the incident wave was small (~0.2 MPa at the focus) and, therefore, its propagation could be considered to be linear. The distance between the transducer and a phase-conjugating amplifier was 202 mm. A direct measurement of acoustic field parameters was performed using a sound-transparent wideband membrane PVDF hydrophone with a sensitive element 0.5 mm in diameter. This provided an opportunity to conduct virtually nondistorting measurements for both the incident and phase-conjugate beams. The hydrophone was connected with a two-coordinate positioning system that scanned the acoustic field with a minimum step of 0.2 mm. A signal from the hydrophone after amplification was digitized by a Tektronix TDS-340A oscilloscope, and then the data were fed to a computer. The generation of a phase-conjugate ultrasonic pulse at a carrier frequency of 5 MHz was performed by an active magnetostriction phase-conjugating element on account of the over-threshold parametric interaction of a 10-MHz magnetic pumping field and the incident acoustic field. The active element was cylindrical, with a length of 150 mm and a diameter of 36 mm. To expand the angular operation range of the

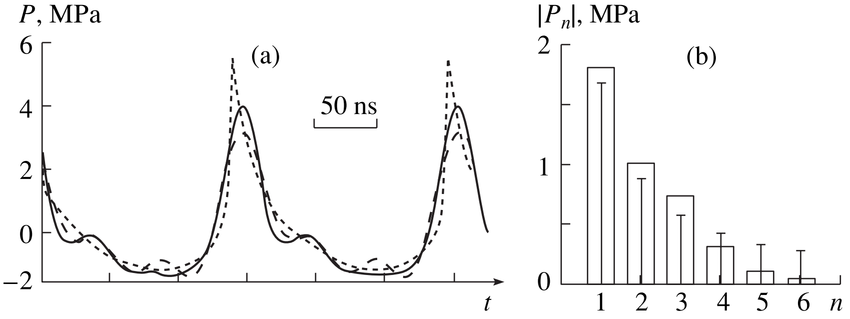

Fig. 2. (a) Wave profiles and (b) spectra of a phase conjugate wave at the focus point. (a) The solid line refers to measurements, dots refer to exact calculation by the Khokhlov–Zabolotskaya–Kuznetsov equation, and the dotted line refers to calculations taking into account only the four first harmonics. (b) Columns represent the experiment, and segments, the calculation [19].

system and to improve the quality of phase conjugation, a system of cylindrical grooves was formed on the operation surface of the active element (see [26, 27]). Because of the parametric pumping of electromagnetic energy into the energy of acoustic waves, the amplitude of the latter grows exponentially during the interaction time and reaches levels sufficient for the intense development of nonlinear effects in a phase-conjugate wave in the process of its propagation in water towards the transducer.

To numerically simulate the propagation of axisymmetric ultrasonic beams in a nonlinear medium, one of the most precise techniques based on the algorithms of the numerical solution of the Khokhlov–Zabolotskaya–Kuznetsov equation and taking into account nonlinearity, absorption, and diffraction was used [28]. This approach provides a good qualitative agreement with experiment [19, 29]. A numerical simulation was conducted with parameters corresponding to the experimental conditions; i.e., linear propagation was assumed for the incident beam and nonlinear propagation for the phase-conjugate beam. Moreover, the finiteness of the aperture of the phase-conjugating element was taken into account, and finally, the amplitude distribution of a phase-conjugate wave in the plane $z = 202$ mm, which corresponded to the position of the output of the phase-conjugating amplifier, was multiplied by a coefficient determined by amplification in the phase-conjugating system.

The results obtained are given in Figs. 2–4. Figure 2 shows the characteristic nonlinear wave profiles and the spectra corresponding to them that are observed in the focus of a phase-conjugate beam [19]. As one can see, the measurements give a peak pressure value that is lower than the calculated one, and the measured wave profile itself does not have the shock front predicted by the calculations. This discrepancy arises because of the limiting character of the frequency range of the hydrophone, which provides an opportunity, in this case, to measure correctly up to four harmonics in the phase-conjugate wave (see the frequency spectrum in Fig. 2b). If, in the process of calculation of waveforms, one takes into account only four harmonics, then, as one can see from Fig. 2a, a better agreement of the calculations with the measurements is obtained.

A comparison of the measurements and calculations for axial and focal (in the plane $z = 84$ mm) pressure distributions in the beams under investigation are given in Fig. 3 [29] in the right and left parts of the figure, respectively. The curves in Fig. 3a demonstrate the linear character of the propagation of an incident beam. Distributions for a phase-conjugate beam are given for two values of the aperture of a phase-conjugating element, namely, 36 mm (Fig. 3b) and 20 mm (Fig. 3c), in order to show the effect of diffraction together with the influence of nonlinearity. One can see from Fig. 3b that higher harmonics are also present in the phase-conjugate beam in the focal plane and that they constitute a noticeable part of the amplitude of the fundamental harmonic. For example, the second harmonic is only two times smaller than the first one. However, as one can see from the comparison of focal distributions in Figs. 3a and 3b, nonlinearity practically does not affect the quality of phase-conjugation focusing. At the same time, the diffraction arising due to the finiteness of the aperture of the phase-conjugating element, which widens the principal maximum of the focal pressure distribution and smoothes the axial distribution in the phase-conjugate beam (Fig. 3c), leads to a strong deterioration in the quality of phase conjugation.

The good agreement of the numerical calculations and of the measurements provides the grounds and the opportunity to monitor, via a numerical simulation, the behavior of phase-conjugate ultrasonic beams up to high values of intensity that have not yet been reached experimentally. The results of such a numerical calculation (in the case of the unrestricted aperture of a phase-conjugating system) are given in Fig. 4 [20]. The dimensionless nonlinear parameter N_f, defined as the ratio of the length of the near field to the length of shock formation in a plane wave, takes on values from 0.1, which corresponds to a weak nonlinearity, to 1.0, when a pronounced shock front arises (Fig. 4c). One can see that, as N_f grows, the maximum of the axial pressure

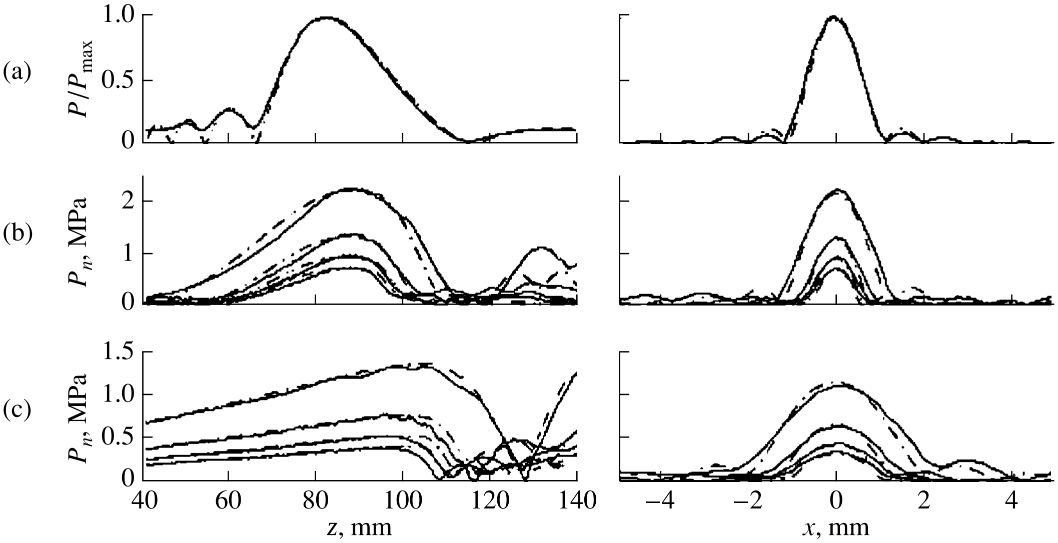

Fig. 3. Comparison of measured (solid line) and calculated (dotted line) data of axial (on the left side) and focal (on the right side) pressure distributions in the plane $z = 84$ mm in the incident (the first row) and phase-conjugate (the second and third rows) beams [29].

distribution is shifted towards the source positioned at $\sigma = 0$ (Fig. 4a) and the oscillations of the focal pressure distribution become smoothed (Fig. 4b) together with a simultaneous decrease in the pressure amplitude at the beam axis (Figs. 4a, 4b). Nevertheless, it is possible to assert that even the formation of a shock front in a phase-conjugate beam is not an obstacle for retaining its focusing ability. Thus, the major factor contributing to the deterioration of the quality of phase conjugation in a homogeneous medium and, in particular, the quality of the reproduction of the focal distribution, is the finiteness of the aperture of the phase-conjugating element.

2. PROPAGATION OF A PHASE-CONJUGATE NONLINEAR WAVE THROUGH AN ABERRATION LAYER

As follows from the results of the preceding section, nonlinearity does not hinder the high-quality phase-conjugation focusing in a homogeneous medium even under the conditions of shockwave formation. At the same time, from a practical point of view, the case in which some inhomogeneities are located in the path of wave propagation is of major interest. If inhomogeneities introduce phase aberrations, then in the case of a linear medium the distortions in an incident wave, which are caused by these inhomogeneities, can be compensated for by the effect of phase conjugation. In this section, we present the main experimental results concerning the transmission of a nonlinear phase-conjugate beam through an aberration layer and demonstrating the possibility of phase-conjugation compensation of phase distortions in a nonlinear medium with inhomogeneities [23].

The experimental scheme presented in Fig. 1 is taken as the basis. A special layer *R* that distorts the acoustic field is introduced into an acoustic path to simulate the inhomogeneities of a medium (Fig. 5).

The layer was manufactured of a silicon polymer. The layer material had the following acoustic parameters: a density of 850 kg/m^3, a sound velocity of 1160 m/s, and an attenuation of 6 dB/cm at a frequency of 5 MHz. One side of the layer was flat and the other side had chaotically located conelike irregularities. The sizes of the bases and heights of the irregularities lay within the range 2–5 mm. Thus, the difference between the phase shifts in water and in the layer at for example, a distance of 3 mm, was greater than 4π. The acoustic impedance of the layer provided sufficiently good acoustic coupling with water. Taking into account the comparatively small layer thickness, it was possible to assume that the distortions introduced into the acoustic beam were mainly of a phase character and that the contribution of the amplitude losses was inessential.

The ability of the layer to introduce noticeable distortions into the transmitted wave at a sufficiently small distance was studied in the case of its position as indicated by number *1* in Fig. 5. The distance of the flat layer surface from the focus was 20 mm. The field produced by the radiator in the focal plane was measured under these conditions. The characteristic form of the curve obtained is given in Fig. 6. The focal field distribution in the absence of the layer is also given for comparison. One can see that the presence of the layer that destroys the focusing strongly affects the distribution typical of a spherically focused beam. Multiple repetitions of such measurements with parallel shifts of the layer by retaining a constant distance to the source produced focus destruction results that were similar in

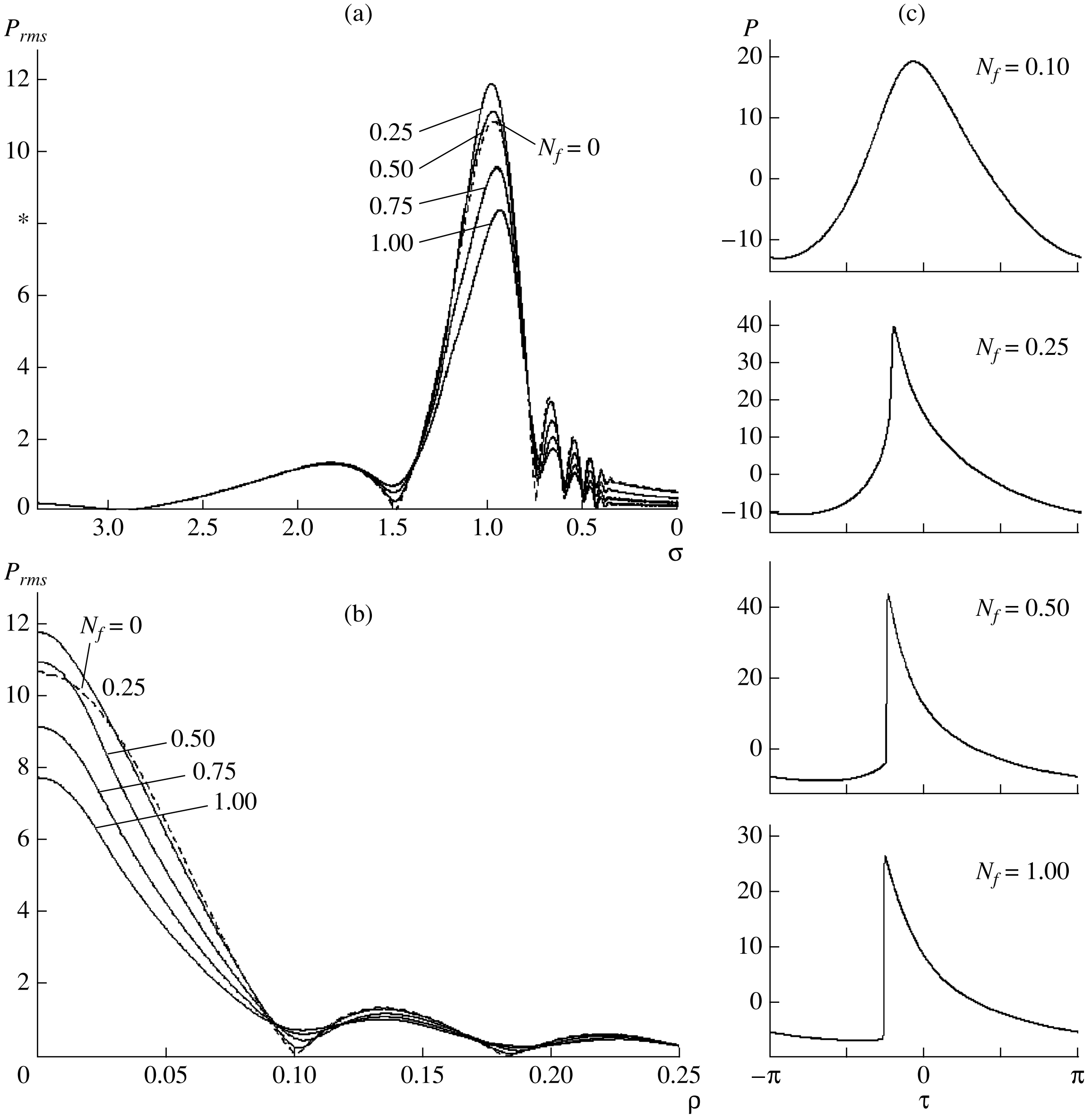

Fig. 4. Numerical calculation of the evolution of axial (right side, top) and transverse (left side, bottom) pressure distributions in the focal plane and the wave profiles at the focus (right side) for the phase-conjugate beam in the case of a varying nonlinearity parameter N_f; σ is the distance to the source normalized to the focal length d: $\sigma = z/d$, where z is the longitudinal coordinate [20].

form and differed in position, shape, and number of peaks. Thereby, a satisfactory quality of the layer as a medium that introduces phase aberrations was confirmed.

For experiments with a phase-conjugate wave, the phase layer was shifted symmetrically with respect to the focus from position *1* to position *2*. In this geometry, aberrations were introduced into the incident wave after it passed the focal area. In this case, it was necessary to eliminate the losses connected with a part of a scattered beam missing the aperture of the phase-conjugating amplifier. A metal tube *T* with an internal diameter of 36 mm and a length of 101 mm, which played the role of an acoustic waveguide, was positioned between the layer and the amplifier for this purpose. Otherwise, as was discovered in the corresponding experiments, the reproduction of the spatial structure of the field of the incident beam was violated.

The results of measurements of the field of a phase-conjugate beam along the axis are given in Fig. 7. A dotted line conditionally denotes the layer position. The scanning region started directly from the layer and had a length of 30 mm. The dashed line shows, for comparison, the pressure distribution in the incident wave. The time profile of the phase-conjugate wave at the initial scanning point is demonstrated in Fig. 7a on the right side, at the bottom. At the left layer boundary, a phase-conjugate wave is clearly nonlinear; i.e., the amplitude

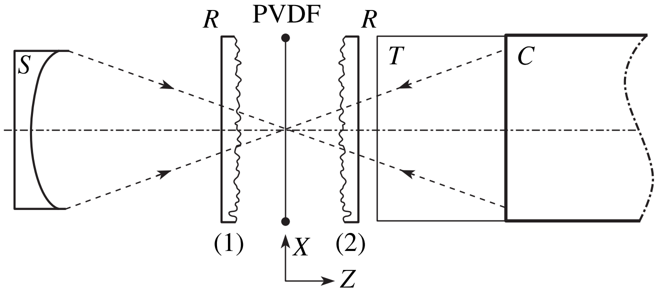

Fig. 5. A simplified scheme of the experiment. The dashed lines show the propagation of incident and phase-conjugate sound waves in the absence of the layer. Here, *S* is an ultrasonic source, *C* is a phase-conjugating amplifier, *T* is a metal tube, *R* is a phase layer, (1) and (2) are the layer positions, and *X* and *Z* are the directions of the hydrophone positioning axes [23].

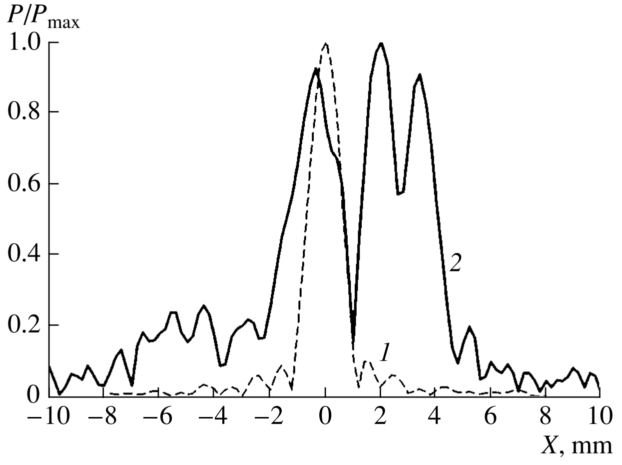

Fig. 6. Focal distribution of the normalized pressure amplitude in the incident wave (*1*) in the absence of the phase layer and (*2*) with the layer present at position *1*. Here, *X* is the distance from the beam axis [23].

of the second harmonic makes up 18% of the amplitude of the first harmonic; the amplitude of the third harmonic, 8%; and the amplitude of the fourth harmonic, 4%. The longitudinal profile of the phase-conjugate beam, on the whole, reproduces well the profile of the incident beam.

Figure 8 gives the transverse distributions of (a) the effective pressure values and (b) the harmonic pressure amplitude in the phase-conjugate beam that were measured in the focal plane of the source. The field distribution in the incident beam is shown by the dashed line. The time profile of the phase-conjugate wave in the focus is plotted at the top in Fig. 8a, on the right side. The amplitude ratio for the fundamental harmonics of the phase-conjugate and incident waves was about 10. In this case, the peak differential pressure in the phase-conjugate wave, i.e., the difference between the positive and negative peaks of the wave profile, was 6.95 MPa. Despite the increase in the relative level of sidelobes in the fundamental harmonic, the field of the nonlinear phase-conjugate wave on the whole demonstrates a high quality of phase-conjugation focusing of an ultrasonic beam in both the position with respect to the axis of the incident beam and the width of the principal maximum. From the point of view of nonlinear ultrasonic imaging, the fact that the energy of higher harmonics is much better localized in the focus region than that of the first harmonic is especially interesting. Thus, this specific characteristic of homogeneous nonlinear media is also retained when the medium is inhomogeneous.

The results of experiments on phase conjugation with amplification that were described in the first sections provide an opportunity to judge the reproduction quality of the acoustic field at the maximum pressure amplitude of the phase-conjugate wave. One can see that automated phase-conjugation focusing of amplified phase-conjugate waves with compensation for phase aberrations produced by the inhomogeneities of the propagation medium is possible even in the case of a considerable nonlinear distortion of the waveform.

3. GENERATION OF THE SECOND ACOUSTIC HARMONIC BY A PHASE-CONJUGATE WAVE IN AN INHOMOGENEOUS REFRACTIVE MEDIUM WITHOUT DISPERSION: APPROXIMATION OF NONLINEAR GEOMETRICAL ACOUSTICS

Results of experimental observations of the compensation of phase distortions in the process of nonlinear propagation of a phase-conjugate wave in the presence of aberration layers [21, 23, 24] were substantiated theoretically in [21, 22]. In the approximation of nonlinear geometrical acoustics, it was demonstrated that retrofocusing in this case is a consequence of two effects: the phase conjugation at the fundamental frequency and the strong correlation of the phases of harmonics generated by the phase-conjugate wave.

For example, within the framework of nonlinear geometrical acoustics, i.e., the approach developed for dispersionless inhomogeneous media in [21], the process of the second harmonic generation in a quasi-linear approximation is described by the following set of equations:

$$\begin{aligned} \hat{L}\{A_1\} &= 0, \\ \hat{L}\{A_2\} &= 2i\omega\beta A_1^2, \end{aligned} \tag{1}$$

where A_n are the amplitudes of harmonics ($n = 1, 2$) and the operator $\hat{L}$ is represented in the form

$$\hat{L} = \frac{\partial}{\partial z} + \nu + (\boldsymbol{\xi}\boldsymbol{\nabla}_\perp).$$

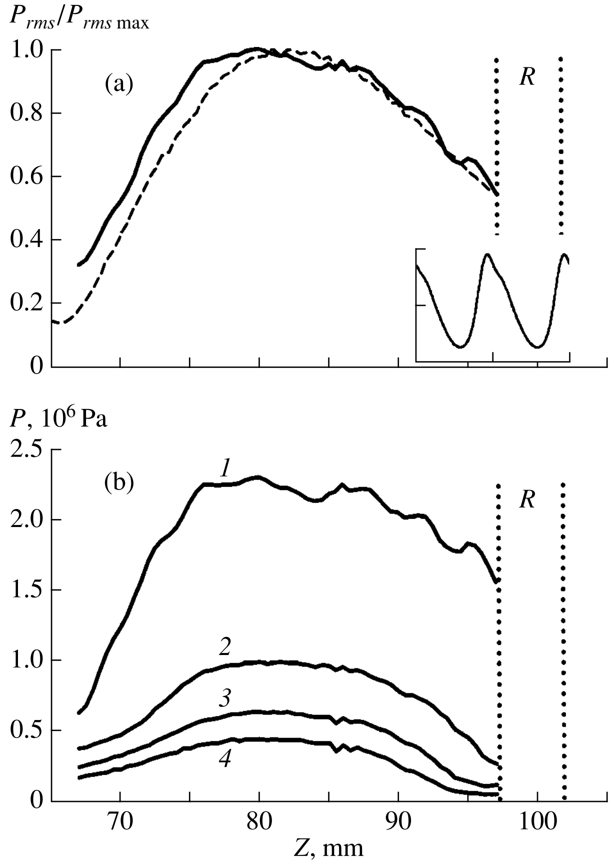

Fig. 7. Distribution of sound pressure along the beam axis: (a) the normalized effective value and (b) the amplitudes of the first four harmonics. The solid curves correspond to the phase-conjugate wave, and the dashed line, to the incident wave. The dotted line indicates the position of the phase layer *R*; numbers *1–4* indicate the numbers of the harmonics, and *Z* is the distance to the source. The shape of the phase-conjugate wave at the beam axis at the point *Z* = 97 mm is given on the right side of Fig. 7a, at the bottom [23].

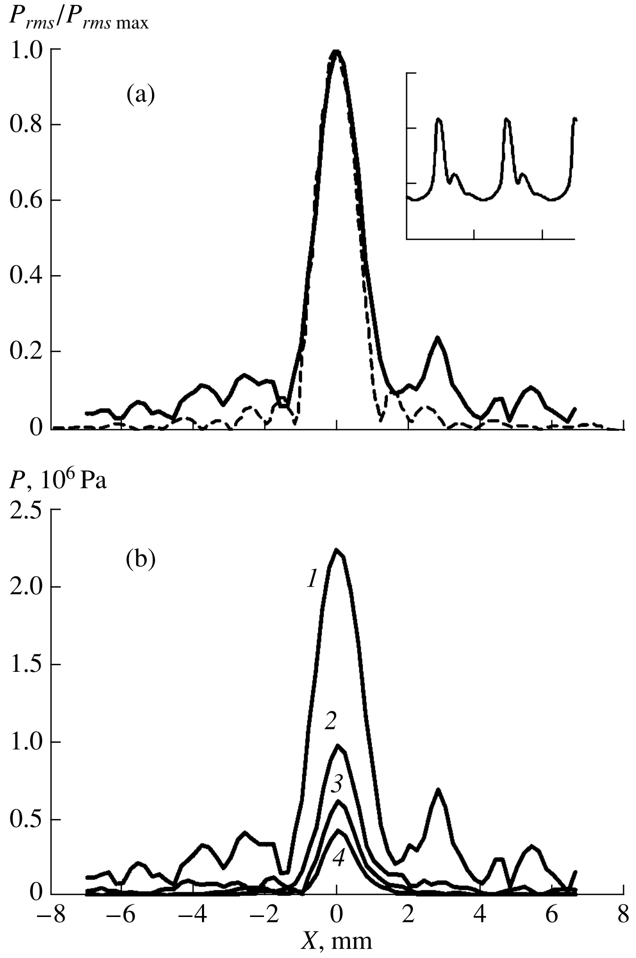

Fig. 8. Focal distribution of the sound pressure field: (a) the normalized effective value and (b) the amplitudes of the first four harmonics. The solid curves correspond to the phase-conjugate wave, and the dashed line, to the incident wave; numbers *1–4* indicate the numbers of the harmonics, and *X* is the distance from the beam axis. The shape of the phase-conjugate wave at the point *X* = 0 is given at the top, on the right side [23].

Here, $\boldsymbol{\xi} = c\nabla_\perp\psi$; $v = -\frac{\partial}{\partial z}\ln\sqrt{\rho c} + \frac{c}{2}(\boldsymbol{\nabla}_\perp^2\psi)$; and ρ, c, and β are the density, sound velocity, and normalized nonlinear parameter, respectively. The eikonal $\varphi_n = -in\omega\Psi(\mathbf{r})$ of the harmonics is described by the general equation [30]

$$\frac{\partial\psi}{\partial z} + \frac{1}{2c}\Phi(\mathbf{r}) + \frac{c}{2}(\boldsymbol{\nabla}_\perp\psi)^2 = 0, \qquad (2)$$

where $\Phi(\mathbf{r})$ is the inhomogeneous part of the refractive index of the medium. The identity of the eikonals reflects the well-known specific feature of the interaction of nonlinear wave harmonics in a dispersionless medium that leads to their cascade generation up to the shock front formation in the case of a fully developed nonlinearity.

In the case of the second harmonic generation under study, the amplitude of the second harmonic can be obtained from Eq. (1) in the form

$$A_2(\mathbf{r}) = Q(\mathbf{r})A_1^2(\mathbf{r}), \qquad (3)$$

where the function $Q(\mathbf{r})$ depends on the eikonal gradient and the parameters of the medium and satisfies the equation

$$\frac{\partial Q}{\partial z} + (\boldsymbol{\xi}\boldsymbol{\nabla}_\perp)Q - vQ = 2i\beta\omega. \qquad (4)$$

Equation (3) shows that, within the framework of nonlinear geometrical acoustics, the spatial distribution of the second harmonic amplitude is modulated by the intensity of the fundamental component in a randomly inhomogeneous medium. Due to the phase conjugation

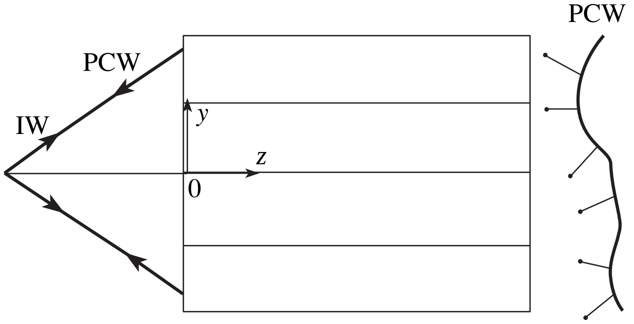

Fig. 9. Statement of the problem: IW refers to the incident wave, and PCW, to the phase-conjugate wave [21].

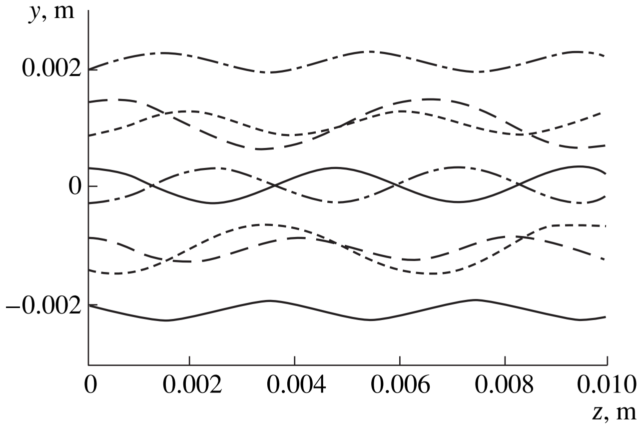

Fig. 10. Acoustic ray pattern in a multilayer medium in the case of a varying refractive index according to the law $\Phi(\mathbf{r}_\perp) = A\sin^2(qy + \theta)$ [22].

of the fundamental component, one can expect that the second harmonic is concentrated within the aperture of the primary acoustic beam propagating from the focus to the phase-conjugating amplifier.

The problem of propagation of the second harmonic in a homogeneous medium between an aberration layer and the focal plane (see Fig. 9) is analogous to the problem on the "phase screen" studied in [31], as applied to the propagation of shockwaves. In a homogeneous medium with the parameters c_0, ρ_0, and β_0, the phase of the focused primary beam is described by the expression $\psi = f(z)r_\perp^2/c_0$. According to the principle of phase conjugation, it is necessary to assume that the fundamental harmonic reproduces its phase–amplitude distribution after being transmitted through an aberration layer. In this case, Eqs. (1–4) have the solution

$$A_2(\mathbf{r}_\perp, z) = A_1^2(\mathbf{r}, z)[Q_1(z) + Q_2(\mathbf{r}_\perp, z)], \qquad (5)$$

where

$$Q_1(z) = 2i\omega_0\beta_0\frac{1}{\gamma(z)}\int_0^z \gamma(z)dz,$$

$$Q_2(\mathbf{r}_\perp, z) = \gamma(z)F[x\gamma(z), y\gamma(z)].$$

Here, $F[x, y]$ is the function describing the boundary conditions for the second harmonic amplitude at the output of the aberration layer ($z = 0$):

$$\gamma(z) = \exp\left(-\int_0^z f(z')dz'\right) \qquad (6)$$
$$= [1 - (1 + iG^{-1})z/d]^{-1},$$

where G is the gain factor of the focusing system and d is the distance between the layer and the focal plane.

The first term in Eq. (5) describes the generation of the second harmonic in the region between the layer and the focal plane. The second term corresponds to the generation in an inhomogeneous layer. The solution $Q(\mathbf{r}_\perp, z)$ to Eq. (4) in the region $z_0 < z < 0$ with the boundary condition $Q(\mathbf{r}_\perp, z_0) = 0$ at the output of the phase-conjugating amplifier ($z = z_0$) defines the function F as $F[x, y] = Q(\mathbf{r}_\perp, z = 0)$. The eikonal in Eq. (4) is tried as a solution to Eq. (2) with the boundary condition $\psi(z = 0) = f(0)r_\perp^2/2c_0$. The latter condition is a consequence of the identity of eikonals for the fundamental and second harmonics. The analysis of a series of particular cases of inhomogeneity (transverse inhomogeneity with an arbitrary dependence on the longitudinal coordinate $\Phi(\mathbf{r}_\perp, z) = \Phi(z)$ and a linear or quadratic dependence of $\Phi(\mathbf{r}_\perp, z)$ on the transverse coordinate $\mathbf{r}_\perp$) shows that the solution $Q(\mathbf{r}_\perp, z) = Q(z)$ does not depend on $\mathbf{r}_\perp$; i.e., $F[x, y]$ = const. A more complex case, in which the inhomogeneity of the refractive index distribution is a periodic function of the transverse coordinate $\Phi(\mathbf{r}_\perp) = A\sin^2(qy + \theta)$, is investigated numerically in [22]. The corresponding pattern of acoustic rays that coincides for both harmonics because of the aforementioned coincidence of eikonals is given in Fig. 10. The evolution of the transverse distribution of the second harmonic amplitude in the course of approaching the focal plane is shown in Fig. 11. One can see that the major part of the energy of the second harmonic is also concentrated near the focus in this sufficiently complex case. A qualitatively analogous result was obtained for the case of a transversely shifted layer, in which $\theta = \pi/2$.

The examples considered above provide an opportunity to conclude that the high quality of retrofocusing in the course of the nonlinear propagation of phase-conjugate beams in an inhomogeneous dispersionless acoustic medium is a rule rather than an exception, which is confirmed by the data from experiments conducted under different conditions [21, 23, 24]. As for the observed narrowing of the focal distribution of the second harmonic of the phase-conjugate wave in comparison with the incident wave, this effect is explained qualitatively by the expressions of the type of Eqs. (3) and (5).

A detailed investigation of the behavior of phase-conjugate beams in the focal region requires one to go beyond the framework of nonlinear geometrical acoustics and to apply some numerical techniques.

In concluding this section, it is necessary to note that the time–space synchronization of harmonics that follows from the eikonal equation (Eq. (2)) occurs not only in the process of second harmonic generation but is rather a general property of the nonlinear retrofocusing of phase-conjugate waves in dispersionless acoustic media. In the last section of this review, this property is illustrated by the example of the phase conjugation of the second harmonic of the primary wave of finite amplitude with the further nonlinear propagation of a phase-conjugate beam.

4. COMPENSATION OF PHASE DISTORTIONS IN A PHASE-CONJUGATING MICROSCOPE IN THE LINEAR MODE OF ULTRASONIC WAVE PROPAGATION

The first experiments on the application of parametric phase conjugation in linear ultrasonic imaging were conducted using model objects with the employment of a piezoceramic active medium in the subthreshold mode of electromagnetic pumping [14]. Figure 12 presents an ultrasonic imaging scheme, and Fig. 13, acoustic images of a test object under the conditions in which a layer introducing strong phase aberrations (Fig. 13a) is present in the acoustic channel: the picture in Fig. 13b is obtained in a common "transmission" way, and the picture in Fig. 13c, via parametric phase conjugation. Comparison of Figs. 13b and 13c clearly demonstrates the effect of compensation for phase distortions, which makes the images of letters clearly visible, unlike the images obtained with the conventional method.

In contrast to the subthreshold mode in piezoceramics, the over-threshold mode implemented in magnetostriction ceramics with pumping by a magnetic field [15, 16] provides many more opportunities in different areas of ultrasonic technology, including ultrasonic imaging. By shifting the amplification necessary to compensate for the attenuation losses from radio-electronic circuits to a phase-conjugating system, it is possible to improve the signal-to-noise ratio in an image. In contrast to the noise of receiving circuits, the noise (or non-phase-conjugate) components of a phase-conjugating amplifier are subjected, as a rule, to efficient spatial filtration by means of the automated adaptation of phase-conjugate waves to inhomogeneities of the medium and to the geometry of the radiating–receiving transducer. Such spatial filtration in the case of the amplification of a phase-conjugate wave was observed experimentally [32]. In this section, we present experimental data on the visualization of the internal structure of a standard serially produced fracture microchip with the help of over-threshold phase conjugation.

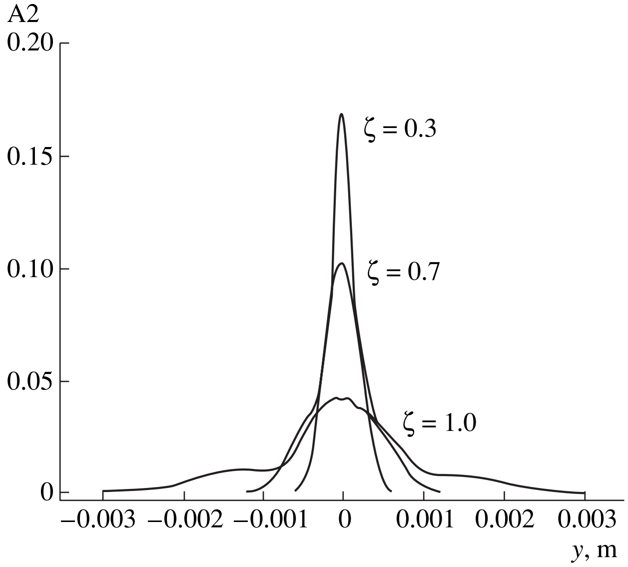

Fig. 11. Evolution of the transverse distribution of the second harmonic amplitude as the distance to the focal plane decreases (A2 is the relative amplitude) [22].

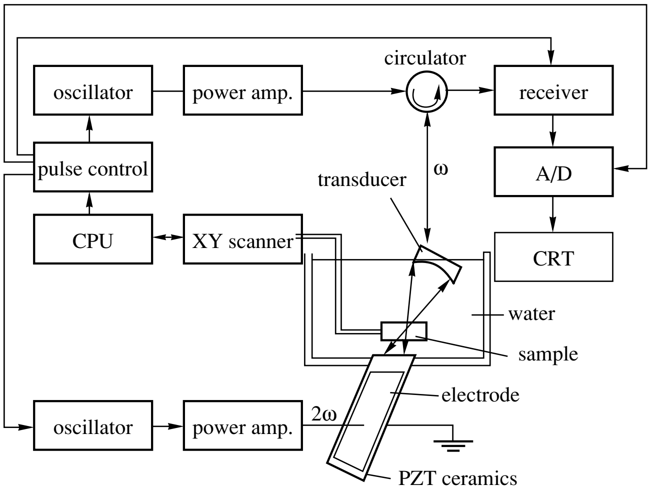

Fig. 12. A model ultrasonic imaging scheme with a phase-conjugating element employing piezoceramics [14].

A simplified scheme of ultrasonic imaging with a phase-conjugating amplifier on the basis of magnetostrictive ceramics is shown in Fig. 14 [14]. A transducer and an object were positioned in a water tank. The object was placed in the focal plane of an ultrasonic transducer with a diameter of 10 mm and a focal length of 3 cm (in water). A cylindrical phase-conjugating element with a diameter of 15 mm and a length of 35 mm, which was made of Ni–Co magnetostrictive ceramics, was located symmetrically with respect to the object in such a way that the cylinder axis coincided with the acoustic axis of the transducer. The distance between the input plane of the phase-conjugating element and

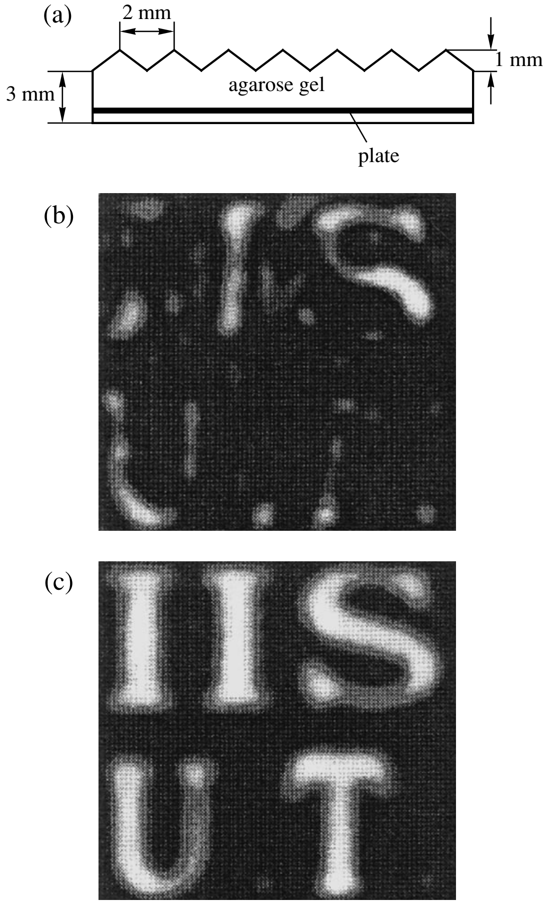

Fig. 13. (b, c) Test acoustic images obtained in the absence of (a) the layer by (b) the conventional transmission method and (c) using the subthreshold parametric ultrasound phase conjugation [13].

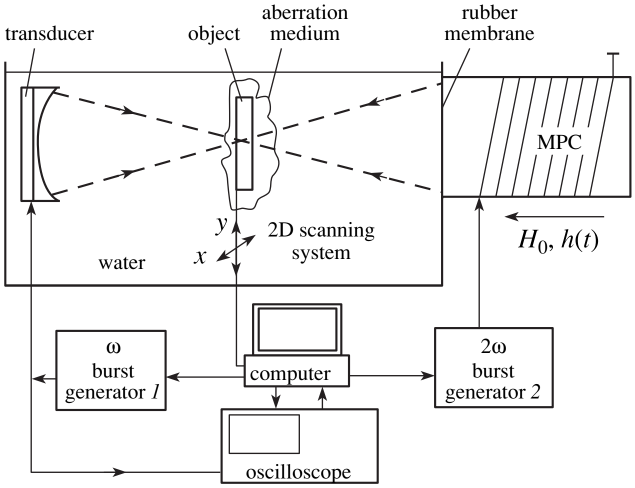

Fig. 14. Simplified model ultrasonic imaging scheme with a phase-conjugating amplifier employing magnetostriction ceramics [14].

the transducer was 85 mm. The working surface of the parametrically active element was introduced in water through an aperture in the basin wall, which was covered by a thin rubber membrane whose external surface was coated with a special acoustic gel to provide an acoustic contact with the ferrite. The transducer was excited by radio pulses with a duration of 2 μs and a carrier frequency of 10 MHz from generator *1*. At the moment when the probing ultrasonic pulse entered the active zone of the phase-conjugating element, a pulse of alternating magnetic field at double sound frequency (i.e., 20 MHz) and with a duration of 20 μs was fed to it from generator *2* through the pumping coil. Under these conditions, the amplification of the phase-conjugating system was 80 dB. A pulse of a phase-conjugate wave, focused at the sample and generated in the phase-conjugating element, propagated in water and was detected by the transducer. In this case, the processes of spatial filtration of the noise component and compensation for phase distortions took place.

The sample that was studied was a standard fracture microchip specially coated with a layer of colophony, which played the role of the medium that introduced aberrations. The layer with the average thickness 3.5 mm was manufactured in several stages in such a way that each subsequent layer was deposited after the end of the crystallization of the preceding one. This procedure provided for the introduction of sufficiently strong distortions into the probing focused ultrasonic beam leaving the layer.

The sample was moved at a step of 100 μm in the focal plane of the transducer with the help of a two-dimensional positioning system. The size of the resulting images was 10×5 mm^2. In the case of line-by-line scanning for each position of the object, a signal from the transducer was digitized in a 10-bit oscilloscope (Le Croy 9430), after which the data arrays fed from the oscilloscope to a computer were transformed into a two-dimensional image obtained in grayscale. As was determined with the help of special measurements, the spatial resolution of the system was 500 μm, which is close to the theoretical limit for these experimental parameters.

Despite the fact that the same transducer was used to radiate and receive the ultrasound, the scheme under consideration is evidently close to the classical "transmission" version of an acoustic microscope. Therefore, to demonstrate the advantages of phase conjugation, images of the same object were obtained using a conventional scheme, in which the phase-conjugating element was replaced by a receiving transducer identical to the radiating one. Here, for the purpose of illustration, two cases were studied: with an aberration layer and without it. The image obtained in the latter case was the "reference" one.

Figure 15a presents a photographic picture of a fracture microchip with the aberration layer deposited on it. The image of the internal structure of the fracture microchip without a layer, which was obtained accord-

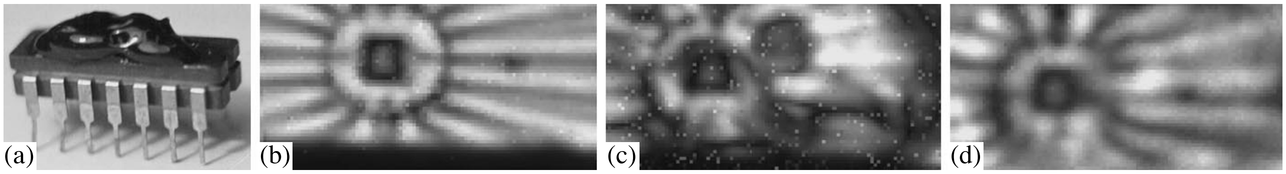

Fig. 15. (a) Photograph of a fracture microchip with a colophony aberration layer applied on top of it with a random shape and structure. (b) Image of the internal structure of the fracture microchip without the layer, with the use of the classical transmission scheme with two transducers. (c) Image of the same fracture microchip region that is distorted by aberrations introduced by the layer. (d) Image obtained using the effect of over-threshold phase-conjugation for the same conditions as in the case of image (c) [14].

ing to the classical "transmission" scheme with two transducers, is given in Fig. 15b. The image of the same fracture microchip region distorted due to the aberrations introduced by the layer is shown in Fig. 15c. Finally, Fig. 15d presents the image obtained using the effect of over-threshold phase conjugation for the same conditions as in Fig. 15c. From a comparison of Figs. 15b–15d, one can see that, although it was impossible to achieve a complete reproduction of the image in Fig. 15b in Fig. 15d, the image in Fig. 15d, obtained with the help of phase conjugation, demonstrates an evident increase in the quality of reproduction of even the fine details of the microcircuit's internal structure in comparison with the image in Fig. 15c, which was obtained by the conventional method.

Generally speaking, it is impossible to improve an image with the help of phase conjugation if the aberration layer located between the transducer and the object introduces distortions that are so strong that they almost completely destroy the focusing of the probing beam. Nevertheless, as was indicated in [14], when sufficiently thin layers are additionally deposited on the side of the object that faces the transducer, acoustic imaging with compensation for phase aberrations proves to be possible.

5. PHASE-CONJUGATION MICROSCOPY USING THE SECOND HARMONIC OF THE PHASE-CONJUGATE WAVE

The technology of over-threshold phase conjugation provides an opportunity to combine the advantages given by both the technique of phase conjugation and the method of harmonic acoustic imaging. In this section, we present the results of experiments designed to demonstrate the feasibility of acoustic imaging with the help of the second harmonic of the phase-conjugate wave [21, 24].

The experimental scheme used in this case is basically analogous to the scheme given in Fig. 14 for the linear mode. The differences are as follows: since, in the receiving mode, a nonlinear ultrasonic wave enriched with harmonics was incident on the transducer, the signal received by the transducer was represented in the form of a Fourier spectrum. The amplitudes of two first harmonics of the received signal were measured for each point of the scanning region, which provided an opportunity to obtain images using both the first and second harmonics of the phase-conjugate wave during a single cycle. A cylindrical phase-conjugating element of an increased size (with a length of 150 mm and a diameter of 29 mm) with a wavy working surface was used in this and subsequent experiments to improve the quality of phase conjugation. The object consisted of two crossed wires 0.12 mm in diameter, which provided an opportunity to determine, in a sufficiently simple way, the resolution achieved in any specific case according to the image obtained. The transverse resolution was measured as the minimal distance between two minimal amplitudes of the received signal that were resolved in a line. The duration of the probing and pumping pulses was 50 μs.

The layer introducing aberrations was manufactured of a silicon polymer and was close in its properties to the one described in Section 4. The average layer thickness was 2 mm. The experimental evaluation of transmission losses in the layer was equal to 4.5 dB at a frequency of 5 MHz.

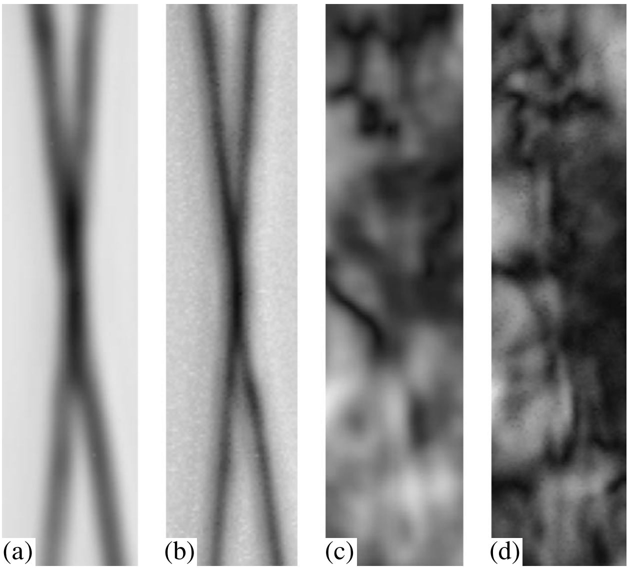

Fig. 16. Acoustic images of the region of wire intersection (a, b) without and (c, d) with the layer. Images obtained at the frequency of 10 MHz are on the left side, and those obtained at the frequency of 20 MHz are on the right side [24].

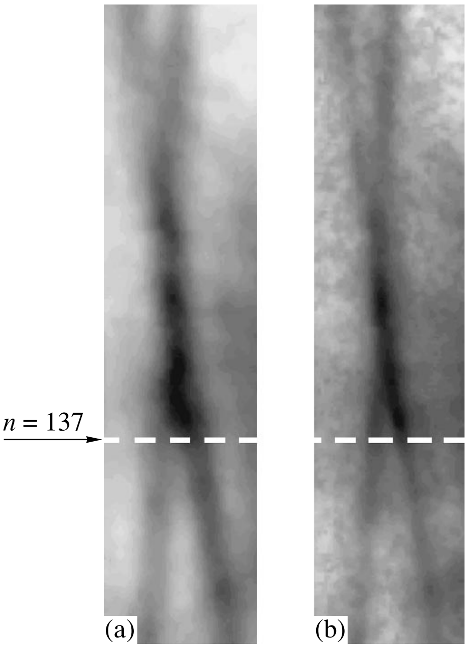

Fig. 17. Acoustic images of the region of wire intersection that were obtained without a layer with the help of phase conjugation. Images obtained at the frequency of 10 MHz are on the left side, and those obtained at the frequency of 20 MHz are on the right side [24].

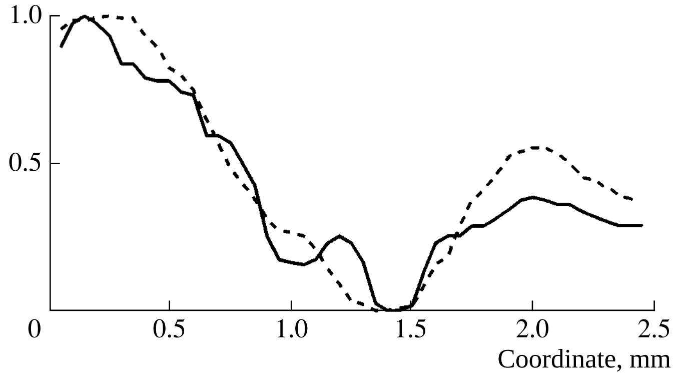

Fig. 18. Distribution of signal level along the row 137 in Fig. 17. The dashed line refers to the signal frequency of 10 MHz, and the solid line, to 20 MHz [24].

The resulting acoustic images of the intersection of the wires are shown in Figs. 16–17 [24]. The dimensions of the region presented in the images are 2.5 × 10 mm. In the case of a scanning step equal to 50 μm, the number of image dots was 50 × 200 = 10000.

Figure 16 presents two pairs of images obtained (a, b) without and (c, d) with the layer with the help of two focused transducers in the transmission mode (see Section 4). The images obtained using the first harmonic (10 MHz) are on the left side (a, c), and those obtained using the second harmonic (20 MHz) are on the right side (b, d). Images in Fig. 17 are grouped according to the same principle, but the difference is that they were obtained using phase conjugation. According to Figs. 16a and 17a, the resolution of the system in both conventional and phase-conjugation versions was 450 and 250 μm at frequencies of 10 and 20 MHz, respectively.

The following conclusions can be drawn from the comparison of Figs. 16 and 17. All images corresponding to the case without the layer differ only slightly. Quite a different situation is observed in the case in which aberrations are introduced into the acoustic channel. One can see that the layer introduces such strong distortions into the images obtained by the conventional technique that the intersection image is almost completely masked. At the same time, in the images obtained with the help of phase conjugation at both harmonics, the intersection can be seen fairly clearly despite the presence of the dark spots originating from uncompensated amplitude distortions. According to the results of Sections 2 and 3, the conjunction of the phase of the second harmonic of the wave radiated by the phase-conjugating element to the phase of the fundamental component provides retrofocusing for the second harmonic as well. Taking into account the corresponding frequency increase, this provides an opportunity to use the nonlinearity of the phase-conjugated wave for acoustic imaging in a phase-inhomogeneous medium with a resolution higher than that in the linear case. The latter property is illustrated in Fig. 18, where the distributions of the signal level along the line shown by dashes in Fig. 17 are shown. One can see that the minimum corresponding to one of the wires is not observed for the signal of the fundamental component (10 MHz), while for the signal of the second harmonic (20 MHz) it is clearly distinguished. In the experiment considered, the system resolution was 600 and 300 μm at frequencies of 10 and 20 MHz, respectively, which differs little from the case in which the object was located in a homogeneous medium.

6. SELECTION OF HARMONICS AT A PARAMETRIC PHASE CONJUGATION OF ULTRASOUND AND THE FREQUENCY MULTIPLICATION IN PHASE-CONJUGATING MICROSCOPY

In the previous sections, we considered the specific features of the formation of phase-conjugate ultrasonic beams of finite amplitude in the mode of phase conjugation with an amplification and under the conditions when the nonlinearity of the incident wave can be ignored. In this case, the fundamental component of the spectrum of the phase-conjugate wave almost reproduced the structure of the field of the incident wave and synchronized the phases of the harmonics generated in the process of its propagation back to the source. At the same time, the parametric technique of phase conjugation can also be used, due to its relatively narrow band, in the mode of selective phase conjugation of single harmonics of the incident wave, when its intensity is sufficient for a noticeable manifestation of the propagation nonlinearity. A specific property of phase conjugation in this case is the fact that the field of the phase-conjugate harmonic, even in the ideal case, cannot reproduce the field of the same harmonic in the incident wave because of the lack of interaction with the harmonic at the fundamental frequency that is necessary for the time reversal. The feasibility of retrofocusing under these conditions becomes questionable. At the same time, the effects of selective phase conjugation of single harmonics are of interest from the point of view of applications and, in particular, because of the prospect of a considerable increase in frequency in systems of harmonic imaging already in the lower orders of nonlinearity. The increase in the resolution of an acoustic microscope in the case of phase conjugation of the second harmonic $2f$ of an incident nonlinear wave at a frequency f with a further analysis of the image of the test object at a frequency $4f$ was demonstrated experimentally in [24]. It was demonstrated that the compensation for phase distortions and the retrofocusing at the object also occur for the $4f$ harmonic. The latter stimulated detailed experimental studies and numerical simulations of the field of a phase-conjugate wave under conditions of selective phase conjugation with amplification of the second harmonic. The experimental results and numerical simulations [33] confirmed that, in the case of a homogeneous nonlinear medium, the retrofocusing of a phase-conjugate harmonic is possible under these conditions, including the case of its nonlinear propagation. A theoretical description of the mechanism of compensation for phase distortions in the process of phase conjugation of the second harmonic with its further propagation in an inhomogeneous nonlinear medium is given in [22].

The simplified experimental scheme [33] is the same as that in Fig. 1. A focusing transducer (Panametrics M307) with a diameter of 27 mm and a focal length of 84 mm radiated an ultrasonic pulse into water. The pulse duration was 30 μs and the carrier frequency was $f = 3$ MHz. The wave excited by the radiator was sufficiently intense so that the generation of higher harmonics ($2f$, $3f$, and so on) occurred in the process of propagation. The level of the second harmonic at distances of 20–25 mm from the radiator did not exceed –35 dB of the level of the first harmonic, which agrees well with the calculation for the case of purely monochromatic radiation. A phase-conjugating element was installed coaxially with the radiator at a distance of 206 mm through an opening in the basin wall. The design and the principle of operation of the phase-conjugating system used and the method of the measurement of the acoustic fields were described in Section 1. The phase conjugation of the second harmonic of the incident wave was provided by parametric pumping. It was a pulse of alternating magnetic field with a duration of 50 μs and a carrier frequency of $2 \times 2f = 12$ MHz, which was generated by a special coil along the axis of the phase-conjugating element at the moment when a pulse of the incident wave entered it. In this case, the amplitude of the generated phase-conjugate wave (at the frequency $2f = 6$ MHz) was, in its turn, sufficient for the intense generation of harmonics ($4f$, $6f$, $8f$, …) in the course of propagation, which is doubtless of interest for many practical applications.

The simulation of the process considered was conducted on the basis of the numerical solution of the Khokhlov–Zabolotskaya–Kuznetsov equation in the time domain. The nonlinear propagation of the incident wave to the phase-conjugating element was calculated under the assumption of piston radiation. The second harmonic of the frequency spectrum ($2f$) was separated with the help of a Fourier transformation in the plane of the working surface of the element, and the values of the Fourier components outside the system aperture were assumed to be equal to zero. The complex conjugate field of the second harmonic was transformed back into the time domain, and, in this case, the value of the system amplification obtained in the experiments was taken into account. Then, the nonlinear propagation of the phase-conjugate and amplified wave back to the radiator was calculated.

The results of measurements and the corresponding calculations are given in Figs. 19–22. Figure 19 presents the (a) axial and (b) transverse distributions of pressure in the incident beam. Transverse scanning was performed at the point $z = 82$ mm, where the second harmonic maximum, which is of interest, is located. The measurements agree quite well with the calculations, and the dependences are typical of a focused beam of finite amplitude. The generation of higher harmonics is observed, their amplitudes grow with distance, and they reach their peaks near the focus. In the focal region, the width of the principal maximum and the relative level of side components decrease with the increase of the harmonic numbers. The time profile of the incident wave at the focal point had typical nonlinear distortions, and the amplitudes of the harmonics $2f$, $3f$, and $4f$ made up 15.6, 3.5, and 2.8% of the first harmonic amplitude, respectively.

The measured distributions of the fundamental harmonic of the phase-conjugate wave (at the frequency $2f$) are given in Fig. 20 in comparison with the incident wave component that is to be phase conjugated. One can see that the phase-conjugate wave is focused. The width of the focal maximum of the fundamental component of the phase-conjugate beam and its axial position differ little from that of the second harmonic of the incident beam. The pressure distributions of the first four harmonics of the beam to be phase conjugated ($2f$, $4f$, $6f$, and $8f$) in the plane $z = 82$ mm and along the beam axis are given in Figs. 21 and 22, respectively. It follows from Fig. 21a that the data on the focal measurements of the harmonics agree well with the numerical model. The calculated and experimental curves for

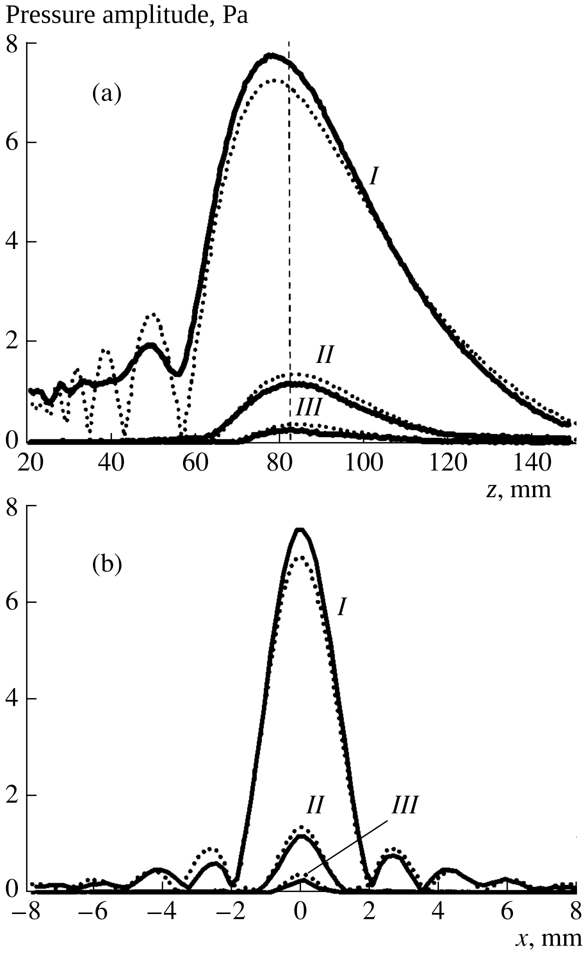

Fig. 19. Distribution of pressure amplitudes for the first three harmonics in the incident beam (a) along the axis and (b) across the beam, at the focus of the second harmonic. Here, z is the distance from the source and x is the distance from the beam axis. The solid lines correspond to the experiment, and the dashed lines, to the calculations. Numbers *I*–*III* correspond to the numbers of harmonics with the frequencies $f = 3$ MHz, $2f = 6$ MHz, and $3f = 9$ MHz, respectively. The dashed line indicates the position of the plane of transverse scanning [33].

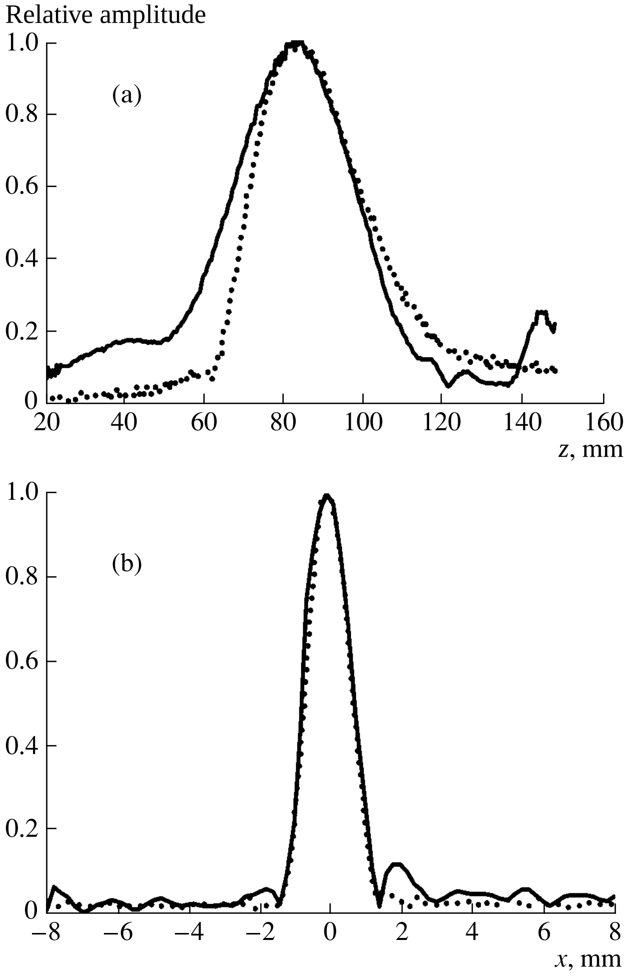

Fig. 20. Comparison of the fields of the fundamental harmonic of a phase-conjugate wave and the second harmonic of an incident wave (a) along the beam axis and (b) across the axis, at the point $z = 82$ mm. The solid line corresponds to the phase-conjugate wave, and the dashed line, to the second harmonic of the incident wave [33].

axial distributions are presented separately in Figs. 22a and 22b for better clarity.

Thus, it was demonstrated both numerically and experimentally that the field of the phase-conjugate wave is also focused and, on the whole, it reproduces well the field of the second harmonic of the incident wave.

As was already indicated, it is possible to design high-resolution systems of phase-conjugation ultrasonic imaging on the basis of the phase conjugation of harmonics. In the case of the same frequency of the phase-conjugate wave, the systems with phase-conjugation of the second harmonic can be better than systems implementing the phase conjugation of the fundamental component because of the reduction of reverberation in the course of propagation due to the reduced relative level of side peaks in the second harmonic of the incident wave and their weakening in the phase-conjugate wave. In the case of a sufficient amplification of the phase-conjugate wave, which provides for its nonlinear propagation back to the source, an acoustic image can be obtained using harmonics, for example, at the fourfold frequency of the incident wave with a corresponding resolution increase.

A simplified scheme of a model of an acoustic microscope implementing the indicated features [24] is similar to that given in Fig. 14. The differences were as follows: an Imasonic transducer with a wide frequency range was excited at a frequency of 5 MHz and used as a receiver for the analysis of pulses at carrier frequencies of 5, 10, and 20 MHz. The crossed thin wires

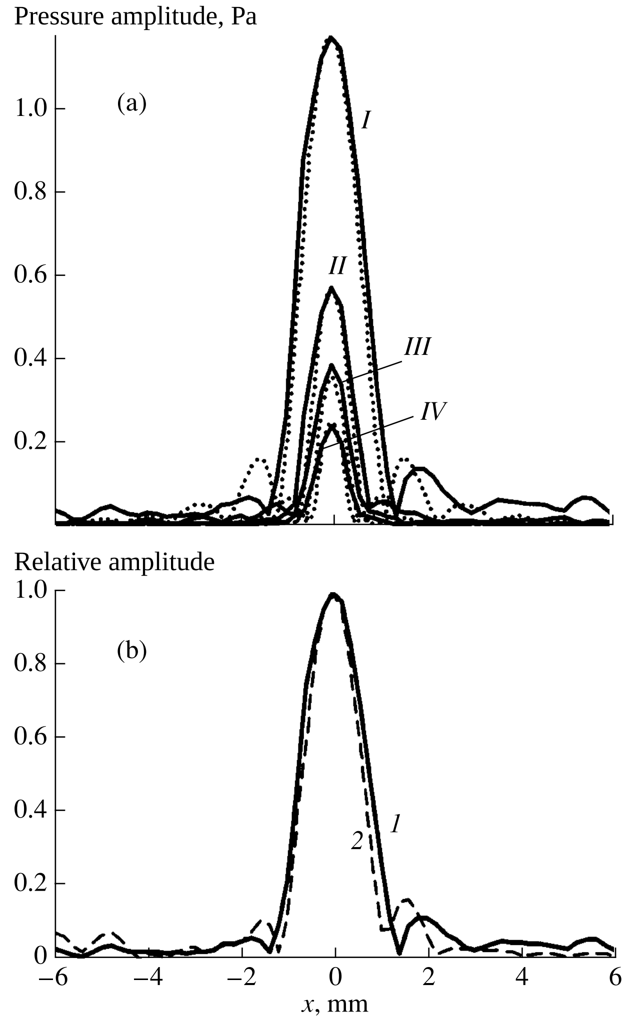

Fig. 21. Transverse distribution of pressure in the phase-conjugate beam at z = 82 mm. (a) Harmonic amplitudes. The solid lines correspond to experiment, and the dashed lines, to calculation. Here, *I–IV* are the numbers of harmonics with the frequencies $2f$ = 6 MHz, $4f$ = 12 MHz, $6f$ = 18 MHz, and $8f$ = 24 MHz, respectively. (b) Comparison of experimental data on phase-conjugation focusing with the help of the phase conjugation of harmonics *I* and *II*. (*1*) harmonic *II* of the incident wave ($2f$ = 6 MHz) is phase-conjugated; (*2*) the fundamental harmonic of the linear incident wave at the frequency of 6 MHz is phase-conjugated [33].

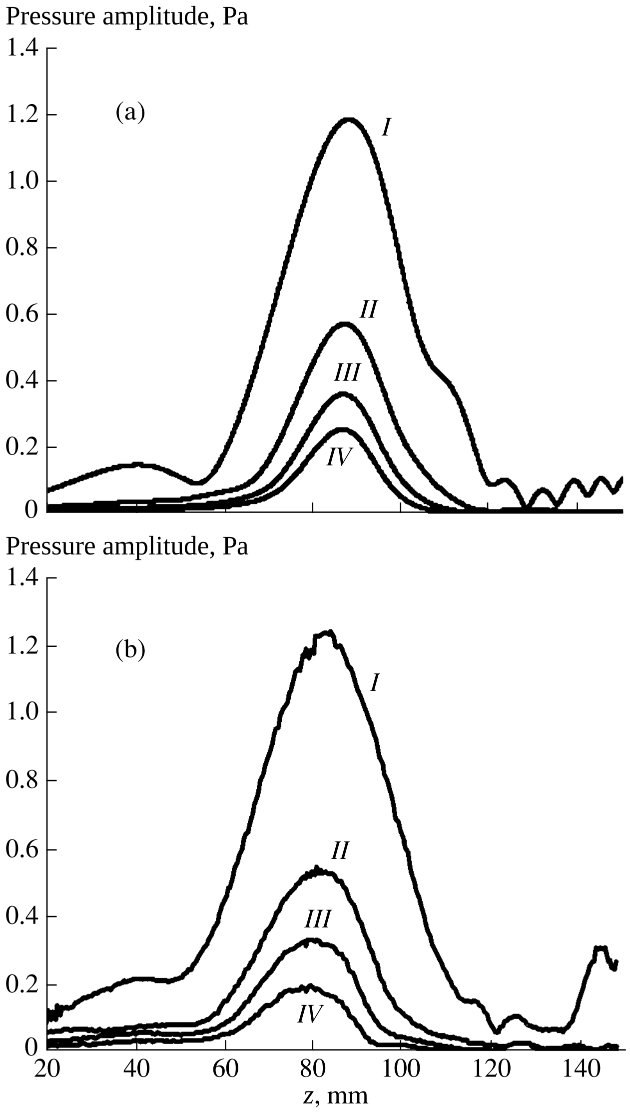

Fig. 22. Dependences of pressure amplitude on the longitudinal coordinate for the first four harmonics of the phase-conjugate beam. (a) Calculation and (b) experiment. Here, z is the distance to the source and *I–IV* are the numbers of harmonics with the frequencies $2f$ = 6 MHz, $4f$ = 12 MHz, $6f$ = 18 MHz, and $8f$ = 24 MHz [33].

described in Section 5 were used as a test object. To simulate a medium producing phase aberrations, a special silicon layer, also described in detail in the preceding sections, was used.

The pumping pulse duration was 50 μs, and the carrier frequency was 20 MHz, which provided the overthreshold mode of parametric phase conjugation with the amplification of ultrasonic pulses of the carrier frequency of 10 MHz. According to the above description, the version in which the carrier frequency of the pulse radiated by the transducer was f = 5 MHz and the amplitude was sufficiently large for the generation of harmonics on the propagation path to the phase-conjugating element was implemented. In this case, the effect of parametric phase conjugation occurred for the second harmonic ($2f$ = 10 MHz) of the incident wave, and the pumping frequency was 20 MHz, as before. After the phase conjugation with amplification, as in the first case, the amplitudes of the two first harmonics (10 and 20 MHz), corresponding to the second and fourth harmonics of the incident wave, were measured.

Figure 23 shows the object images obtained according to the conventional transmission scheme without using an aberration layer. The “reference” images in Figs. 23a and 23b were obtained according to the conventional transmission scheme, in which a phase-con-

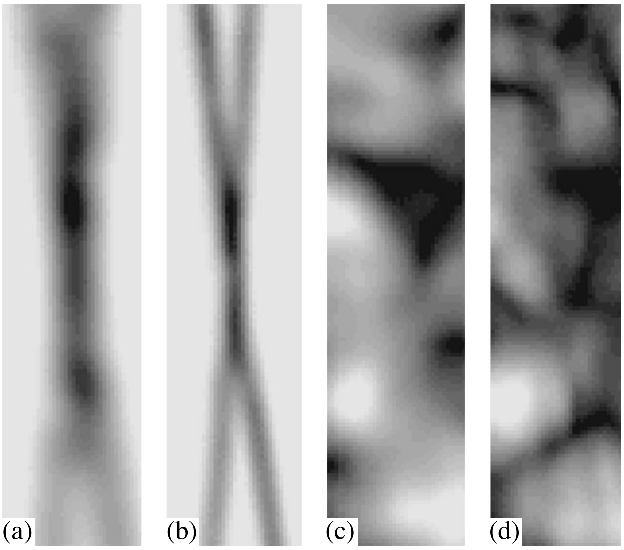

Fig. 23. Acoustic images of the region of wire intersection (a, b) without and (c, d) with the layer. Images obtained at the frequency of 5 MHz are on the left side, and images obtained at the frequency of 10 MHz are on the right side [24].

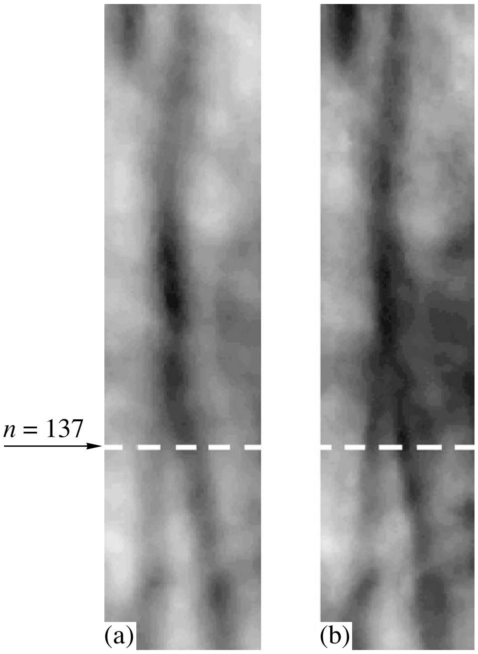

Fig. 24. Acoustic images of the region of wire intersection that were obtained in the presence of a layer with the help of phase conjugation of the second harmonic of the incident wave. Images obtained at the frequency of 10 MHz are on the left side, and images obtained at the frequency of 20 MHz are on the right side [24].

jugating element was replaced by a focusing receiving transducer that detected the first (5 MHz) and second (10 MHz) harmonics of the acoustic signal. The analysis of these images produced the following values of the system resolution: 450 and 250 μm at 10 and 20 MHz, respectively. The images in Figs. 23c and 23d were obtained in the same conventional way but in the presence of an aberration layer. At both frequencies, they demonstrate an almost total masking of the object.

The images obtained using phase conjugation of the second harmonic (10 MHz) of the incident wave in the presence of the layer are given in Fig. 24. In this case, the (a) first and (b) second harmonics of the phase-conjugate wave (10 and 20 MHz, respectively) were detected. Thus, the experimental conditions were identical to the case shown in Fig. 23.

A comparison of the images obtained via the two methods indicated the following. First, both images obtained using phase conjugation demonstrate the effect of distortion compensation: the object becomes visible. This can be explained by the synchronization of the phase of the second harmonic of the phase-conjugate wave with the phase of the fundamental component of the incident wave, which is reconstructed by means of the effect of time reversal (see also Section 3). The field distribution for the second harmonic of the phase-conjugate wave follows the distribution for the focused first one in the course of its propagation through the aberration layer. The plot in Fig. 25 shows the amplitude distribution of the signal along one of the lines of the images shown in Fig. 24. The measured value of the resolution at the frequency of 10 MHz was equal to 500 μm, and it was 300 μm at the frequency 20 MHz, which is close to the values obtained according to the data of Fig. 18. Note again that, in this case, the phase conjugation was performed for the second harmonic of the incident wave generated by a radiator operating at a frequency of 5 MHz. The relatively high noise level in Figs. 17b and 24b can be explained by the droop of the amplitude–frequency characteristic of the transducer with the resonance frequency 10 MHz. It is also clear that the distortion compensation at the frequency 20 MHz is incomplete.

The results given in Figs. 20–22, 24, and 25 provide grounds for the following conclusions. Over-threshold phase-conjugation can be used successfully for the phase conjugation of selected harmonic components of incident radiation. The amplitude of the phase-conjugate wave in the case of over-threshold phase conjugation with amplification can be sufficiently high for the wave to evolve nonlinearly in the process of propagation. In this case, the aberrations introduced by the propagation medium are compensated by both the general properties of the effect of phase conjugation and the synchronization of harmonic phases in the nonlinear acoustic wave. The resolution obtained for a certain frequency of the received signal (10 or 20 MHz) is approximately the same, independently of which (the first or the second) harmonic of incident radiation was phase conjugated. Therefore, in the case of radiation of an incident wave at a frequency of 5 MHz in the presence of strong phase distortions, a higher resolution was obtained for the second and fourth harmonics.

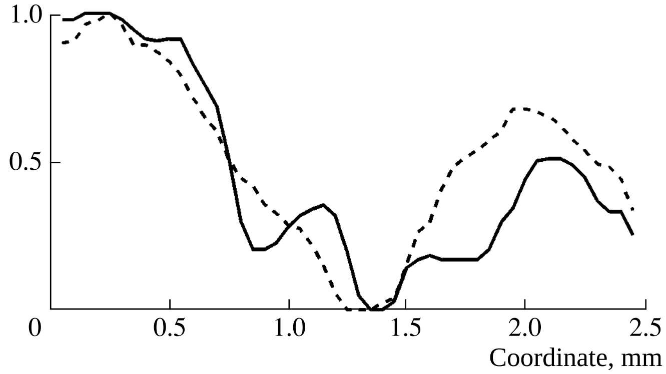

Fig. 25. Distribution of the signal level along row 137 in Fig. 24. The dashed line corresponds to the signal frequency of 10 MHz, and the solid line, to 20 MHz [24].

Implementation of the technique of over-threshold phase conjugation provides an opportunity to combine spectral selection with parametric phase conjugation and a subsequent generation of higher harmonics. In this case, a simultaneous growth of the system resolution and compensation for phase distortions in acoustic images are observed. It is necessary to note in conclusion that, due to the high amplification realized in the case of over-threshold phase conjugation, the scheme considered above can be also used with higher harmonics, for example, the third and fourth ones.

CONCLUSIONS

The experimental and theoretical results described above demonstrate many fundamental features of the phenomenon of phase conjugation under the conditions of nonlinear propagation of ultrasonic waves. As has been demonstrated above, a violation of the invariance of the acoustic field with respect to time reversal under the conditions of phase conjugation with amplification does not prevent automated retrofocusing of phase-conjugate waves in dispersionless nonlinear media. The compensation for phase distortions introduced by inhomogeneity of the propagation medium is observed in the retrofocusing of a phase-conjugate wave not only in the linear propagation mode but also under the conditions of a cascade harmonic generation up to the formation of shockwave profiles. It is demonstrated that the retrofocusing in an inhomogeneous refractive medium is observed in both the phase conjugation of the fundamental harmonic and the selective phase conjugation of the single harmonic components of the incident nonlinear sound wave.

The results obtained can serve as a basis for the application of phase conjugation in nonlinear ultrasonic imaging. The possibility of combining the advantages of the phase-conjugation technique and harmonic imaging with simultaneous compensation for phase distortions and a higher resolution of acoustic imaging is demonstrated.

The experiments described above reveal the good prospects for the utilization of phase-conjugation amplifiers operating in the over-threshold mode of magnetoacoustic parametric interaction as an efficient instrument for physical studies in nonlinear acoustics.

ACKNOWLEDGMENTS

The work on this review was initiated by L.M. Lyamshev. To our great regret, he is not with us anymore. However, we consider ourselves to be indebted to his memory to present this paper.

The research was supported in part by the US Civilian Research and Development Foundation for the Independent States of the Former Soviet Union, project no. RP2-2367-MO-02. The work of the Russian participants was partially supported by the Russian Foundation for Basic Research, project nos. 00-15-96636, 02-02-16916, 01-02-16610, and 02-02-22002; by the Foundation of the President of the Russian Federation, grant no. NSh-1553.2003.2; by the French foundation “Programmes Internationaux de Cooperation Scientifique,” project no. PICS 1573; and by the Russian–French program “PAI-RUSSIER, Dossier no. 04585TK.”

We are especially grateful to Academician F.V. Bunkin for his constant attention to the work on parametric phase conjugation of ultrasound.

REFERENCES

1. T. Christopher, IEEE Trans. Ultrason. Ferroelectr. Freq. Control **44**, 125 (1997).
2. B. Ward, A. C. Baker, and V. F. Humphrey, J. Acoust. Soc. Am. **101**, 143 (1997).
3. M. A. Averkiou, D. N. Roundhill, and J. E. Powers, in *Proceedings of the IEEE Ultrasonic Symposium*, Ed. by S. C. Schneider *et al.* (IEEE, 1997), Vol. 2, p. 1561.
4. *Nonlinear Acoustics*, Ed. by M. F. Hamilton and D. T. Blackstock (Academic, New York, 1997), pp. 256–259.
5. M. Averkiou, in *Proceedings of IEEE Ultrasonic Symposium* (2000), Vol. 2, p. 1563.
6. R. Kompfner and R. A. Lemons, Appl. Phys. Lett. **28**, 295 (1976).
7. I. Solodov, Ultrasonics **36**, 383 (1998).
8. P. Wu and T. Stepinski, in *Proceedings of IEEE Ultrasonic Symposium* (2000), Vol. 1, p. 801.
9. A. P. Brysev, F. V. Bunkin, L. M. Krutyanskiĭ, *et al.*, Pis’ma Zh. Éksp. Teor. Fiz. **61**, 454 (1995) [JETP Lett. **61**, 464 (1995)].
10. A. P. Brysev, L. M. Krutyanskiĭ, and V. L. Preobrazhenskiĭ, Usp. Fiz. Nauk **168**, 877 (1998) [Phys. Usp. **41**, 793 (1998)].
11. M. Fink, C. Prada, and F. Wu, in *Proceedings of IEEE Ultrasonic Symposium* (1989), Vol. 2, p. 681.
12. K. Yamamoto, M. Ohno, A. Kokubo, *et al.*, J. Acoust. Soc. Am. **106**, 1330 (1999).
13. K. Yamamoto, M. Ohno, A. Kokubo, *et al.*, J. Acoust. Soc. Am. **106**, 1339 (1999).

14. A. Brysev, L. Krutyansky, P. Pernod, and V. Preobrazhensky, Appl. Phys. Lett. **76**, 3133 (2000).
15. A. P. Brysev, F. V. Bunkin, D. V. Vlasov, *et al.*, Akust. Zh. **34**, 986 (1988) [Sov. Phys. Acoust. **34**, 567 (1988)].
16. A. P. Brysev, F. V. Bunkin, D. V. Vlasov, *et al.*, Akust. Zh. **34**, 1120 (1988) [Sov. Phys. Acoust. **34**, 642 (1988)].
17. A. P. Brysev, L. M. Krutyansky, and V. L. Preobrazhensky, Bull. Russ. Acad. Sci., Ser. Phys., Suppl. Phys. Vibr. **9** (1), 52 (2001).
18. A. P. Brysev, F. V. Bunkin, M. F. Hamilton, *et al.*, Akust. Zh. **44**, 738 (1998) [Acoust. Phys. **44**, 641 (1998)].
19. A. P. Brysev, L. M. Krutyansky, V. L. Preobrazhensky, *et al.*, in *Nonlinear Acoustics at the Turn of the Millennium: Proceedings of 15th ISNA, Goettingen, Germany, 1999*, Ed. by W. Lauterborn and T. Kurz (Am. Inst. Phys., Melvill, N.Y., 2000), Vol. 1, p. 183.
20. K. B. Cunningham, M. F. Hamilton, A. P. Brysev, and L. M. Krutyansky, J. Acoust. Soc. Am. **109**, 2668 (2001).
21. Yu. Pylnov, P. Pernod, and V. Preobrazhensky, Appl. Phys. Lett. **78**, 553 (2001).
22. V. Preobrazhensky and P. Pernod, in *Proceedings of 17th International Congress on Acoustics* (Rome, 2001), Vol. 1, Part A, p. 25.
23. A. P. Brysev, F. V. Bunkin, R. V. Klopotov, *et al.*, Pis'ma Zh. Éksp. Teor. Fiz. **73**, 434 (2001) [JETP Lett. **73**, 389 (2001)].
24. A. Brysev, F. Bunkin, L. Krutyansky, *et al.*, IEEE Trans. Ultrason. Ferroelectr. Freq. Control **49** (4), 409 (2002).
25. N. S. Bakhvalov, Ya. M. Zhileĭkin, and E. A. Zabolotskaya, *Nonlinear Theory of Sound Beams* (Nauka, Moscow, 1982; Am. Inst. Phys., New York, 1987).
26. A. P. Brysev, F. V. Bunkin, L. M. Krutyanskiĭ, *et al.*, Akust. Zh. **43**, 244 (1997) [Acoust. Phys. **43**, 207 (1997)].
27. A. Brysev, R. Klopotov, and L. Krutyansky, Ultrasonics **40**, 329 (2002).
28. Y.-S. Lee and M. F. Hamilton, J. Acoust. Soc. Am. **97**, 906 (1995).
29. A. Brysev, K. Cunningham, M. Hamilton, *et al.*, in *Proceedings of the 17th International Congress on Acoustics, ICA17* (Rome, 2001), CD-version.
30. O. Rudenko and A. K. Sukhorukova, Akust. Zh. **37**, 753 (1991) [Sov. Phys. Acoust. **37**, 392 (1991)].
31. O. Rudenko and V. Khokhlova, Akust. Zh. **40**, 126 (1994) [Acoust. Phys. **40**, 111 (1994)].
32. A. P. Brysev, F. V. Bunkin, D. V. Vlasov, *et al.*, Opt. Acoust. Rev. **1** (1), 107 (1990).
33. A. P. Brysev, F. V. Bunkin, M. F. Hamilton, *et al.*, Akust. Zh. **49**, 18 (2003) [Acoust. Phys. **49**, 19 (2003)].

Translated by M. Lyamshev

Acoustical Physics, Vol. 50, No. 6, 2004, pp. 641–646. Translated from Akusticheskiĭ Zhurnal, Vol. 50, No. 6, 2004, pp. 744–750.
Original Russian Text Copyright © 2004 by Bardyshev.

Testing Underwater Bottom-Moored Antenna Arrays in the Sea and in a Man-Made Lake

V. I. Bardyshev
Andreev Acoustics Institute, Russian Academy of Sciences, ul. Shvernika 4, Moscow, 117036 Russia
e-mail: bvp@akin.ru

Received May 15, 2003

Abstract—Measurements of response, gain, and noise immunity are carried out for an underwater compensated additive receiving array with randomly spaced hydrophones that is moored at the bottom of a man-made lake with multimode sound propagation. The in-sea locating ability of a similar array is demonstrated with the sources of noiselike signals at frequencies of 5–100 Hz. A dedicated numerical processor is developed and tested for processing the signals received by a random underwater array. *© 2004 MAIK “Nauka/Interperiodica”.*

Receiving underwater acoustic arrays moored at the sea bottom are used for monitoring ship traffic in watched regions [1]; for exploring biological [2], seismic [3], and other sources of sound signals; and for studying sound propagation in the ocean. If some hydrophones fail or shift from their positions, the array elements become randomly spaced with a mean distance $b > \lambda/2$ between the array nodes (λ is the acoustic wavelength). By using the methods of acoustical positioning, one can measure the coordinates of the shifted hydrophones and, by properly compensating the array, restore its working ability [4].

The theory [5–7] offers a way of obtaining the characteristics of random compensated thinned arrays in a homogeneous medium that does not distort signals. In natural underwater waveguides with inaccurately specified parameters and multimode propagation, the calculations of the array characteristics prove to be unreliable and experimental studies become important. In natural environments, the array response, rather than its directivity pattern, [8, 9] is usually measured. In some cases, it is advantageous to perform such measurements in freshwater basins of sufficient size [9]. Such navigable basins are close to coastal sea regions in character of sound propagation and in sources of ambient noise. With some restrictions, data from measurements carried out in freshwater basins can be recalculated to the conditions of sea regions with an appropriate scale factor K, which characterizes the increase in all sizes, including the acoustic wavelength. In comparison with in-sea experiments, the freshwater measurements are much less expensive, simpler in implementation, and not limited by meteorological factors and time.

This paper reports on the measurements of the response, gain, and noise immunity of a randomly thinned compensated additive array in the Ivan’kovskoe freshwater man-made lake (the so-called Moscow Sea). The specific feature of this lake is an abnormally low velocity c_b = 100–300 m/s of the compressional waves in the upper layer of the bottom sediments, which is caused by the presence of small methane bubbles produced by anaerobic bacteria [10–13]. Similar values of c_b = 76–168 m/s have been obtained in a freshwater basin in the USA [14].

According to measurements at $kH \geq \pi$ and $r/H > 2$–3, normal-wave (mode) sound propagation takes place in the Ivan’kovskoe lake [10]. Here, $k = 2\pi/\lambda$, r is the horizontal distance between the transmission and reception points, and H is the lake depth. At $\pi \leq kH < 6.5$, only the first mode propagates (for single-mode propagation, the experimental data agree with the calculations). At $kH > 6.5$, modes of the first and higher orders propagate [10].

In view of the aforementioned considerations, let us use the approximate expressions proposed in [12]:

$$p(t) = p_0 r^{-1/2} \exp(iwt) \times \sum_{n=1}^{N} m_n^{-1/2} \exp(-im_n r) \sin(l_n z_0) \sin(l_n z), \tag{1}$$

$$m_n = (k^2 - l_n^2)^{1/2} \approx [k^2 - (\pi n/H)^2 - i\pi\rho_b c_b n^2/\rho f H_b^3]^{1/2},$$

$$l_n = \frac{n\pi}{H_b}(1 + i\xi), \quad \xi = \rho_b c_b/w\rho H_b, \quad N = 2H_b/\lambda,$$

$$H_b = H + \Delta H,$$

where $p(t)$ is the varying sound pressure, t is the current time, r is the distance, p_0 is the amplitude of the sound pressure normalized to r = 1 m, i is the imaginary unit, $w = 2\pi f$, f is the frequency, m_n and l_n are the horizontal and vertical components of the wave vector, n is the ordinal number of the mode, N is the maximal number

Table 1

f, Hz	$\bar{H}$, m	H, m	H_0, m	$k\bar{H}$	kr	N	N_e
290	3.7	3.8	4.7	4.8	91.4	1	1
400	3.9	4.0	4.9	11.2	126.1	2	1
3150	4.4	4.5	5.4	62.1	993.2	19	8

of the propagating mode, and $\Delta H = 0.15$ m. A point omnidirectional sound source is at a depth z_0.

At $\xi \ll 1$, one can set $l_n = n\pi/H_b$, and the phase velocity of the signal is

$$v_n = c[1 - (n\lambda/2H_b)^2]^{-1/2}. \tag{2}$$

The amplitude of the nth mode takes the form

$$\begin{aligned} p_n(r) &= p_0 r^{-1/2}\exp(-\alpha_n r) m_n^{-1/2}\sin(l_n z_0), \\ m_n &= [k^2 - (n\pi/H_b)^2]^{1/2}. \end{aligned} \tag{3}$$

The attenuation coefficient of the nth mode can be written as

$$\alpha_n = \rho_b c_b c n^2/4\rho f^2 H_b^3 [I - (n\lambda/2H_b)^2]^{1/2}, \tag{4}$$

and the amplitude distribution in this mode is

$$p_n(Z) \approx \sin(\pi n z/H_b)\sin(\pi n z_0/H_b). \tag{5}$$

The aforementioned expressions were confirmed in a laboratory experiment with the use of an experimental system modeling the underwater sound channel with the given parameters and pressure-release boundaries. Qualitatively, the equations were also confirmed in measurements [12] performed at the Ivan'kovskoye lake at a frequency of 3200 Hz with $kH = 27.7$.

In [13], the sound pressure and oscillation velocity computer-calculated with a more accurate algorithm were compared with the data obtained at the Ivan'kovskoye lake on the propagation of a tonal signal at $N > 1$. A qualitative but not quantitative confirmation of the calculations was demonstrated. At $kr \gg 1$, the phases of the modes are rather sensitive to changes in their phase velocities under the influence of varying depths and acoustic parameters of the bottom along the propagation path. One cannot measure these parameters with the required accuracy and detail, and reliable calculations are impossible. However, the calculations can serve as qualitative estimations and for the elucidation of the experimental data.

Let us proceed to our experiments at the Ivan'kovskoye lake. First of all, the propagation conditions were tested on the experimental path. The depths were measured, and the water and sediments were sampled along the path. Water temperature, wind speed, and the height of wind waves were periodically measured. The temperature was constant within the water layer and equaled +7°C. The water salinity proved to be lower than the sensitivity of the probe (less than 1‰). The calculated sound speed in the water was $c = 1434.8$ m/s. The wind speed was lower than 2 m/s with a resulting rms elevation of the surface of $\sigma \approx 2$ cm, which was much lower than the acoustic wavelength $\ll\lambda$; hence, the surface scattering was weak. The distance was $r = 72$ m, and the depths along the propagation path deviated from the mean value $\bar{H}$ by ±0.9 m with a horizontal roughness scale of about 30 m. Table 1 summarizes the depths H_0 and H at the transmission and reception points, the parameter $k\bar{H}$, and the calculated higher numbers N and N_e of the propagating and energy-dominating modes. The latter modes are treated as those that, in total, contain 90% or more of the signal energy at the distance r. The different depths in the measurements at different frequencies are caused by the variable operation regime of the nearby hydroelectric station and overflow dam during the experiment. According to Eq. (4), the attenuation coefficient of the modes is approximately proportional to n^2, and the modes with numbers $n > N_e$ are strongly attenuated at $kr \gg 1$. The quantities N and N_e were calculated according to Eqs. (1)–(4).

The sound source was deployed on a cable at the depth z_0, which was measured from the water surface to its geometric center. The lifting device was installed on a platform mounted on piles. At the distance $r = 72$ m from the source, a marked vertical mast, along which the receiving hydrophone could move, was bottom-moored. The mast was also used to measure the water level and the depth H. The ratio of the signal to the interfering noise was higher than 20 dB. Figure 1 shows the measured and calculated dependences $|p(z)|$ of the signal amplitudes on depth. The calculations were performed according to Eqs. (1)–(5). At frequencies of 290 and 400 Hz, the experimental dependences agree well with the calculated ones. At 290 Hz, the first mode is the only propagating one, while at 400 Hz the first and second modes propagate. However, the attenuation coefficient of the second mode is relatively high, and the first mode predominates at the reception points. The data obtained agree well with the model of the underwater sound channel with pressure-release boundaries, which is given by Eqs. (1)–(5). At the frequency 3150 Hz, the measured dependence $|p(z)|$ does not coincide with the calculated one but rather corresponds to the interference of at least five energy-dominating modes. These results are in qualitative agreement with the channel model at hand.

On the whole, these results agree well with those obtained earlier [10–13]. In further calculations, Eqs. (1)–(5) are used, and, according to the recommendations of [10], the following values are specified: $c_b = 200$ m/s and $\rho_b = 1950$ kg/m^3.

On the extension of the path used in measuring $|p(z)|$, a random antenna array was bottom-moored. The signal source was at the same point specified earlier: $z_0 = 3$ m and $H_0 = 4.7$ m. A continuous noise signal was

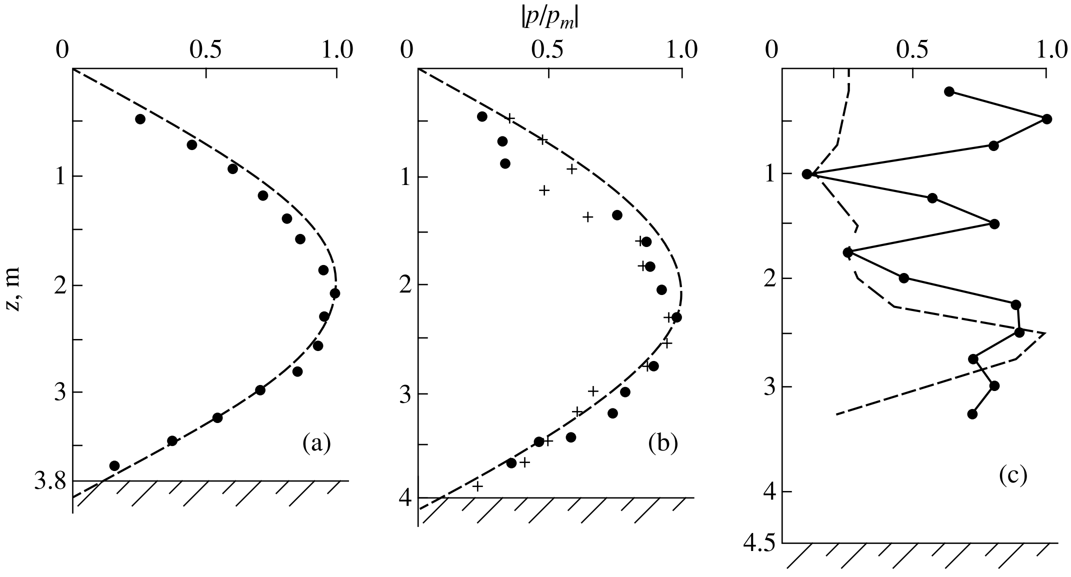

Fig. 1. Calculated (dashed curve) and measured (dots and crosses) depth dependences of the pressure amplitude for tonal sound signals. The amplitudes are normalized to their maximal values. The distance is 72 m from the source. The signal frequencies are as follows: f = (a) 290, (b) 400 (crosses indicate the results of a repeated measurement), and (c) 3150 Hz. According to [12], the value of H is increased by 0.15 m in the calculations.

transmitted in the frequency band 2500–3000 Hz with the central frequency $\bar{f}$ = 2750 Hz. At c = 1434.8 m/s, the mean acoustic wavelength $\lambda = 0.52$ m corresponded to the latter frequency. The array was mounted on a flat rigid frame and then bottom-moored. The number of hydrophones was $J = 8$, and their centers were at a height of 0.5 m above the bottom. The depth of the basin was $\bar{H}$ = 4.2 m on the path and at the point where the array was placed. Figure 2 shows the layout of the experiment. The array is inscribed into a rectangle with the dimensions 7.5 × 2.5 m. The random offsets of the hydrophone phase centers from the ones shown was no greater than 0.5 cm. The position of the array relative to the transmission point was determined by a measuring tape and amended by acoustic means. In the latter procedure, the source of the noise signal was replaced by a sparker that was deployed at the same point A and emitted intense short pulses. The difference in the arrival times t_{1j} of the sound pulses was measured at the receiver points 1 and j with the standard deviation $\sigma t = 1.3 \times 10^{-5}$ s. The standard deviation of the distance differences from point A to points 1 and j is $\sigma r_{1j} = U_1 \sigma t$, where U_1 is the calculated group velocity of the first mode. In our case, $U_1 \approx c$ and $\sigma r_{1j} \approx 0.02$ m at frequencies of several kilohertz. According to the layout of the experiment, the length of the array baseline is $d = BC$ = 7.5 m = 14.4λ. The rms deviation of the array nodes from the baseline is 0.8 m. The rms deviation of the nodes from those of the equivalent equidistant linear array with the parameters $N = 8$, $d = 7.5$ m, and the internode distance $b = 1.07$ m is 0.37 m along the baseline. The array can be treated as a thinned one, because $b > \lambda$. The distance from the transmission point to the array center is $AD = r = 112.7$ m with $kr = 1361.8$. Table 2 summarizes the calculated mode parameters at point D. It is permissible to assume that the sound field is formed by six initial modes at the array nodes. Modes of higher numbers undergo strong attenuation in their propagation or are only weakly excited.

In processing the outputs of the array hydrophones, powers of both signals and noise were measured along with the normalized cross-correlation functions of the signals and noise received by pairs of hydrophones, the array response as a function of the compensation angle, and the noise immunity of the array. A standard algo-

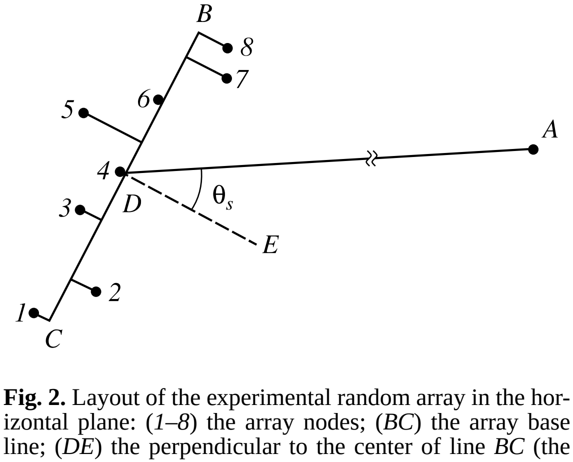

Fig. 2. Layout of the experimental random array in the horizontal plane: (*1*–*8*) the array nodes; (*BC*) the array base line; (*DE*) the perpendicular to the center of line *BC* (the directrix); and (*A*) the transmission point. The distance to the transmission point is $AD = r = 112.7$ m; $\theta_s = 32°$.

Table 2

n	α_n	v_n, m/s	$\lvert p_n\rvert/\lvert p_4\rvert$
1	2.19×10^{-5}	1434.4	0.66
2	8.82×10^{-4}	1445.2	0.77
3	2.02×10^{-3}	1458.6	0.54
4	3.62×10^{-3}	1478.0	1.0
5	5.74×10^{-3}	1504.1	0.17
6	8.85×10^{-3}	1537.8	0.15
7	1.18×10^{-2}	1581.0	0.005

rithm for processing the output of an additive compensated array was used:

$$D_{asp}(\theta) = \sum_{q=1}^{Q} \left\{ \sum_{j=1}^{J} p_{spj}[t_q - \tau_{1j}(\theta)] \right\}^2, \qquad (6)$$

where $D_{asp}(\theta)$ is the measured array response, i.e., the energy of the signal plus noise at the output of the processing system at the compensation angle θ; q is the ordinal number of the signal sample; j is the ordinal number of the node and the corresponding array channel; J is the number of nodes; P_{spj} is the amplitude of the input signal plus noise for the qth sample; $\tau_{1j}(\theta)$ is the instrumental delay time in the jth channel relative to the first one at the compensation angle θ; $\tau_{1j}(\theta) = d_{1j}\sin\theta_{kj}/V_1$, $\theta_{kj} = (\theta + \theta_{1j})$; θ_{1j} is the angle between the line connecting the first and jth nodes and the array baseline; and d_{1j} is the distance between the first and jth nodes. The time of signal accumulation is $T = (Q - 1)/f_d$, where f_d is the sampling frequency. In our case, $Q = 4096$ and $T = 0.2$ s.

Thus, the signal processing procedure consisted of the time compensation in each array channel, then the summing and squaring of the signals, and, finally, their accumulating over the realization with duration T.

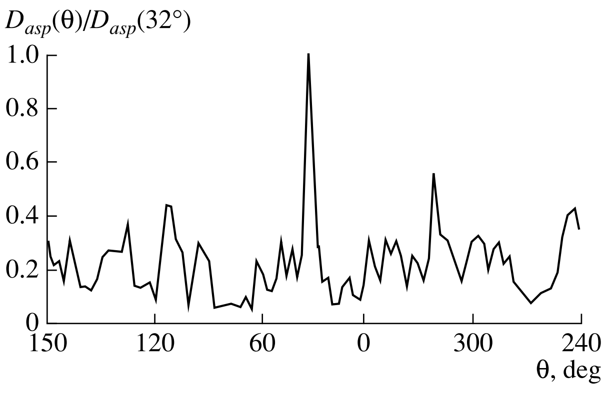

Fig. 3. Measured array response versus the compensation angle θ. The response is normalized to its maximal value at $\theta = \theta_s$.

The array response $D_{ap}(\theta)$ to noise was determined according to Eq. (6), where the quantity p_{spj} was replaced by the noise sample p_{pj} at a switched-off signal source.

Upon averaging over all array channels at the input of the processing system, the energy D_{sp} of the signal plus noise, the energy D_p of noise, and the energy D_s of the signal were calculated as follows:

$$D_{sp} = \frac{1}{J}\sum_{q=1}^{Q}\sum_{j=1}^{J} p_{spj}^2(t_q), \quad D_p = \frac{1}{J}\sum_{q=1}^{Q}\sum_{j=1}^{J} p_{pj}^2(t_q),$$

$$D_s = D_{sp} - D_p.$$

The input signal-to-noise ratio averaged over all channels is $E = D_s/D_p$, and, in our case, $E = 1800$ and $D_s \approx D_{sp}$.

The array response to the signal is $D_{as}(\theta) = D_{asp}(\theta) - D_{ap}(\theta)$. The signal-to-noise ratio at the output of the processing system is $E_a(\theta) = [D_{asp}(\theta) - D_{ap}(\theta)]/D_{ap}(\theta) \approx D_{asp}(\theta)/D_{ap}(\theta)$, $E_a(\theta) \gg 1$, and $D_{as}(\theta) \approx D_{asp}(\theta)$ in our case.

Figure 3 shows the measured dependence of the array response for the compensation angle θ. This dependence is normalized to its maximal value at $\theta = \theta_s$. The side lobes of the response are irregular, which is common to a random array, and all side lobes are lower than the main one in their levels. The maximal level of the side lobes is 0.56; this value is 2.5 dB lower than the level of the main lobe. Thus, a unilateral bearing of a single sound source can be measured. The mean level of the side lobes, which is equal to 0.21, is much higher than the value of $1/E = 5.5 \times 10^{-4}$, and, therefore, the external noise practically does not distort the array response.

The mean level of the side lobes must be close to the value $1/J = 0.125$, which is 2.3 dB lower than the measured level, if the signal is fully correlated ($R_{sij} = 1$) over the array aperture for the compensation angle θ_s and if the interfering noise is fully decorrelated ($R_{pij} = 0$, $i \neq j$).

The measured angular width of the main lobe in the array response is $\Delta\theta_e = 7°$ at a level of –3 dB. For the sake of comparison, we estimate the width $\Delta\theta_T$ of the main lobe in the directivity pattern of a linear compensated array with our values of d, λ, and θ_s. According to [15],

$$\Delta\theta_T = \theta_2 - \theta_1, \quad \theta_{1,2} = \arcsin\left(\sin\theta_s \pm 1.39\frac{\lambda}{\pi d}\right). \qquad (7)$$

If $\lambda = V_1/\bar{f} = 0.52$ m, we obtain $\Delta\theta_T = 5°$.

The observed increase in the width of the main lobe and the deterioration of other array characteristics can be attributed to the decrease in the spatial signal correlation in the course of multimode propagation in the underwater sound channel. To prove this statement, let us estimate the spatial correlation of the signal in view of the phase velocities of the energy-dominating modes. Let the reception points i and j be positioned at the same depths in a vertically stratified waveguide and at the distances r_i and r_j from the transmission point: $r_i - r_j = \Delta r > 0$. A noiselike signal with a uniform spectrum in the frequency band $w_2 - w_1 = \Delta w > 0$ propagates as a sum of energy-dominating modes with the ordinal numbers 1, …, N, which have equal amplitudes and phase velocities $v_1, \ldots, v_N$, $v_N - v_1 = \Delta v > 0$. At point i, the phase of a tonal signal with frequency w_1 is $\varphi_i(w_1) \in \left[w_1\left(t - \frac{r_j}{v_1}\right),\ w_1\left(t - \frac{r_j}{v_N}\right)\right]$. Similar relations are valid for the frequency w_2 at point j. If the instrumental time delay $\Delta t = \Delta r/v_1$ is introduced into the signal at point j, the phase of the signal will be within the interval $\varphi_j(w_1) \in \left[w_1\left(t - \frac{r_j}{v_1}\right),\ w_1\left(t - \frac{r_j}{v_N} - \frac{\Delta r}{v_1}\right)\right]$ at the frequency w_1. Then, for the frequencies w_1 and w_2 at points i and j, the maximal phase difference of the signals will be $\varphi_{ijm}(w_1) = w_1\frac{\Delta r \Delta v}{v_1 v_N}$ and $\varphi_{ijm}(w_2) = w_2\frac{\Delta r \Delta v}{v_1 v_N}$. The cross-correlation function r_{ij} of the tonal signals at points i and j is related to their phase difference as follows: $R_{ij} = \cos\varphi_{ij}$. Specifying $\bar{\varphi}_{ij} \approx \varphi_{ijm}/2$ for the mean phase difference of the noiselike signal, we arrive at the following estimate:

$$R_{ij} \approx \frac{1}{\bar{\varphi}_{ij}(w_2) - \bar{\varphi}_{ij}(w_1)} \int\limits_{\varphi_{ijm}(w_1)}^{\varphi_{ijm}(w_2)} \cos x dx$$

$$= \frac{\sin\bar{\varphi}_{ij}(w_2) - \sin\bar{\varphi}_{ij}(w_1)}{\bar{\varphi}_{ij}(w_2) - \bar{\varphi}_{ij}(w_1)}.$$

At $\varphi_{ijm}(w_1), \varphi_{ijm}(w_2) \ll 1$, $\sin x \approx x - x^3/6$, and

$$R_{ij} \approx 1 - \frac{1}{24}\left(\frac{\Delta r \Delta v}{v_1 v_N}\right)^2 (w_1^2 + w_1 w_2 + w_2^2)$$

$$= 1 - \frac{\pi^2}{6}\left(\frac{\Delta r \Delta v}{v_1 v_N}\right)^2 (f_1^2 + f_1 f_2 + f_2^2) \tag{8}$$

$$= 1 - \frac{\pi^2}{2}\left(\frac{\Delta r \Delta v f_0}{v_1 v_N}\right)^2 \left[1 + \frac{1}{3}\left(\frac{\Delta f}{f_0}\right)^2\right], \quad f_0 = \sqrt{f_1 f_2}.$$

Equation (8) shows the need for limiting the array size, the central frequency, and the operative frequency band in order to retain the spatial correlation of the signal over the array aperture. In addition, for lower signal frequencies, the correlation undergoes a lower loss due to scattering by random inhomogeneities in the underwater sound channel and to errors in positioning the array nodes.

In our measurements, $f_1 = 2500$ Hz, $f_2 = 3000$ Hz, $v_i = 1437.4$ m/s, $v_N = 1537.8$ m/s, and $\Delta v = 100.4$ m/s, and, according to Eq. (8), $R_{ij} \geq 0.5$ at $\Delta r \leq 2.5$ m. This condition is met for the array nodes with numbers 2 to 5, for which the aperture is $d_{25} = 3.56$ m and the angle is $\theta_s = 2°$. Hence, only half of the array efficiently works. Actually, Eq. (7) yields the following value for a solid array with $d_{25} = 3.56$ m and $\theta_s = 2°$: $\Delta\theta_T = 7.5°$, which is close to the measured value.

With a full correlation of the signal at all array nodes, the array gain is $K_T = 20\log J$. At $J = 8$, $K_T = 18.1$ dB. In our case, the measured gain value is $K_e = 10\log D_{as}(\theta_s)/D_s = 15.5$ dB. The gain loss $\Delta K = K_T - K_e = 2.6$ dB is caused by the signal decorrelation. It can be shown that

$$K = 10\log\{J[(J-1)\bar{R} + 1]\} \tag{9}$$

if the signal powers are equal at all array nodes. Here, $\bar{R}$ is the normalized cross-correlation function averaged over all channel pairs:

$$\bar{R} = \frac{1}{J(J-1)}\sum_{i=1}^{J}\sum_{j=1}^{J} R_{ij}, \quad i \neq j.$$

In our measurements, $\bar{R} = 0.5$, $J = 8$, and, according to Eq. (9), $K = 15.5$ dB.

Some loss in the gain may be caused by errors in positioning the array nodes. This loss can be estimated by the following formula [4]: $\Delta K = -10\log[1 - (2\sigma r/\lambda)^2]$. In our case, $\sigma r = 0.02$ m, $\lambda = 0.52$ m, and $\Delta K = 0.15$ dB.

According to [1, 15], the following expression can be used to estimate the noise immunity π of an additive array with equal signal-to-noise ratios at all its nodes:

$$\Pi = 10\log\sum_{i=1}^{J}\sum_{j=1}^{J} R_{ij} / \sum_{i=1}^{J}\sum_{j=1}^{J} R_{pij}. \tag{10}$$

Here, R_{pij} is the normalized cross-correlation function of noise in the pairs of nodes with numbers i and j. With $R_{pij} = 0$ at $i \neq j$ and $R_{pij} = 1$ at $i = j$, we obtain

$$\Pi = 10\log[(J-1)\bar{R} + 1]. \tag{11}$$

In our case $\bar{R} = 0.5$, $R_{pij} \approx 0$, and, according to Eq. (11), $\Pi = 6.5$ dB. The measured value is $\Pi_e = 10\log E_a/E = 6.8$ dB. With a full correlation of the signals $R_{ij} \equiv 1$ and $J = 8$ $\Pi_T = 10\log J = 9$ dB. The loss in noise immunity due to the signal decorrelation will be $\Delta\Pi = \Pi_T - \Pi_e = 2.2$ dB.

Thus, the observed deterioration of the useful properties of a randomly thinned additive compensated array, namely, the broadening of the main lobe in the array response, the increase in the level of the side lobes, and the losses in the gain and noise immunity, can be explained by the decorrelation of the signals in the course of the multimode waveguide propagation rather than by the drawbacks of the array itself. In such an environment, the same losses would be also observed with an equidistant half-wave array with the same length. The measured losses were no higher than 3 dB. The array retained the ability to indicate the unilateral bearing of the noise source, and, hence, it still could operate efficiently.

On the basis of the results obtained, a dedicated numerical processing system (DNPS) was developed for processing signals of random fixed and drifting arrays. In a compact casing of the DNPS, the following devices were mounted: a 16-channel analog-to-digital converter, a dedicated processor, and a display terminal at which the information was displayed in digital and graphical forms. The frequency band of the input signals is 2–100 Hz. The sampling frequencies are 250 to 2000 Hz. The accumulation time is 8.2 to 65.6 s. The maximal length of the compensated array is 3 km along the direction to the source. The coordinates of the array nodes are entered into the processor by a keyboard. An operation mode is possible when the array nodes are automatically positioned with the use of pulsed or continuous noiselike signals that are emitted from two or more spaced points. Up to 32 lobes of the directivity pattern can be formed, along with up to seven distance focusing zones if the source is in the Fresnel zone of the array. Four responses of the array can be stored in the system memory. The operator can display a chosen response. From each array lobe, the signal can be fed to an additional external device, either in analog or in digital form.

The DNPS was tested in combination with an experimental fixed underwater receiving array that was linear and equidistant. The array was laid on the bottom of a sea shelf slope at a depth of 460 m. At the array nodes, omnidirectonal hydrophones were placed at steps of 10 m. The array received the signals in the frequency band of 5–100 Hz.

For processing by the DNPS, 16 hydrophones were chosen and were randomly spaced at 10–60 m. These hydrophones formed a random linear array with a 600-m aperture. With the DNPS, 32 lobes were formed within a sector of 180°. Because of the symmetry of the array, similar lobes were also formed on the other side of the array baseline. Thus, an all-around scanning took place, which resulted in a bilateral bearing: two bearings that were symmetric about the array baseline corresponded to each noise source. The signals received in each directivity lobe were fed to a digital spectrum analyzer with a resolution of 1 Hz. Simultaneously with the acoustic measurements, the sea region was surveyed by a radar station. The acoustic observations were performed for several days. One to six noise sources were detected in the area scanned by the array. The spectral analysis showed the existence of harmonic components in all detected noise sources, which is characteristic of signals produced by rotating ship propellers. According to the radar observations, most of the noise sources detected were ships passing at distances of 10–50 km from the array. In some cases, the array–DNPS system detected the sounds of rotating propellers that were not identified by the radar. The acoustically obtained bearings coincided with those detected by the radar to an accuracy of 1°–2° near the array directrix and 10°–20° near the array baseline; these values corresponded to the calculated widths of the lobes of the directivity pattern. The angular accuracy of the radiolocation was about 1°.

The experimental measurements and the tests carried out in the freshwater basin and in the coastal sea region demonstrated the possibility of using long, fixed, bottom-moored compensated additive arrays with random hydrophone positions for locating sources of noise signals that propagate in an underwater waveguide in the form of a sum of normal waves. Also, the efficiency and reliability of the system developed for the processing of signals received by a long (up to 600 m) random array were revealed at frequencies of several tens of hertz.

REFERENCES

1. R. J. Urick, *Principles of Underwater Sound* (McGraw-Hill, New York, 1975; Sudostroenie, Leningrad, 1978).
2. B. Mohl, W. Wahlberg, and A. Heerfort, J. Acoust. Soc. Am. **109**, 434 (2001).
3. S. P. Lappo, B. V. Levin, E. V. Sasorova, *et al.*, Dokl. Akad. Nauk **388**, 805 (2003).
4. V. I. Bardyshev, Akust. Zh. **49**, 342 (2003) [Acoust. Phys. **49**, 285 (2003)].
5. Y. T. Lo, IEEE Trans. Antennas Propag. **12** (3), 257 (1964).
6. L. L. Gazelyan, G. A. Inyutin, and L. G. Sodin, *Experience in the Development of Two-Dimensional Antenna Arrays with a Random Distribution of Emitters* (Svyaz', Moscow, 1972), pp. 17–25 [in Russian].
7. Ya. S. Shifrin, *Problems of the Statistical Theory of Antennas* (Sovetskoe Radio, Moscow, 1970) [in Russian].
8. *Handbook on Hydroacoustics*, Ed. by A. P. Evtyutov *et al.* (Sudostroenie, Leningrad, 1988) [in Russian].
9. V. A. Zverev, P. I. Korotin, A. A. Matveev, *et al.*, Akust. Zh. **47**, 227 (2001) [Acoust. Phys. **47**, 184 (2001)].
10. F. I. Kryazhev and N. A. Petrov, *A Report of the Acoustics Institute, USSR Acad. Sci.* (Moscow, 1959).
11. F. I. Kryazhev, Akust. Zh. **6**, 65 (1960) [Sov. Phys. Acoust. **6**, 60 (1960)].
12. L. N. Zakharov, S. N. Nesterov, and É. G. Fedoseeva, Akust. Zh. **10**, 293 (1964) [Sov. Phys. Acoust. **10**, 250 (1964)].
13. V. I. Bardyshev, L. N. Zotova, T. G. Zubieva, and V. N. Chekoĭda, *A Report of the Acoustics Institute, USSR Acad. Sci.* (Moscow, 1987).
14. J. L. Jones, C. B. Leslie, and L. E. Barton, J. Acoust. Soc. Am. **30**, 142 (1958).
15. M. D. Smaryshev and Yu. Yu. Dobrovol'skiĭ, *Hydroacoustic Antennas: Handbook on Calculation of the Directional Properties of Hydroacoustic Antennas* (Sudostroenie, Leningrad, 1984) [in Russian].

Translated by E. Kopyl

Acoustical Physics, Vol. 50, No. 6, 2004, pp. 647–650. Translated from Akusticheskiĭ Zhurnal, Vol. 50, No. 6, 2004, pp. 751–755.
Original Russian Text Copyright © 2004 by Bobrovnitskiĭ.

We congratulate our colleague Yu.I. Bobrovnitskiĭ upon awarding him the title of Honorary Member of the International Institute of Acoustics and Vibration—the greatest award for a specialist in this field of science. Earlier, six well-known acousticians were honored with this title:

David G. Crighton (UK), Per V. Bruel (Denmark),
Leo Beranek (USA), Maa Dahyou (China),
Richard H. Lyon (USA), Heinrich Kuttruf (Germany).

We wish Yuri Ivanovich Bobrovnitskiĭ further success.

The Editorial Board of Acoustical Physics

A New Solution to the Problem of an Acoustically Transparent Body

Yu. I. Bobrovnitskiĭ
Blagonravov Institute of Mechanical Engineering, Russian Academy of Sciences,
M. Khariton'evskiĭ per. 4, Moscow, 101990 Russia
e-mail: bobrovni@orc.ru

Received May 2, 2004

Abstract—The method of active impedance matching is applied to the well-known problem of an acoustically transparent body. Two laws of active force control, by velocity and by pressure, are obtained for solving the problem. *© 2004 MAIK "Nauka/Interperiodica".*

The problem of making an arbitrary body acoustically transparent (nonscattering) was formulated and solved in the 1960s by several authors independently [1–6]. All solutions obtained at that time were based on the factorization of the acoustic field (i.e., on the separation of the field into the incident and scattered components) using the Helmholtz–Huygens integral operator and on the subsequent compensation of the scattered field component by additional sources of sound (actuators). In the method proposed by Malyuzhinets [2, 3], a body is surrounded by four acoustically transparent closed surfaces. Two inner surfaces carry continuously distributed sensors for measuring the pressure and the normal velocity, which are necessary for the factorization of the field. Two outer surfaces (also called Huygens surfaces) carry continuously distributed monopole and dipole actuators, which radiate into the outer region and thus compensate the scattered component without distorting the total field in the inner region. The actuators are controlled by the signals received from the sensors. The main disadvantage of the Malyuzhinets solution and other solutions based on the Huygens principle is the difficulty of realizing in practice measuring and active surfaces with the aforementioned properties: these surfaces, which are covered with closely spaced material sensors or actuators, should be acoustically transparent. The use of discretely positioned transducers instead of continuously distributed ones partially overcomes the aforementioned difficulty but also creates other ones [7–10]. Therefore, the problem of an acoustically transparent body, a particular case of the more general problem of the scattered acoustic field control, which has a wide practical application, continues to attract the interest of researchers (see, e.g., [10–15]).

The present paper suggests a new way of solving the problem of an acoustically transparent body without using the Huygens principle. The problem is solved by the method of active impedance matching [16], which requires no preliminary factorization of the field. In practice, the solution is realized by a set of vibration sensors and actuators positioned on the surface of a body; for example, this may be a thin active (smart) coating. The paper presents a theoretical solution illustrated by an example with a spherical scatterer.

Consider an inhomogeneous elastic body placed in a medium that is not necessarily homogeneous and unbounded. The body occupies a volume V and is bounded by a surface S, which is the contact surface between the body and the medium. In the medium outside the body, some sources are present. In the absence of the body, they produce a pressure field $p_i(x)$, which is called the incident field in the following consideration. In the presence of the body, whose acoustic properties are assumed to be different from those of the medium, the field component $p_s(x)$ scattered by the body is present. The problem is formulated as follows: by using an additional (active) force $f_a(s)$ applied to the contact surface and generating an active field component $p_a(x)$, it is necessary to compensate the scattered component so as to obtain $p_s(x) + p_a(x) = 0$, where x is the coordinate of an arbitrary point of the medium outside the body.

Let us refine the statement of the problem. The total pressure field consists of three components:

$$p(x) = p_i(x) + p_s(x) + p_a(x). \tag{1}$$

The quantities available for the measurements are the current values of pressure $p(s)$ and normal velocity $v(s)$ of the total field at the surface of the body, $s \in S$. We assume that the vibrations of the medium and the body are linear with the conventional boundary conditions that are satisfied at the contact surface S; namely, the normal velocities of the body and the medium at the surface are identical, the normal stresses in the elastic body are equal to the pressure in the medium, and the tangential stresses are equal to zero. The vibrations are assumed to be harmonic in time, and the factor $\exp(-i\omega t)$ is omitted in the following calculations.

The problem will be solved by the method of active impedance matching [16], which, in the case under consideration, is as follows. The surface S is divided into N small elements ΔS_j, and, within each element, the pressure and the normal velocity are taken to be constant. Let us introduce the vectors p and v, whose components are the amplitudes of the forces and normal velocities, respectively, of the total field (1) at the surface S:

$$p = [p(s_1)\Delta S_1; \ldots; p(s_N)\Delta S_N]^T, \quad v = [v(s_1); \ldots; v(s_N)]^T. \tag{2}$$

Here, s_j is the coordinate of a point of the surface element ΔS_j. Similar notations can be introduced for each component of the total field (1): for example, p_s and v_s are N-vectors of type (2) for the scattered field, etc.

Now, let us introduce three square matrices of order N: Z, Z_i, and Z_r. Matrix Z is the impedance matrix of the body in vacuum. It determines the relation between the vector of external forces $f = [f_1, \ldots, f_N]^T$ applied to surface elements ΔS_j and the vector of normal velocities $v = [v_1, \ldots, v_N]^T$ acquired by the surface elements under the effect of these forces: $f = Zv$. The matrix Z_i is determined in a similar way: it is an $N \times N$ impedance matrix of the medium in the volume of the body, i.e., the impedance matrix of an isolated volume V filled with the medium, with respect to N external forces f_j, each of which is uniformly distributed over its respective surface element ΔS_j ($j = 1, \ldots, N$). Finally, the third matrix Z_r is the impedance matrix of the medium outside the body, i.e., the radiation matrix of the body. The positive direction of forces and normal velocities at the surface S is assumed to be the direction of the outer normal.

It can be easily verified that the field components satisfy the relations:

$$\begin{gathered} p_i + Z_i v_i = 0, \quad p_s - Z_r v_s = 0, \quad p_a - Z_r v_a = 0, \\ p_i + p_s + Z(v_i + v_s) = 0. \end{gathered} \tag{3}$$

For example, for the incident field, the quantity $(-p_i)$ is the N vector of forces acting on the medium enclosed in the volume V from the side of the medium outside this volume. Since, by definition, these forces are related to the vector of response v_i via the matrix Z_i, the first of relations (3) is satisfied. Other relations are verified in the same way.

Let us introduce two $N \times N$ matrices of scattering coefficients, R and Q, for pressure and for normal velocity, respectively, to describe the relation between the scattered and incident field components on the surface S of the body:

$$p_s = Rp_i, \qquad v_s = Qv_i. \tag{4}$$

Using relations (3), we obtain the formulas

$$\begin{aligned} Q &= (Z_r + Z)^{-1}(Z_i - Z) = (YZ_r + I)^{-1}(YZ_i - I), \\ R &= (Y_r + Y)^{-1}(Y_i - Y) = (ZY_r + I)^{-1}(ZY_i - I), \end{aligned} \tag{5}$$

where I is the unit matrix of order N; and $Y = Z^{-1}$, $Y_i = Z_i^{-1}$, and $Y_r = Z_r^{-1}$ are mobility matrices. Formulas (5) represent the generalization of the known Fresnel formulas, which describe the scattering (reflection and transmission) of plane waves by flat obstacles, to an arbitrary case of scattering. From Eqs. (4) and (5), it follows that the scattered field is completely determined by the three impedance matrices introduced above and, naturally, by the incident field. From these formulas, it also follows that the scattered field is absent and the body is acoustically transparent only if the impedance matrix Z of the body in vacuum is identical to the matrix Z_i of the medium enclosed in the volume V of the body; i.e., if the body does not differ from the medium in terms of the response of the surface S to an external acoustic action. In particular, this means that none of the bodies, neither active nor passive, with a locally responding surface, i.e., with a diagonal impedance matrix Z, can be acoustically transparent, because the matrix Z_i of the medium is nondiagonal.

Let an active force vector $f_a = [f_{a1}, \ldots, f_{aN}]^T$ be applied to the surface S of the body, where f_{aj} is the resultant of active forces acting on the surface element ΔS_j. Then, the velocity vector given by Eq. (2) takes the form

$$v = v_i + Qv_i + (Z + Z_r)^{-1} f_a. \tag{6}$$

Assume that the active forces are proportional to the amplitudes of the total normal velocity of the surface: $f_a = Av$, where A is the matrix to be determined. Substituting this expression in Eq. (6), we obtain that the total velocity v of the surface is equal to the velocity of the incident field, v_i, on the condition that $A = Z - Z_i$. It can be easily verified that, in this case, the total pressure p on the surface coincides with the pressure p_i of the incident field. Thus, under the effect of active forces

$$f_a = (Z - Z_i)v, \tag{7}$$

the total field at the surface of the body does not differ from the incident field; i.e., the scattered field component proves to be compensated by the active component. Consequently, the active field component also compensates the scattered component at any point outside the body (this statement can be proved, e.g., by using the Helmholtz–Huygens integral) and the body becomes nonscattering.

Now, let us assume that the active forces are proportional to the pressure amplitudes of the total field given by Eq. (2) at the surface S: $f_a = Bp$. Then, from Eq. (6), in the same manner as above, we obtain $B = I - ZY_i$, and the active forces

$$f_a = (I - ZY_i)p, \tag{8}$$

applied to the surface of the body also completely compensate the scattered field, which makes the body acoustically transparent.

Thus, two laws are obtained for controlling the active forces—Eqs. (7) and (8)—and these laws solve the problem under study. If law (7) is used, the active forces are proportional to the current velocity amplitudes measured on the surface of the body. In the case pertaining to law (8), the active forces are proportional to the pressure amplitudes of the total field, which are measured at the surface of the body. To decide which of the two laws is preferable, one should consider the specific (additional) conditions of the problem, for example, which quantity is measured with the higher accuracy or whether or not the body itself is a source of radiation. However, in both cases of control, either by velocity or by pressure, the matrices Z and Z_i (or Y_i) are assumed to be known. The impedance matrix Z_i of the medium in the volume of the body is calculated from the density of the medium ρ, the velocity of sound in the medium c, and the geometric parameters of the body. The matrix Z of the "dry" body can be calculated in simple cases. In the general case, it can be obtained experimentally by measuring the scattered field with a special excitation by external sources of sound. One of the versions of this method is described in [17].

The above consideration suggests the following conclusions. An arbitrary body can be made acoustically transparent by active methods only. No passive coating can make the body nonscattering in the general case. When any active method is used, the active forces must act on the whole closed surface of the body, and the control over these forces must be global in the sense that the active force applied to each surface element depends on the field amplitudes measured on all other surface elements. No active system with local control (when each active force is only controlled by the field measured at the point of its application) can provide a complete compensation for the scattered field component (except for certain limiting cases). Finally, from the solution presented above, it follows that the preliminary factorization of the field (the separation of the scattered component) is not necessary for solving the problem: the body can be made nonscattering by using the active forces that are controlled by the current amplitudes of the total field at the surface of the body.

As an example, let us consider a spherical body of radius a in a homogeneous unbounded space. The aim is to make this body acoustically transparent by using an active force of type (7) or (8) distributed over its surface. This problem can be solved analytically, and, instead of dividing the surface of the body into elements, it is more convenient to use continuous dependences and impedances with respect to the forces distributed in spherical harmonics.

Let an incident field $p_i(r, \theta)$ (where r and θ are spherical coordinates), generated by some external source, be present in the space in the absence of the body. For simplicity, this field is assumed to be axially symmetric (independent of the third coordinate). At the surface $r = a$, the field can be expanded in spherical harmonics $\psi_n(\theta)$ as

$$p_i(a, \theta) = \sum_{n=0}^{\infty} p_{in}\psi_n(\theta), \quad v_i(a, \theta) = \sum_{n=0}^{\infty} v_{in}\psi_n(\theta).$$

The expansion coefficients of these series are related by the formulas

$$v_{in} = \frac{p_{in}}{Z_{in}}, \quad Z_{in} = -i\rho c\frac{j_n(ka)}{j'_n(ka)}, \quad n = 0, 1, \dots . \tag{9}$$

Here, the quantity Z_{in} is the specific impedance of the medium in the spherical volume of radius a with respect to the external action in the form of the nth spherical harmonic applied to the surface $r = a$.

Now, let us place a spherical elastic body of radius a at the coordinates origin. The properties of this body with respect to continuously distributed external actions are assumed to be axially symmetric and, hence, can be characterized by a set of surface impedances in vacuum Z_n (where $n = 0, 1, \dots$), which correspond to distributions in spherical harmonics. The presence of the body gives rise to a scattered field of the form

$$p_s(r, \theta) = \sum_{n=0}^{\infty} p_{sn}\psi_n(\theta)\frac{h_n(kr)}{h_n(ka)}.$$

At the surface of the body, the pressure and the radial velocity of this field are expressed as

$$p_s(a, \theta) = \sum_{n=0}^{\infty} p_{sn}\psi_n(\theta), \quad v_s(a, \theta) = \sum_{n=0}^{\infty} v_{sn}\psi_n(\theta),$$

where

$$v_{sn} = \frac{p_{sn}}{Z_{rn}}, \quad Z_{rn} = i\rho c\frac{h_n(ka)}{h'_n(ka)}, \quad n = 0, 1, \ldots \quad (10)$$

are the specific impedances of the exterior of the body, or, in other words, the radiation impedances of the body vibrating in spherical harmonics. At the surface of the body, the following boundary conditions are satisfied:

$$p_{in} + p_{sn} + Z_n(v_{in} + v_{sn}) = 0, \quad n = 0, 1, 2, \ldots .$$

Substituting Eqs. (9) and (10) in this expression, we obtain the *n*th scattering coefficients for pressure and velocity (by analogy with Eqs. (5)) in the form

$$R_n = \frac{p_{sn}}{p_{in}} = \frac{Y_{in} - Y_n}{Y_{rn} + Y_n}, \quad Q_n = \frac{v_{sn}}{v_{in}} = \frac{Z_{in} - Z_n}{Z_{rn} + Z_n}.$$

Let us apply a velocity-controlled active force to the surface of the body:

$$f_a(\theta) = \sum_{n=0}^{\infty} v_n(Z_n - Z_{in})\psi_n(\theta), \quad (11)$$

where v_n is the amplitude of the *n*th spherical harmonic of the current radial velocity component of the vibrating surface of the body. For this velocity amplitude, the following equation of the type of Eq. (6) is valid:

$$v_n = v_{in} + Q_n v_{in} - Q_n v_n.$$

This yields $v_n = v_{in}$, and, performing some simple transformations, we obtain $p_n = p_{in}$. Thus, active force (11) completely compensates for the scattering. In a similar way, it can be shown that a pressure-controlled active force also completely compensates for the scattered field component and makes the body acoustically transparent.

REFERENCES

1. G. D. Malyuzhinets, in *Proceedings of III All-Union Symposium on Wave Diffraction* (Nauka, Moscow, 1964), p. 113.
2. G. D. Malyuzhinets, Tr. Akust. Inst. Akad. Nauk SSSR, No. 15, 124 (1971).
3. M. V. Fedoryuk, Tr. Akust. Inst. Akad. Nauk SSSR, No. 15, 169 (1971).
4. M. Jessel, in *Proceedings of 6th International Congress on Acoustics* (Tokyo, 1968), Paper F-5-6.
5. M. Jessel and G. Mangiante, J. Sound Vibr. **23**, 383 (1972).
6. G. Mangiante, J. Acoust. Soc. Am. **61**, 1516 (1977).
7. M. P. Zavadskaya, A. V. Popov, and B. L. Égel'skiĭ, Akust. Zh. **21**, 732 (1975) [Sov. Phys. Acoust. **21**, 451 (1975)].
8. S. I. Konyaev, V. I. Lebedev, and M. V. Fedoryuk, Akust. Zh. **25**, 887 (1979) [Sov. Phys. Acoust. **25**, 500 (1979)].
9. A. A. Mazanikov, V. V. Tyutekin, and M. V. Fedoryuk, Akust. Zh. **26**, 759 (1980) [Sov. Phys. Acoust. **26**, 428 (1980)].
10. Yu. I. Bobrovnitskiĭ, N. M. Ostapishin, and S. N. Panov, in *Proceedings of XI All-Union Acoustical Conference* (Akad. Nauk SSSR, Moscow, 1991), Sect. K, p. 21.
11. S. Ise, Acust. Acta Acust. **85** (1), 78 (1999).
12. I. A. Urusovskiĭ, Akust. Zh. **32**, 560 (1986) [Sov. Phys. Acoust. **32**, 354 (1986)].
13. A. A. Mazanikov, Akust. Zh. **46**, 89 (2000) [Acoust. Phys. **46**, 76 (2000)].
14. C. Scandrett, J. Acoust. Soc. Am. **111**, 893 (2002).
15. S. Uosukainen, J. Sound Vibr. **267**, 979 (2003).
16. Yu. I. Bobrovnitskiĭ, Akust. Zh. **49**, 731 (2003) [Acoust. Phys. **49**, 620 (2003)].
17. Yu. I. Bobrovnitskii and G. Pavic, J. Sound Vibr. **261**, 527 (2003).

Translated by E. Golyamina

Acoustical Physics, Vol. 50, No. 6, 2004, pp. 651–656. Translated from Akusticheskiĭ Zhurnal, Vol. 50, No. 6, 2004, pp. 756–761.
Original Russian Text Copyright © 2004 by Boev.

Scattering of High-Frequency Waves by Surfaces in Continuous Media with Allowance for Rereflections

N. V. Boev
Rostov State University, Bol'shaya Sadovaya ul. 105, Rostov-on-Don, 344006 Russia
e-mail: boyev@math.rsu.ru

Received April 21, 2003

Abstract—This study is devoted to the development of the ray theory of diffraction in application to arbitrary (nonconvex) smooth obstacles in the scalar case. A three-dimensional problem is considered. An asymptotic method of estimating the diffraction integrals is described. The method is based on the multidimensional stationary phase approach. The diffraction integrals are obtained on the basis of the generalization of the Kirchhoff physical theory of diffraction. Explicit expressions are derived for the pressure in the reflected wave in the cases of its single and double reflections. *© 2004 MAIK "Nauka/Interperiodica".*

A precise investigation of the scattering of high-frequency waves by surfaces in continuous media encounters considerable difficulties when the wavelength is much smaller than the average size of the obstacles [1]. In this case, numerical methods, such as the finite-element and boundary-element methods, require a grid with a large number of nodes, which leads to an instability in the calculations.

To overcome this difficulty, different asymptotic approaches have been developed, such as the Keller geometrical theory of diffracted rays, the Kirchhoff theory, creeping waves, etc. Analytical methods suitable for this class of problems are described in detail in [2–5].

The main limitation of the ray methods is related to the fact that they mainly apply to convex obstacles, because only for these objects can the "light" and "shadow" zones be easily separated.

Among the recent publications, one should note the paper [6], which uses a method based on the analytical continuation of the scattered field, the idea of which dates back to Rayleigh's works.

The diffraction problem is considerably complicated when the boundary surface of the scatterer allows rereflections of waves. In principle, multiple reflections can be studied in terms of the ray rereflections, for example, on the basis of the Keller geometrical theory of diffraction. However, no publications can be found to provide the formulas for multiple reflections in an explicit form. Only particular two-dimensional problems are known [7], the solutions to which are obtained for reflectors of canonical shape in the case of twofold reflections.

The alternative method developed in this paper is based on the study of the Kirchhoff multiple diffraction integrals with the use of the multidimensional stationary phase approach. The proposed method makes it possible to represent the amplitude of the rereflected wave field in a unique explicit form for an arbitrary number of rereflections from the surface of one or several scatterers [8]. The present paper is devoted to the study of a particular case of twofold reflections, which, in the framework of the proposed method, provides the basis for studying the problem of an arbitrary number of multiple reflections.

Let us first describe the method for determining the pressure in a singly reflected wave.

Let a high-frequency monochromatic spherical wave originating from a point x_0 of an acoustic medium be incident on the surface S of an obstacle. One of the main informative parameters of the scattered field is the pressure in the reflected wave at a point x. The pressure in the reflected wave is known to be determined by the direction of the wave incidence and by the small vicinity of the point of specular reflection, $y^* \in S$. Hence, for higher frequencies, the pressure in the reflected wave can be determined in terms of the ray concepts on the basis of the stationary phase approach. This approach was used earlier in solving the planar problem [9, 10].

If any ray of the form of $x_0 - y - x$ is reflected from the surface S ($y \in S$) only once (Fig. 1), then, according to the Kirchhoff physical theory of diffraction, the pressure $p(x)$ in the reflected wave is determined by the integral [11]

$$p(x) = \iint_S 2p^{inc}(y)\frac{\partial \Phi}{\partial n_y} dS, \qquad (1)$$

provided that the boundary S of the obstacle is acoustically hard, i.e., $\partial p/\partial n|_S = 0$. Here, $p^{inc}(y)$ is the pressure in the incident wave at the boundary S, Φ is the potential of the fundamental solution (Green's function), n_y is

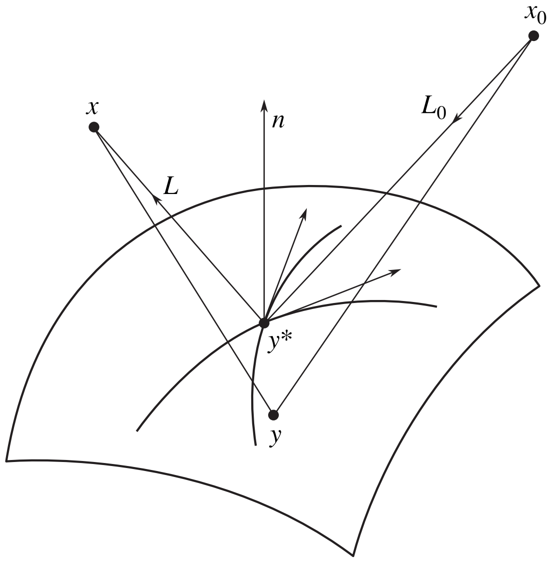

Fig. 1. Single reflection of a high-frequency acoustic wave from a smooth obstacle.

the outer normal to the surface S at the point y, k is the wave number, and

$$\begin{aligned} p^{inc}(y) &= |x_0-y|^{-1}\exp(ik|x_0-y|), \\ \Phi &= (4\pi)^{-1}|x-y|^{-1}\exp(ik|x-y|). \end{aligned} \tag{2}$$

For $k \longrightarrow \infty$,

$$\begin{aligned} \frac{\partial\Phi}{\partial n_y} &= ik\cos\gamma(4\pi)^{-1}|x-y|^{-1} \\ &\times\exp(ik|x-y|)[1+O(k^{-1})], \end{aligned} \tag{3}$$

where γ is the angle between the normal n_y and the direction of incidence of the ray $x_0 - y$; $|x_0 - y|$ and $|x - y|$ are the distances between the points x_0 and $y \in S$ and between the points x and y, respectively.

When the ray is incident from the point x_0, the surface S has a point y^* where the ray intersects it and where the normal to the surface together with the incident ray determine the plane in which the reflected ray lies. Let us denote $|x_0 - y^*| = L_0$ and $|x - y^*| = L$. Then, from Eqs. (1)–(3), we obtain the following basic representation (the nonoscillating functions are factored out from under the integral sign):

$$\begin{aligned} p(x) &= \frac{ik}{2\pi}\frac{\cos\gamma}{L_0L}\iint\limits_S\exp(ik\varphi)dS, \\ \varphi &= |x_0-y|+|x-y|. \end{aligned} \tag{4}$$

The ray representation can be obtained from Eq. (4) by using the stationary phase approach [12]. When estimating integral (4), it is necessary to take into account the points y from a small vicinity of the point y^*. Let us relate the small vicinity of the point $y^* \in S$ to the right-handed coordinate system determined by the normal and the surface curvature lines at the point $y^* \in S$. Then, an arbitrary point $y \in S$ from the vicinity of the point y^* will have the coordinates $y[\Delta s_1, \Delta s_2, -0.5(k_1(\Delta s_1)^2 + k_2(\Delta s_2)^2)]$, where Δs_1 and Δs_2 are the arc increments along the curvature lines, $k_1 = R_1^{-1}$ and $k_2 = R_2^{-1}$ are the principal curvatures and R_1 and R_2 are the principal curvature radii of the surface S at the point $y^* \in S$, and $k_1(\Delta s_1)^2 + k_2(\Delta s_2)^2$ is the second quadratic form of the surface at the point y^* of surface S with respect to the curvature lines.

Let us apply the cosine theorem to the triangles x_0y^*y and xy^*y:

$$\begin{aligned} |x_0-y|^2 &= L_0^2+|\Delta\mathbf{s}|^2-2L_0|\Delta\mathbf{s}|\cos\angle x_0y^*y, \\ |x-y|^2 &= L^2+|\Delta\mathbf{s}|^2-2L|\Delta\mathbf{s}|\cos\angle xy^*y. \end{aligned} \tag{5}$$

From the scalar product of the vector $\{\cos\alpha, \cos\beta, \cos\gamma\}$, which is the unit vector of y^*x_0, with $\Delta\mathbf{s} = \{\Delta s_1, \Delta s_2, -0.5[(k_1(\Delta s_1)^2 + k_2(\Delta s_2)^2]\}$ and the scalar product of the vector $\{-\cos\alpha, -\cos\beta, \cos\gamma\}$, which is the unit vector of y^*x, with $\Delta\mathbf{s}$, we obtain

$$\begin{aligned} |\Delta\mathbf{s}|\cos\angle x_0y^*y &= \Delta s_1\cos\alpha+\Delta s_2\cos\beta \\ &+0.5(k_1(\Delta s_1)^2+k_2(\Delta s_2)^2)\cos\gamma, \end{aligned}$$

$$\begin{aligned} |\Delta\mathbf{s}|\cos\angle xy^*y &= -\Delta s_1\cos\alpha-\Delta s_2\cos\beta \\ &+0.5(k_1(\Delta s_1)^2+k_2(\Delta s_2)^2)\cos\gamma. \end{aligned}$$

If we ignore the quantities that are small compared to $(\Delta s_1)^2$, $\Delta s_1\Delta s_2$, and $(\Delta s_2)^2$, from Eqs. (5) we obtain the representations

$$\begin{aligned} |x_0-y| &= L_0-\Delta s_1\cos\alpha-\Delta s_2\cos\beta \\ &+0.5(L_0^{-1}\sin^2\alpha+k_1\cos\gamma)(\Delta s_1)^2 \\ &-L_0^{-1}\cos\alpha\cos\beta\Delta s_1\Delta s_2 \\ &+0.5(L_0^{-1}\sin^2\beta+k_2\cos\gamma)(\Delta s_2)^2, \end{aligned}$$

$$\begin{aligned} |x-y| &= L+\Delta s_1\cos\alpha+\Delta s_2\cos\beta \\ &+0.5(L^{-1}\sin^2\alpha+k_1\cos\gamma)(\Delta s_1)^2 \\ &-L^{-1}\cos\alpha\cos\beta\Delta s_1\Delta s_2 \\ &+0.5(L^{-1}\sin^2\beta+k_2\cos\gamma)(\Delta s_2)^2. \end{aligned}$$

Hence,

$$\begin{aligned} \varphi &= L_0+L+0.5d_{11}(\Delta s_1)^2+d_{12}\Delta s_1\Delta s_2 \\ &+0.5d_{22}(\Delta s_2)^2, \end{aligned}$$

where

$$d_{11} = (L_0^{-1} + L^{-1})\sin^2\alpha + 2k_1\cos\gamma;$$

$$d_{12} = -(L_0^{-1} + L^{-1})\cos\alpha\cos\beta;$$

$$d_{22} = (L_0^{-1} + L^{-1})\sin^2\beta + 2k_2\cos\gamma.$$

The absence of the first degrees of Δs_1 and Δs_2 in the phase φ means that the point y^* of the direct ray reflection corresponds to a stationary value of the phase φ. Thus, the principal term of the asymptotics of integral (4) is determined by the coefficients multiplying $(\Delta s_1)^2$, $\Delta s_1\Delta s_2$, and $(\Delta s_2)^2$ and can be derived from Eq. (4) by applying the two-dimensional stationary phase approach [12]:

$$p(x) = \cos\gamma\frac{\exp\left\{i\left[k(L_0 + L) + \frac{\pi}{4}(\delta_2 + 2)\right]\right\}}{L_0L\sqrt{|\det(D_2)|}},$$

where D_2 is the Hessian of the symmetric structure ($d_{ij} = d_{ji}$; $i, j = 1, 2$) and $\delta_2 = \mathrm{sign}D_2$ is the difference between the numbers of positive and negative eigenvalues of matrix D_2.

With allowance for the equality $d_{21} = d_{12}$, the final result has the following form:

$$p(x) = \frac{\exp\left\{i\left[k(L_0 + L) + \frac{\pi}{4}(\delta_2 + 2)\right]\right\}}{\sqrt{\left|(L_0 + L)^2 + 2L_0L(L_0 + L)(k_2\sin^2\alpha + k_1\sin^2\beta)\cos^{-1}\gamma + 4L_0^2L^2K\right|}}. \qquad (6)$$

Here, $K = k_1k_2$ is the Gaussian curvature of the surface S at the point y^* and $\{-\cos\alpha, -\cos\beta, -\cos\gamma\}$ is the vector that determines the direction of incidence of the ray $x_0 - y^*$ in the chosen coordinate system.

For formula (6), we consider two limiting cases. If $k_1 = k_2 = 0$, Eq. (6) yields the known result for the pressure in a wave reflected from a plane: $p(x) = -(L_0 + L)^{-1}\exp[ik(L_0 + L)]$.

In the case of backscattering in the far field, Eq. (6) coincides with the representation given in [11]:

$$p(x) = 0.5iL_0^{-2}\sqrt{R_1R_2}\exp\left[i\left(2kL_0 + \frac{\pi}{4}\delta_2\right)\right].$$

Formula (6) was derived for the case of a high-frequency wave incident on a convex surface. If the wave is incident on a concave surface, the principal curvatures k_1 and k_2 should be considered as negative.

Formula (6) for the pressure in a wave singly reflected from an acoustically hard surface is given in [13]. There, it is derived in terms of the Keller geometrical theory of diffraction. This means that the principal term of the asymptotics of the diffraction integral coincides with the result of calculating the pressure in the reflected wave with the geometrical theory of diffraction. At the same time, the application of the Keller geometrical theory of diffraction, which is based on the use of divergence coefficients, becomes fairly cumbersome even in the case of a twofold reflection. If we consider the problem of an N-fold (N is arbitrary) reflection of a high-frequency wave from a surface, it is more convenient to rely on the estimate of a $2N$-fold diffraction integral using the multidimensional stationary phase approach. For studying the general case of an arbitrary number of rereflections, the basic problem is that of a twofold reflection, which is considered below.

A direct application of the Kirchhoff approximation is impossible in this case [4], because it does not describe multiply reflected waves. If in Green's formula we replace $p^{inc}(y)$ by the geometrical-optics primary field, the Kirchhoff approximation will yield a singly reflected wave. A twice-reflected wave is obtained only when the boundary pressure $p^{inc}(y)$ includes both the primary field and its single reflection. To solve the problem of the twofold reflection, we begin with the modification of the Kirchhoff approximation [4]. We determine the twice-reflected waves by performing the integration over the vicinity S_2 of the second point of specular reflection y_2^* for the rays obtained as a result of the single reflection from the vicinity S_1 of the first point of specular reflection y_1^*. This modification means that, when determining the principal term of the asymptotics of the fourfold diffraction integral, we operate in the framework of calculating the pressure amplitude in the twice-reflected wave in terms of the geometrical theory of diffraction.

Let us consider the secondary reflection of the ray $x_0 - y_1^* - y_2^* - x_3$ issuing from the point x_0 and arriving at the point x_3 (Fig. 2). The points y_1^* and y_2^* may belong to one surface or to two different surfaces. The pressure at the point of reception, $p(x_3)$, is given by the formula

$$p(x_3) = \iint_{S_2} 2p(y_2)\frac{\partial\Phi}{\partial n_2}dS_2.$$

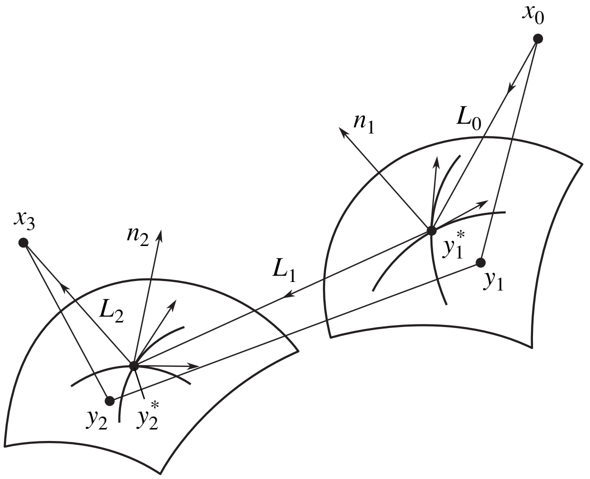

Fig. 2. Double reflection of a high-frequency acoustic wave from a smooth obstacle.

Here, $p(y_2)$ is the pressure in the incident wave at the point $y_2 \in S_2$ of the vicinity of the point y_2^*; this pressure is determined after the first reflection from the vicinity S_1 of the point y_1^*.

At the same time, the pressure $p(y_2)$ is expressed by a similar formula:

$$p(y_2) = \iint\limits_{S_1} 2p^{inc}(y_1)\frac{\partial\Phi}{\partial n_1}dS_1.$$

Taking into account that the pressure

$$p^{inc}(y_1) = |x_0 - y_1|^{-1}\exp(ik|x_0 - y_1|)$$

determines the incident field caused by the point source x_0, we can write the following basic representation:

$$p(x_3) = -\left(\frac{k}{2\pi}\right)^2 \frac{\cos\gamma_1\cos\gamma_2}{L_0L_1L_2}\iint\limits_{S_2}\iint\limits_{S_1} e^{ik\varphi}dS_1dS_2, \quad (7)$$

$$\begin{gathered}\varphi = |x_0 - y_1| + |y_1 - y_2| + |y_2 - x_3|,\\ |x_0 - y_1^*| = L_0, \quad |y_1^* - y_2^*| = L_1, \quad |y_2^* - x_3| = L_2.\end{gathered} \quad (8)$$

As in the case of a single reflection, we relate the vicinities of the points of direct specular reflection, $y_1^* \in S_1$ and $y_2^* \in S_2$, to the right-handed Cartesian coordinates determined by the normals n_1 and n_2 and by the curvature lines. Along the curvature lines, we determine the arc lengths $\Delta s_1^{(1)}$ and $\Delta s_2^{(1)}$ in the vicinity S_1 of the point y_1^* and the arc lengths $\Delta s_1^{(2)}$ and $\Delta s_2^{(2)}$ in the vicinity S_2 of the point y_2^*. As above, for small $\Delta s_1^{(i)}$ and $\Delta s_2^{(i)}$ (i = 1, 2), we obtain

$$\begin{aligned}|x_0 - y_1| &= L_0 - \Delta s_1^{(1)}\cos\alpha_1 - \Delta s_2^{(1)}\cos\beta_1\\ &+ 0.5(L_0^{-1}\sin^2\alpha_1 + k_1^{(1)}\cos\gamma_1)(\Delta s_1^{(1)})^2\\ &- L_0^{-1}\cos\alpha_1\cos\beta_1\Delta s_1^{(1)}\Delta s_2^{(1)}\\ &+ 0.5(L_0^{-1}\sin^2\beta_1 + k_2^{(1)}\cos\gamma_1)(\Delta s_2^{(1)})^2,\\ |y_2 - x_3| &= L_2 - \Delta s_1^{(2)}\cos\alpha_2 + \Delta s_2^{(2)}\cos\beta_2\\ &+ 0.5(L_2^{-1}\sin^2\alpha_2 + k_1^{(2)}\cos\gamma_2)(\Delta s_1^{(2)})^2\\ &- L_2^{-1}\cos\alpha_2\cos\beta_2\Delta s_1^{(2)}\Delta s_2^{(2)}\\ &+ 0.5(L_2^{-1}\sin^2\beta_2 + k_2^{(2)}\cos\gamma_2)(\Delta s_2^{(2)})^2.\end{aligned}$$

Let us find the term $|y_1 - y_2| = |y_2y_1|$ in the phase φ given by Eq. (8). We consider this distance in the coordinate system related to the point y_2^*. In this coordinate system, we denote the coordinates of the points $y_2(\xi_2, \eta_2, \zeta_2)$, $y_1(\xi_1, \eta_1, \zeta_1)$, and $y_1^*(\xi_1^0, \eta_1^0, \zeta_1^0)$. Then, we represent the vector y_2y_1 in the form

$$\begin{gathered}y_2y_1 = y_2^*y_1^* + Ay_1^*y_1 - y_2^*y_2,\\ y_2y_1 = \{\xi_1 - \xi_2, \eta_1 - \eta_2, \varsigma_1 - \varsigma_2\};\\ y_2^*y_1^* = \{\xi_1^0, \eta_1^0, \varsigma_1^0\},\\ y_i^*y_i = \{\Delta s_1^{(i)}, \Delta s_2^{(i)}, -0.5(k_1^{(i)}(\Delta s_1^{(i)})^2 + k_2^{(i)}(\Delta s_2^{(i)})^2)\},\\ i = 1, 2.\end{gathered}$$

Here, the matrix $A = (a_{ij})$ (i, j = 1, 2, 3) is an orthogonal matrix determining the change from the basis of the Cartesian coordinate system at the point y_2^* to the basis of the Cartesian coordinate system at the point y_1^*.

Note that the second integral in Eq. (7) is only determined by the distances $|x_0 - y_1|$, $|y_1 - y_2|$, and $|y_2 - x_3|$ and by the shapes of the surfaces S_1 and S_2 and does not depend on their rotation about the ray $y_1^* - y_2^*$ when the relative positions of S_1 and x_0 and the relative positions of S_2 and x_3 are retained. In this connection, in the case of the twofold reflection of the ray $x_0 - y_1^* - y_2^* - x_3$, when the surfaces S_1 and S_2 with the planes formed by the normal n_1 and the ray $x_0 - y_1^*$ and by the normal n_2 and the ray $y_2^* - x_3$, respectively, rotate as a solid whole about the ray $y_1^* - y_2^*$, the pressure $p(x_3)$ at the point x_3 will remain unchanged. In what follows, we consider the pressure $p(x_3)$ when the ray $x_0 - y_1^* - y_2^* - x_3$ lies in a single plane.

Then, the elements a_{ij} of the orthogonal matrix A have the form

$$\begin{Bmatrix} a_{11} \\ a_{21} \end{Bmatrix} = G_{12}^{-1}\left[\cos\beta_1 \begin{Bmatrix} \cos\beta_2 \\ -\cos\alpha_2 \end{Bmatrix}\right.$$

$$\left. - \cos\alpha_1 \begin{Bmatrix} \cos\alpha_2 \\ \cos\beta_2 \end{Bmatrix} \cos(\gamma_1 + \gamma_2)\right],$$

$$\begin{Bmatrix} a_{12} \\ a_{22} \end{Bmatrix} = G_{12}^{-1}\left[\cos\alpha_1 \begin{Bmatrix} -\cos\beta_2 \\ \cos\alpha_2 \end{Bmatrix}\right.$$

$$\left. - \cos\beta_1 \begin{Bmatrix} \cos\alpha_2 \\ \cos\beta_2 \end{Bmatrix} \cos(\gamma_1 + \gamma_2)\right],$$

$$\begin{Bmatrix} a_{13} \\ a_{23} \end{Bmatrix} = \begin{Bmatrix} -\cos\alpha_2 \\ -\cos\beta_2 \end{Bmatrix} \frac{\sin(\gamma_1 + \gamma_2)}{\sin\gamma_2},$$

$$\begin{Bmatrix} a_{31} \\ a_{32} \end{Bmatrix} = \begin{Bmatrix} \cos\alpha_1 \\ \cos\beta_1 \end{Bmatrix} \frac{\sin(\gamma_1 + \gamma_2)}{\sin\gamma_1},$$

$$a_{33} = -\cos(\gamma_1 + \gamma_2), \quad G_{12} = \sin\gamma_1 \sin\gamma_2.$$

With allowance for the properties of an orthogonal matrix and with the relations

$$\begin{aligned} & a_{11}\xi_1^0 + a_{21}\eta_1^0 + a_{31}\zeta_1^0 \\ & = L_1(a_{11}\cos\alpha_2 + a_{21}\cos\beta_2 + a_{31}\cos\gamma_2) \\ & = L_1\cos\alpha_1, \end{aligned}$$

$$\begin{aligned} & a_{12}\xi_1^0 + a_{22}\eta_1^0 + a_{32}\zeta_1^0 \\ & = L_1(a_{12}\cos\alpha_2 + a_{22}\cos\beta_2 + a_{32}\cos\gamma_2) \\ & = L_1\cos\beta_1, \end{aligned}$$

$$\begin{aligned} & a_{13}\xi_1^0 + a_{23}\eta_1^0 + a_{33}\zeta_1^0 \\ & = L_1(a_{13}\cos\alpha_2 + a_{23}\cos\beta_2 + a_{33}\cos\gamma_2) \\ & = -L_1\cos\gamma_1 \end{aligned}$$

the term $|y_1 - y_2|$ in the phase φ given by Eq. (8) is reduced to the form

$$|y_1 - y_2| = L_1 + \sum_{i=1}^{2}\left[(-1)^{i+1}\{\Delta s_1^{(i)}\cos\alpha_i\right.$$

$$+ \Delta s_2^{(i)}\cos\beta_i + b_i(\Delta s_1^{(i)})^2 + c_i(\Delta s_2^{(i)})^2\}$$

$$\left. - L_1^{-1}\cos\alpha_i\cos\beta_i\Delta s_1^{(i)}\Delta s_2^{(i)} + \sum_{j=1}^{2} m_{ij}\Delta s_i^{(1)}\Delta s_j^{(2)}\right],$$

$$\begin{Bmatrix} b_1 \\ c_1 \end{Bmatrix} = 0.5\left[L_1^{-1}\begin{Bmatrix} \sin^2\alpha_1 \\ \sin^2\beta_1 \end{Bmatrix} + \begin{Bmatrix} k_1^{(1)} \\ k_2^{(1)} \end{Bmatrix}\cos\gamma_1\right],$$

$$\begin{Bmatrix} b_2 \\ c_2 \end{Bmatrix} = 0.5\left[L_1^{-1}\begin{Bmatrix} \cos^2\alpha_2 \\ \cos^2\beta_2 \end{Bmatrix} + \begin{Bmatrix} k_1^{(2)} \\ k_2^{(2)} \end{Bmatrix}\cos\gamma_2\right],$$

$$\begin{Bmatrix} m_{11} \\ m_{12} \end{Bmatrix} = (L_1 G_{12})^{-1}\left[\cos\beta_1 \begin{Bmatrix} \cos\beta_2 \\ -\cos\alpha_2 \end{Bmatrix}\right.$$

$$\left. - \cos\alpha_1 \begin{Bmatrix} \cos\alpha_2 \\ \cos\beta_2 \end{Bmatrix} Q_{12}\right],$$

$$\begin{Bmatrix} m_{21} \\ m_{22} \end{Bmatrix} = -(L_1 G_{12})^{-1}\left[\cos\alpha_1 \begin{Bmatrix} \cos\beta_2 \\ -\cos\alpha_2 \end{Bmatrix}\right.$$

$$\left. + \cos\beta_1 \begin{Bmatrix} \cos\alpha_2 \\ \cos\beta_2 \end{Bmatrix} Q_{12}\right],$$

$$Q_{12} = \cos\gamma_1\cos\gamma_2.$$

Hence, we have

$$\begin{aligned} \varphi & = |x_0 - y_1| + |y_1 - y_2| + |y_2 - x_3| \\ & = L_0 + L_1 + L_2 + 0.5d_{11}(\Delta s_1^{(1)})^2 + d_{12}\Delta s_1^{(1)}\Delta s_2^{(1)} \\ & + d_{13}\Delta s_1^{(1)}\Delta s_1^{(2)} + d_{14}\Delta s_1^{(1)}\Delta s_2^{(2)} + 0.5d_{22}(\Delta s_2^{(1)})^{(2)} \\ & + d_{23}\Delta s_2^{(1)}\Delta s_1^{(2)} + d_{24}\Delta s_2^{(1)}\Delta s_2^{(2)} + 0.5d_{33}(\Delta s_1^{(2)})^2 \\ & + d_{34}\Delta s_1^{(2)}\Delta s_2^{(2)} + 0.5d_{44}(\Delta s_2^{(2)})^2, \end{aligned}$$

where

$$\begin{Bmatrix} d_{11} \\ d_{22} \end{Bmatrix} = (L_0^{-1} + L_1^{-1})\begin{Bmatrix} \sin^2\alpha_1 \\ \sin^2\beta_1 \end{Bmatrix} + 2\begin{Bmatrix} k_1^{(1)} \\ k_2^{(1)} \end{Bmatrix}\cos\gamma_1,$$

$$\begin{Bmatrix} d_{33} \\ d_{44} \end{Bmatrix} = (L_1^{-1} + L_2^{-1})\begin{Bmatrix} \sin^2\alpha_2 \\ \sin^2\beta_2 \end{Bmatrix} + 2\begin{Bmatrix} k_1^{(2)} \\ k_2^{(2)} \end{Bmatrix}\cos\gamma_2,$$

$$d_{12} = -(L_0^{-1} + L_1^{-1})\cos\alpha_1\cos\beta_1, \tag{9}$$

$$d_{34} = -(L_1^{-1} + L_2^{-1})\cos\alpha_2\cos\beta_2,$$

$$d_{13} = m_{11}, \quad d_{14} = m_{12}, \quad d_{23} = m_{21}, \quad d_{24} = m_{22}.$$

The absence of terms with the first degrees of $\Delta s_j^{(i)}$ $(i, j = 1, 2)$ in the phase φ shows that the points $y_1^* \in S_1$ and $y_2^* \in S_2$ of the direct ray reflection correspond to a stationary value of the phase φ (Eq. (8)).

The final result can be obtained from Eq. (7) by applying the stationary phase approach [6]:

$$p(x_3) = B\frac{\exp\left\{i\left[k(L_0+L_1+L_2)+\frac{\pi}{4}(\delta_4+4)\right]\right\}}{L_0L_1L_2\sqrt{|\det(D_4)|}}, \quad (10)$$

where $B = \cos\gamma_1\cos\gamma_2$ and $D_4 = (d_{ij})$ $(i, j = 1, 2, 3, 4)$ is the Hessian of the symmetric structure with its elements d_{ij}, $i \le j$ being reduced to formula (9). Here, $\delta_4 = \operatorname{sign}D_4$ is the difference between the numbers of positive and negative eigenvalues of the matrix D_4.

Explicit expressions (6) and (10) obtained above show that the pressure $p(x)$ in the reflected wave is determined by the principal curvatures, the Gaussian curvature of the surface at the points of specular reflection, the distances between the points of specular reflection, the distances of these points from the source of waves and from the point of reception of the reflected wave, and the directions of the incident waves.

The method developed above is asymptotic. Formulas (6) and (10) for calculating the amplitudes of singly reflected and a twice-reflected waves, respectively, are valid for $kd \gg 1$, $kR_2^{(m)} \gg 1$, and $kR_2^{(m)} \gg 1$, where d is the characteristic size of the scatterer and $R_1^{(m)}$ and $R_2^{(m)}$ $(m = 1, 2)$ are the principal curvature radii of the surface at the points of specular reflection y_1^* and y_2^*.

The proposed method opens up the way for determining an expression in a closed form for the ray amplitude in the case of an arbitrary number of rereflections of acoustic or elastic waves.

ACKNOWLEDGMENTS

I am grateful to Prof. M.A. Sumbatyan and Prof. Yu.A. Ustinov for the attention paid to this study and for useful discussions. This work was supported by a grant from the President of the Russian Federation in Support of Leading Scientific Schools, grant no. NSh-2113.2003.1.

REFERENCES

1. V. M. Babich and V. S. Buldyrev, *Asymptotic Methods in Short Wave Diffraction Problems* (Nauka, Moscow, 1972) [in Russian].
2. H. Hönl, A. W. Maue, and K. Westpfahl, *Theorie der Beugung* (Springer, Berlin, 1961; Mir, Moscow, 1964).
3. Yu. A. Kravtsov and Yu. I. Orlov, *Geometrical Optics of Inhomogeneous Media* (Nauka, Moscow, 1980) [in Russian].
4. V. A. Borovikov and B. E. Kinber, *Geometrical Theory of Diffraction* (Svyaz’, Moscow, 1978) [in Russian].
5. P. L. Uslengni, *Theory of the Scattering Waves* (Academic, New York, 1978).
6. Do Dyk Tkhang and A. G. Kyurkchan, Akust. Zh. **49**, 51 (2003) [Acoust. Phys. **49**, 43 (2003)].
7. E. A. Shtager, *Radio Wave Scattering by Bodies of Complex Shapes* (Radio i Svyaz’, Moscow, 1986) [in Russian].
8. N. V. Boev and M. A. Sumbatyan, Dokl. Akad. Nauk **392**, 614 (2003) [Dokl. Phys. **48**, 540 (2003)].
9. I. D. Druzhinina and M. A. Sumbatyan, Akust. Zh. **38**, 470 (1992) [Sov. Phys. Acoust. **38**, 257 (1992)].
10. M. A. Sumbatyan and N. V. Boyev, J. Acoust. Soc. Am. **95**, 2346 (1994).
11. E. L. Shenderov, *Wave Problems in Hydroacoustics* (Sudostroenie, Leningrad, 1972) [in Russian].
12. M. V. Fedoryuk, *The Saddle-Point Method* (Nauka, Moscow, 1977) [in Russian].
13. D. A. McNamara, C. W. I. Pistorius, and J. A. G. Malherbe, *Introduction to the Uniform Geometrical Theory of Diffraction* (Artech House, Norwood, 1990).

Translated by E. Golyamina

Acoustical Physics, Vol. 50, No. 6, 2004, pp. 657–663. Translated from Akusticheskiĭ Zhurnal, Vol. 50, No. 6, 2004, pp. 762–769.
Original Russian Text Copyright © 2004 by Galkin, Pankova.

Characteristics of Sound Signals on a Quasi-Stationary Track between the Josephine and Ampere Seamounts

O. P. Galkin and S. D. Pankova
Andreev Acoustics Institute, Russian Academy of Sciences, ul. Shvernika 4, Moscow, 117036 Russia
e-mail: bvp@akin.ru

Received December 17, 2003

Abstract—Experimental data are presented on the measurement of the cross-correlation coefficients and the differences in the arrival times (temporal spectra) of acoustic signals transmitted through a 210-km-long quasi-stationary track in the Atlantic Ocean. At the summit of the Josephine Seamount, a continuous pseudonoise signal was emitted in the one-third-octave band with a mean frequency of 630 Hz. The signal was received at the Ampere Seamount by a 40-m flexible vertical array with a directivity pattern in the form of a static fan of 32 lobes. The width of each lobe was ~3°. At a signal-to-noise ratio of about 3 dB and with an incomplete resolution of multipath signals by the array, the correlation coefficients reached a value of 0.48. The rms fluctuations of the differences in the arrival times varied from 1.8 to 3.1 ms depending on the signal arrival angles. The factors responsible for the low correlation coefficients and the relatively high fluctuations of the arrival time differences are discussed. Apparently, one of the factors is the presence of short-period internal waves. *© 2004 MAIK “Nauka/Interperiodica”.*

Recently, particular emphasis has been placed upon the problems of sound propagation in complicated acoustic oceanic conditions. Many publications are devoted to modeling the sound fields for the case of signal propagation in a shallow sea, on a coastal shelf, and in the presence of internal waves [1–4]. However, to make theoretical predictions about the sound field structure that corresponds to actual characteristics and their variability is rather difficult in many cases, especially in complicated conditions of sound propagation. In light of this, it is necessary to carry out experimental measurements on stationary tracks with a subsequent comparison of the field data with the results of calculations.

The interest in studying acoustic signal propagation on a coastal shelf or on continent slopes is dictated by the necessity of constructing stationary hydroacoustic systems. These are necessary for monitoring certain oceanic regions, as well as for the reception of acoustic signals caused by some large-scale natural phenomena, such as, e.g., underwater earthquakes generating tsunami. In these cases, it is necessary to take into account the spatial and temporal features of the sound field structure that are caused not only by the hydrological characteristics of a specific oceanic region but by the bottom relief as well.

It is known that the reasons for the instability of sound waves propagating in a water medium can be both spatial-temporal variations in the oceanic characteristics, primarily in the sound velocity field, and a change in the positions of the transmission and reception points, for example, during an experiment with drifting ships. In order to separate the influence of the spatial instability of the experimental geometry from that of oceanic spatial-temporal variations on the characteristics of signals propagating between the source and the receiver, an attempt was made to construct a stationary track. To construct such a track in the open ocean with depths of several kilometers is a very difficult problem. Therefore, for carrying out such investigations, two research vessels (transmitting and receiving) were anchored at the summits of the Josephine and the Ampere seamounts. The seamounts are located in the eastern part of the Atlantic Ocean, near the Strait of Gibraltar. The ocean depth around them reaches 4000–4900 m.

Let us consider acoustic-hydrological conditions of the experiments in more detail.

Just before the ships were anchored, extensive topographic surveys were made in the region of the seamounts. For example, Fig. 1a presents the results of such a survey around the Josephine Seamount, and Fig. 1b shows the image of this seamount that was obtained using special echo sounders. Several duplicate images of the summit of this seamount in Fig. 1b were obtained because of the multiple reflections of the echo-sounder pulse from the summit itself and from the ocean surface. It is seen that the summit represents an almost smooth plateau with very steep (up to 30°) slopes.

In accordance with the data on the bottom relief in the region of the selected seamounts, the transmitting ship was anchored at the summit of the Josephine Seamount at the sea depth H ~ 180 m, while the receiving ship was anchored at the summit of the Ampere Seamount, at H ~ 140 m. The separation between the points

1063-7710/04/5006-0657$26.00 © 2004 MAIK “Nauka/Interperiodica”

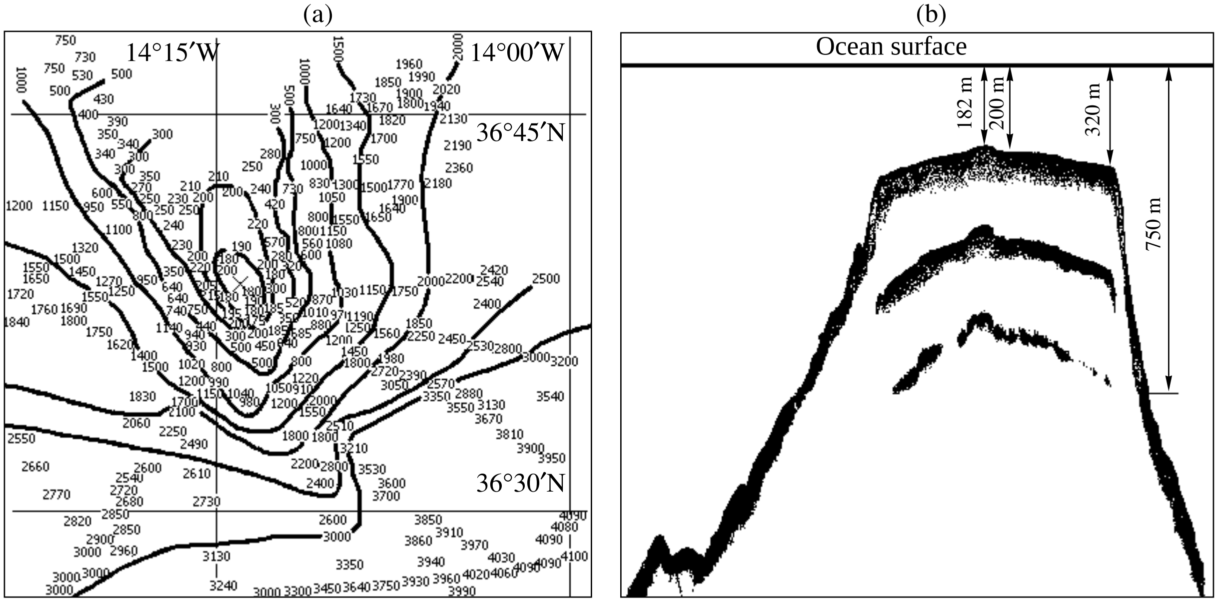

Fig. 1. (a) Results of a topographic survey around the Josephine Seamount and (b) the relief of the seamount obtained by a special echo sounder. The cross indicates the position of the emitting ship.

of emission and reception was ~210 km. As is known, the length of train cables put overboard is usually greater than the sea depth by a factor of 1.5. Therefore, the positions of the ships could be changed within some limits determined by both the length of the train cables and the wind situation or the underwater currents. Since possible changes in the distance between the sound source and the receiving system are generally small, such tracks are commonly considered to be stationary. However, in a strict sense, the experiments were carried out on a track that should be considered to be quasi-stationary.

In connection with the fact that the slopes of the seamounts in the immediate vicinity of their summits were within 15° to 30°, the ocean depth reached 4000 m at a distance of 20 km from the sound source and at a distance of 30 km from the receiving system. The maximal depth along the propagation track was ~4900 m. Thus, the sea depth exceeded 4 km for the major part of the 210-km-long track of sound-signal propagation. The source was put down to a depth of 110 m, and the center of a 40-m receiving system was at a depth of 55 m. Figure 2 shows the general bottom relief along the track, and the inset in the middle of this figure shows the measured depth dependence of the sound velocity $c(z)$.

As is seen, the sound propagation conditions are characterized by the presence of the two coupled waveguides: the underwater sound channel with its axis at a depth of ~500 m and the underwater sound channel with its axis at a depth of ~2000 m. During the acoustic experiments, the wind speed at the emission and reception points varied within 8–10 m/s. On the ocean surface, the wind waves predominated and the surface state corresponded to Beaufort IV (the rms deviation of the surface was 0.3–0.5 m).

The experiments were carried out as follows. An omnidirectional sound source carried by the ship that was anchored at the Josephine Seamount emitted a continuous pseudonoise signal in the one-third-octave band from 560 to 710 Hz with a mean frequency of 630 Hz. The multipath signal was received on the other ship anchored at the Ampere Seamount with the use of a 40-m vertical line array consisting of 296 nonequidistantly arranged receivers. The latter were combined into 74 phase centers. Being formed digitally, the static fan of 32 lobes of the directivity pattern provided the survey of the angular structure of the sound field in the vertical plane in the range of ±48° (here, the plus and minus signs refer to the signals arriving from above and from below, respectively). At the mean signal frequency of 630 Hz, the spatial resolution for each of the 32 lobes of the directivity pattern was ~3° (at the level of 0.7). Note that the correlation interval determined by the frequency band of the emitted signal was 7 ms.

For the correlation processing, we took only the lobes that were related to the signal arrival angles in the vertical plane and that had the highest signal-to-noise ratio. The cross-correlation coefficients were determined, as were the arrival-time differences (the so-called temporal spectrum) between the signals received by different lobes of the static fan, i.e., between the signals received under different angles.

Let us consider now the results of the correlation processing of the signals.

Figure 3 (on the left) shows the signal amplitudes A received by three lobes of the directivity pattern of the

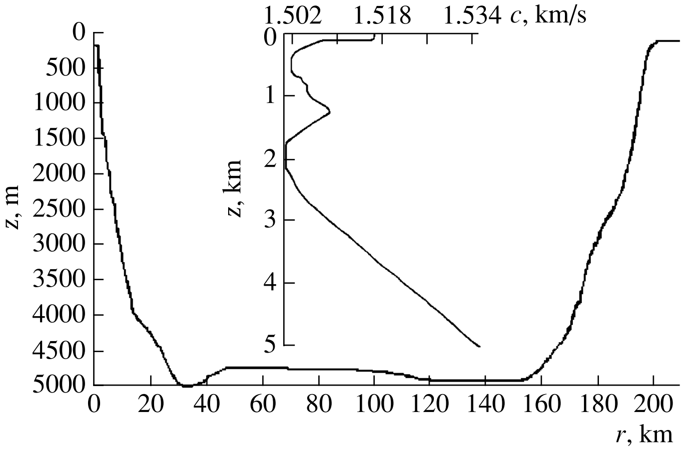

Fig. 2. General bottom relief along the 210-km-long track and the sound velocity profile (the inset in the middle).

static fan. The amplitudes averaged over a one-second-long realization of the received signals are represented on a linear scale along the ordinate axis; the observation time (in minutes) t is represented by the abscissa; the interval between the measurements is 1 min. The slope angles of the lobes of the directivity pattern of the static fan α are indicated on top: $\alpha_1 = 2.7°$, $\alpha_2 = -6.7°$, and $\alpha_3 = -5.4°$. It is necessary to note that all amplitudes in the realizations under consideration (Figs. 3a–3c) are normalized by the same maximum value that occurred in one of them. As a reference for calculating the cross-correlation functions, we choose the signal that had the maximal signal-to-noise ratio. It is taken from the realization for which the temporal amplitude variations of the signal and its spectrum are shown in Fig. 3a. In each of the plots of $A(t)$ (Figs. 3a–3c), the first values (the thicker lines) allow us to estimate the levels of interference arriving under the indicated angles α, since they were recorded at the instants when the useful signal was not emitted.

The energy spectra $S(f)$ of the received signals are shown on the right of Fig. 3 (on the logarithmic scale). As seen from the curves $S(f)$, the signal-to-noise ratio in the frequency range of 0.56–0.71 kHz does not exceed 3 dB. The small value of the signal-to-noise ratio in the experiment is explained not only by the losses in the signal levels due to reflection from the bottom and partially from the rough surface of the ocean but also by the relatively high noise of the working mechanisms of the receiving ship. In particular, the center of the receiving array was at a distance of 55 m from the ship hull, while the upper receivers were only at a distance of 35 m from it.

The dependences of the cross-correlation coefficient R on the time delay τ that were obtained by averaging over 1.024 s are shown in Fig. 4. The cross-correlation coefficient R is represented on the linear scale along the ordinate axis, and the abscissa represents the delays τ between the signals in the interval of ±100 ms. Here, 16 sequential realizations $R(\tau)$ corresponding to a 15-min observation are presented for two pairs of directions of the signal arrivals. Figure 4a refers to the case in which the determination of the cross-correlation between the signals falling into two lobes of the directivity pattern, one of which is directed under the angle $\alpha_1 = 2.7°$ and the other under the angle $\alpha_2 = -6.7°$. Figure 4b shows similar plots of the cross-correlation between the signals with the arrival angles $\alpha_1 = 2.7°$ and $\alpha_3 = -5.4°$.

The multimodal character of $R(\tau)$ is a consequence of the multipath propagation. It is caused by the fact that some signals, although they propagate over various rays, have very close arrival angles and, therefore, fall into a common lobe of the array directivity pattern. As seen from Fig. 4, practically every subsequent realization $R(\tau)$ differs in the form of its correlation peaks from the previous realization separated from it by only a 1-min interval. In addition, many realizations contain different numbers (in some cases, up to 5–7) of correlation peaks. Naturally, the cross-correlation coefficient for each of the signals received by two different lobes of the directivity pattern noticeably decreases. This is related to the fact that other signals that fall in the same lobes but that arrive outside the correlation interval determined by the frequency band play the role of signal-generated noise. Therefore, the values of the correlation coefficients, even for the largest peaks in every realization, are small and lie within 0.32–0.44 for the signals with the arrival angles α_1 and α_2 and within 0.27–0.48 for the signals with the arrival angles α_1 and α_3.

The temporal spectra, i.e., the set of arrival-time differences of the same signal received by various lobes, are presented in Fig. 5. For the signals with the arrival angles α_1 and α_2, they are shown in Fig. 5a, and for the signals with the angles α_1 and α_3, in Fig. 5b. Here, the time delays τ corresponding to the positions of the cor-

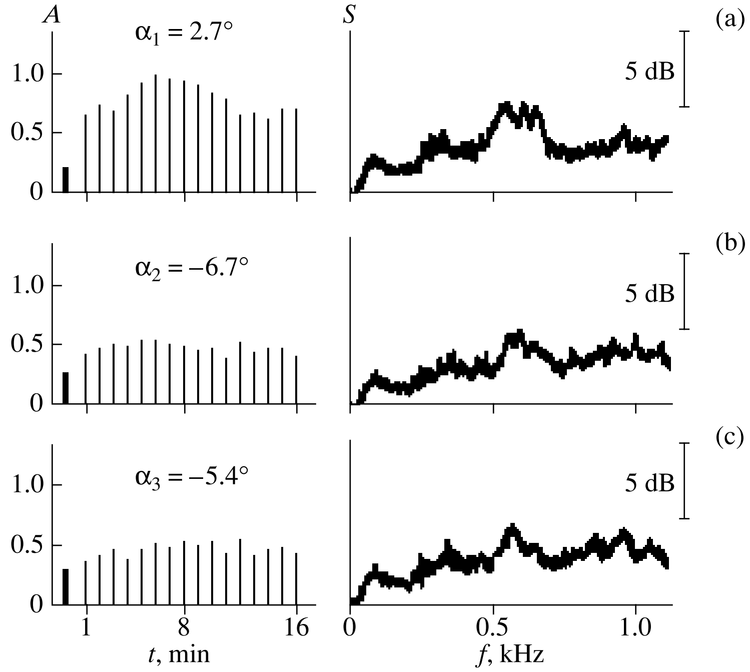

Fig. 3. Amplitudes (on the left) and frequency spectra (on the right) of the signals received by the directivity patterns of the static fan for the arrival angles: (a) $\alpha_1 = 2.7°$, (b) $\alpha_2 = -6.7°$, and (c) $\alpha_3 = -5.4°$.

relation peaks on the τ axis in Fig. 4 are represented by the ordinate, and the instants of their recording, by the abscissa. Various symbols correspond to different values of the cross-correlation coefficient $|R|$: the dark circles refer to $|R| \geq 0.3$, and the crosses, to $|R| < 0.3$. In spite of the instability of the delays τ, one can trace several more or less stable components in the temporal spectra (Fig. 5). They precisely indicate that several signals fall into the same lobes of the directivity pattern. These signals propagate with the different arrival times over various rays, which can be resolved in the correlation processing. These components have the mean values of arrival-time differences ~–3, ~13, and ~43 ms for the signals with the turning angles of the lobes $\alpha_1 = 2.7°$ and $\alpha_2 = -6.7°$ (Fig. 5a), as well as 0 and ~14 ms for $\alpha_1 = 2.7°$ and $\alpha_3 = -5.4°$ (Fig. 5b). The rms fluctuations σ_τ (averaged over 9–15 measurements) vary within 2.1–3.1 and 1.8–2.5 ms, respectively. These values of σ_τ exceed similar values obtained in the experiments studying sound propagation in an underwater sound channel through the same distances in the deep ocean.

A special feature of the ray pattern of sound propagation shown in Fig. 6a is the clear separation of the rays into two groups: one part of the signals propagates only in the upper sound channel, and the other group travels over the whole thickness of the waveguide. The calculation of the sound-field structure on the track under study showed that the energy signals propagating only in the upper sound channel have launch angles at the source located over the summit of the Josephine Seamount that do not exceed ~±5°–6°. In this case, the signals are reflected no less than once from the sloping bottom at the seamount summit. All the rest of the energy signals traveling over the rays with launch angles greater than 6° are also reflected from the bottom, but now they pass over the whole waveguide thickness. In the region of the Ampere Seamount, the signals again are reflected from the sloping bottom and arrive at the receiving array. The rays corresponding to the arrival directions of these signals are shown in Fig. 6b. Considering this end segment of the track, one can see three groups of rays. According to the calculation, each group contains several rays with close grazing angles. One group has the arrival angle ~2°, the second has ~–8.5°, and the third, ~–6°.

It is precisely these three groups of signals that were received in the experiment by three lobes of the static fan of the directivity pattern of the array. The rest of the 29 lobes of the fan did not detect the signals, because the latter were below the noise level. The reception of a great number of the signals by each of the three lobes of the pattern resulted in both the multimodal character of the correlation functions and the decrease in each separate peak. In addition, the structure of the correlation functions undergoes noticeable changes within one minute.

However, such variability of the temporal spectra and the correlation coefficients should not be directly related to the fact that the measurements were carried out on a quasi-stationary track, i.e., under certain changes in the distance between the emitting and

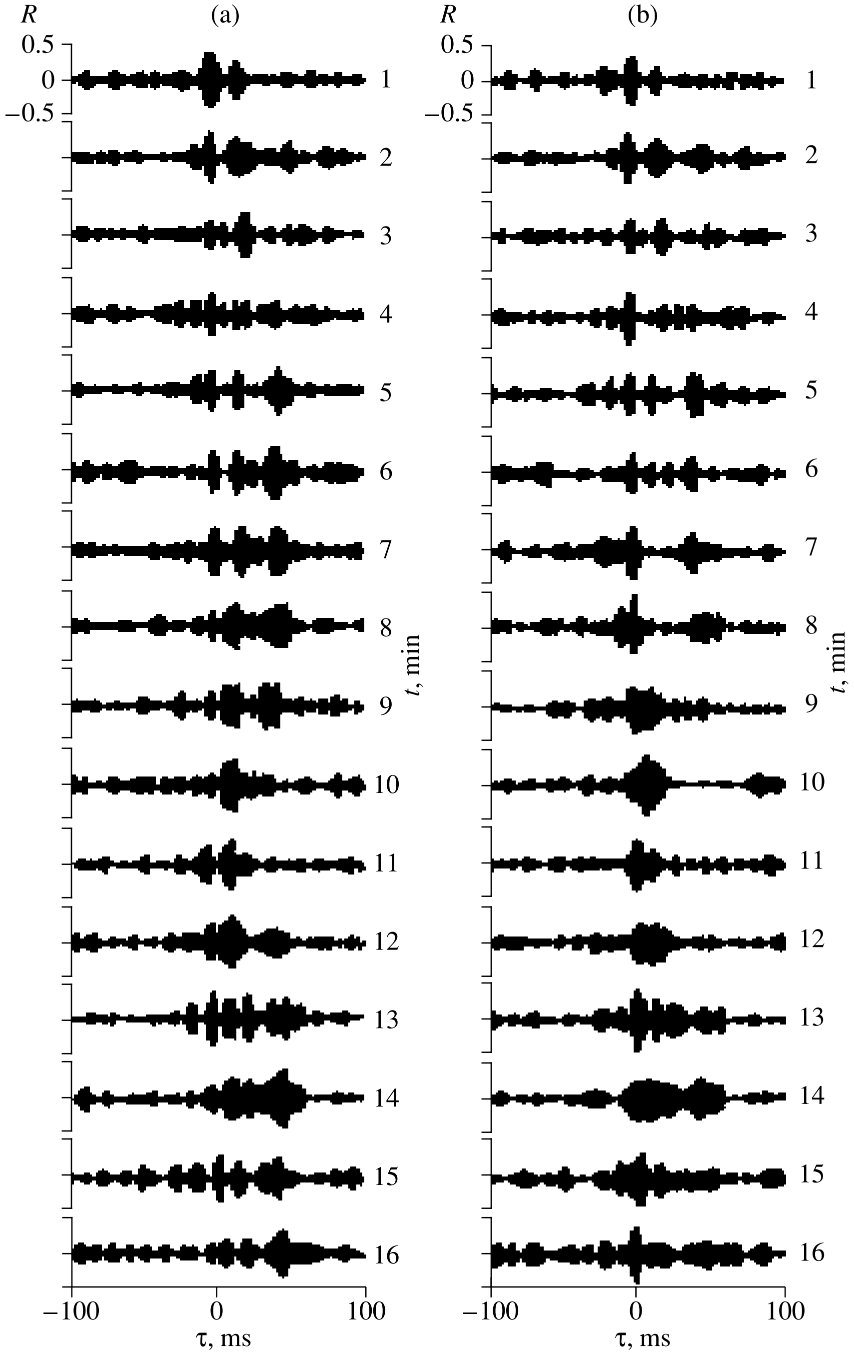

Fig. 4. Variability of the cross-correlation coefficient between signals with the following arrival angles: (a) $\alpha_1 = 2.7°$ and $\alpha_2 = -6.7°$; (b) $\alpha_1 = 2.7°$ and $\alpha_3 = -5.4°$.

receiving systems because of the underwater currents and the wind effect on the anchored ships. Under the conditions of a quasi-stationary track, the separation between the ships during such a short time could be changed due to the above-mentioned factors only by several tens of meters (20–30 m). Moreover, as the calculations show, the distance between the anchored ships during the whole experiment (under very adverse conditions) could be changed by no more than several hundreds of meters (200–300). Such changes, when operating in the deep ocean at distances of ~200 km, do not lead to noticeable modifications of the sound field structure. It is known, for example, that even on drifting ships the correlation characteristics of the signals, as well as the angular and temporal spectra of the sound field, prove to be stable and reproducible in subsequent measurements [5–7], including during operation on the deep-water part of the track under study [8]. A quite dif-

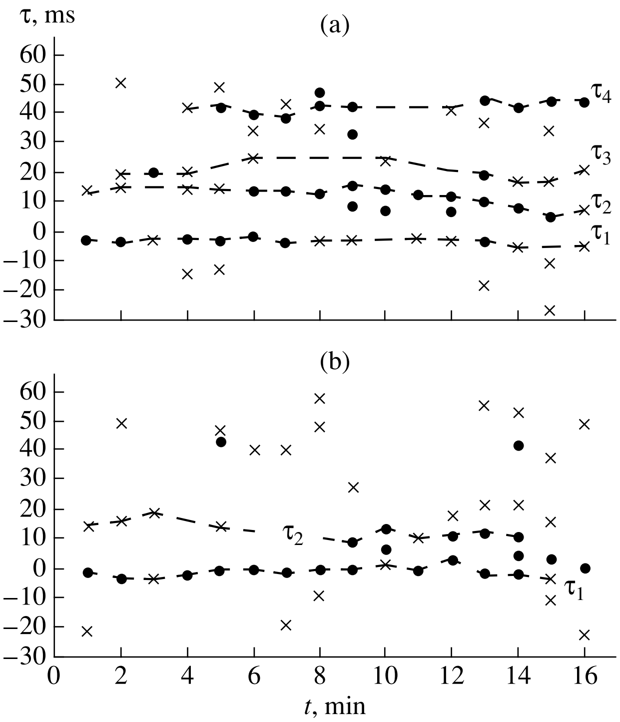

Fig. 5. Variability of temporal spectra for the signals with the following arrival angles: (a) $\alpha_1 = 2.7°$, $\alpha_2 = -6.7°$; (b) $\alpha_1 = 2.7°$ and $\alpha_3 = -5.4°$.

ferent situation arises in our case, in which the emission and reception points are located in shallow water with a sloping bottom. Their movement relative to the bottom changes the sites from which the signals are reflected, and the reflections are different for various rays. Therefore, small changes in the positions of the corresponding points influence in different ways the temporal delays of signals falling onto the same lobe, although the signals propagate over different rays. However, calculations show that a small displacement of the correspondents, which may happen during one minute, should not lead to such changes of the field structure as were observed in the experiments.

Another reason for the sound-field variations and, apparently, the main one, may be the short-period internal waves that are related to the presence of a pronounced thermocline (Fig. 2). This thermocline is located at depths from 65 to 110 m, where the sound velocity varies by 10.5 m/s. As the depth increases, the sound velocity decreases to the very bottom at each of the seamount summits but with smaller gradients. First, such a depth dependence of the sound velocity leads to a situation in which all the rays are reflected from the bottom at very short initial and end sites of the track (as we noted previously). Second, in the test regions on shallow-water parts of the track in the thermocline, short-period internal waves must be present. Their upper frequency corresponds to the Brunt–Vaisala frequency. The latter is determined from the following formula (see, for example, [9]):

$$N = \left(\frac{g}{\rho}\frac{d\rho}{dz} - \frac{g^2}{c^2}\right)^{\frac{1}{2}} \approx \left(\frac{g}{\rho}\frac{d\rho}{dz}\right)^{\frac{1}{2}},$$

where N is the circular frequency, g is the gravitational acceleration, ρ is the water density, z is the depth, and c is the sound velocity in water.

For the aforementioned velocity difference, $\Delta\rho \approx 1.33 \times 10^{-3}$ g/cm^3 and, therefore, $\frac{d\rho}{dz} \approx 2.9 \times 10^{-5}$ g/cm^4; then, $N \approx 1.7 \times 10^{-5}$ s^{-1}, and the minimal period of an internal wave is $T \approx 6.5$ min.

Thus, the experiments described above were most likely carried out in the presence of the short-period internal waves with a period of 10–20 min, which is typical for the conditions under consideration. Such waves, as is known, propagate with a speed of 1–1.5 m/s. Therefore, in shallow water, the hydrological conditions in the narrow upper water layer, even within one minute, continuously varied, which caused changes in the vertical ray refraction. It should be noted that, contrary to horizontal refraction, the internal waves affect the vertical refraction for any direction of their propagation relative to the track. A variable vertical refraction in the upper layer leads to much greater spatial changes of the sites on the sloping bottom where the signal reflections happen, as compared to the small movements of the corresponding points in space, with all ensuing consequences.

Having considered the results of the experiments on the quasi-stationary track including the Josephine and the Ampere Seamounts, we can sum up our results.

The correlation characteristics of continuous pseudonoise signals in the frequency range 0.56–0.71 kHz and the stability of their temporal spectra were investigated on a 210-km-long track.

It is shown that almost each realization of the cross-correlation function of the signals arriving in various lobes of the directivity pattern differs from the previous realization separated by a short one-minute interval. This is related to the fact that each lobe of the pattern receives several signals, sometimes up to seven in number. Therefore, even small fluctuations of the signal intensity and the travel times over the rays connecting corresponding points lead to noticeable changes in the shapes of separate correlation peaks.

It is shown that, because of the multipath character of the sound propagation that leads to the appearance of signal-generated noise, the maximum of the cross-correlation coefficients of the signals received under different angles in the vertical plane does not exceed 0.44–0.48.

Different factors are considered that, in a short one-minute interval, can change the cross-correlation functions and the differences in the signal-arrival times at the site of the receiving system. It is noted that, most likely,

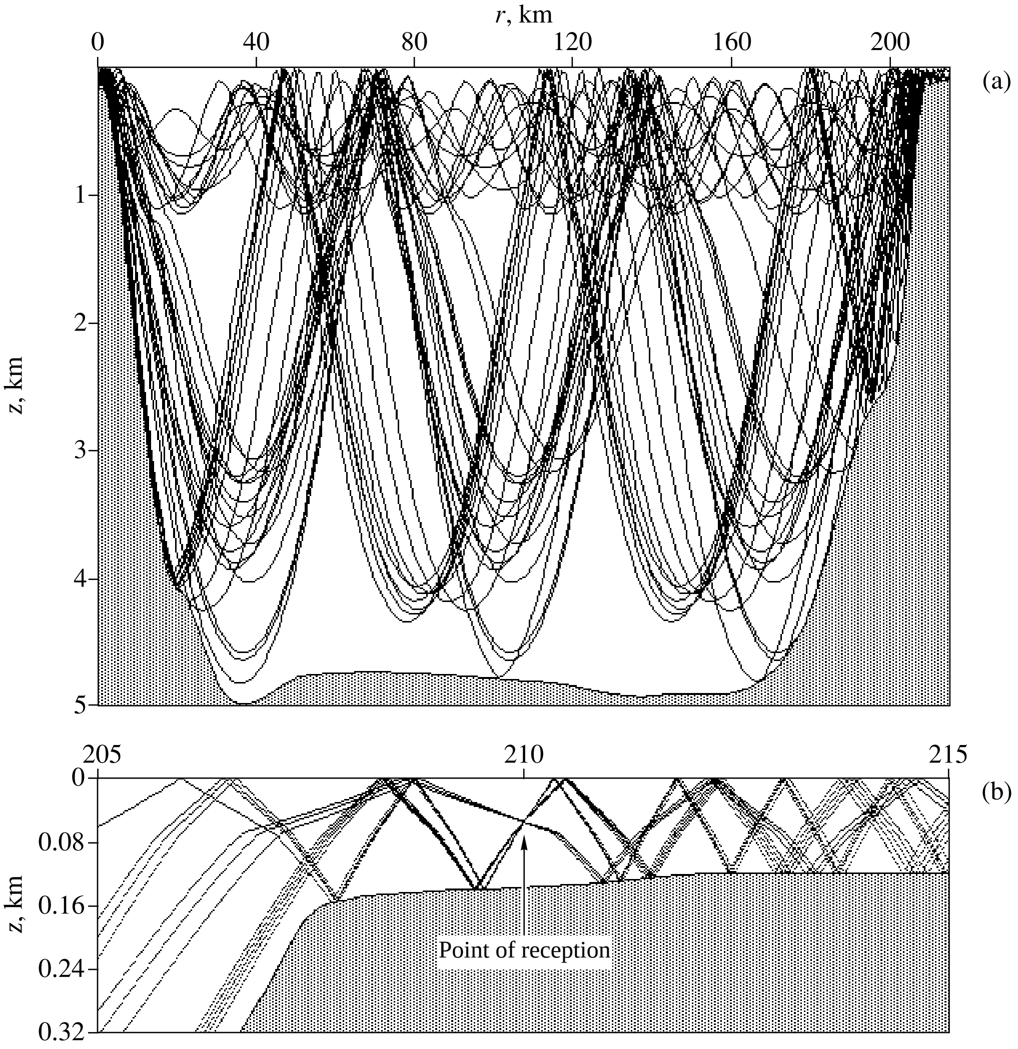

Fig. 6. (a) Ray pattern of the sound field between the Josephine and the Ampere seamounts and (b) a fragment at the site of the receiving array.

the main factor is the presence of short-period internal waves with a period of 10–20 min, which exist in the region of the summits of the Josephine and Ampere seamounts. Owing to this, the rms fluctuation of the differences in the signal arrival times reaches 2.5–3.1 ms, which noticeably exceeds the corresponding values obtained at the same distances in the deep ocean.

ACKNOWLEDGMENTS

This work was supported by the Russian Foundation for Basic Research, projects nos. 03-02-16565, 02-02-17325 and NSh-1277.2003.5.

REFERENCES

1. D. P. Knobles, R. A. Koch, L. A. Thompson, *et al.*, J. Acoust. Soc. Am. **113**, 205 (2003).
2. P. Joseph, J. Acoust. Soc. Am. **113**, 758 (2003).
3. R. Oba and S. Finette, J. Acoust. Soc. Am. **111**, 769 (2002).
4. M. R. Dungan and D. R. Dowling, J. Acoust. Soc. Am. **112**, 1842 (2002).
5. O. P. Galkin and S. D. Pankova, Akust. Zh. **41**, 216 (1995) [Acoust. Phys. **41**, 184 (1995)].
6. O. P. Galkin and S. D. Pankova, Akust. Zh. **44**, 57 (1998) [Acoust. Phys. **44**, 44 (1998)].
7. O. P. Galkin and S. D. Pankova, Akust. Zh. **46**, 467 (2000) [Acoust. Phys. **46**, 400 (2000)].
8. K. V. Avilov, O. P. Galkin, A. E. Lenets, *et al.*, in *Proceedings of IX School–Seminar of Academician L. M. Brekhovskikh on Acoustics of the Ocean* (GEOS, Moscow, 2002), p. 37.
9. *Sound Transmission through a Fluctuating Ocean*, Ed. by S. M. Flatte (Cambridge Univ. Press, Cambridge, 1979; Mir, Moscow, 1982).

Translated by Yu. Lysanov

Acoustical Physics, Vol. 50, No. 6, 2004, pp. 664–669. Translated from Akusticheskiĭ Zhurnal, Vol. 50, No. 6, 2004, pp. 770–775.
Original Russian Text Copyright © 2004 by Gogolinskiĭ, Kosakovskaya, Useinov, Chaban.

Measurement of the Elastic Moduli of Dense Layers of Oriented Carbon Nanotubes by a Scanning Force Microscope

K. V. Gogolinskiĭ*, Z. Ya. Kosakovskaya, A. S. Useinov*, and I. A. Chaban*****
** Technological Institute of Superhard and Novel Carbon Materials,*
ul. Tsentral'naya 7a, Troitsk, Moscow oblast, 142190 Russia
*** Institute of Radioengineering and Electronics, Russian Academy of Sciences,*
ul. Mokhovaya 11, Moscow, 103907 Russia
**** Andreev Acoustics Institute, Russian Academy of Sciences,*
ul. Shvernika 4, Moscow, 117036 Russia
e-mail: chaban@akin.ru

Received February 3, 2004

Abstract—A technique is developed for measuring the modulus of elasticity of a material with a Nanoscan scanning force microscope on the basis of measuring the dependence of probe vibration frequency on the penetration depth of the needle into the specimen. This technique makes it possible to study materials with elastic moduli from 50 to 1000 GPa. The Young moduli of dense films of carbon nanotubes oriented at angles of 45° and 90° to the quartz substrate are measured. From their ratio, the Young modulus in the direction perpendicular to the tubes and the anisotropy of the elastic moduli are determined. A comparison of these values with the corresponding values obtained for a nanotube film deposited on a silicon substrate is carried out. On the basis of this comparison, a conclusion is made concerning the interaction between single-layer nanotubes and between nanotubes in a mixture of single-layer and multilayer ones. © *2004 MAIK "Nauka/Interperiodica".*

Since the discovery of a new carbon modification, namely, carbon nanotubes, in 1991, the physical properties of these objects have been intensively studied all over the world [1, 2]. Experiments were carried out with both isolated nanotubes and nanotube bundles, as well as with layers formed by various methods. These layers may consist of oriented and disoriented nanotubes, and the tubes may be single-layer or multilayer ones, integrated into bundles or not integrated. The properties of nanotubes and their layers proved to be unique in many respects. In particular, carbon nanotubes have a very high value of the Young modulus (above 1 TPa), with a considerably smaller shear modulus [3]; their electrical properties strongly depend on deformation [4]; they may be in a metallic or semiconductor state, and ballistic electron transport with zero electric resistance is possible in them; the interior of nanotubes can be filled with atoms of various elements; and nanotube layers exhibit an intense autoelectronic emission. Every year, new prospects arise for the application of this unique material. The layers of nanotubes are used to produce efficient "cold" cathodes [5]; nanotubes are filled with various materials for their storage and slow consuption; composites are strengthened with nanotubes [3]; nanotubes are used in the fabrication of vacuum microelectronic devices; and, finally, different ways of using nanotubes in medicine are being investigated.

Since many methods exist for fabricating nanotube layers, and every method introduces its own structural features in the material, no generally recognized values of the physical parameters of nanotube layers have been determined until now. A somewhat better situation occurs for isolated nanotubes.

The present paper is aimed at studying the elastic properties of dense layers of oriented carbon nanotubes. We study films of nanotubes uniformly oriented relative to the substrate at angles of 90° and 45°. These are of particular interest because of the anisotropy of the physical properties of individual nanotubes. Each nanotube in the layers has an exit both to the substrate and to the opposite side.

The nanotube layers were fabricated by depositing carbon atoms on a substrate surface using an electron-beam vacuum evaporation of pure graphite. The details of this method can be found in [6]. We used silicon and quartz substrates. The layers on the silicon substrate consist of a mixture of multilayer tubes from 3 to 5 nm in diameter and single-layer tubes of diameter 1.1 nm. The layers deposited on a quartz substrate consist, for the most part, of single-layer nanotubes about 1 nm in diameter. Figure 1 shows a photograph of the structure of a nanotube layer deposited on a quartz substrate, which was obtained using a scanning tunnel microscope. The tubes are arranged in bundles with a bundle radius of 3–5 nm and a distance of 1–2 nm between the bundles. The bonds between the nanotubes in the bundles are covalent and, between the bundles, they are van der Waals.

The measurements were performed with the use of a Nanoscan scanning probe microscope (SPM) intended for investigating the surfaces and mechanical properties of materials (including superhard ones) and thin films (coatings) [7].

A piezoceramic resonator with a high flexural rigidity of the cantilever ($k_3 \sim 10^4$–10^5 N/m) and a resonance frequency of about 12 kHz was used as a probe. A trihedral diamond pyramid with an apex angle of about 60° was used as a needle; the effective radius of the needlepoint is about 100 nm. The instrument makes it possible to obtain an image of the relief and a map of the distribution of the elastic properties, as well as to perform the measurements of the hardness and the elastic modulus of materials, including materials with high values of mechanical parameters (hardness up to 100 GPa and elastic modulus up to 1000 GPa). The values of the Young modulus and Poisson's ratio of the needle are $E = 1140$ GPa and $\nu = 0.07$, respectively.

The procedure for measuring the elastic modulus of the material is based on recording the change in the frequency of probe vibration with the penetration of the needle into the specimen. In the process of measurement, the cantilever with the needle fixed to its free end vibrates in the direction normal to the specimen surface. The base of the cantilever moves step by step normally to the surface, and the change in the resonant frequency $\Delta f = f - f_0$ is measured as a function of the displacement of the cantilever base. Unlike the widely known "loading curves," these dependences may be called "advance curves," since the displacement, rather than the load, is the quantity represented by the abscissa axis.

For the interpretation of the advance curves, a model of the interaction of the probe with the specimen and a model of the contact of the needlepoint with the surface were proposed (Figs. 2a, 2b). The mechanical model of the interaction between the probe and the specimen can be represented as a load vibrating between two springs (Fig. 2a). The cantilever is represented as an elastic element with a rigidity k_p. The rigidity of the contact area is designated by k_c and is determined by the magnitude of deformation and by the elastic properties of the needle and the material under study. The model of the contact of the needlepoint with the surface is constructed under the assumption that the main contribution to the interaction between the needle and the specimen is made by the elastic repulsive forces caused by the deformation of the material.

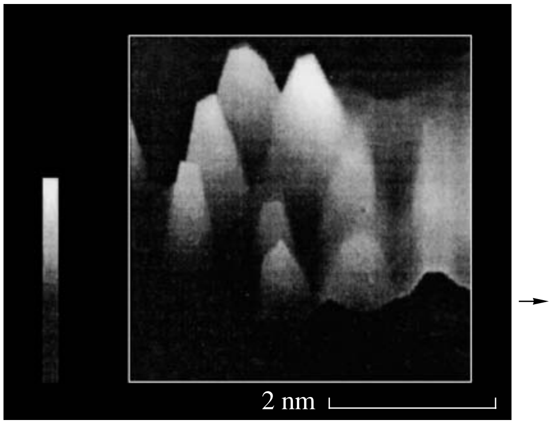

Fig. 1. A photograph of the structure of a layer of carbon nanotubes deposited on a quartz substrate; the photograph is taken by a scanning tunnel microscope.

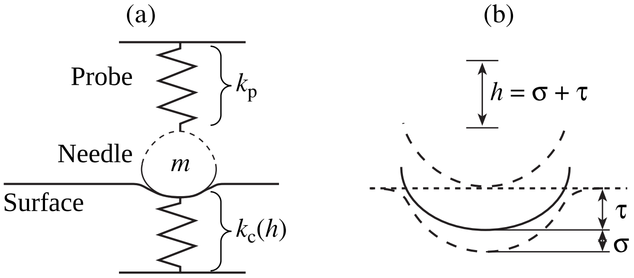

Fig. 2. (a) Mechanical model of the interaction between the needle and the specimen and (b) the model of the contact of the needlepoint with the surface.

In the models, the following designations are used: k_p is the constant of flexural rigidity of the cantilever in the direction of vibrations, k_c is the rigidity of the contact area, $m = k_p/(2\pi f_0)^2$ is the effective mass of the system, f_0 is the natural resonance frequency of the cantilever in the absence of contact with the surface, h is the displacement of the cantilever base, σ is the deformation of the needle, and τ is the deformation of the specimen. The elastic moduli of the needle and the specimen are denoted by E_n and E, respectively.

Below, by the modulus of elasticity E we mean the quantity $E = E'/(1 - \nu^2)$, where E' is the Young modulus and ν is Poisson's ratio. Since, for the great majority of materials, Poisson's ratio lies in the range from 0 to 0.5, it is the Young modulus that plays the dominant part in the quantity E. For the case of hard and superhard materials, which are characterized by high values of elastic moduli and low values of Poisson's ratio, the difference between the quantities E' and E usually does not exceed 5%.

The solution of the equation of motion of the system represented in Fig. 2a gives the following dependence of the variation in probe vibration frequency on the rigidity of the contact area:

$$\Delta f = (f_0/2k_p)k_c(h). \tag{1}$$

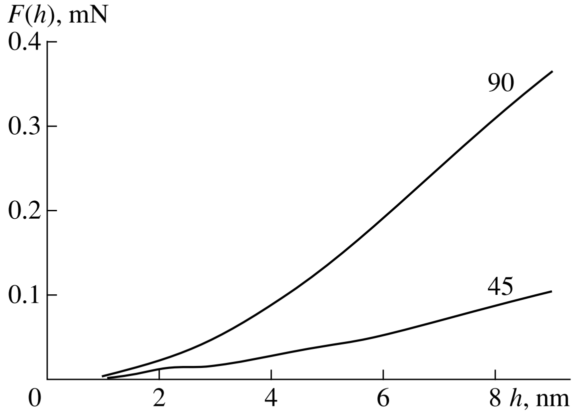

Fig. 3. Pressing force as a function of the depth of needle penetration into the film for the 90° and 45° films of nanotubes on a silicon substrate.

The rigidity of the contact area $k_c(h)$ may be determined by using the Hertz model [8]. Denoting the force arising owing to the summary deformation h in the Hertz model by F_H and the needle radius by R, we obtain

$$k_c(h) = \partial F_H/\partial h = 2\sqrt{R}\frac{E_nE}{E_n+E}\sqrt{h}. \qquad (2)$$

The final formula for the dependence of the change in the probe vibration frequency on the displacement of its base h has the form

$$\Delta f = \frac{f_0\sqrt{R}}{k_p}E\frac{E_n}{E_n+E}\sqrt{h}. \qquad (3)$$

Taking the square of Eq. (3), we obtain

$$(\Delta f)^2 = \alpha^2 h,$$

where

$$\alpha = \frac{f_0\sqrt{R}}{k_p}E\frac{E_n}{E_n+E} = \frac{f_0\sqrt{R}}{k_p}E^* = c_pE^*.$$

It is convenient to introduce the probe coefficient c_p for describing the combined parameters of the probe and the needle, which are usually known with insufficient accuracy. Thus, if we construct a plot of $(\Delta f)^2$ versus h, a straight line will be observed in the operating range. Measuring the slope of this line and taking the square root of its value, it is possible to determine the value of α, which is the main quantity to be measured.

Before the measurement, the needle and the probe should be calibrated using a standard specimen for determining the coefficient c_p. To determine c_p, the advance curve is measured for a standard specimen with a known value of its elastic modulus E_{st}. Then, the slope α_{st}^2 is determined from the curve. The value of c_p is calculated from the expression $c_p = \alpha_{st}/E_{st}^*$. The proposed method makes it possible to measure the elastic moduli of materials with respect to a standard material with a known modulus of elasticity. The experimental evaluation of this method was carried out with a number of specimens with known values of elastic moduli [9].

In the experiment involving the measurement the elastic modulus of a layer of nanotubes, the condition $E_n \gg E$ was satisfied so that the correction for the needle deformation could be neglected. Then, Eq. (3) can be reduced to

$$f - f_0 = \frac{f_0\sqrt{R}}{k_p}E\sqrt{h}. \qquad (4)$$

In [10], the advance curves were obtained for a layer of nanotubes deposited on a silicon substrate with an orientation of 90° relative to the substrate.

In [11], the dependence of the pressing force F on the displacement of the cantilever base h for 90° and 45° films deposited on a silicon substrate was determined:

$$F(h) = 2k_p\int_0^h \frac{f-f_0}{f_0}dh. \qquad (5)$$

This plot, taken from [11], is given in Fig. 3.

In this study, we present the results of measuring the dependence of the square of the frequency shift on the probe displacement for 90° and 45° films deposited on a quartz substrate. The corresponding curves are shown in Fig. 4. In these measurements, the needlepoint radius R was about 100 nm and the constant of flexural rigidity of the probe k_p was about 6×10^4 N/m. Figure 5 shows the relief of the surfaces of the investigated films. The measured map of mechanical properties (moduli of elasticity) practically reproduces the surface relief: the convex parts of the surface have a greater modulus of elasticity. As is seen from Fig. 4, there are two rectilinear portions of the curves with an inflection at the penetration depth of 5–6 nm from the beginning of the frequency rise or 3–4 nm from the point of touching the film surface. We believe that the modulus of elasticity of the film is determined by the first rectilinear portion of the curve and that the inflection and the second portion are connected with the beginning of the deformation of the substrate. The first rectilinear portion for a 90° film corresponds to the value of the Young modulus of 100 ± 9 GPa, and the second rectilinear portion corresponds to the value of 148 ± 7 GPa. For the 45° film, the first rectilinear portion corresponds to the value of the Young modulus of 84 ± 9 GPa, and the second rectilinear portion corresponds to the value of 118 ± 10 GPa.

Let us briefly consider the factors responsible for the decrease by an order of magnitude in the Young modulus of a nanotube layer compared to the Young modulus of a single nanotube. The main factor is the bend of the nanotubes. The forces required bend to a nanotube that

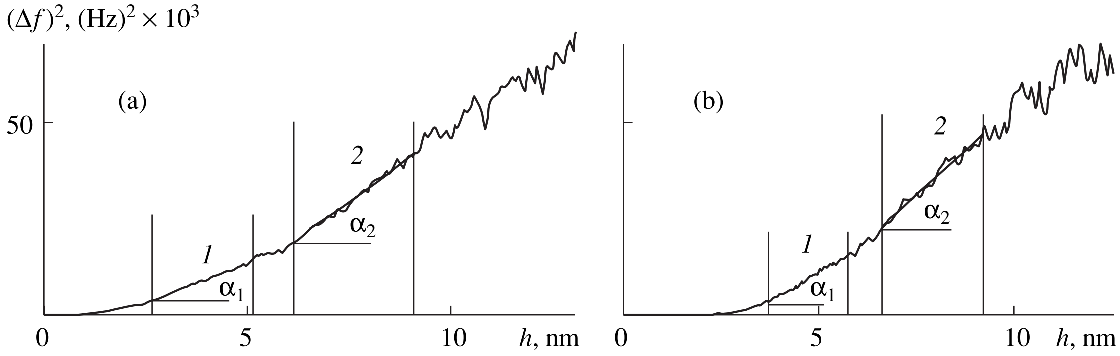

Fig. 4. Frequency shift squared as a function of the probe displacement for the (a) 45° and (b) 90° films of nanotubes on a quartz substrate.

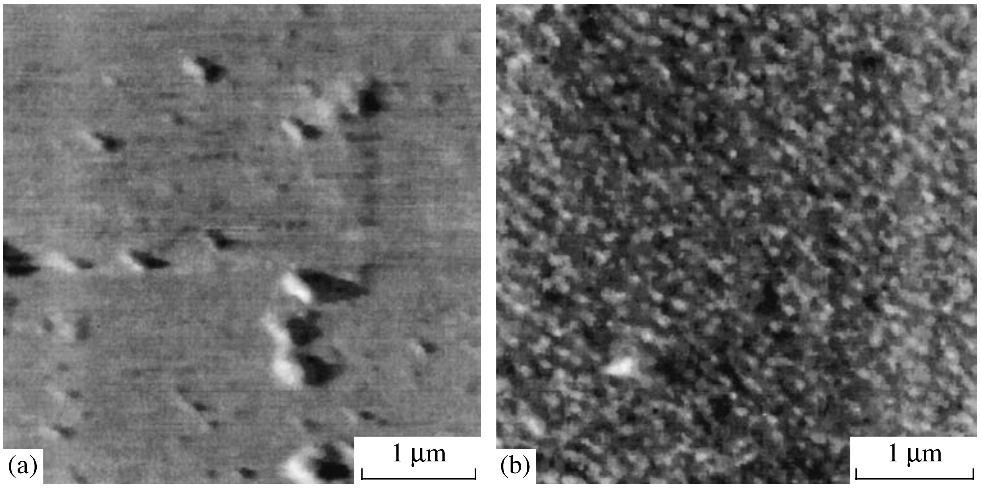

Fig. 5. Surface relief for the (a) 45° and (b) 90° films of nanotubes on a quartz substrate.

is already bent are several times smaller than the forces required for stretching or compressing a nanotube [3]. In the specimens under study, nanotubes are combined into bundles. In the bundles, the nanotubes are bent. An isolated bundle of nanotubes, unlike a separate nanotube, has a Young modulus on the order of several hundreds of GPa [3], which is close to the values determined for the nanotube layers under study. In [12], the elastic modulus of a layer of normally oriented nanotubes (produced by a similar method) deposited on plates made of yttrium aluminum garnet was measured using a microwave resonator. The initially measured elastic modulus across the layer was of the order of 1 TPa. However, after two weeks it became almost three times smaller. In [12], this effect was explained by the self-doping of the carbon nanotube layer with substrate atoms. A similar effect cannot be completely ruled out in our measurements.

Below we show that, using the results of our study and the results reported in [11], it is possible to find the yet unknown Young modulus corresponding to compression in the direction perpendicular to the nanotube orientation for both silicon and quartz substrates. The comparison of these moduli will allow us to draw a conclusion regarding the character of interaction between the nanotubes.

Let us consider a layer of nanotubes oriented at an angle β to the substrate (Fig. 6). In Fig. 6, instead of a layer, a single nanotube is shown. The upper surface of the layer coincides with the *xy* plane. The origin of coordinates coincides with the needlepoint at the first instant of contact. The pressing force of the needle *F*, which is directed along the *z* axis, can be resolved into two components at the point of contact: along the nanotube and perpendicular to it ($F = F_1 + F_2$). The component F_1 produces a displacement u_1 along the nanotube, and the component F_2 produces a displacement u_2 in the perpendicular direction. These displacements, to a certain accuracy, are connected with the force *F* by the relations [8]

$$u_1 = F\sin(\beta)\frac{1}{\pi E_1 r}, \quad u_2 = F\cos(\beta)\frac{1}{\pi E_2 r}, \qquad (6)$$

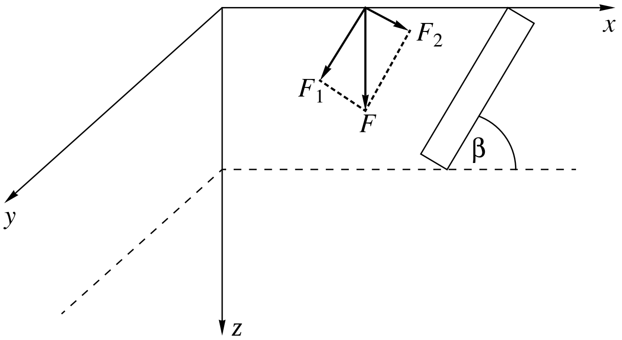

Fig. 6. Illustration to the calculation.

where E_1 and E_2 are the moduli of elasticity along and across the nanotubes, respectively, and $r = (x^2 + y^2 + z^2)^{1/2}$. The displacement along the z axis is

$$\begin{aligned} u &= u_1 \sin(\beta) + u_2 \cos(\beta) \\ &= F\left[\frac{\sin^2(\beta)}{\pi E_1 r} + \frac{\cos^2(\beta)}{\pi E_2 r}\right]. \end{aligned} \tag{7}$$

For $E_1 = E_2 = E$, we obtain the relation given in [8] for the displacement in the z direction as a function of the applied force for an isotropic medium:

$$u = F\frac{1}{\pi E r}.$$

Thus, for the modulus of elasticity measured in the direction of the z axis, we can write

$$E = \left[\frac{\sin^2(\beta)}{E_1} + \frac{\cos^2(\beta)}{E_2}\right]^{-1}. \tag{8}$$

For $\beta = 45°$, Eq. (6) for the elastic modulus takes the form

$$E_{45} = 2\left[\frac{1}{E_1} + \frac{1}{E_2}\right]^{-1}. \tag{9}$$

Similarly, for $\beta = 90°$, $E_{90} = E_1$. The difference Δ in the elastic moduli, which we will determine for the 90° and 45° films, is equal to

$$\Delta = E_1\left(1 - 2\left[1 + \frac{E_1}{E_2}\right]^{-1}\right). \tag{10}$$

The relative change in the elastic modulus at the transition from a 90° film to a 45° one equals

$$d = \frac{\Delta}{E_1} = 1 - 2\left[1 + \frac{E_1}{E_2}\right]^{-1}. \tag{11}$$

Table

h, nm	$F_{45}(h)/F_{90}(h) = b$
2	0.5
4	0.29
6	0.26
8	0.27

From the experimental value of d, we determine the modulus E_2:

$$E_2 = E_1\left(\frac{1-d}{1+d}\right). \tag{12}$$

It is possible to measure the ratio b of the elastic modulus of a 45° film to the elastic modulus of the 90° film:

$$b = \frac{2}{E_1}\left(\frac{1}{E_1} + \frac{1}{E_2}\right)^{-1}. \tag{13}$$

Using the quantity b, the modulus E_2 can be represented as

$$E_2 = E_1\left(\frac{b}{2-b}\right). \tag{14}$$

The values of b determined for various values of h from the curve in Fig. 3 are given in the table. The ratio $F_{45}(h)/F_{90}(h)$ coincides with the ratio b of the corresponding moduli.

As follows from the table, the mean value of b is equal to 0.33. Then, the value of $b/(2 - b)$ is 0.20, so that $E_2 = 0.20E_1$. As was found in the present study, E_1 is approximately equal to 100 GPa, which yields E_2 = 20 GPa for the film on the silicon substrate. The value of b obtained in this study for the quartz substrate is about 0.84, which gives $b/(2 - b) = 0.72$. In this case, E_2 = 72 GPa. Thus, the forces arising with the displacements in the direction normal to the tubes proved to be 3.5 times greater for the single-layer films compared to the films consisting of a mixture of single-layer and multilayer tubes.

In [13], the Young moduli were theoretically calculated for a film consisting of single-layer nanotubes arranged parallel to each other according to the triangular lattice rule. The estimates made in [13] for the Young modulus across the tubes give a value as small as several GPa. As is shown in the present work, the experiment gives an order of magnitude (or even two orders of magnitude) greater value for this modulus.

ACKNOWLEDGMENTS

This work was supported by the Russian Foundation for Basic Research, project nos. 03-02-17499 and 01-02-18017.

REFERENCES

1. R. Saito and M. S. Dresselhaus, *Physical Properties of Carbon Nanotubes* (Imperial College, London, 1998).
2. A. V. Eletskiĭ, Usp. Fiz. Nauk **167**, 945 (1997) [Phys. Usp. **40**, 899 (1997)].

3. E. T. Thostenson, Z. Ren, and Tsu-Wei Chou, Compos. Sci. Technol. **61**, 1899 (2001).
4. L. Liu, C. S. Jayanthi, and S. Y. Wu, Phys. Rev. B **64**, 033412 (2001).
5. J.-M. Bonard, J.-P. Salvetat, T. Stockli, *et al.*, Appl. Phys. A **69**, 245 (1999).
6. Z. Ya. Kosakovskaya, L. A. Chernozatonskiĭ, and V. A. Fedorov, Pis'ma Zh. Éksp. Teor. Fiz. **56** (1), 26 (1992) [JETP Lett. **56**, 26 (1992)].
7. K. V. Gogolinskiĭ and V. N. Reshetov, Zavod. Lab. **64** (6), 30 (1998).
8. L. D. Landau and E. M. Lifshitz, *Course of Theoretical Physics*, Vol. 7: *Theory of Elasticity*, 4th ed. (Nauka, Moscow, 1987; Pergamon, New York, 1986).
9. A. S. Useinov, Prib. Tekh. Éksp., No. 1, 136 (2004).
10. I. S. Grudzinskaya, Z. Ya. Kosakovskaya, V. N. Reshetov, and A. A. Chaban, Akust. Zh. **47**, 632 (2001) [Acoust. Phys. **47**, 548 (2001)].
11. K. V. Gogolinskiĭ, Z. Ya. Kosakovskaya, V. N. Reshetov, and A. A. Chaban, Akust. Zh. **48**, 760 (2002) [Acoust. Phys. **48**, 673 (2002)].
12. G. D. Mansfel'd, Yu. V. Gulyaev, Z. Ya. Kosakovskaya, *et al.*, Fiz. Tverd. Tela (St. Petersburg) **44**, 649 (2002) [Phys. Solid State **44**, 674 (2002)].
13. V. N. Popov, V. E. Van Doren, and M. Balkanski, Solid State Commun. **114** (7), 395 (2000).

Translated by A. Svechnikov

Acoustical Physics, Vol. 50, No. 6, 2004, pp. 670–676. Translated from Akusticheskiĭ Zhurnal, Vol. 50, No. 6, 2004, pp. 776–782.
Original Russian Text Copyright © 2004 by Dvoesherstov, Cherednik, Petrov, Chirimanov.

Numerical Analysis of the Properties of Slit Electroacoustic Waves

M. Yu. Dvoesherstov, V. I. Cherednik, S. G. Petrov, and A. P. Chirimanov
Lobachevsky State University, pr. Gagarina 23, Nizhni Novgorod, 603950 Russia
e-mail: dvoesh@rf.unn.ru

Received March 17, 2003

Abstract—The properties of slit electroacoustic waves that propagate in a system of two semi-infinite piezoelectric media separated by a vacuum gap, in a system consisting of a thin piezoelectric plate and a semi-infinite piezoelectric medium separated by a gap, and in a system consisting of two thin piezoelectric plates separated by a vacuum gap are studied. The process of transformation of slit electroacoustic waves to generalized surface acoustic waves or to Lamb waves is considered. © *2004 MAIK "Nauka/Interperiodica".*

As is known [1–4], slit electroacoustic waves (SEAWs) may propagate in a system of two semi-infinite piezoelectric crystalline media separated by a thin air gap. The energy of these waves is localized near the boundaries of the piezoelectric half-spaces and exponentially decays on both sides of the gap toward the depth of both piezoelectric media. Mechanical displacements in the two piezoelectric media are related to each other through the air gap by the electrostatic field accompanying the wave. It should be noted that an SEAW can also propagate in more complex configurations of piezoelectric media. These include, for example, a system consisting of a thin piezoelectric plate and a piezoelectric half-space with a gap between them or a system of two thin piezoelectric plates separated by a gap (when the plate thickness is $H \approx \lambda$, where λ is the wavelength). The interest in studying this type of waves arises from the fact that the SEAWs can be used in designing various kinds of acoustoelectronic pressure and temperature sensors or liquid and gas analyzers [4, 5].

An analytical calculation of the properties of SEAWs propagating in a system of two identical piezoelectric half-spaces separated by a gap was first carried out in [1–3]. In these publications, transverse slit acoustic waves with displacements u_2 in the boundary plane were studied, because the piezoelectric crystal cuts considered there satisfied the crystallographic symmetry conditions [6]. From the theory of surface acoustic waves (SAWs), it is known that, if the X_1X_3 saggital plane is perpendicular to the axis of twofold rotation of the crystal about one of the crystallographic axes of the crystal, i.e., the X, Y, or Z axis, then, X_1 is the direction of propagation of the "pure" acoustic mode (the Gulyaev–Bleustein mode) characterized by only one purely transverse component of mechanical displacement u_2 and an accompanying electric potential φ. If the saggital plane is a mirror symmetry plane of the crystal, the X_1 axis is the direction of propagation of the "pure" acoustic mode characterized by two components of mechanical displacement, u_1 and u_3, and an accompanying electric potential φ (the pure Rayleigh mode). In all other cases, a SAW has all three components of mechanical displacement, namely, u_1, u_2, and u_3, and an electric potential (φ). The same crystallographic symmetry conditions can be applied to SEAWs.

In this paper, we theoretically study the properties of the general type of SEAWs propagating in a system of two piezoelectric crystals of any crystallographic symmetry. In the most general case, in both media the SEAWs will have not one transverse u_2 but rather all three components of mechanical displacement u_i, where $i = 1, 2, 3$. We also study the properties of more complex SEAWs that propagate in a system of two different semi-infinite piezoelectric media separated by an air gap, in a system consisting of a thin piezoelectric plate and a semi-infinite piezoelectric medium with a gap between them, and in a system of two thin piezoelectric plates separated by a gap. We theoretically calculate the basic parameters of different modes of the SEAWs (the phase velocity V, the electromechanical coupling coefficient K^2, and the temperature coefficient of delay TCD).

Let us first consider a system that consists of two semi-infinite piezoelectric media separated by a vacuum gap whose width H is smaller than the wavelength λ (Fig. 1). Let the plane $X_3 = 0$ lie in the middle of the gap. The X_1 axis is the direction of propagation of a SEAW with a wave number $K = 2\pi/\lambda$. The electric energy of the SEAW is localized within the gap, and the mechanical displacements reach their maxima at the boundaries of the piezoelectric media, $X_3 = \pm H/2$, and exponentially decay on both sides of the gap in the depths of the two media. If the two piezoelectric media are identical and have the same orientation, the distribution of the electric potential φ in the gap may be symmetric or antisymmetric and, hence, in this case, both symmetric and antisymmetric modes of the SEAW may propagate in the system under consideration. Unlike the classical SAW propagating over a free surface of the crystal, the velocity V of the SEAW depends on the wavelength λ. This spatial dispersion is related to the presence of a finite size (the gap width H) in the given structure and is analogous to the dispersion of waves in waveguides [3].

The general solution for such a wave can be obtained by solving the equations of the elasticity theory and electrostatics for both media [6, 7]. In addition, it is necessary to use ten boundary conditions. The mechanical and electric boundary conditions at the boundaries of piezoelectric media 1 and 2 ($X_3 = \pm H/2$) with a gap are as follows:

the zero values of the normal components of the stress tensor T_{3i} are

$$\begin{gathered} T^1_{31} = 0, \quad T^1_{32} = 0, \quad T^1_{33} = 0 \text{ at } X_3 = H/2, \\ T^2_{31} = 0, \quad T^2_{32} = 0, \quad T^2_{33} = 0 \text{ at } X_3 = -H/2, \end{gathered} \tag{1}$$

and the continuity of the electric potential φ and the normal component of the electric induction D_3 are

$$\begin{gathered} \varphi^V = \varphi^1, \quad D^1_3 = D^V_3 \text{ at } X_3 = H/2, \\ \varphi^V = \varphi^2, \quad D^2_3 = D^V_3 \text{ at } X_3 = -H/2. \end{gathered} \tag{2}$$

In the general form, the displacements u_i and the potential φ in each piezoelectric medium (media 1 and 2) can be represented as a sum of four partial waves ($u_4 = \varphi$):

$$\begin{gathered} u^1_i = A_m C_{im} \exp(jK\beta^1_m X_3)\exp[jK(X_1 - Vt)], \\ u^2_i = B_m D_{im} \exp(jK\beta^2_m X_3)\exp[jK(X_1 - Vt)]. \end{gathered} \tag{3}$$

Here, A_m, C_{im}, B_m, and D_{im} are the amplitude factors, $\beta^{1,2}_m$ are the coefficients of attenuation along the X_3 axis, V is the wave velocity, and i and m are the indices: $i = 1$–4 (coordinates and potential) and $m = 1$–4 (partial mode number), where a summation is implied over repeated indices m.

Substituting these solutions into the set of equations of the elasticity theory, we obtain the Christoffel equations, from which we can calculate the partial wave amplitudes C_{im} and D_{im} and the coefficients $\beta^{1,2}_m$. Since the displacement amplitudes should decay in the depths of the media, from the complex attenuation coefficients $\beta^{1,2}_m$ found for the first and second media it is necessary to chose the coefficients that have a physical meaning, i.e., that comply with the condition of the wave localization near the surfaces of the two crystals.

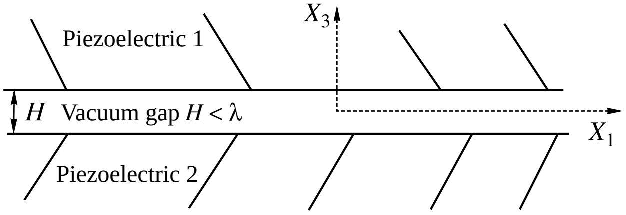

Fig. 1. System of two semi-infinite piezoelectric media separated by a gap.

The electric potential inside the vacuum gap, φ^V, is determined from the solution to the Laplace equation and can be represented in the form

$$\begin{aligned} \varphi^V = {} & (\Phi_s \cosh(KX_3) + \Phi_a \sinh(KX_3)) \\ & \times \exp(jK(X_1 - Vt)). \end{aligned} \tag{4}$$

The unknown coefficients Φ_s, Φ_a, A_m, and B_m are determined from the set of ten complex homogeneous equations that are obtained from the boundary conditions formulated above.

The number of unknowns and the number of equations can be reduced to eight if we preliminarily express the coefficients Φ_s and Φ_a in terms of the potentials of both media at their boundaries. The two ways of determining the coefficients Φ_s, Φ_a, A_m, and B_m are fully equivalent. Then, using the Farnell–Jones approach [6], we can determine the phase velocity V of the SEAW by solving the set of linear homogeneous boundary equations obtained from conditions (1) and (2).

As an example, in Fig. 2 we present the calculated dependences of the phase velocity V on the normalized width of the vacuum gap H/λ for the antisymmetric (curve A) and symmetric (curve S) modes of the SEAW propagating in a system of two identical lithium niobate piezoelectric crystals specified as YX-cut $LiNbO_3$ with the Eulerian angles $\phi = 0°$, $\theta = 90°$, and $\Psi = 0°$ [8]. From Fig. 2, one can see that the velocity of the modes of the SEAW exhibits a dispersion and, when $H/\lambda > 0.01$, the modes of the SEAW transform to a common SAW ($V_{SAW} = 3.7178$ km/s) propagating in the given direction of the piezoelectric crystal.

If two different piezoelectric crystals or identical piezoelectric crystals of different cuts are used, the very structure of the wave becomes asymmetric with respect to the center of the gap. In this case, the existence of purely symmetric and purely antisymmetric modes of the SEAW is impossible. However, solutions exist for the distorted quasi-symmetric and quasi-antisymmetric modes of the SEAW. The greater the difference between the piezoelectric crystals in their material properties and crystallographic symmetry, the stronger the distortions of the SEAW modes are. As an example, Fig. 3 presents the calculated values of the phase velocity of the SEAW modes propagating in a system of two identical piezoelectric media of different crystal cuts, namely, YX-cut $LiNbO_3$(0°, 90°, 0°) and XY-cut

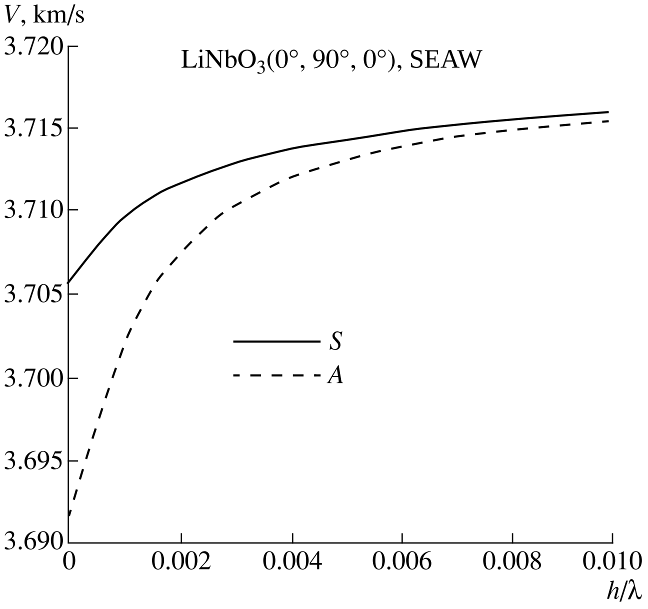

Fig. 2. Dependence of the phase velocity V on H/λ for the (A) antisymmetric and (S) symmetric modes of the SEAW in a system of two identical piezoelectric media, *YX*-cut $LiNbO_3$.

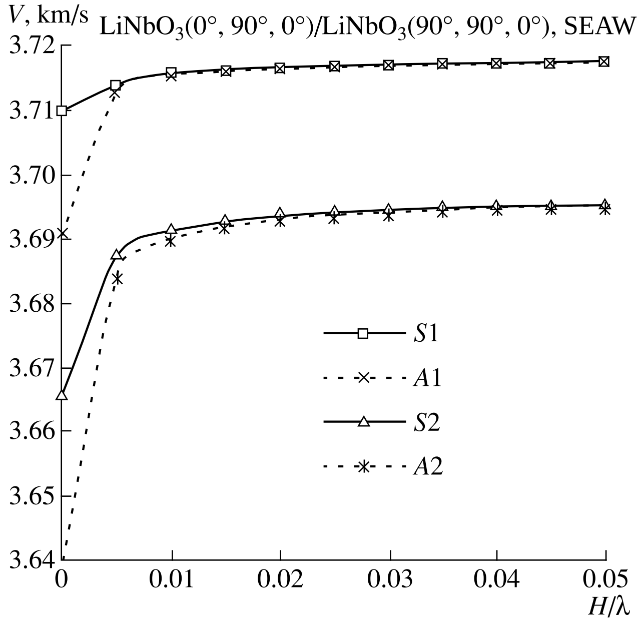

Fig. 3. Dependence of the phase velocity of the SEAW modes on H/λ in a system of two piezoelectric media: *YX*-cut $LiNbO_3$ and *XY*-cut $LiNbO_3$ with a gap between them.

$LiNbO_3$(90°, 90°, 0°), separated by a gap. For these crystal cuts, the crystallographic symmetry conditions [6] are not satisfied. From Fig. 3, one can see that solutions exist for two quasi-symmetric modes (curves $S1$ and $S2$) and two quasi-antisymmetric modes (curves $A1$ and $A2$) of the SEAW. As the gap width increases ($H/\lambda > 0.01$), these modes are transformed to SAWs propagating in the *YX*-cut ($V_{SAW} = 3.7178$ km/s) and *XY*-cut lithium niobate ($V_{SAW} = 3.696$ km/s), respectively.

An analysis of the properties of SEAWs propagating in a system that consists of a thin piezoelectric plate and a semi-infinite piezoelectric medium with a gap between them is of special interest, because precisely this type of structure seems to be promising for the development of acoustoelectronic sensors. To find the solutions, one can use the method described above. However, if the thickness of the piezoelectric plate $H2$ is comparable with the wavelength λ, the energy of the wave will be distributed over the whole thickness of the plate and, therefore, the solution for u_i in the plate should be represented as a sum of eight partial waves with allowance for all eight attenuation coefficients β_m ($m = 1, 2, \ldots, 8$) along the X_3 axis. It is also necessary to add four boundary conditions for the upper free boundary of the piezoelectric plate: the zero values of the normal components of the stress tensor T_{3i} and the continuity of the normal component of the electric induction. Then, one has to solve a set of 14 complex homogeneous boundary equations (or 12 equations, if the coefficients Φ_s and Φ_a are preliminarily determined).

Figure 4 shows a family of curves representing the calculated phase velocities of the symmetric mode of the SEAW versus the normalized gap width H/λ in a system consisting of a piezoelectric plate made of *YX*-cut quartz SiO_2(0°, 90°, 0°), a vacuum gap, and a semi-infinite piezoelectric crystal of *YX*-cut quartz SiO_2(0°, 90°, 0°) for different values of the thickness of the upper plate: $H2/\lambda = 0.2$, 5, 6, 7, and 10 (curves denoted as $H2 = 0.2$, $H2 = 5$, $H2 = 6$, $H2 = 7$, and $H2 = 10$). From this figure one can see that, as the thickness of the upper plate $H2/\lambda$ decreases, the phase velocity of the SEAW mode also decreases. When the gap width increases to $H > 0.1\lambda$, the SEAW mode transforms to a SAW propagating in the *YX*-cut quartz ($V_{SAW} = 3.1605$ km/s). In addition, two solutions exist simultaneously for electroacoustic symmetric and antisymmetric Lamb modes [9, 10] propagating in the upper piezoelectric quartz plate. These Lamb modes exhibit a velocity dispersion. Unlike the case of a single free piezoelectric plate, in the system under consideration the values of the Lamb mode velocities depend on both the plate thickness $H2$ and the gap width H. Figure 5 shows the calculated dependences of the velocity of the antisymmetric Lamb mode on the gap width H/λ for two different values of the thickness of the *YX*-cut quartz plate: $H2/\lambda = 0.2$ with the Lamb mode velocity $V = 1.657$ km/s (curve $H2 = 0.2$), and $H2/\lambda = 1$ with the Lamb mode velocity $V = 2.97898$ km/s (curve $H2 = 1$).

Note that the structure considered above is fundamentally asymmetric with respect to the center of the gap. Therefore, even if the piezoelectric plate and the medium are made of the same material and have identical orientations, the SEAW modes will also be quasi-symmetric or quasi-antisymmetric. When the gap width increases, one mode transforms to a SAW propagating along the surface of the half-space and the other mode transforms to a Lamb mode propagating in the upper piezoelectric plate.

In a system consisting of two thin piezoelectric plates separated by a gap, the propagation of piezoelectrically active modes of the SEAW is also possible. Let us consider the system shown in Fig. 6. Here, *H*1 and *H*2 are the thicknesses of the upper and lower piezoelectric plates and *H* is the width of the gap between them. This kind of system is of interest because it allows one to study the process of transformation of the SEAW modes. For example, if the thicknesses of the two plates are *H*1, *H*2 $\gg \lambda$, in the general case we obtain two classical modes of the SEAW that propagate in a system of two piezoelectric half-spaces separated by a gap. As the gap width increases, the SEAW transforms to the common SAWs propagating along the surfaces of the two piezoelectric media. If the thicknesses of the two plates are *H*1, *H*2 $\approx \lambda$, an increase in the gap width will lead to a transformation of the SEAW to electroacoustic Lamb modes propagating in the piezoelectric plates. When the thickness of one plate is comparable to the wavelength λ and the thickness of the other plate is much greater than λ, the SEAW will transform to a common SAW propagating in the piezoelectric medium and to Lamb modes propagating in the piezoelectric plate.

A general solution for the SEAW in such a system can be obtained by representing the corresponding solutions for the mechanical displacements and the electric potential in the form of eight partial waves propagating in each of the plates. In this case, the number of boundary conditions will be greater, and it is necessary to find a solution to a set of 18 complex homogeneous boundary equations (or 16 equations).

As an example, Fig. 7 shows the calculated velocities of the symmetric and antisymmetric modes of the SEAW (the curves marked as mode *1* and mode *2*) propagating in the system of two identical piezoelectric plates made of langasite (LGS) with the (0°, 140°, 25°) orientation and with the thickness $H2 = H1 = \lambda$ versus the gap width H/λ. As the gap width increases to $H/\lambda > 0.1$, the velocities of these modes tend to the velocities of the Lamb modes propagating in the piezoelectric plates. This means that the SEAW modes transform to the corresponding Lamb modes. Figure 8 displays the calculated velocities of the fundamental symmetric and antisymmetric Lamb modes (curves *S* and *A*) versus the plate thickness $H1/\lambda$. It should be noted that, in a single plate, an increase in its thickness to $H1 > 0.5\lambda$ leads to the appearance of a family of electroacoustic Lamb modes of higher orders [9, 10] (not shown in the figure), which transform to common SAWs as the plate thickness increases. In a system of two piezoelectric plates separated by a gap, symmetric (V_S = 2.8153 km/s) and

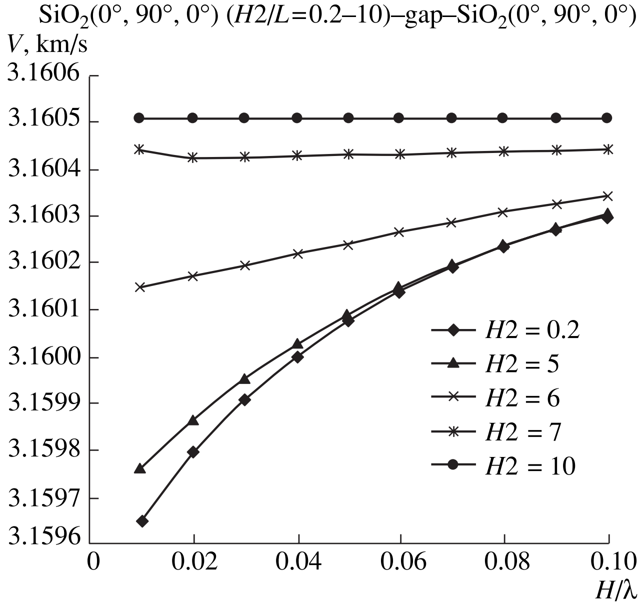

Fig. 4. Dependence of the phase velocity of the SEAW on H/λ in a system consisting of a *YX*-cut SiO_2 piezoelectric plate and a *YX*-cut SiO_2 piezoelectric medium with a gap between them for different values of the plate thickness: *H*2 = 0.2, 5, 6, 7, and 10.

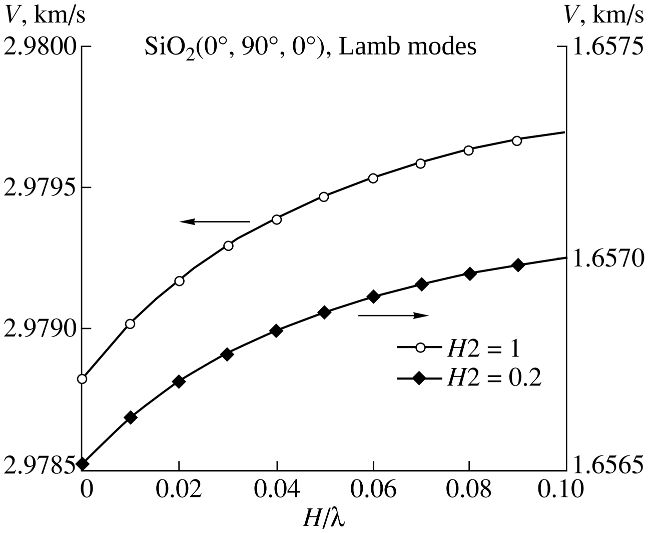

Fig. 5. Dependence of the velocity of the antisymmetric Lamb mode on the gap width H/λ for two different values of the *YX*-cut quartz plate thickness: *H*2 = 0.2 and 1.

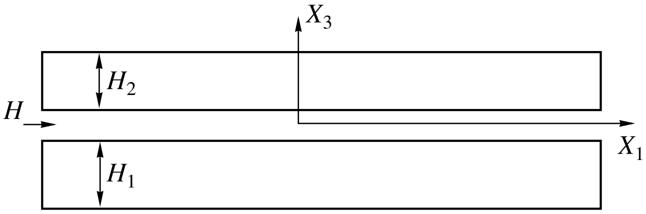

Fig. 6. System of two piezoelectric plates separated by a gap.

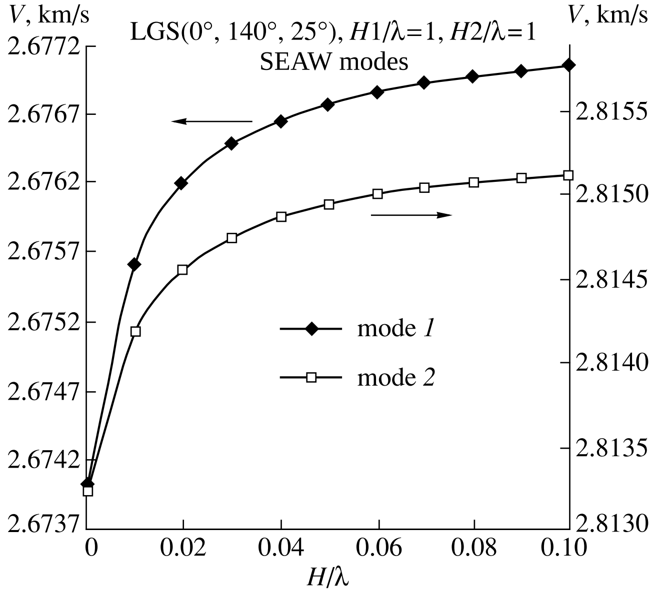

Fig. 7. Dependences of the velocities of the symmetric and antisymmetric modes of SEAW (modes *1* and *2*) on H/λ in a system of two piezoelectric plates made of langasite (LGS) with the orientation (0°, 140°, 25°).

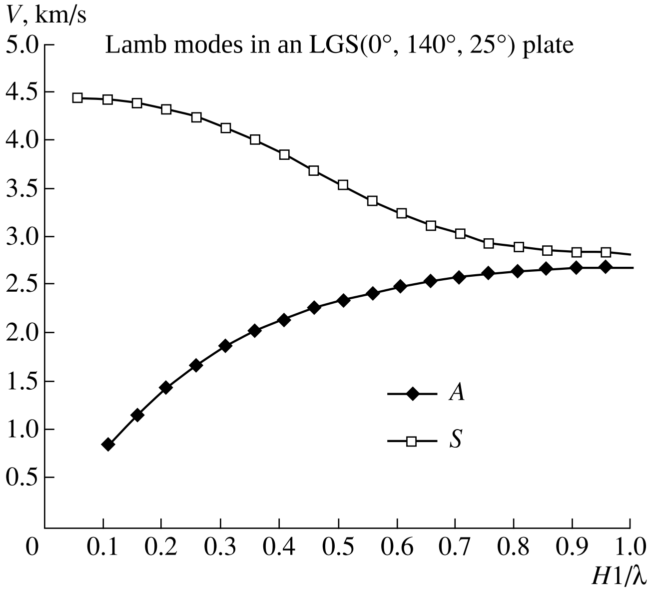

Fig. 8. Dependences of the velocities of the fundamental (*S*) symmetric and (*A*) antisymmetric Lamb modes on H/λ in an LGS(0°, 140°, 25°) piezoelectric plate.

antisymmetric ($V_A = 2.6773$ km/s) modes of the SEAW (see Fig. 7) transform to Lamb modes with an increase in the gap width (see Fig. 8). Finally, when the thicknesses of the two langasite plates are $H2$, $H1 > 5\lambda$, an increase in the gap width to $H > 0.1\lambda$ leads to the transformation of the SEAW to a common SAW propagating over the free surface of the langasite (V_{SAW} = 2.744 km/s).

It should be noted that one of the difficulties in solving the equations described above is that, in such complex piezoelectric crystal structures, several solutions simultaneously exist for one or another type of wave. Therefore, when searching for a specific mode, it is necessary to chose a sufficiently narrow interval of velocities, because, according to the Farnell–Jones approach, the phase velocity of the wave V is the parameter of the problem that is scanned to find the zero determinant of the boundary conditions [6, 11].

After calculating the phase velocity of the wave, it is possible to determine all other parameters of the wave. As is known [6], the electromechanical coupling coefficient K^2 for a SAW, which determines the efficiency of the wave excitation by an interdigital transducer positioned on the surface of the piezoelectric crystal, is calculated by the formula $K^2 = 2(V_0 - V_S)/V_0$, where V_0 and V_S are the SAW velocities along the open and metallized surfaces of the piezoelectric crystal.

Unlike SAWs, SEAWs propagate in a system of two piezoelectric crystals separated by a gap. If one of the piezoelectric crystal surfaces is metallized, the SEAW itself disappears, because the electric field connecting the oscillations in the two piezoelectric media proves to be shorted out, and the two half-spaces become completely isolated. However, to estimate the efficiency of excitation of the SEAW, it is possible to determine the electromechanical coupling coefficient K2 in a similar way. For example, if the SEAW is excited by an interdigital transducer positioned on the surface of the upper piezoelectric crystal, we have

$$K_U^2 = 2(V_0 - V_S)/V_0, \tag{5}$$

where V_0 is the velocity of the SEAW and V_S is the SAW velocity along the metallized surface of the upper piezoelectric crystal. If the SEAW is excited by an interdigital transducer placed on the surface of the lower piezoelectric crystal, we have $K_l^2 = 2(V_0 - V_S)/V_0$, where V_0 is the velocity of the SEAW and V_S is the SAW velocity along the metallized surface of the lower piezoelectric crystal.

For a system of two thin piezoelectric plates separated by a gap, the value of K^2 for SEAWs can be determined for a greater number of variants, depending on the positions of the interdigital transducers (four variants of positioning on one of the four surfaces) and on the state of each of the outer surfaces (metallized or free) that carries no interdigital transducer.

We used formula (5) to calculate the value of K_U^2 for the SEAW as a function of the normalized gap width H/λ in a system of two piezoelectric media consisting of langasite LGS with the orientation (0°, 140°, 25°). The calculations showed that the value of K_U^2 drastically decreases with increasing gap width. For example, for the gap width $H = 0.0001\lambda$, we obtain K_U^2 = 0.22%, and for $H = 0.05\lambda$, K_U^2 = 0.0046%. This means that the efficiency of the excitation of SEAWs drastically decreases as the gap width increases.

It is well known [12, 13] that, in a single thin piezoelectric plate made of lithium niobate (lithium tantalate, etc.) of a given orientation (an *XY*-cut, *YX*-cut, or *ZX*-cut plate), the propagation of a quasi-*SH*-wave is also possible, and this wave has a very high value of K^2 (up to 33%) at a certain plate thickness. For example, for an *XY*-cut $LiNbO_3$ plate with the thickness $H = 0.1\lambda$, the value of K^2 is $K^2 \approx 36\%$ and the phase velocity is V = 4.372 km/s [12, 13]. In fact, this is a fast transverse shear-horizontal wave propagating in the piezoelectric plate and containing almost no mechanical displacement component u_3 normal to the surface. Hence, the *SH* wave can propagate in a plate that is in contact with a liquid without any radiation loss caused by the energy transfer from the wave to the liquid medium.

In a system of two thin piezoelectric plates separated by a gap, the propagation of a fast *SH* mode of the SEAW is possible, and this mode has a high value of K^2 and a velocity V equal to that of the *SH* wave propagating in a single plate. Figure 9 shows the calculated velocities V_0 of the fast *SH* mode of the SEAW (curves *V*(0.1), *V*(0.2), and *V*(0.5)) and the values of K^2 (curves *K*(0.1), *K*(0.2), and *K*(0.5)) for three values of the thickness of both piezoelectric plates made of *XY*-cut $LiNbO_3$ ($H1/\lambda = H2/\lambda$ = 0.1, 0.2, and 0.5) versus the gap width H/λ. The value of K^2 was calculated in this case under the condition that the interdigital transducers are placed on the outer surface of the upper plate (i.e., V_S and V_0 in formula (5) refer to this surface) while other three surfaces are free. From Fig. 9, one can see that, as in the case of a single plate, the maximal value of K^2 calculated from Eq. (5) is obtained for the *SH* mode of the SEAW when the thickness of both plates is $H1/\lambda = H2/\lambda = 0.1$. For example, when the gap width is $H/\lambda = 0.01$, we have $K^2 \approx 9\%$, which is noticeably greater than the value of K^2 for a SAW in lithium niobate ($K_{SAW}^2 \approx 5.5\%$).

In a system of two plates separated by a thin gap, as well as in a single plate, many solutions and many modes are possible. In addition to the solutions shown in Fig. 9, there are modes with lower and higher velocities. For example, for the same conditions as in Fig. 9, for $H1/\lambda = H2/\lambda = 0.1$ (plates) and $H/\lambda = 0.01$ (gap), there is a wave with a lower velocity V_0 = 4.04727 km/s and $K^2 \approx 20.7\%$ and a wave with a higher velocity V_0 = 6.4753 km/s and $K^2 \approx 4.83\%$.

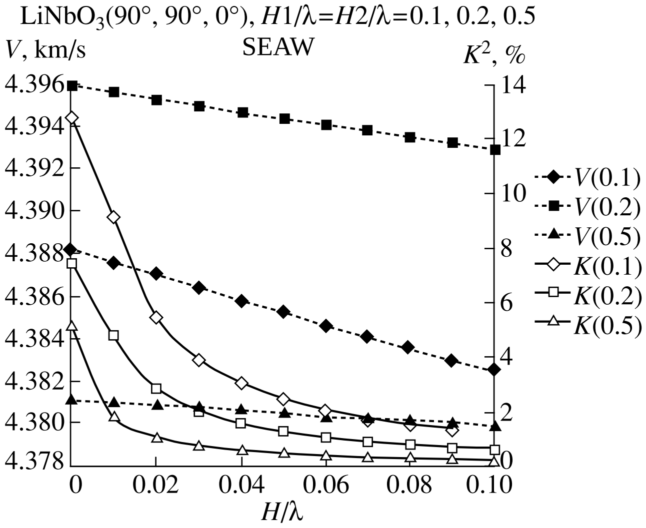

Fig. 9. Velocity *V* of the fast mode of the SEAW (curves *V*(0.1), *V*(0.2), and *V*(0.5)) and the electromechanical coupling coefficient K^2 (curves *K*(0.1), *K*(0.2), and *K*(0.5)) as functions of the gap width H/λ for three values of the piezoelectric plate thickness: $H1/\lambda$ = 0.1, 0.2, and 0.5.

Another important parameter of the wave is the temperature coefficient of delay (TCD). For a SAW in a single medium, TCD = α – TCV = $\alpha - 1/V \times (\partial V/\partial t)$, where α is the coefficient of linear thermal expansion of the medium, TCV is the temperature coefficient of velocity of the SEAW, and t is the temperature. In the case of the SEAW, the value of TCV for the SEAW is uniquely determined. However, since we have a system of two different piezoelectric media, an ambiguity arises in the determination of the TCD for the SEAW, because the value of α may be different in different media. Hence, we can determine two values of the TCD for the SEAW: one for the upper and one for the lower piezoelectric media with respective coefficients of linear expansion. The TCD of a real device will be determined by the coefficient of linear thermal expansion of the medium on which the interdigital transducers are placed, because the thermal expansion of the other medium will have no effect on them in this case.

Our calculations showed that, even in the case of two identical piezoelectric media with the same orientation, the values of TCD for SEAW somewhat differ from the value of TCD calculated for common SAWs. For example, in a system of two piezoelectric media thermally stable for SAWs, namely, LGS(0°, 140°, 25°) ($TCD_{SAW} = -0.09 \times 10^{-6}$/K), with a gap $H = 0.5\lambda$ between them, the value of TCD for the SEAW is equal to -1.5×10^{-6}/K and depends on the width of the gap.

The materials constants for $LiNbO_3$, SiO_2, and LGS were taken from [14–16].

Thus, in this paper we described the method for a numerical calculation of the parameters of various kinds of SEAWs that propagate in piezoelectric media of any crystallographic symmetry class and their configurations. We considered the processes of transformation of SEAWs to SAWs in the case of two half-spaces or to electroacoustic Lamb modes in the case of a system of two thin piezoelectric plates separated by a gap. We showed that the velocity of SEAW modes is determined by the properties of both piezoelectric media and depends on the width of the gap. We proposed a system of two thin piezoelectric plates made of *XY*-cut (or *YX*-cut) lithium niobate with a gap between them, for which the slit electroacoustic wave has a high value of the electromechanical coupling coefficient. This structure can be used in the design of high-efficiency acoustoelectronic pressure sensors and gas and liquid analyzers.

REFERENCES

1. N. V. Gulyaev and V. P. Plesskiĭ, Akust. Zh. **23**, 716 (1977) [Sov. Phys. Acoust. **23**, 410 (1977)].
2. M. K. Balakirev, S. V. Bogdanov, and A. V. Gorchakov, Fiz. Tverd. Tela (Leningrad) **21**, 2508 (1979) [Sov. Phys. Solid State **21**, 1448 (1979)].
3. M. K. Balakirev and I. A. Gilinskiĭ, *Waves in Piezoelectric Crystals* (Nauka, Novosibirsk, 1982), p. 240 [in Russian].
4. P. A. Pyatakov, Akust. Zh. **47**, 836 (2001) [Acoust. Phys. **47**, 739 (2001)].
5. M. Veleekoop, Ultrasonics **36**, 7 (1998).
6. *Surface Wave Filters: Design, Construction, and Use*, Ed. by H. Mathews (Wiley, New York, 1977; Radio i Svyaz', Moscow, 1981).
7. *Acoustic Surface Waves*, Ed. by A. A. Oliner (Springer, New York, 1978; Mir, Moscow, 1981).
8. M. P. Shaskol'skaya, *Acoustic Crystals* (Nauka, Moscow, 1982), p. 632 [in Russian].
9. S. Tonami, A. Nishikata, and Y. Shimizu, Jpn. J. Appl. Phys., Part 1 **35** (5b), 3002 (1996).
10. M. Yu. Dvoesherstov, V. I. Cherednick, and A. P. Chirimanov, in *Proceedings of IV International Conference on Wave Electronics and Its Applications* (St. Petersburg, 2001), ISBN 5-8088-0059-5, p. 32.
11. M. Yu. Dvoesherstov, V. I. Cherednik, and A. P. Chirimanov, Izv. Vyssh. Uchebn. Zaved., Radiofiz. **43**, 801 (2000).
12. B. D. Zaitsev, S. G. Joshi, and I. E. Kuznetsova, in *Proceedings of IEEE Ultrasonics Symposium* (1998), p. 419.
13. S. G. Joshi, B. D. Zaĭtsev, and I. E. Kuznetsova, Akust. Zh. **47**, 336 (2001) [Acoust. Phys. **47**, 282 (2001)].
14. G. Kovacs, M. Anhorn, H. Engan, *et al.*, in *Proceedings of IEEE Ultrasonics Symposium* (1990), p. 435.
15. Y. Shimizu and Y. Yamamoto, in *Proceedings of IEEE Ultrasonics Symposium* (1980), p. 420.
16. A. Bungo, C. Jian, and K. Yamaguchi, in *Proceedings of IEEE Ultrasonics Symposium* (1999), p. 333.

Translated by E. Golyamina

Acoustical Physics, Vol. 50, No. 6, 2004, pp. 677–684. Translated from Akusticheskiĭ Zhurnal, Vol. 50, No. 6, 2004, pp. 783–791.
Original Russian Text Copyright © 2004 by Didenkulov, Zverev, Ivanov, Ivanova.

Measured and Calculated Vertical Structure of a Sound Field in the Ocean

I. N. Didenkulov, V. A. Zverev, V. P. Ivanov, and G. K. Ivanova

Institute of Applied Physics, Russian Academy of Sciences,
ul. Ul'yanova 46, Nizhni Novgorod, 603950 Russia
e-mail: ivg@hydro.appl.sci-nnov.ru

Received February 5, 2003

Abstract—Results of measuring the monochromatic sound field with a dipping probe in the deep ocean are presented. The sound speed profile in the region of measurements had a minimum at a depth of 1600 m. The experiment was carried out in the Atlantic Ocean with the use of two vessels separated by a distance of approximately four ray cycles (~240 km). The experimental data are compared with the calculations based on a new concept of the Brillouin waves for describing the vertical structure of the sound field produced by rays. It is shown that a satisfactory agreement between experiment and calculation can be achieved by fitting the parameters of the experiment. Such a procedure allows one to refine or even to determine the experimental conditions, which not are always known. The proposed method of calculation offers an opportunity for solving inverse problems of ocean acoustics. *© 2004 MAIK "Nauka/Interperiodica".*

INTRODUCTION AND THE STATEMENT OF THE PROBLEM

In view of development of the methods of ocean tomography, measurements of the vertical distribution of the sound field become topical. This distribution is what mainly determines the amplitudes of rays (modes) in oceanic waveguides. The measurements of the vertical structure are usually carried out with the use of vertical arrays [1, 2]. However, they cover a small range of depths, because the development and installation of sufficiently long arrays encounters engineering difficulties. The usual length of vertical arrays is no greater than 100 m [1, 2]. A different method of measuring the vertical structure, which allows one to substantially increase the range of depths, is also known. This method involves using a dipping hydrological-acoustical probe (DHAP), which simultaneously measures the sound pressure and the depth of the receiving device [3]. The use of the DHAP is advantageous in that, first, an equivalent of a continuous array is obtained and, second, this array can be rather long.

Different methods of processing the vertical profiles of the sound field are known. In [4], a special method of averaging was proposed to eliminate fine fluctuation maxima and minima from the sound field amplitude. By applying this method, the conclusion was drawn that the positions of zones with a relatively high concentration of sound energy can be adequately predicted by computations based on the ray theory. Another method of averaging the fluctuations of the sound field amplitude is also possible, namely, the spectral analysis of experimental data. With this method, one changes from the amplitude description of the sound field to the spectral one, and the fluctuations are flattened out in the calculated spectra.

To explain the results of the processing of experimental records, a comparison with some theoretical model is required. Nowadays, studies are in progress to refine the methods of calculating the sound field in oceanic waveguides with an underwater sound channel (USC) [3, 5–7].

The objectives of this work are to measure the vertical structure of the sound field in the ocean by using a uniformly deployed DHAP, to perform a spectral processing of the measured structure, to calculate the vertical sound field profile for the experimental conditions with the use of the method described in [3, 6], and to compare the experimental data with the calculations.

EXPERIMENTAL PROCEDURE AND RESULTS

The experimental measurements of the vertical sound field structure were performed in November 1989, in the deep-water part of the Atlantic Ocean. The USC axis was at a depth of 1600 m. A near-surface maximum in the sound speed occurred at a depth of 60 m. The sound speed near the bottom was higher than in the near-surface maximum. The acoustic pressure and the immersion depth were measured by the DHAP, which was uniformly lowered. The signal from the DHAP was recorded on magnetic tape. The length of the vertical survey with the DHAP was about 100–150 m at depths of 360–520 m. A monochromatic sound source that operated at a frequency of 233.3 Hz was at the depth of the near-surface maximum of the sound speed.

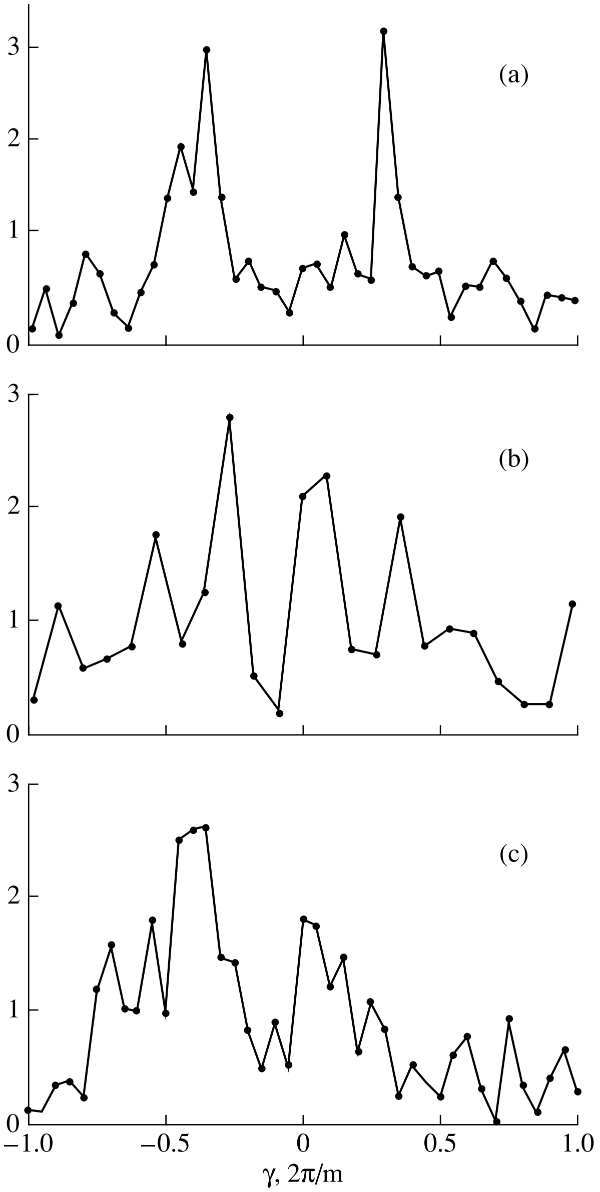

Fig. 1. Spatial spectra obtained from the records of the vertical profile of the sound field: DHAP survey nos. (a) 11, (b) 6, and (c) 12.

The ocean depth remained constant (5 km) on the main part of the path between the sound source and the receiving system. However, the experimental site was above the flank of an underwater mount that was located behind the propagation path. Therefore, the ocean depth in the region of measurements was substantially smaller than the depth on the entire path, namely, about 2.6 km. According to the bottom profiles available, the angle α between the mount flank and the horizontal was about ~8°. With these values of the depth and bottom slope, the length of the flank towards the transmitting vessel was 17 km in the horizontal.

During the experiment, both vessels, one with the sound source and the other with the receiving DHAP system, drifted at a distance of less than 230–240 km from each other; this distance could vary only due to the drift. Approximately an hour before the experiment, the ocean depth in the region of the DHAP immersion and the coordinates of both vessels were measured. The depth was 2.6 km, and the calculated distance was x = 233 km. This distance corresponds to the end of the fourth cycle of the ray trajectories, between the turning point near the bottom and the point of reflection from the surface. The relief and the exact value of the bottom slope remained unknown. The rate of deployment of the DHAP was constant. The duration of the recording of the sound field varied from 100 to 150 s, depending on the depth range surveyed. The time interval between successive surveys, including the probing duration itself, was 4 to 5 min. Twelve surveys were performed in the experiment.

The processing of the records consisted in obtaining the spatial spectrum for the vertical distribution of the sound field. The specificity of processing of the DHAP data consisted in that the signal was recorded in successive instants of time as the probe was lowered rather than over the entire depth simultaneously, as in the case of an ordinary vertical array. Therefore, the signal was represented as a time sequence by taking into account the dependences of the signal phase and the probe depth on time.

Because the signal recorded during the DHAP immersion was actually a time signal, its coherence was verified. To do so, the record of an individual survey was broken up into two or three parts. The spectral analysis was performed for both the entire survey and its parts. The result is that the main maxima in the spectra of the entire record and the parts coincide. Therefore, one can treat the recorded sound field as a coherent one for the whole interval of depths surveyed.

Let us consider the results of the spectral processing of the vertical sound field profiles obtained. Figures 1a–1c show the spatial spectra for profile nos. 11, 6, and 12. The depth intervals were 127, 70.5, and 129 m, respectively. The horizontal axis represents the spatial frequency γ (in units of 2π/m) for the vertical profile of the sound field. The vertical coordinate is the absolute value of the spectral amplitude. The resolution of the spectral analysis is individual to each plot and equals the separation of the adjacent dots in the spectrum.

The spatial spectra noticeably differ from each other. This feature indicates the changes in the bathymetric parameters for different profiles. The spectra shown exhibit several maxima at both positive and negative spatial frequencies (the same is true for other spectra). For instance, negative frequencies predominate in the spectrum of profile no. 12. A sort of symmetry can be seen in Figs. 1a and 1b. At the same time, the absolute values of the frequencies in the maxima are different on either side of the point $\gamma = 0$. Thus, they are equal to –0.34 and +0.3 2π/m in Fig. 1b. Apart from a slight difference in these values, the spectrum can be treated as that of a single mode excited in the waveguide.

The values of the spatial frequencies ($\gamma \sim 0.3$–0.4 2π/m) are characteristic of rays propagating at high grazing angles. Actually, the greatest value of γ corresponds to the USC axis for the purely water-propagating rays. For the conditions at hand, it does not exceed 0.25 2π/m. Higher spatial frequencies correspond to rays propagating at higher grazing angles. However, such rays undergo multiple reflections from the bottom and surface along the entire path, and their contribution to the received signal is insignificant. Therefore, the most probable explanation for the values of $\gamma > 0.25$ 2π/m is the assumption that the signal arrives at the DHAP after a single reflection from the inclined bottom area in the vicinity of the reception point. Actually, at the reflection from the inclined surface, the propagation angle of the ray changes by a doubled value of the surface slope α relative to the horizontal. The addition of $2\alpha = 16°$ to the propagation angle of the water rays leads to an increase in the spatial frequency in the vertical spectrum to the values of 0.3–0.4 2π/m. Let us confirm the experimental results and their explanation by calculations.

CALCULATIONS AND COMPARISON WITH EXPERIMENT

In addition to the sound speed, the main quantities that govern the vertical structure of the sound field are the distance to the source, the depth, and, in our case, the slope of the bottom. We did not aim to achieve an exact coincidence between the experimental data and the calculations. Our task was, first, to obtain a qualitative (and quantitative, as far as possible) agreement between calculations and experiment and, second, to determine the intervals of parameter variations that lead to noticeable changes in the calculated spectra of the sound field.

The calculations were performed using the method described in [3, 6]. The vertical coordinates were calculated for the rays that intersect the plane x = const as a function of the launch angle at the source. These coordinates are denoted as $z(\theta)$, where θ is the launch angle (relative to the vertical). The projections $\gamma(z)$ of the wave vector on the vertical axis z were also computed. From the values of the function $\gamma(z)$, the vertical sound field profile produced by all rays was calculated. The spectrum of the calculated sound field was compared with the spectrum of the experimental profile for the depth interval surveyed by the DHAP. Note that the function $z(\theta)$ indicates the vertical coordinates (at the end points of the trajectories) for all rays in the vertical plane x = const, and the function $\gamma(z)$ gives a general idea of the spectrum of the vertical structure of the sound field.

To clarify the influence of the sloping bottom on the formation of the vertical profile of the sound field along the path, let us consider the sound propagation in a waveguide with a flat bottom at a depth of 5 km, $\alpha = 0$. Because of the source position at the horizon of the near-surface maximum of the sound speed, all water rays touch the surface.

Figures 2a and 2b show the vertical coordinates $z(\theta)$ for the rays leaving the source at the angle θ and crossing the plane $x = 231$ km. The projections $\gamma(z)$ of the wave vectors on the z axis are also shown for these rays. The horizontal axis in Fig. 2a represents the absolute value of the launch angle θ (relative to the z axis). The vertical coordinate is the waveguide depth measured from the surface. The solid and dashed curves correspond to the rays that leave the source towards the surface ($\theta < 0$) and towards the bottom ($\theta > 0$), respectively. Figures 2a and 2b show how many rays arrive at each point z. The water rays do not reach the depth $z <$ 2 km or, hence, the DHAP. Here, we do not present the calculated sound field and its spectrum for two reasons. First, as was mentioned above, the rays do not produce vertical structures with frequencies $\gamma > 0.25$ 2π/m in the waveguide of the type at hand. Second, in our case, the water rays do not reach the DHAP at all. Such a calculation is described in [3] for $\alpha = 0$ and $x =$ 240 km (a part of the rays that arrived at the DHAP in this experiment). Let us consider the features of the curves $z(\theta)$ and $\gamma(z)$ (Figs. 2a and 2b) in more detail, because these features are also characteristic of rays reflected from the inclined bottom.

The specificity of the function $z(\theta)$ is the presence of extrema. The vertical coordinates of the rays, $z(\theta)$, first decrease with a varying angle θ and, then, upon reaching the minimal value, increase as θ monotonically varies. As in an ideal waveguide, the rays produce two branches of vertical coordinates, in which z changes in opposite directions. These two branches of the function $z(\theta)$ can be treated as an analog of counter-propagating waves (the Brillouin waves) in an ideal waveguide, where they exist because of the opposite-signed (but equal-valued) projections of the wave vector on the z axis. According to Fig. 2b, the projections of the wave vector are different in value and equal in sign for the rays corresponding to different branches of $z(\theta)$. Thus, the vertical structure of the sound field in the USC is close to that produced by the Brillouin waves in an ideal waveguide but differs from it in both sign and value of the wave-vector projection on the z axis. This situation is considered in more detail in [6], where a generalized concept of the Brillouin waves is introduced, as applied to the USC. The fact that a sound field structure similar to that produced by the Brillouin waves exists in the USC allows one to assume that an analog of modes is present in the spectrum of the sound field.

Let us consider a probable explanation for the extrema of the function $z(\theta)$. In considering the horizontal structure of ray trajectories, it is common to use

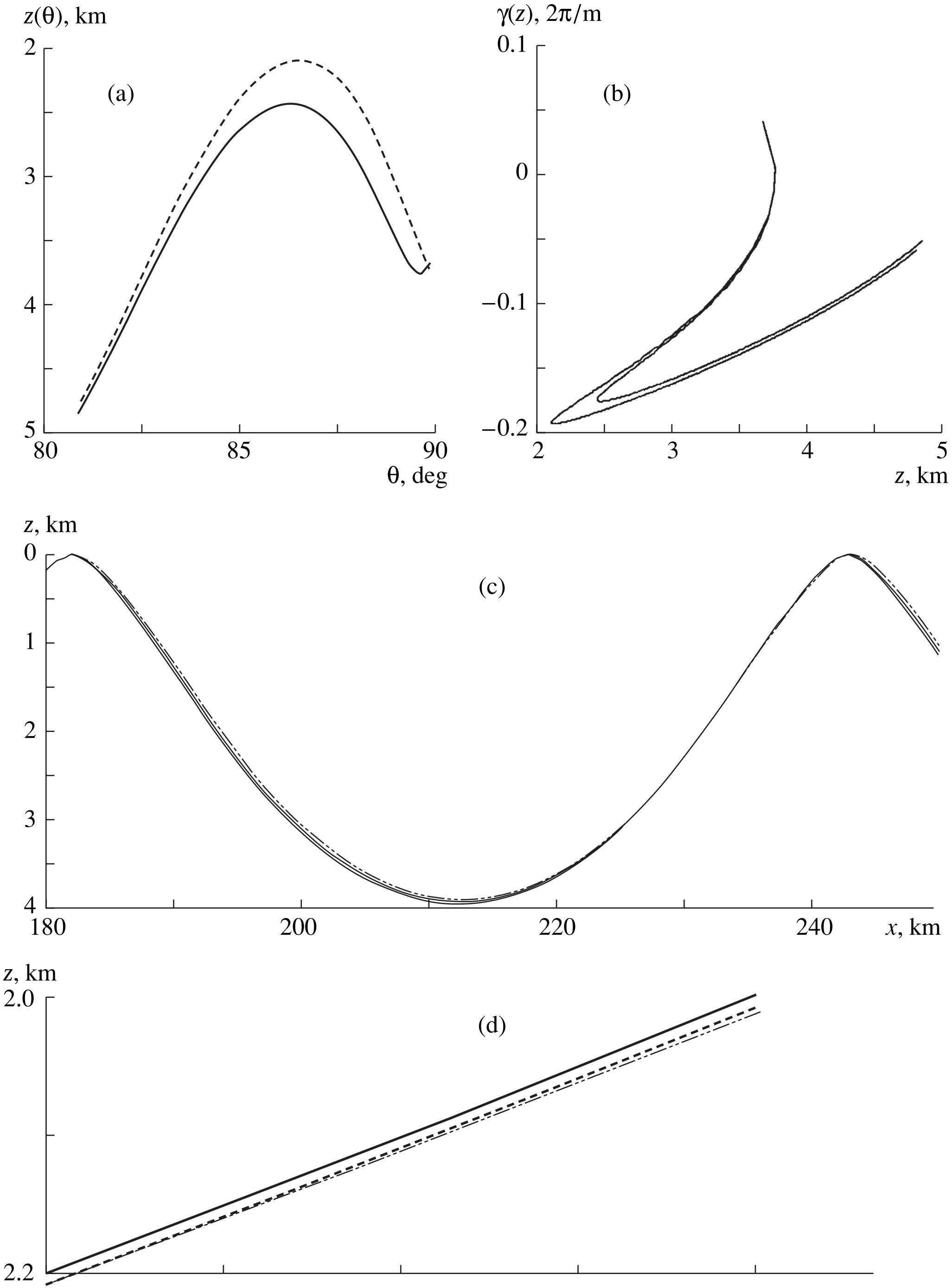

Fig. 2. Calculated characteristics of the vertical profiles of the sound field for $x = 231$ km, $H = 5$ km, and $\alpha = 0°$. The solid and dashed curves correspond to the rays leaving the source towards the surface and bottom, respectively: (a) depth $z(\theta)$ of ray arrivals at the z axis versus the launch angle, (b) projections $\gamma(z)$ of the wave vector of the rays on the z axis, (c) trajectories of adjacent rays producing the caustic, and (d) caustic on an enlarged scale.

the concept of the envelope of the ray family (the caustics) at which the focusing factor tends to infinity, because the derivative of the horizontal coordinate with respect to the launch angle tends to zero: $dx/d\theta = 0$ [8]. When the vertical structure of the sound field is considered, the derivative of the z coordinate will appear in the focusing factor. Let us show that the point with the coordinates $x = 231$ km and $z = z_{\min}$, where $dz/d\theta = 0$, belongs to a caustic. Figure 2c shows a group of ray trajectories. The central trajectory in the group is one that passes through the minimum of the function $z(\theta)$ of Fig. 2a for the rays that leave the source towards the bottom. Two other curves are chosen so that their near-bottom turning points are 25 m shallower or deeper, respectively, than the turning point of the central curve. A caustic domain can be clearly seen where the three trajectories nearly coincide. This domain is shown in Fig. 2d on a larger scale. The two trajectories adjacent to the central one lie on the same side of the central one. More information on caustics can be found in [8] (page 48). Returning to Fig. 2a, note that the maximum of the function $z(\theta)$ on the solid curve near $\theta \sim 90°$ is not the caustic: it is produced by the rays in the vicinity of the near-bottom turning point. This conclusion will be confirmed below.

Let us consider the functions $\gamma(z)$, the projections of the ray wave vector on the z axis at $x = 231$ km, from Fig. 2b. As usual, the positive direction of $\gamma(z)$ coincides with the direction of the z axis. The notations of the curves are the same as in Fig. 2a. The curves with different signs of the launch angles are close to each other, except for the domains of the caustics. In our case, $\gamma(z) < 0$ for most of the rays. An exception is a small group of rays leaving the source towards the surface at angles close to 90°. For these rays, the turning point lies near the bottom, where $\gamma(z) = 0$. After turning, the function $\gamma(z)$ changes its sign, as seen from Fig. 2b. Note that the absolute values of $\gamma(z)$ are much lower than the experimental values of the spectral components of the sound field (Figs. 1a–1c). The functions $\gamma(z)$ and $z(\theta)$ are both double-valued. The rays arriving at the same point have different values of $\gamma(z)$. This difference leads to beatings in the sound field along the z axis, and two close frequencies can be observed in the spatial spectrum if the resolution is sufficient [3].

Let us now consider the waveguide with an inclined bottom. By fitting the distance, depth, and bottom slope in computations, we tried to obtain a spectrum that is close to that shown in Fig. 1a. This spectrum has the simplest shape, with two main maxima. It is evident that such a shape may correspond to a signal reflected by a smooth area of the inclined bottom. The information on the sea depth can be treated as reliable. In fitting the parameters of the calculation, we specified the following values: the distance 231 km between the source and the DHAP, the depth 2.6 km, and the bottom slope $\alpha = 7°$. The bottom surface is assumed to be smooth in the computations.

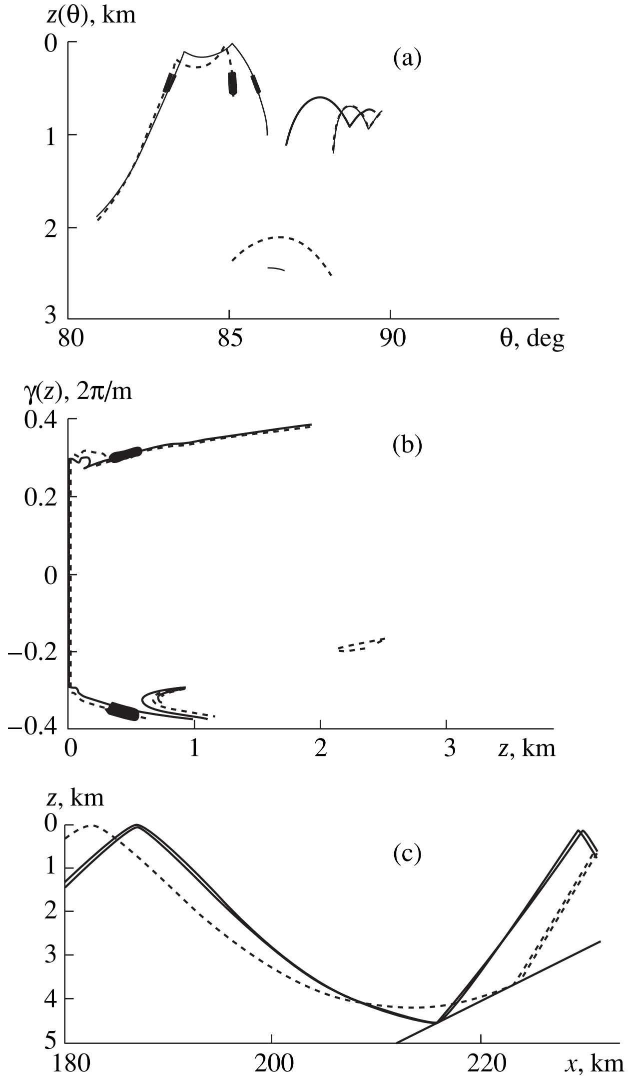

Fig. 3. Calculated characteristics of the vertical profiles of the sound field for $x = 231$ km, $H = 5$ km, and $\alpha = 7°$. The solid and dashed curves correspond to the rays leaving the source towards the surface and bottom, respectively: (a) depth $z(\theta)$ of ray arrivals at the z axis versus the launch angle, (b) projections $\gamma(z)$ of the wave vector of the rays on the z axis, and (c) trajectories of the boundary rays leaving the source towards the bottom and arriving at the DHAP.

Figures 3a and 3b show the curves $z(\theta)$ and $\gamma(z)$ calculated with the inclined bottom. The curves are much more complicated than those in Figs. 2a and 2b. The water rays remain only in the domain $z > 2$ km with $\theta \sim 85°–87.2°$ and do not arrive at the DHAP. All rays, except for the water ones, undergo a single reflection from the flank. Thus, all rays arriving at the DHAP are singly bottom-reflected rays. Their coordinates are accentuated by solid curves. The trajectories of the rays leaving the source towards the bottom and arriving at the DHAP at $z = 0.36–0.52$ km are shown in Fig. 3c. As in the case of $\alpha = 0$, two opposite branches of the function $z(\theta)$ exist. The rays that have positive projections of the wave vector on the z axis appear: $\gamma(z) < 0$ at $\theta > \theta_{\text{ref}}$ and $\gamma(z) > 0$ at $\theta < \theta_{\text{ref}}$, where θ_{ref} is the launch angle of the ray reflected from the surface at $x = 231$ km. Thus, in contrast to Fig. 2b, $\gamma(z) > 0$ for a large number of rays at this distance, the absolute value of the vertical spatial frequencies increased up to 0.4 2π/m, and many rays have become closer to the surface. In addition, the structure of the vertical distribution has become more complicated, and new caustics have appeared. The functions $z(\theta)$ and $\gamma(z)$ are now multivalued rather than

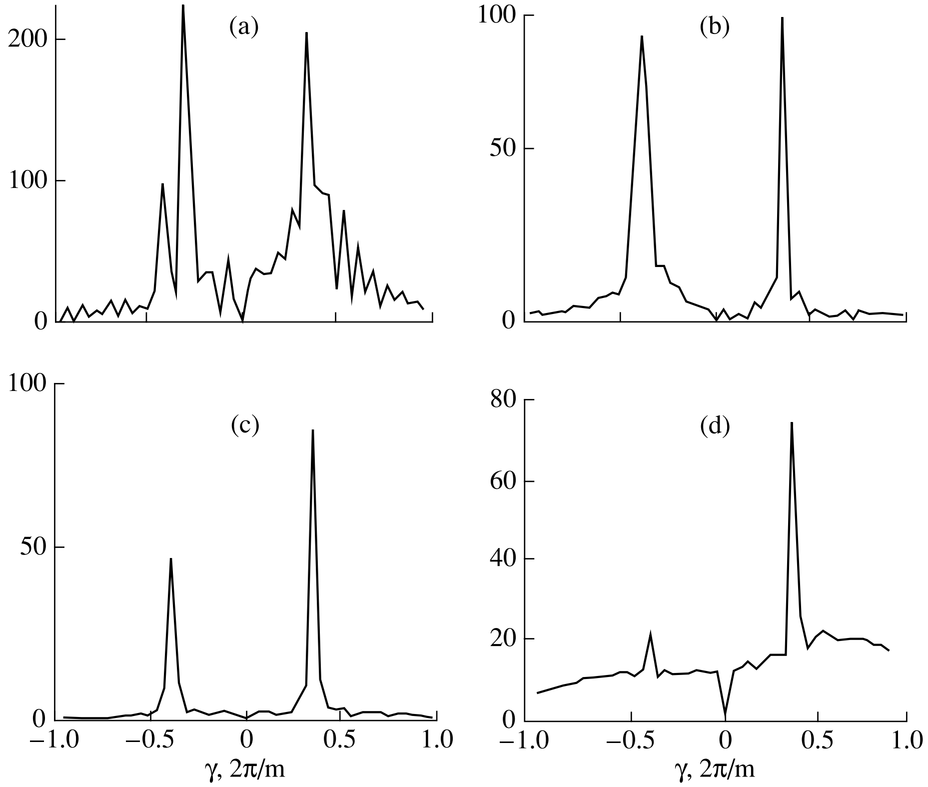

Fig. 4. Spatial spectra of the vertical structure of the calculated sound field for $H = 2.6$ km and $\alpha = 7°$ at different distances from the source: x = (a) 230, (b) 230.5, (c) 231, and (d) 232 km.

two-valued (as in Figs. 2a and 2b). Therefore, a greater number of rays arrive at one point. For instance, nine rays arrive at $z = 0.8$ km.

To estimate the effect of small changes in distance from the source, the sound field and its spectrum were calculated at four distances, 230, 230.5, 231, and 232 km, for the rays that arrived at the DHAP. The functions $z(\theta)$ and $\gamma(z)$ for these distances are similar to those presented in Figs. 3a and 3b for $x = 231$ km. The difference is in the number of caustics, in their positions on the θ, z plane, and in the value of θ_{ref}. The calculated spatial spectra are shown in Figs. 4a–4d. The spatial frequency is expressed in units of 2π/m. At all four distances, the spectrum consists of two maxima at positive and negative frequencies. The shape and amplitude of the maxima vary as the distance x changes. When x increases, the amplitude of the negative-frequency maximum decreases. At positive frequencies, the amplitude first increases, then decreases. The difference in the shapes of the maxima is caused by caustics occurring in the depth interval surveyed by the DHAP. These caustics lead to either broadening of the maximum, as in Fig. 4a, or to an increase in the spectrum basement, as in Fig. 4d.

The absolute values of the frequencies corresponding to two maxima are slightly different: –0.39 and +0.35. Their values do not vary as the distance from the source changes, except for in Fig. 1a, where the caustic exists. The calculated spectrum shown in Fig. 4b, x = 230.5 km, is the one closest to the experimental spectrum shown in Fig. 1b. The frequencies of the maxima in Fig. 1b are –0.34 and +0.3 2π/m. The calculated and measured values of the spatial frequencies coincide to an accuracy of a single interval of resolution. Thus, by fitting a number of parameters, the calculated vertical spectrum of the sound field is found to be rather close to the experimental spectrum, both in its shape and in the values of the spatial frequencies. In our case, small variations of the distance lead to noticeable changes in the amplitudes of the spectral maxima. The frequencies of the main maxima do not change as the distance from the source varies. Only their shape and amplitude exhibit variations. Note that, apart from a small difference in the frequencies of the maxima, both the calculated and experimental (Fig. 1a) spectra are similar to the spectrum of a single mode. This closeness confirms the validity of the generalized concept of Brillouin waves for the USC.

Let us consider how the change in the bottom slope influences the spectrum of the sound field. Figures 5a–5d show the spectra for different bottom slopes: α = 6.2°, 6.5°, 6.7°, and 8°, respectively. The spectra of Figs. 5a and 5b are calculated for $x = 230$ km: those of Figs. 5c and 5d correspond to $x = 231$ km. Generally, an increase in the slope from 6.2° to 8° leads to an increase in the absolute values of the frequencies corresponding to the maxima. The similarity of the negative maxima

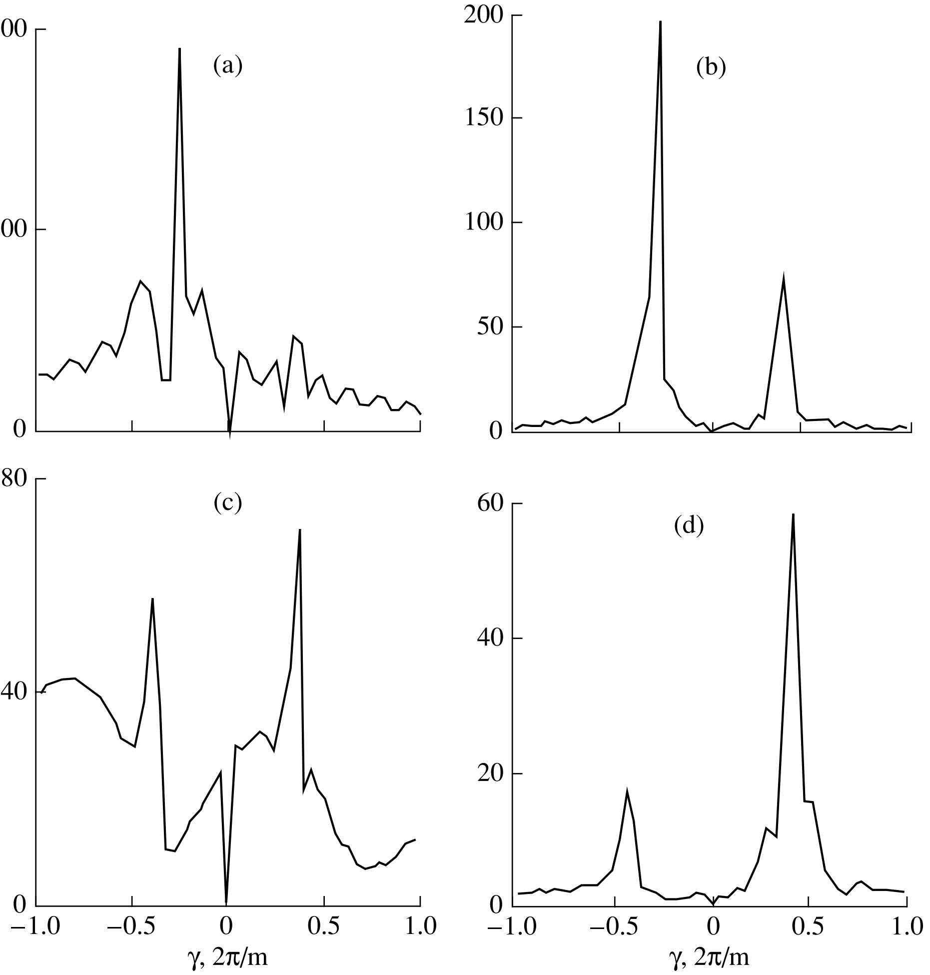

Fig. 5. Spatial spectra of the vertical structure of the calculated sound field at $H = 2.6$ km and $x = 230$ km for different bottom slopes: α = (a) 6.2° and (b) 6.5°. Same at $x = 231$ km: α = (c) 6.7° and (d) 8°.

in Figs. 5a and 5b and the positive maxima in Figs. 5b and 5c can be caused by the presence of caustics of the function $z(\theta)$ in the DHAP depth interval. The absolute values of the frequencies corresponding to the maxima slightly increase as the bottom slope increases: from –0.28 to –0.43 2π/m for $\gamma < 0$ and from +0.31 to +0.39 2π/m for $\gamma > 0$.

Figures 6a and 6b illustrate the effect of depth variations in the region of the DHAP immersion. Figure 6a shows the calculated spectrum of the vertical structure of the sound field for an ocean depth of 2.4 km, with a distance of 230 km from the source and a bottom slope of $\alpha = 7°$. With these values of the parameters, no negative frequencies occur in the spectrum, and the positive frequency of the maximum is lower than in Fig. 4a, where the ocean depth is 2.6 km. Such a behavior occurs despite the fact that the bottom slope did not change. The decrease in the frequency of the maximum can be explained by assuming that, prior to reflections from the flank, the bottom-reflected rays had smaller grazing angles than in Fig. 4a. In Fig. 6b, the bottom slope is also changed: $\alpha = 8°$. As a result, a maximum appeared at the negative frequency, and the positive frequency of the maximum became higher that in Fig. 6a.

The calculations performed above lead to the conclusion that changes in each of the three parameters cause a change in the rays that constitute the sound field. This phenomenon cannot be avoided, and, hence, one cannot exactly predict how the spectrum will change when a parameter changes.

Let us compare the experimental and calculated characteristics of the sound field in more detail. First of all, note that the fitted distance and bottom slope lead to a good agreement between the calculated spectrum and one of the spectra obtained from the experimental data. This agreement confirms the correctness of the fitted parameters and proves the validity of the proposed mechanism governing the formation of the vertical profile of the sound field by the rays reflected from the inclined bottom. As for other experimental spectra, their complicated structure can be caused by the roughness of the flank surface, that is, by differently inclined

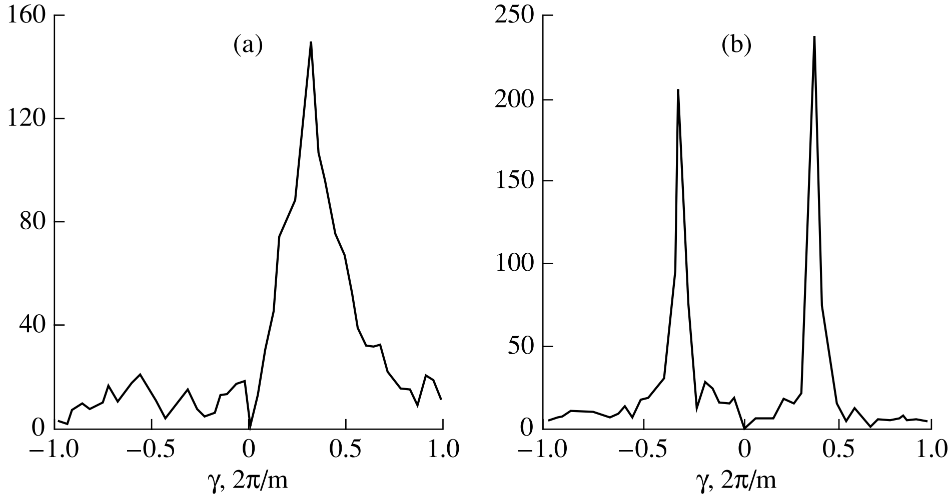

Fig. 6. Spatial spectra of the vertical structure of the calculated sound field at the depth H = 2.4 km for x = (a) 230 and (b) 231 km and α = (a) 7° and (b) 8°.

areas of the flank. Because of a slow drift of the vessels, a change in the reflecting surfaces occurred, along with a change in the ray trajectory segments that touch the bottom. All of these factors determined the complicated structure of the spectra and caused their variation from one survey to another.

We did not consider the effect of variations in the sound speed profile, $c(z)$, along the path on the vertical structure of the sound field. As it was mentioned above, the maximal value of $\gamma(z)$ is determined by the value of $c(z)$ at the channel axis and by the maximal sound speed at one of the waveguide boundaries. The variations of these values will lead to a change in the maximal value of $\gamma(z)$. In the experiment at hand, variations of $c(z)$ along the path were not measured. Evidently, such variations of $c(z)$ will influence the depth of rays arriving at a given distance. Therefore, the result of fitting all the parameters that characterize the experiment will also depend on the variations of $c(z)$ along the path. The effect of the variations can be taken into account in the framework of the ray theory.

The study described in this paper led to the following conclusions. The use of the DHAP for measuring the vertical structure of the sound field proved to be quite advantageous. This conclusion can be confirmed by the good agreement of the calculated spectrum with that obtained in one of the measurements. Such an agreement offers an opportunity for solving some inverse problems of ocean acoustics. By appropriate calculations, one can determine unknown experimental parameters or refine their values. From the sound field profile measured in one region of the ocean, the sound field in another region can be determined.

REFERENCES

1. Ya. S. Karlik, B. V. Kerzhakov, A. P. Kovalev, *et al.*, Preprint No. 542, IPF RAN (Nizhni Novgorod Inst. of Applied Physics, Russian Academy of Sciences, 2000).
2. Ya. S. Karlik, B. V. Kerzhakov, A. P. Kovalev, *et al.*, in *Proceedings of Nizhni Novgorod Acoustic Session* (TALAM, Nizhni Novgorod, 2002), p. 39.
3. V. A. Zverev, V. P. Ivanov, and G. K. Ivanova, in *Proceedings of the 9th School–Seminar of Academician L. M. Brekhovskikh* (GEOS, Moscow, 2002), p. 128.
4. L. M. Brekhovskikh, V. V. Goncharov, S. A. Dremuchev, *et al.*, Akust. Zh. **36**, 824 (1990) [Sov. Phys. Acoust. **36**, 461 (1990)].
5. M. A. Wolfson and S. Tomsovic, J. Acoust. Soc. Am. **109**, 2693 (2001).
6. V. A. Zverev and G. K. Ivanova, Akust. Zh. **49**, 632 (2003) [Acoust. Phys. **49**, 535 (2003)].
7. C. T. Tindle, J. Acoust. Soc. Am. **112**, 464 (2002).
8. L. M. Brekhovskikh and Yu. P. Lysanov, *Fundamentals of Ocean Acoustics* (Gidrometeoizdat, Leningrad, 1982; Springer, New York, 1991).

Translated by E. Kopyl

Acoustical Physics, Vol. 50, No. 6, 2004, pp. 685–693. Translated from Akusticheskiĭ Zhurnal, Vol. 50, No. 6, 2004, pp. 792–801.
Original Russian Text Copyright © 2004 by Zverev.

The Principle of Acoustic Time Reversal and Holography

V. A. Zverev

Institute of Applied Physics, Russian Academy of Sciences,
ul. Ul'yanova 46, Nizhni Novgorod, 603600 Russia
e-mail: zverev@hydro.appl.sci-nnov.ru

Received February 5, 2003

Abstract—On the basis of earlier results (V. A. Zverev, *Radiooptics* (1975)), the principle of the time reversal of waves (TRW) with the use of a time-reversed signal is considered (M. Fink *et al., Time-Reversed Acoustics,* Rep. Prog. Phys. **63** (2000)). Both the common mathematical basis and the difference between the TRW and holography are revealed. The following conclusions are drawn: (i) to implement the TRW, it is necessary that the spatial and time coordinates be separated in the initial signal; (ii) two methods of implementing the TRW are possible, namely, the time reversal and the use of an inverse filter; (iii) certain differences exist in the spatial focusing by the TRW and holography; and (iv) on the basis of the theory developed, a numerical modeling of the TRW becomes possible. *© 2004 MAIK “Nauka/Interperiodica”.*

Earlier [1–5], an original concept of the time reversal of waves was considered. Until now, this concept has only found application in acoustics. To implement the time reversal of waves (TRW) in propagation through a complex (scattering and dispersion) medium, one should store the received signal, reverse the direction of time in it, and send the time-reversed signal into the same medium. In [1–5], such a technique is called “time-reversed acoustics.” To clarify the essence of the proposed technique and to prove its feasibility, the authors of [1–5] refer to the general theoretical considerations, although they rely on brilliantly performed experiments as well. Based on the general theoretical considerations of [1–5], one cannot perform any quantitative estimations. These considerations also do not provide the validity conditions of the TRW. The comparison [1–3] with the wave-front inversion (WFI), which is carried out in a monochromatic wave field, does not fully reveal the essence of the problem stated. On the one hand, it is argued [1–3] that the procedure of TRW is mathematically equivalent to that of WFI for a monochromatic wave, because the time Fourier transform of $p(r, -t)$ is the complex conjugate Fourier transform of $p(r, t)$. On the other hand, it was shown experimentally [2] that there is no full analogy between the TRW and WFI procedures. Actually, both statements are true. There is a common mathematical basis for the TRW and WFI, which should be considered so as to demonstrate both the similarity and the difference between the two methods along with their applicability. This is the main problem to be solved here. The solution of this problem is substantially simplified by the fact that, as early as 1975 [6], a unified mathematical approach was used to develop two descriptions of wave fields, namely, the spatial and time descriptions. The spatial description of a monochromatic wave field was related to WFI, while the time description, to the TRW.

According to [6], let us transform the mathematical descriptions of WFI and TRW to a common form. Let us begin with WFI. To describe the propagation of monochromatic wave fields, the concept of a complex amplitude $p(x, y, z)$ is usually applied. Such an amplitude is a complex function whose modulus is the wave amplitude and whose argument is the wave phase. Here, x, y, and z are the coordinates in the Cartesian coordinate system, with the z axis directed along the direction of wave propagation. The propagation of a monochromatic wave from the plane $z = 0$, at which the initial distribution of the complex amplitudes is specified, to the plane $z = z$ is described by the formula [6]

$$p(x, y, z) = \frac{1}{4\pi^2}\iint g(u_1, u_2)\zeta(z, u_1, u_2) \times \exp(iu_1x + iu_2y)du_1du_2. \tag{1}$$

Here, $u_{1,2}$ are the spatial frequencies corresponding to the transverse coordinates x and y, $g(u_1, u_2)$ is the Fourier spectrum of the complex amplitude $p(x, y, 0)$ in the plane $z = 0$, and $\zeta(z, u_1, u_2)$ is the spatial frequency response of the propagation channel between the planes $z = 0$ and $z = z$. For a free space, this response is

$$\zeta(z, u_1, u_2) = \exp(iz\sqrt{k^2 - u_1^2 - u_2^2}), \tag{2}$$

where z is the distance passed by the wave in free space, $k = 2\pi/\lambda$, and λ is the wavelength.

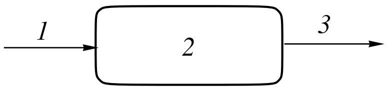

Fig. 1. Functional diagram of the linear system: (*1*) the input signal, (*2*) the filter, and (*3*) the output signal.

In the spectral representation, Eq. (1) takes the form [6]

$$g_z(u_1, u_2) = \zeta(z, u_1, u_2) g_0(u_1, u_2), \tag{3}$$

where g_z is the spatial spectrum of the field in transverse coordinates in the plane $z = z$ and g_0 is the same spectrum in the plane $z = 0$.

Equations like (1) and (3) can be interpreted, with the use of the functional diagram of Fig. 1, as a signal $p(x, y, 0)$ passing through a filter with the frequency response $\zeta(z, u_1, u_2)$. Below, the WFI procedure for a monochromatic wave is considered on the basis of Eq. (3). Such a form corresponds to wave propagation in free space. If the space involves inhomogeneities, such as lenses or other volume scatterers, the wave propagation in such complex media cannot be described by a single formula of form (3). Therefore, let us restrict our consideration to the WFI procedure in free space, which is quite sufficient for the problem at hand.

To implement the WFI, one should take the complex conjugate of function (1) obtained at the filter output and use it as the initial wave field. Methods of obtaining the complex conjugate distributions of complex amplitudes by analog methods exist in both optics and acoustics. We do not consider these methods here. Let the wave fields at hand be such that they can be stored and then reproduced by introducing the required corrections into them. The complex conjugate field $p^*(x, y, z)$ should be passed through the same filter (a fraction of the free space with the same length). As a result, substituting the complex conjugate field $p^*(x, y, z)$ into Eq. (3), we obtain the relation

$$g_{2z}(u_1, u_2) = \zeta(z, u_1, u_2) g_z^*(u_1, u_2). \tag{4}$$

By substituting the expression for g_z^* of Eq. (3) into Eq. (4), we derive

$$g_{2z}(u_1, u_2) = \zeta(z, u_1, u_2)\zeta^*(z, u_1, u_2) g_0^*(u_1, u_2). \tag{5}$$

The latter equation is just the desired form of the mathematical representation of the WFI. The complex amplitude of the signal obtained in the WFI procedure will be found as the inverse Fourier transform of Eq. (5). Such a transformation of the wave field is performed in holography. Therefore, for the WFI in a monochromatic field in free space, one can use the term "holography."

Let us consider the problem of representing the output TRW signal in a form analogous to Eq. (5). To begin with, let us generalize Eq. (1) to the case of polychromatic wave fields. In doing so, we use the method given in [6]. Now, the polychromatic wave field $A(x, y, 0, t)$ is specified in the plane $z = 0$. Let us find the Fourier spectrum of this field as a function of a single argument, namely, time t. We denote this spectrum as $C_A(x, y, 0, \omega)$. Then, the process of wave propagation can be again represented in form (1), if the initial complex amplitude $C_A(x, y, 0, \omega)$ is specified as

$$\begin{aligned} P(x, y, z, t) = {} & \frac{1}{8\pi^3}\iiint_{\infty\infty\infty} g_C(u_1, u_2, \omega)\zeta(\omega, u_1, u_2) \\ & \times \exp(iu_1x + iu_2y - i\omega t)\,du_1du_2d\omega. \end{aligned} \tag{6}$$

Here, $g_C(u_1, u_2, \omega)$ is the spatial Fourier spectrum of the function $C_A(x, y, 0, \omega)$.

To proceed to the TRW, it is necessary that the initial function $A(x, y, 0, t)$ be a function with independent variables of the type [6]

$$A(x, y, z, t) = \sum_n A_n(x, y, z) F_n(t). \tag{7}$$

A point wave source of the following form is an example of such a function:

$$A(x, y, 0, t) = \delta(x - x_0)\delta(y - y_0) F(t). \tag{8}$$

Substituting Eq. (8) into Eq. (6), we obtain

$$\begin{aligned} & P(x, y, z, t) \\ & = \frac{1}{2\pi}\int C_F(\omega) p(x, y, z, \omega) \exp(-i\omega t)\,d\omega, \end{aligned} \tag{9}$$

where $C_F(\omega)$ is the Fourier spectrum of the function $F(t)$ and $p(x, y, z, \omega)$ is the complex amplitude given by Eq. (1); $p(x, y, z, \omega)$ is a function of ω, because $k = \omega/c$, where c is the velocity of wave propagation. The dependence obtained can be interpreted by the diagram of Fig. 1, in analogy with Eq. (1). Thus, a time description of wave propagation has been obtained that can be applied to the case of Eq. (8). The complex amplitude $p(x, y, z, \omega)$ as a function of frequency can serve as the frequency response of the time filter obtained.

The resulting time-domain description of wave propagation is the theoretical basis for the TRW procedure. This process consists of two steps [1]. At the first step, a short pulse is produced by a point source. The transmitted signal propagates as a spherical wave, which is scattered by the inhomogeneities of the medium. As a result of scattering, a train of partially overlapping pulses arrives at the reception point:

$$y(t) = \sum_j R_j F(t - t_j). \qquad (10)$$

Here, $F(t)$ is the form of the initially transmitted pulse, t_j is the time of signal propagation from the transmission to reception point with scattering by the jth scatterer, and R_j is the scattering coefficient for this scatterer.

In the spectral representation, Eq. (10) has the form

$$C_y(\omega) = C_F(\omega) z(\omega), \qquad (11)$$

where $z(\omega)$ is the temporal frequency response of the propagation channel: $z(\omega) = \sum_j R_j \exp(i\omega t_j)$.

The received signal given by Eq. (10) is stored. This procedure is obligatory for proceeding to the second step. At the second step, the stored signal is time reversed and again transmitted from the same reception point into the same medium, which is supposed to be frozen for the time of the first and second steps of the procedure. Thus, we have a time-reversed signal $y(-t)$ at the second step. Its spectrum is the complex conjugate of the spectrum of the initial signal. The spectrum of the signal transmitted at the second step is the complex conjugate of spectrum (11): $C_y^*(\omega)$. The spectrum of the signal received at the transmission point can be found from a formula of the form of Eq. (11) under the assumption that the form and the spectrum of the frequency response of the propagation channel remain unchanged during the signal propagation in both directions, because the distribution of the delays is independent of the propagation direction. Thus, as a result of the first and second steps, the spectrum of the signal received at the transmission point takes the form

$$C_r(\omega) = z(\omega) z^*(\omega) C_F^*(\omega). \qquad (12)$$

At the second step, the form of the signal at the transmission point is given by the inverse Fourier transform of Eq. (12).

Thus, we have obtained the result of the TRW in a form analogous to that of holography (i.e., to the result of the WFI in a monochromatic wave field in free space), that result being expressed by Eq. (5).

Relations (5) and (12) can be interpreted in a common way with the use of the functional diagram of Fig. 1. The two former factors, appearing in Eqs. (5) and (12), play the role of the frequency response of the wave-reversing filter (WRF), and the third factor is the spectrum of the signal at the WRF input. The frequency responses of both WRFs are the squared absolute values of the functions and contain a constant component that does not depend on frequency. Therefore, in both cases the input signal is produced at the WRF output. In the case of the TRW, this signal is $F(t)$, i.e., the initial pulse as a function of time. In the case of WFI, it is the input image. Because of the interference phenomena in the medium, the WRF frequency response of the TRW procedure is entirely nonuniform, which results in the correlation noise [7]. In the transparency band, the WRF frequency response of the WFI procedure is uniform and, hence, free from the correlation noise.

The impulse responses (spectra of the frequency responses) of both WRFs are the autocorrelation functions of the free-space impulse responses in the case of holography or those of the time-domain wave system in the case of the TRW [6]. The properties of these frequency responses differ entirely from each other, and, respectively, the WFI and TRW procedures are different in spite of the similar forms of Eqs. (5) and (12) that describe the procedures. Thus, the autocorrelation function of the free-space impulse response, which is the Fourier transform of the modulus of Eq. (2), has the following form [6] at $z \gg \lambda$:

$$\Phi(x, y) = \frac{k}{2\pi\sqrt{x^2 + y^2}} J_1(k\sqrt{x^2 + y^2}), \qquad (13)$$

where $J_1(r)$ is the first-order Bessel function of r. At $z \gg \lambda$, such a frequency response transmits all spatial frequencies without distortions in the frequency band satisfying the condition [6]

$$u_1^2 + u_2^2 \le k^2. \qquad (14)$$

This condition determines the maximum spatial width of the spectrum of the signal with a complex amplitude for the WFI procedure. According to Eq. (5), the shape of the signal at the WFI output is governed by the shape of the complex conjugate input signal $p^*(x, y, 0)$ in the spatial frequency band given by Eq. (14). In this case, if the initial signals have a finite spatial spectrum limited by Eq. (14) (the situation that is characteristic of holography), the WFI procedure produces the output wave field that is identical to the input one.

Let us consider the TRW transformation from the same point of view. The WRF frequency response of the TRW procedure does not imply limitations like Eq. (14). In the TRW, the time-domain spectrum of the signal is limited by nothing but the passband of the medium.

In contrast to the WFI, which is considered in the spatial domain, the TRW transformation produces a result that depends on both time and space. The time dependence is directly governed by Eq. (12), but the dependence on the spatial coordinates is not determined by this equation: it is rather described by a similar relation through the spatial dependence of the correlation function of the time-domain impulse responses. To obtain the spatial dependence of the

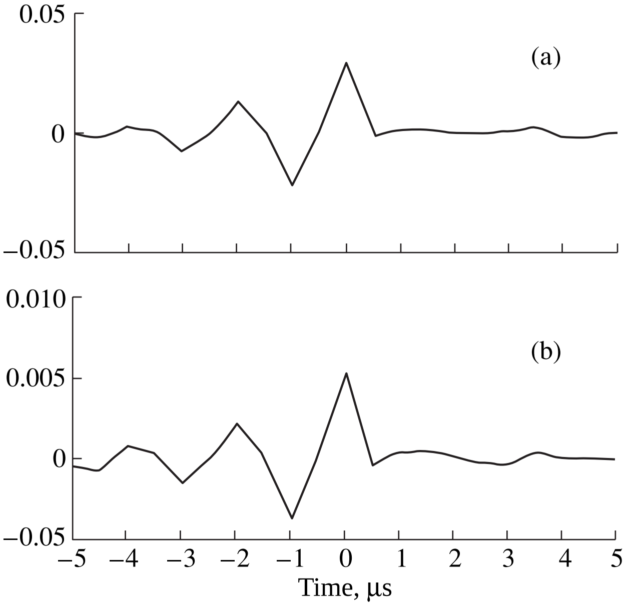

Fig. 2. Shape of the pulses received at the second step. The data are taken from [8] and transformed according Eq. (12) with (a) full and (b) truncated realizations.

TRW, one must change the second step of the procedure. If, at the second step, the signal is received at some point differing from that of transmission, Eq. (12) should be written as follows:

$$C_{ra}(\omega) = z_a(\omega)z^*(\omega)C_F^*(\omega). \qquad (15)$$

Here, as in Eq. (12), $z^*(\omega)$ is the transfer function from the transmission point to the reception point at the first step of the procedure. A new function $z_a(\omega)$ appeared, which is the transfer characteristic from the transmission point at the first step to the reception point at the second step. The function

$$Z(a, \omega) = z_a(\omega)z^*(\omega), \qquad (16)$$

which is the spectrum of the cross-correlation function of the corresponding filter responses, determines the spatial dependence of the TRW result or the focusing of the TRW-produced signal. This feature makes the spatial transformation produced by the TRW considerably different from holography. As was mentioned above, the WFI spatial transformation corresponds to the input signal (see Eq. (14)). In the TRW, the spatial transformation (focusing) does not depend on the signal form and is fully determined by Eq. (16) or by the cross-correlation of the filter responses. Thus, one cannot accept the statement of [2] that the TRW procedure is nothing but a broadband WRI and the WFI procedure is just a narrowband TRW.

For focusing of waves in the TRW, the same restrictions are imposed on the spectrum of spatial frequencies as in the WFI. The point is that the signals in the TRW also propagate in the form of waves, and waves of an arbitrary nature are limited by a condition similar to Eq. (14). Actually, waves with spatial frequencies that do not satisfy inequality (14) are inhomogeneous ones, and their amplitudes exponentially decrease with distance.

This fact is clearly illustrated by the brilliant experiment described in [8]. The two measurements of [8], which differed from each other in time windows at the second step of the procedure, led to entirely different sizes of the focal areas. With the shortened signal (measurement (a)), the size of the focal spot was λ/2, while the time window of the full length signal (measurement (b)) led to a focal spot with a size of λ/14, equal to the size of the signal transmitter. If condition (14) could be ignored, the results of measurements (a) and (b) should coincide. A full-scale experiment does not allow one to ignore inequality (14), but a numerical experiment does. Figure 2 illustrates the numerical experiment based on Eq. (12) with the same parameters as in [8]. The signals are shown in the form of the second-step time dependences at the reception point. The numerically obtained time dependences corresponding to measurements (a) and (b) are rather similar to each other: they both follow the shape of the initial pulse (with the reversed time). Relation (15), which governs the spatial focusing, has the same mathematical structure as Eq. (12). Therefore, according to the numerical simulation, the results of the spatial focusing in measurements (a) and (b) are also identical if one ignores inequality (14).

The difference in the data of measurements (a) and (b), which was clearly demonstrated by the experiment, is the consequence of the fact that, in measurement (b), the signal traveled no distance in the medium, and, hence, condition (14) had no influence on the experimental results. Measurement (a) is quite different in this sense. In this measurement, because of the shorter transmitted pulse, the signal passed through some distance in the medium and underwent a spatial filtration according to Eq. (14). Therefore, the size of the focal spot increased to λ/2. The difference in the distances traveled by the signal in the medium in measurements (a) and (b) is caused by the fact that the points of transmission and reception coincided in this experiment. In this case, with the full-length window (measurement (b)) at the first stage, the initial signal travels no path in the medium and immediately arrives at the receiver where it is stored. At the second step, the time-reversed signal is transmitted. In this case, the initial part of the signal changes to the last one, which also travels no distance in the medium. The situation changes if the initial part of the signal is eliminated. At both the first and the second step, the signal passes through some distance in the medium. Therefore, the result of the experiment is strongly influenced by the failure to satisfy condition (14). This is the fact that was clearly confirmed by the experiment described in [8], and that is why the data of the experiment are far from confirming the effect of overcoming the diffraction limit (as the authors of [8] mistakenly argue). On the contrary, the experiment clearly shows the existence of the diffraction limit. It should be noted that the term "diffraction limit" is usually attributed to focusing systems, but no such systems were present in the experiment of [8].

There is one more substantial difference between the WFI and the TRW. While the WFI procedure can be performed in a unique way, two methods can be used to implement the TRW [7]. With the second method, the signal processing at the second step changes. Namely, instead of the time-reversed signal at the second step, a signal is formed whose form is determined by the Fourier spectrum of the inverse frequency spectrum and then sent to the transmission point. The spectrum of such a signal received at the transmission point is as follows:

$$C_Y(\omega) = \frac{1}{z(\omega)C_F(\omega)}z(\omega). \qquad (17)$$

As a result, one obtains unity divided by the spectrum of the transmitted signal at the transmission point. To find the form of the transmitted signal, the received signal should be additionally processed. Namely, one must divide unity by the spectrum of the received signal and then take the Fourier transform of this fraction. No additional processing is needed if the function $F(t)$ has a uniform spectrum ($F(t) = \delta(t)$) in the entire frequency band used. Let us denote this processing method as inverse filtration. The inverse-filtration method has an advantage in that it leads to no noise in the TRW time realization. The inverse filtration can be applied only to those parts of the signal spectrum at which the modulus of the function $z(\omega)$ differs from zero. The parts at which this modulus is equal to zero should be excluded. With the inverse filtering procedure, the TRW spatial focusing is governed by the ratio of the frequency responses: $z_a(\omega)/z(\omega)$. This ratio is influenced by the correlation noise.

The aforementioned considerations are sufficient to numerically demonstrate a number of important TRW features mentioned in [1–5]. Let us consider the experiment reported in [1, 2], in which focusing was studied in the course of wave propagation through a layer of volume inhomogeneities. Figure 3 shows the layout of the numerical implementation for the experiment similar to that described in [1, 2]. This layout corresponds to that of the experiment discussed in [1] and shown in Fig. 1 of this paper. A point source A of a short pulsed signal is shown at the left (Fig. 3). The pulse is specified so that the spectrum of function $F(t)$ is equal to unity in the frequency band at hand. In this case, the function $F(t)$ can be treated as a delta function. In Fig. 1 of [1], a reflector of the signal is shown as the source. Note that the result of the experiment will agree with that reported in [1] if the signal scattered by the reflector is very short. Evidently, it is not always possible to excite such a pulse by manipulating, from the transmission point, the view of the propagation through an arbitrary scattering layer.

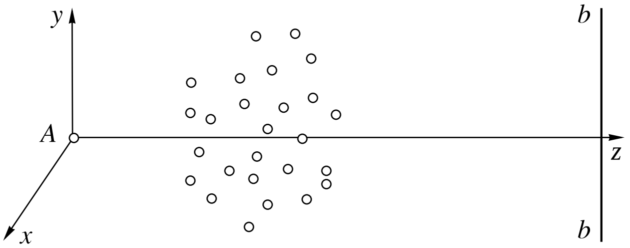

Fig. 3. Layout of the numerical experiment. The z axis of the Cartesian coordinate system is directed from the source of the pulsed signal (point A) to the center of the b–b line, along which the elements of the transmitting–receiving array are positioned.

At the right of Fig. 3, the receiving antenna array consisting of 64 elements is shown. As will be demonstrated below, the number of antenna elements is of no fundamental importance. To obtain the effect of spatial focusing shown [1], it is sufficient to use a receiving array that consists of a single element. Between the source A located at the origin of coordinates and the receiving array, 32 point scatterers are placed to form the scattering volume. It is supposed that each scatterer scatters the incident radiation in all directions. In [1, 2], a volume scatterer is used that consists of a number of wires, just as in our layout.

Note that the numerical experiment implies a single scattering, while the experiment of [1, 2], as the authors of these works argue, was accompanied by multiple scattering. Multiple scattering is difficult to numerically model, and one should be sure that it is really needed before making an attempt to do so. However, the multiplicity of scattering is not proven in [1, 2], and one may suppose that there was actually a single scattering. For the TRW procedure, the problem of the scattering order is of no importance. Therefore, the experimental results give no information on that subject, but the experimental layout of illuminating the scatter does give the necessary information. The illumination was performed by the central element of the transmitting–receiving antenna array positioned behind the scatterer. The specificity of such a layout is that the signal emitted by the only central element and then scattered by the scatterer is not composed of a single short pulse. It rather takes the form shown in Fig. 4. With such a pulse, the experiment cannot yield the result obtained in [1, 2].

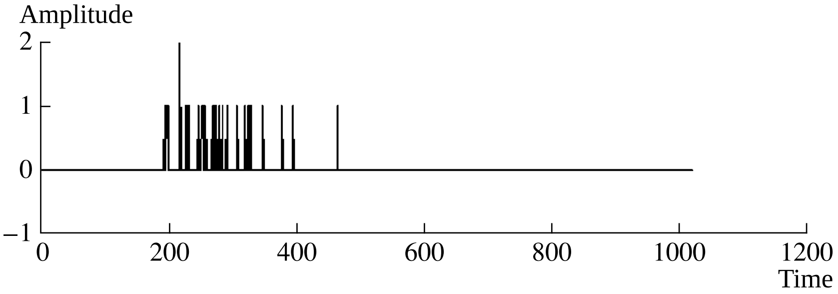

Fig. 4. Signals at the receiving element positioned at the center of the transmitting–receiving array.

Why, then, was this result nevertheless obtained in [1, 2]? The reason is that the scatterers used (wires) had a small target strength. Therefore, the scattered signal was observed on the background of a much more intense signal transmitted through the medium surrounding the wires. The shortness of this signal allowed the experimenters to use the method of illuminating the scatterer that was reported in [1, 2]. Because the scattering is weak in comparison with the direct signal, one can neglect the effects of multiple scattering by the wires and mathematically model the experiment [1, 2] in the way used here.

The modeling was performed in the following way. From the geometrical considerations (Fig. 3), the distance from the transmission point to each scatterer was determined to be

$$R_m = \sqrt{x_m^2 + y_m^2 + z_m^2}. \qquad (18)$$

Here, m is the ordinal number of the scatterer, and x_m, y_m, and z_m are the coordinates of this scatterer. Then, the distance between the transmission point and each element of the receiving array was found to be

$$Ra_{m,n} = \sqrt{x_m^2 + (y_m - a_n)^2 + (r - z_m)^2}. \qquad (19)$$

Here, a_n is the coordinate of the nth array element and r is the distance to the transmitting–receiving array. The distance between the transmission point and each array element through each of the m scatterers is given by the sum of Eqs. (18) and (19):

$$D_{m,n} = R_m + Ra_{m,n}. \qquad (20)$$

In view of Eqs. (18)–(20), Eq. (10) was used to find the response of each element of the receiving array to the pulse sent by the transmitter. Figure 4 shows an example of such a response.

Then, the TRW procedure was modeled. Both the aforementioned methods of implementing the TRW were used in the modeling. Let us begin with the correlation procedure (Eq. (15)) proposed in [1–5].

Let us find the transfer characteristics of the channels (filters) from the transmission point A to each element of the receiving array. Such frequency characteristics are fully determined by the delays given by Eq. (20):

$$z_{k,n} = \sum_m \exp\left(i\frac{2\pi}{L}kD_{m,n}\right). \qquad (21)$$

Neither the distribution nor the values of the delays depend on the direction of wave propagation. Hence, Eq. (21) equally describes the channel of signal propagation in the reverse direction, from the output of the filter to its input. Let us transform the signals received by n elements of the array in a way implied by the TRW procedure. One should change the sign of the time in each received signal and then send it back to the transmitter. The spectrum of the signal with the reversed time is the complex conjugate (Eq. (21)). To find the signal at the filter output as a function of time, let us use Eq. (12) with a subsequent Fourier transformation of the result. We obtain

$$y_n(t) = \frac{1}{2\pi}\sum_k z_{k,n}^* z_{k,n} \exp\left(i\frac{2\pi}{L}kt\right). \qquad (22)$$

This relation determines the response of the matched filter to the function with which it is matched, or the correlation function of the response of the device at hand to the short pulse sent from point A (Fig. 3). Thus, the result of the TRW procedure is obtained as a function of time at point A. This result can be found in [1, 2].

It is advantageous to obtain the result of the TRW procedure not only at point A but also at neighboring points along the y axis (Fig. 3) in order to estimate the effect of the focusing of the reversed wave. To do so, according to Eq. (15) one should change the shape of the frequency response of the filter through which the time-reversed signal passes. To the frequency response, it is necessary to add the differences in the path lengths from each mth scatterer to each point q of the y axis. (Let us suppose that there are 64 such points with spacings equal to unity.) The desired distance can be found to be

$$R_{m,q} = \sqrt{x_m^2 + (y_m - q)^2 + z_m^2}. \qquad (23)$$

This relation should replace the quantity R_m in Eq. (20) to specify the set of delays for the signal propagating in the backward direction. The resulting formula takes the form

$$y_{n,q}(t) = \frac{1}{2\pi}\sum_k zo^*_{k,n,q} z_{k,n} \exp\left(i\frac{2\pi}{L}kt\right). \qquad (24)$$

Here, $zo_{k,n,q}$ is the frequency response of the filter for backward propagation. This response is obtained from Eq. (21) in view of Eq. (23).

To make use of the entire array aperture, one should sum Eq. (24) over all n transmitting–receiving elements:

$$Y_q(t) = \sum_n y_{n,q}(t). \qquad (25)$$

The second method of implementing the TRW, which is based on the use of the inverse filter (Eq. (17)), is built from the same bricks as the first method, though they put together in a different order. These bricks are the filter frequency responses (Eq. (21)) and the quantities $zo_{k,n,q}$ appearing in Eq. (24). In the second TRW method, the same frequency responses are used in a different combination. The final formula has the following form:

$$Y2_q(t) = \frac{1}{2\pi}\sum_n\sum_k \frac{zo_{k,n,q}}{z_{k,n}} \exp\left(i\frac{2\pi}{L}kt\right). \qquad (26)$$

There is a caveat in using Eq. (26): the quantity $z_{k,n}$ appearing in the denominator of Eq. (24) can become zero at certain points. To avoid errors caused by these zeros, it is sufficient to set Eq. (26) to be equal to zero if the modulus of $z_{k,n}$ takes a value below some threshold level.

Figures 5–7 illustrate the calculations performed with Eqs. (24)–(26). In Fig. 5, the responses of the time-reversed signals are shown as functions of time. These responses were obtained with the value of q that corresponds to point A, i.e., to the point of transmission. This figure illustrates both methods of implementation of the TRW. Note that the entire receiving array is not used. The plots show the TRW results obtained in transmitting the time-reversed signal from a single point. According to Fig. 5, a short pulse is observed, which is similar to the signal obtained in the experiment described in [1, 2]. Figure 6 illustrates the focusing of the signal in space and time. This focusing is numerically obtained without using the entire transmitting–receiving array: only individual (arbitrary) array elements are used. What, then, is the role of the array, and is it necessary at all?

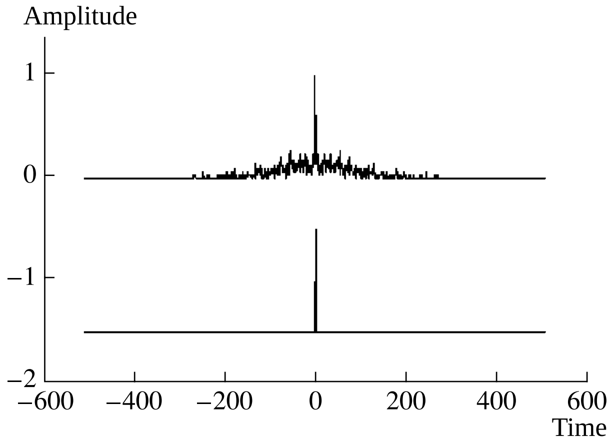

Fig. 5. The TRW result observed at point A (Fig. 2) as a function of time. Only one element of the b–b array is used. The upper and lower plots correspond to the correlation transformation [1] and the inverse filtration, respectively.

The experiments described in [1, 2] show that the signal is focused more sharply in the TRW procedure than in using the array in free space. In [2], experimental data are presented for various numbers of elements in the receiving array: from 1 to 128. In all cases, the focusing effect was observed independently of the number of array elements. The calculations lead to the same conclusion. To implement the focusing observed, there is no need for a receiving array: a single point receiver is quite sufficient. The focusing obtained in the experiments is a direct consequence of Eqs. (25)–(27). The point is that the filter through which the secondary signal passes is the matched one only in the case in which the points of transmission and reception coincide. Otherwise, Eqs. (25) and (27) differ from each other, and the filter proves to be partially matched or completely unmatched. A similar result will be obtained if the signal formed by the TRW procedure is considered for a different direction from point A. Near point A, the response is close to the signal at point A in its amplitude. But if one moves away in an arbitrary direction to a considerable distance, the filter will become unmatched and the response will decrease.

One could possibly draw the following conclusion: that in the experiment, one can restrict the array to a single element instead of the antenna consisting of 128 or more receiving elements, and the result should be the same. However, the situation is somewhat more complex. The experiment with a single receiver instead of the array may fail. Here, the key factor is not in the

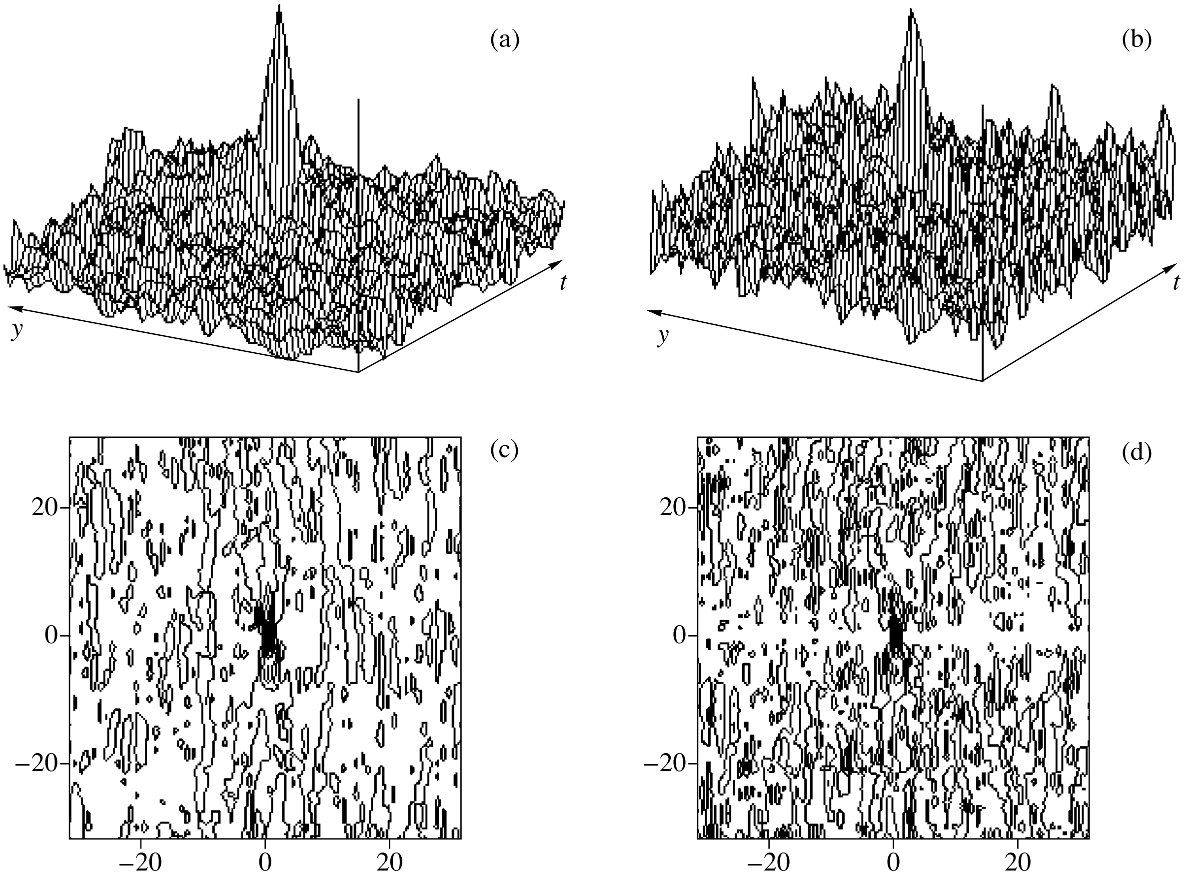

Fig. 6. TRW result as a function of time and *y* coordinate. Only one element of the transmitting–receiving array is used. The plots (a, c) on the left and (b, d) on the right correspond to the correlation transformation [1] and the inverse filtration, respectively. In the plots (c, d) with isocurves, the time and the *y* coordinate are represented by the vertical and horizontal axes, respectively.

directivity of the array but rather the noise immunity of the 128 independent receiving channels in comparison with a single one. This statement is confirmed by the experiment described in [2], as well as by calculations. The TRW effect with a single receiver will exist, but it will be weak. Instead, if the effects of 128 receivers are summed, the TRW gain will significantly increase and become quite noticeable. Figure 7 illustrates this statement: here, the output of the entire array is shown according to Eqs. (25) and (26). The signal is substantially stronger and less polluted than in Fig. 6 corresponding to a single array element.

Figures 6 and 7 show the data obtained both at the second step of the TRW procedure and with the method of inverse filtration. Both methods provide spatial focusing. The inverse-filtering method offers more noise immunity only in finding the time-domain response. In other situations, this method leads to a lower noise immunity. Figures 6 and 7 confirm the latter statement. It is especially noticeable in the isocurves of Figs. 6d and 7d, which illustrate the space–time focusing: there is a white strip across the plots. This strip is free of the correlation noise. With the inverse filtration, the noise is higher in other points of the time–coordinate plane. The origin of such a lower noise immunity is clear: small values of $z(\omega)$ increase the noise. Nevertheless, the inverse-filtration method is of fundamental importance in spite of its evidently low noise immunity. The existence of this method prevents efforts to fully reduce the TRW procedure “to the time reversal of the signal,” as in [1–5].

To conclude, let us emphasize the common features of the TRW and WFI. Both the TRW and WFI procedures realize wave inversion with focusing in space. Both methods allow one to obtain the inverse field free of the influence of the medium in which the waves propagate. It is especially important that both the TRW and WFI, when repeatedly applied, offer the opportunity to separate the received signals in their intensities, as in [1, 9, 10].

Because of its similarity to holography and the simplicity of its implementation, the TRW method is a great advantage for acoustics. The TRW method has

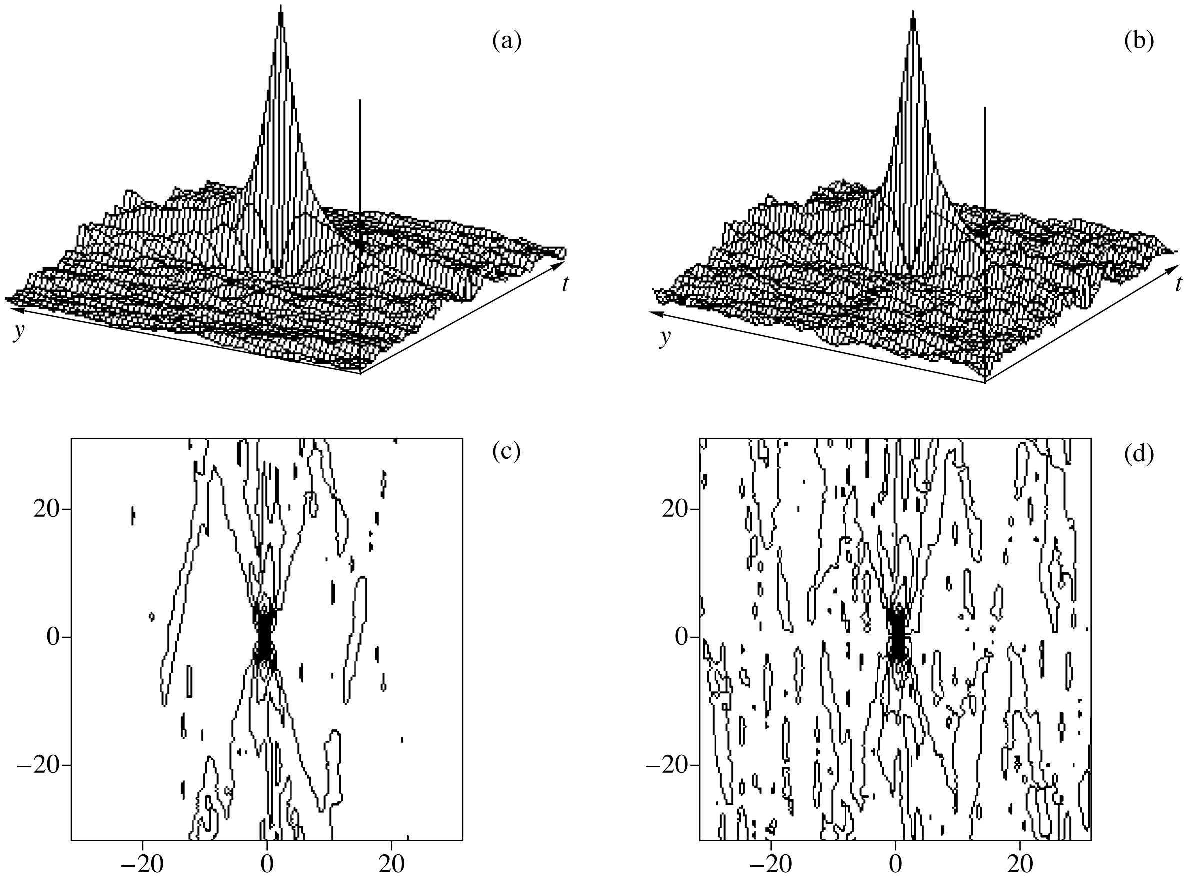

Fig. 7. The TRW result as a function of time and *y* coordinate. The entire transmitting–receiving array, consisting of 64 elements, is used. Plots (a, c) on the left and (b, d) on the right correspond to the correlation transformation [1] and the inverse filtration, respectively. In the plots (c, d) with isocurves, the time and the *y* coordinate are represented by the vertical and horizontal axes, respectively.

already given rise to a number of new ideas [7–13]. Undoubtedly, this method will also yield new interesting results in future.

ACKNOWLEDGMENTS

I am grateful to V.I. Talanov for interest in this paper and for useful discussions that contributed to its improvement. I am also grateful to the reviewer of the journal for valuable advice and assistance in improving the manuscript. This work was supported by the Russian Foundation for Basic Research, project nos. 00-15-96741 and 02-02-17056.

REFERENCES

1. M. Fink, D. Cassereau, A. Derode, *et al.*, Rep. Prog. Phys. **63**, 1933 (2000).
2. A. Derode, A. Tourin, and M. Fink, Ultrasonics **40**, 275 (2002).
3. M. Fink, IEEE Trans. Ultrason. Ferroelectr. Freq. Control **39** (5), 555 (1992).
4. F. Wu, J.-L. Thomas, and M. Fink, IEEE Trans. Ultrason. Ferroelectr. Freq. Control **39** (5), 567 (1992).
5. D. Cassereau and M. Fink, IEEE Trans. Ultrason. Ferroelectr. Freq. Control **39** (5), 579 (1992).
6. V. A. Zverev, *Radiooptics* (Sovetskoe Radio, Moscow, 1975) [in Russian].
7. V. A. Zverev, Akust. Zh. **50**, 614 (2004) [Acoust. Phys. **50**, 523 (2004)].
8. J. de Rosny and M. Fink, Phys. Rev. Lett. **89**, 124301 (2002).
9. V. A. Zverev, Akust. Zh. **50**, 198 (2004) [Acoust. Phys. **50**, 158 (2004)].
10. V. A. Zverev, Akust. Zh. **50**, 469 (2004) [Acoust. Phys. **50**, 394 (2004)].
11. V. A. Zverev, Akust. Zh. **50**, 62 (2004) [Acoust. Phys. **50**, 52 (2004)].
12. V. A. Zverev, Akust. Zh. **49**, 814 (2003) [Acoust. Phys. **49**, 695 (2003)].
13. E. Kerbat, C. Prada, D. Casserean, and M. Fink, IEEE Trans. Ultrason. Ferroelectr. Freq. Control **49** (8), 1103 (2002).

Translated by E. Kopyl

Acoustical Physics, Vol. 50, No. 6, 2004, pp. 694–698. Translated from Akusticheskiĭ Zhurnal, Vol. 50, No. 6, 2004, pp. 802–807.
Original Russian Text Copyright © 2004 by Kaplunov, Kirillova, Postnova.

Dispersion of Waves in a Plane Acoustic Layer with Flexible Elastic Walls

Yu. D. Kaplunov*, I. V. Kirillova, and Yu. A. Postnova****
** Institute for Problems of Mechanics, Russian Academy of Sciences,*
pr. Vernadskogo 101-1b, Moscow, 117526 Russia
e-mail: golden@ipmnet.ru
*** Chernyshevski State University, ul. Astrakhanskaya 83, Saratov, 410026 Russia*
e-mail: postnova_ja@mail.ru

Received February 18, 2004

Abstract—A plane acoustic layer bounded by elastic membranes is considered. Dispersion relations for symmetric and antisymmetric waves are derived. The limit behavior of dispersion curves is investigated for wave numbers tending to zero and to infinity. With the use of the resulting asymptotic expansions, the two-point Pade approximations are constructed. The orthogonality relations for eigenmodes are presented. © *2004 MAIK "Nauka/Interperiodica".*

Multiple papers dealing with the Rayleigh–Lamb transcendental equations for a plane elastic layer (see, e.g., [1, 2]) form the current methodology of linear waveguide dispersion analysis. This methodology includes, in particular, the consideration of the limit behavior of dispersion curves for different relationships between the wave number and the angular frequency. The corresponding asymptotic dependences offer important initial information for constructing universal models describing the dynamics of plates and shells [3].

This paper extends the qualitative approach developed for the Rayleigh–Lamb equation to the case of wave dispersion in a plane acoustic layer bounded by elastic membranes. Such a waveguide is of interest for modeling a number of man-made and biological hydroelastic systems with flexible walls. In this context, we note that motions of the membranes are described by the equations of the theory of elasticity for a prestressed body in the low-frequency asymptotic approximation [4].

In what follows, we derive asymptotic formulas for the roots of the derived dispersion equation near the zero and cutoff frequencies and for the wave number tending to infinity. With these formulas, we determine the asymptotic laws of acoustic pressure distribution throughout the layer thickness. We suggest (possibly for the first time) describing the dispersion curves in terms of the two-point Pade approximations, which, in the limiting cases, turn into the conventional long- and short-wave approximations. The efficiency of the approximate formulas is demonstrated by correlating the approximate results with those obtained numerically from the initial dispersion equation. The dispersion analysis is concluded with a derivation of the orthogonality conditions for oscillation modes, which are, in a certain sense, similar to the orthogonality conditions for the Lamb waves in a plane elastic layer (see, e.g., [5]).

1. DISPERSION RELATIONS

Consider a plane acoustic layer with flexible walls in the form of membranes spaced by a distance $2H$ (Fig. 1). The equations of motion for the membranes and the acoustic medium can be written in the form

$$\frac{\partial^2 w}{\partial x^2} - \frac{1}{c^2}\frac{\partial^2 w}{\partial t^2} \pm \frac{p}{c^2 \rho h} = 0,$$

$$\frac{\partial^2 p}{\partial x^2} + \frac{\partial^2 p}{\partial y^2} - \frac{1}{c_0^2}\frac{\partial^2 p}{\partial t^2} = 0, \qquad (1.1)$$

$$\frac{\partial^2 v}{\partial t^2} = -\frac{1}{\rho_0}\frac{\partial p}{\partial y},$$

where x and y are the longitudinal and transverse coordinates, t is time, c is the velocity of an elastic wave in a membrane, c_0 is the velocity of sound in the acoustic medium, h is the membrane thickness, ρ is the density of the membrane material, ρ_0 is the density of the medium, w and v are the displacements of the membranes and the medium, p is the acoustic pressure, and the plus (minus) sign in the first equation corresponds to the upper (lower) membrane (see Fig. 1). The condition of no leakage through the membranes is as follows:

$$v|_{y = \pm H} = w. \qquad (1.2)$$

We introduce dimensionless variables and unknowns according to the formulas

$$\begin{gathered}[\xi, \zeta, \tau] = [x, y, c_0 t]/H, \\ [w, v] = H[w^*, v^*], \quad p = c_0^2 \rho_0 p^*. \end{gathered} \tag{1.3}$$

In the further analysis, we will omit the asterisk.

After a direct substitution of Eqs. (1.3), system of equations (1.1) assumes the dimensionless form

$$\begin{gathered}\varepsilon^2 \frac{\partial^2 w}{\partial \xi^2} - \frac{\partial^2 w}{\partial \tau^2} \pm \kappa p = 0, \\ \frac{\partial^2 p}{\partial \xi^2} + \frac{\partial^2 p}{\partial \zeta^2} - \frac{\partial^2 p}{\partial \tau^2} = 0, \\ \frac{\partial^2 v}{\partial \tau^2} = -\frac{\partial p}{\partial \zeta},\end{gathered} \tag{1.4}$$

where $\kappa = \frac{H\rho_0}{h\rho}$ and $\varepsilon = \frac{c}{c_0}$.

Consider the propagation of a harmonic wave with a dimensionless frequency ω and a dimensionless wave number χ. We seek the solution in the form

$$[w, v, p] = [W, V(\zeta), P(\zeta)] \exp[i(\omega\tau - \chi\xi)]. \tag{1.5}$$

Then, system of equations (1.4) assumes the form

$$\begin{gathered} W = \pm \frac{\kappa P}{\varepsilon^2 \chi^2 - \omega^2}, \\ \frac{d^2 P}{d\zeta^2} + (\omega^2 - \chi^2) P = 0, \\ \frac{dP}{d\zeta} = \omega^2 W. \end{gathered} \tag{1.6}$$

In the case of symmetric oscillation modes (the amplitude $P(\zeta)$ is an even function), the solution to the boundary-value problem in (1.6) and (1.2) is given by the formulas

$$P(\zeta) = \frac{\omega^2 \cosh(\beta\zeta)}{\beta \sinh\beta} W, \quad V(\zeta) = \frac{\sinh(\beta\zeta)}{\sinh\beta} W, \tag{1.7}$$

with $\alpha^2 = \varepsilon^2\chi^2 - \omega^2$ and $\beta^2 = \chi^2 - \omega^2$, where ω and χ satisfy the dispersion equation

$$\frac{\alpha^2 \beta^2}{\omega^2} \frac{\tanh(\beta)}{\beta} = \kappa. \tag{1.8}$$

In the antisymmetric case (the amplitude $P(\zeta)$ is an odd function), we have

$$P(\zeta) = \frac{\omega^2 \sinh(\beta\zeta)}{\beta \cosh\beta} W, \quad V(\zeta) = \frac{\cosh(\beta\zeta)}{\cosh\beta} W \tag{1.9}$$

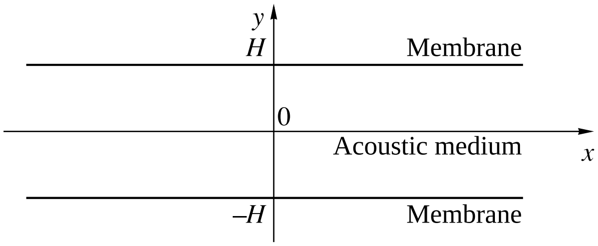

Fig. 1. Geometry of the problem.

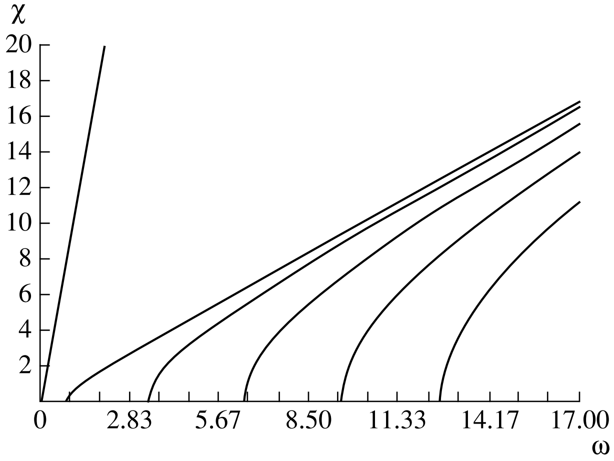

Fig. 2. Dispersion curves for the symmetric case.

under the condition that the dispersion relation

$$\frac{\alpha^2 \beta^2}{\omega^2} \frac{\coth(\beta)}{\beta} = \kappa \tag{1.10}$$

holds. Figures 2 and 3 show the dispersion curves of the fundamental and higher-order modes for symmetric and antisymmetric cases at $\varepsilon = 0.1$ and $\kappa = 1$.

2. ASYMPTOTIC ANALYSIS

Let us analyze the limit behavior of the dispersion curves for the wave numbers tending to zero and to infinity. Expanding Eqs. (1.8) and (1.10) in powers of the wave number χ for $\chi \longrightarrow 0$, we obtain the long-wave asymptotics of the fundamental mode. It has the form

$$\omega = \frac{\varepsilon}{\sqrt{\kappa}} \chi^2 + O(\chi^4) \tag{2.1}$$

in the symmetric case and

$$\omega = \frac{\varepsilon}{\sqrt{1 + \kappa}} \chi + O(\chi^3) \tag{2.2}$$

in the antisymmetric case.

As the wave number tends to infinity, the symmetric and antisymmetric fundamental modes turn into the

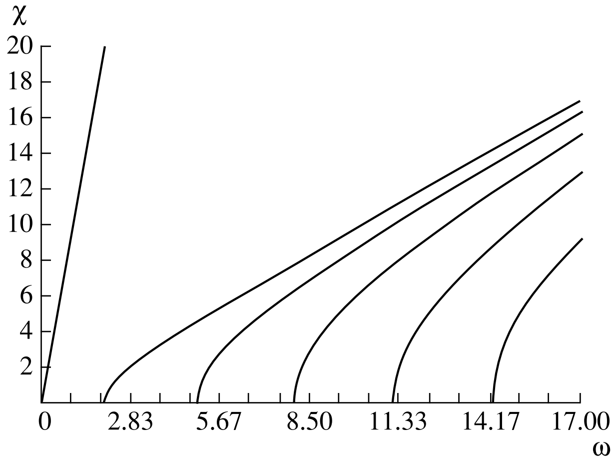

Fig. 3. Dispersion curves for the antisymmetric case.

surface wave whose limiting velocity of propagation coincides with the velocity c of waves in the membrane. Replacing the hyperbolic tangent and cotangent in Eqs. (1.8) and (1.10) with unity and setting $\alpha^2 \sim \omega$, we obtain the asymptotic formula

$$\omega = -\frac{\kappa\varepsilon}{2\sqrt{1-\varepsilon^2}} + \varepsilon\chi + O\left(\frac{1}{\chi}\right), \quad (\chi \geqslant 1). \tag{2.3}$$

At $\chi = 0$, dispersion equations (1.8) and (1.10) yield equations for cutoff frequencies b_n, $n = 1, 2, \ldots$:

$$\begin{aligned} b_n\tan(b_n) &= \kappa; \quad b_n \approx \pi(n-1), \quad n \geqslant 1, \\ b_n\cot(b_n) &= -\kappa; \quad b_n \approx -\frac{\pi}{2} + \pi n, \quad n \geqslant 1. \end{aligned} \tag{2.4}$$

The corresponding high-frequency long-wave asymptotics have the form

$$\omega = b_n + \frac{A_n}{b_n}\chi^2 + O(\chi^4), \tag{2.5}$$

where

$$A_n = \frac{1}{2} + \frac{\varepsilon\kappa}{b_n^2 + \kappa^2 + \kappa}. \tag{2.6}$$

Unlike the fundamental modes, the phase velocity of higher-order modes at infinity tends to the velocity of bulk waves c_0 in the acoustic medium. We seek the asymptotic behavior of these modes for $\chi \longrightarrow \infty$ in the form

$$\omega = \chi + \frac{C_n}{\chi} + O\left(\frac{1}{\chi^2}\right). \tag{2.7}$$

Substituting expansion (2.7) in dispersion relations (1.8) and (1.10), we obtain the equations for C_n:

$$\begin{aligned} \sqrt{2C_n}\tan\sqrt{2C_n} &= \frac{\kappa}{1-\varepsilon^2}; \quad C_n \approx \frac{1}{2}\pi^2(n-1)^2, \quad n \geqslant 1, \\ \sqrt{2C_n}\cot\sqrt{2C_n} &= -\frac{\kappa}{1-\varepsilon^2}; \\ C_n &\approx \frac{\pi^2}{8}(2n-1)^2, \quad n \geqslant 1. \end{aligned} \tag{2.8}$$

The method of the two-point Pade approximations (see, e.g., [6]) allows the transformation of the asymptotics obtained above into fractionally rational formulas that exhibit a given limit behavior near zero and at infinity. They have the form

$$\omega = \frac{\dfrac{\varepsilon}{\sqrt{\kappa}}\chi^2 - \dfrac{\kappa\varepsilon}{2\sqrt{1-\varepsilon^2}}\chi^3 + \varepsilon\chi^4}{1+\chi^3} \tag{2.9}$$

for the symmetric fundamental mode,

$$\omega = \frac{\dfrac{\varepsilon}{\sqrt{1+\kappa}}\chi - \dfrac{\kappa\varepsilon}{2\sqrt{1-\varepsilon^2}}\chi^2 + \varepsilon\chi^3}{1+\chi^2} \tag{2.10}$$

for the antisymmetric fundamental mode, and

$$\omega = \frac{b_n + \dfrac{A_n}{b_n}\chi^2 + C_n\chi^4 + \chi^6}{1+\chi^5} \tag{2.11}$$

for the higher-order modes.

Figures 4 and 5 show the dispersion curves obtained for the fundamental modes from the exact solution and asymptotic formulas (at $\varepsilon = 0.1$, $\kappa = 1$) suitable for estimating the behavior of the dispersion equation roots near the cutoff frequencies (Eqs. (2.1) and (2.2)) and for large wave numbers (Eq. (2.3)); in addition, these figures show the corresponding Pade approximations (Eqs. (2.9) and (2.10)). Figures 6 and 7 show similar curves for higher-order modes. One can see that the quality of Pade approximations degrades with increasing mode number n, which is related to the increase in the coefficient C_n in formula (2.11).

The above expansions offer the possibility of obtaining the asymptotic laws for the acoustic pressure distribution throughout the layer thickness. For fundamental modes, they have the form

$$P = \left(\frac{\omega}{\chi}\right)^2 W, \quad (\chi \leqslant 1) \tag{2.12}$$

in the symmetric case and

$$P(\zeta) = \omega^2\zeta W, \quad (\chi \leqslant 1) \tag{2.13}$$

in the antisymmetric case.

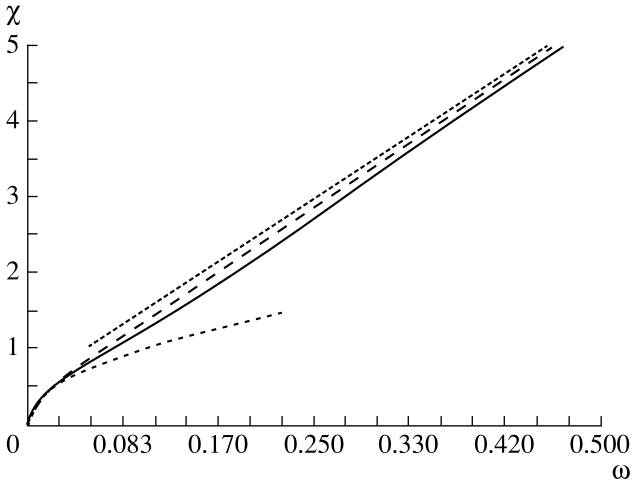

Fig. 4. Symmetric fundamental mode (solid line) and its asymptotics (dotted lines) for $\chi \gg 1$ and $\chi \ll 1$, and the Pade approximation (dashed line).

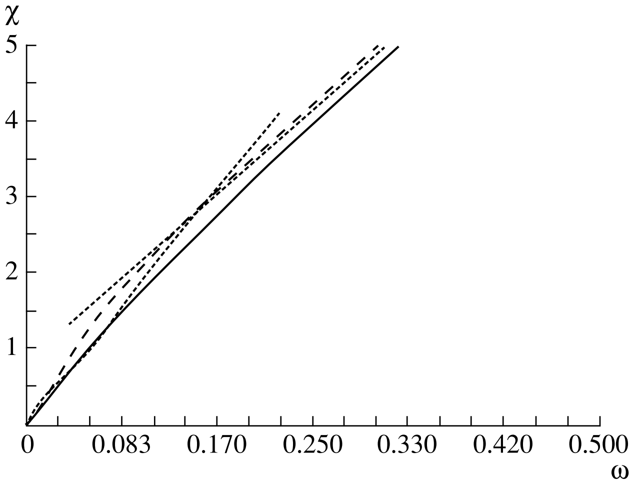

Fig. 5. Antisymmetric fundamental mode (solid line) and its asymptotics (dotted lines) for $\chi \gg 1$ and $\chi \ll 1$, and the Pade approximation (dashed line).

For the symmetric higher-order modes, we have

$$P(\zeta) = -\frac{\omega^2 W}{b_n \sin(b_n)}\Bigg[\cos(b_n\zeta) - \left\{\frac{2A_n - 1}{2b_n}\left(\cot(b_n) + \frac{1}{b_n}\right)\cos(b_n\zeta) + \sin(b_n\zeta)\zeta\right\}\chi^2\Bigg], \quad (\chi \ll 1), \tag{2.14}$$

$$P(\zeta) = -\frac{\omega^2\cos(\sqrt{2C_n}\zeta)}{\sqrt{2C_n}\sin(\sqrt{2C_n})}W, \quad (\chi \gg 1). \tag{2.15}$$

Similar formulas for the antisymmetric higher-order modes have the form

$$P(\zeta) = \frac{\omega^2 W}{b_n \cos(b_n)}\Bigg[\sin(b_n\zeta) + \left\{\frac{2A_n - 1}{2b_n}\left(\tan(b_n) - \frac{1}{b_n}\right)\sin(b_n\zeta) + \cos(b_n\zeta)\zeta\right\}\chi^2\Bigg], \quad (\chi \ll 1), \tag{2.16}$$

$$P(\zeta) = -\frac{\omega^2\sin(\sqrt{2C_n}\zeta)}{\sqrt{2C_n}\cos(\sqrt{2C_n})}W, \quad (\chi \gg 1). \tag{2.17}$$

3. ORTHOGONALITY RELATIONS

Let us reduce Eq. (1.6) to the eigenvalue problem

$$\frac{d^2P}{d\zeta^2} + \lambda P = 0 \tag{3.1}$$

with boundary conditions

$$\frac{dP}{d\zeta} \pm a(\lambda)P = 0, \quad (\zeta = \pm 1), \tag{3.2}$$

where

$$a(\lambda) = \frac{\kappa\omega^2}{-\varepsilon^2\lambda + \omega^2(1-\varepsilon^2)}$$

and introduce the spectral parameter $\lambda = -\beta^2$. Because the boundary conditions depend on the spectral parameter, problem (3.1), (3.2) does not belong to the class of problems described by the classical Sturm–Liouville theory [7]. To determine the orthogonality relations in

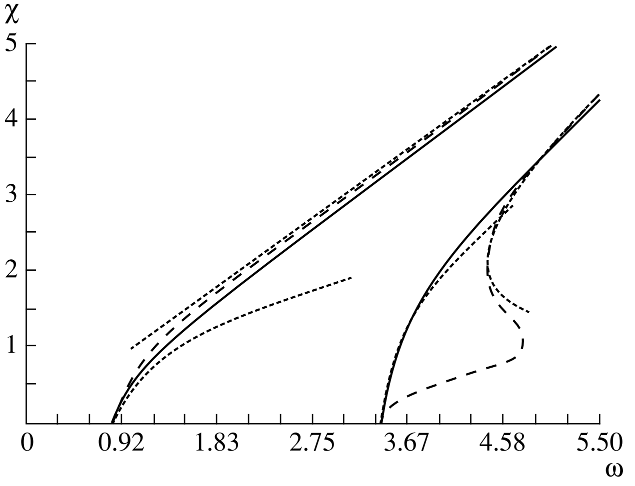

Fig. 6. Asymptotics for the symmetric higher-order modes (solid lines) (n = 1, 2) and their asymptotics (dotted lines) for $\chi \gg 1$ and $\chi \ll 1$, and the Pade approximations (dashed lines).

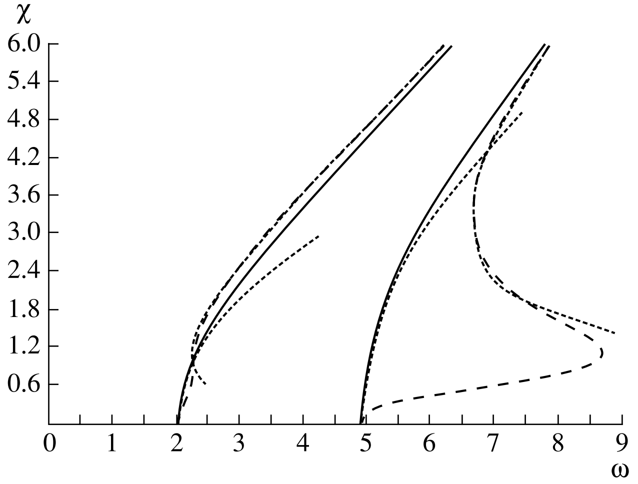

Fig. 7. Asymptotics for the antisymmetric higher-order modes (solid lines) ($n = 1, 2$) and their asymptotics (dotted lines) for $\chi \gg 1$ and $\chi \ll 1$, and the Pade approximations (dashed lines).

our case, we write Eq. (3.1) for eigenfunctions P_n and P_m ($n \neq m$) and the corresponding eigenvalues λ_n and λ_m and subtract the second equation from the first one. The result will be

$$\frac{d}{d\zeta}[P_n P_m' - P_m P_n'] + (\lambda_n - \lambda_m) P_n P_m = 0. \tag{3.3}$$

Integrating Eq. (3.3) from –1 to 1 and taking into account the fact that

$$\begin{aligned} \varepsilon^2 \lambda_i + \omega^2(\varepsilon^2 - 1) &= \kappa\omega^2 \frac{P_i(1)}{P_i'(1)} \\ &= -\kappa\omega^2 \frac{P_i(-1)}{P_i'(-1)}, \quad (i = n, m), \end{aligned} \tag{3.4}$$

we obtain the integral form of Eq. (3.3):

$$(\lambda_n - \lambda_m)\left[\frac{\varepsilon^2}{\kappa\omega^2} F_{nm} + \int_{-1}^{1} P_n(\zeta) P_m(\zeta) d\zeta\right] = 0, \quad n \neq m, \tag{3.5}$$

where

$$F_{nm} = P_n'(1) P_m'(1) + P_n'(-1) P_m'(-1). \tag{3.6}$$

As a consequence, we obtain

$$\frac{\varepsilon^2}{\kappa\omega^2} F_{nm} + \int_{-1}^{1} P_n(\zeta) P_m(\zeta) d\zeta = 0, \quad n \neq m. \tag{3.7}$$

Calculating now the left-hand side of Eq. (3.7) for $n = m$, we obtain the orthogonality relation for the eigenfunctions of problem (3.1), (3.2) in the form

$$\frac{\varepsilon^2}{\kappa\omega^2} F_{nm} + \int_{-1}^{1} P_n(\zeta) P_m(\zeta) d\zeta = \delta_{nm} B_n, \tag{3.8}$$

where

$$F_{nm} = [P_n'(1)]^2 + [P_m'(-1)]^2, \tag{3.9}$$

$$B_n = \frac{\varepsilon^2}{\kappa\omega^2} F_{nn} + \int_{-1}^{1} P_n^2(\zeta) d\zeta, \tag{3.10}$$

and δ_{nm} is the Kronecker delta.

Note that similar orthogonality conditions for acoustic waveguides with flexible walls were suggested earlier in [8].

ACKNOWLEDGMENTS

This work was supported by the Royal Society, London.

REFERENCES

1. U. K. Nigul, Izv. Akad. Nauk SSSR, Ser. Fiz.–Mat. Nauk **12** (3), 284 (1963).
2. R. D. Mindlin, in *Proceedings of the 1st Symposium on Naval Structural Mechanics* (Pergamon, New York, 1958), p. 199.
3. J. D. Kaplunov, L. Yu. Kossovich, and E. V. Nolde, *Dynamics of Thin-Walled Elastic Bodies* (Academic, San Diego, 1998).
4. J. D. Kaplunov, E. V. Nolde, and G. A. A. Rogerson, Proc. R. Soc. London, Ser. A **456**, 2589 (2000).
5. Yu. I. Bobrovnitskiĭ, Akust. Zh. **18**, 513 (1972) [Sov. Phys. Acoust. **18**, 432 (1972)].
6. I. F. Obraztsov, I. B. Nerubaĭlo, and I. V. Andrianov, *Asymptotic Methods in Building Mechanics of Thin-Walled Structures* (Mashinostroenie, Moscow, 1991) [in Russian].
7. E. C. Titchmarsh, *Eigenfunction Expansions Associated with Second-Order Differential Equations*, 2nd ed. (Clarendon Press, Oxford, 1962; Inostrannaya Literatura, Moscow, 1960), Part 1.
8. D. P. Warren, J. B. Lawrie, and I. M. Mohamed, Wave Motion **36** (2), 119 (2002).

Translated by A. Vinogradov

Acoustical Physics, Vol. 50, No. 6, 2004, pp. 699–703. Translated from Akusticheskiĭ Zhurnal, Vol. 50, No. 6, 2004, pp. 808–812.
Original Russian Text Copyright © 2004 by Kobelev.

Parameters of Microparticles Responsible for the Monopole Sound Scattering in a Liquid

Yu. A. Kobelev
Institute of Applied Physics, Russian Academy of Sciences, ul. Ul'yanova 46, Nizhni Novgorod, 603950 Russia
e-mail: soustova@hydro.appl.sci-nnov.ru

Received April 15, 2003

Abstract—A monopole scattering of sound by microparticles in a liquid is considered for microparticles of two types: spherically symmetric particles similar to gas bubbles in a liquid and disk-shaped gas-filled particles whose bases may oscillate in antiphase. A transformation of the scattering amplitude to the function that, in particular, describes the oscillations of a particle removed from the liquid is proposed. This function extends the possibilities of the acoustic diagnostics of such particles. Estimates of the sound velocity in water containing disk-shaped particles suggest that the sound velocity increase observed in sea water with plankton can be explained by the monopole scattering of sound from a single plankton particle modeled as a rigid gas-filled disk with oscillating parts of its bases. *© 2004 MAIK "Nauka/Interperiodica".*

In problems of sound behavior in media with discrete inhomogeneities (particles), it may be necessary to develop a model of acoustic wave scattering by individual particles, which, in principle, allows one to describe the acoustic field in the medium and, in a number of cases, to identify the particles. For example, in [1], an attempt is made to determine the shape and type of plankton from backscattered acoustic waves; in [2], an anomalously high attenuation of acoustic waves in a liquid containing zero-buoyancy plankton is explained by oscillations of particles whose center of mass is offset from the point at which the buoyancy force is applied. Of interest are the experimental measurements of the velocity of sound in sea water containing plankton [3, 4], where the velocity of sound was found to increase with respect to that in the pure liquid in the frequency range from a few kilohertz to hundreds of kilohertz. Whereas the model developed in [1] refers to acoustic wavelengths equal to anywhere from fractions of the particle size to a few particle sizes, the wavelengths dealt with in [3, 4] are much longer than the particle size, which allows one to categorize the interaction between the particles and sound by the type of the scattering: monopole, dipole, etc. In this case, the characteristics of individual scattering types can experimentally be found by measuring this process for one particle and revealing how the particle parameters (elasticity, mass, added mass of the liquid, etc.) responsible for this type of oscillations are related to the amplitude of the scattered acoustic waves. Of course, this study cannot do without theoretical models of particle oscillations, which should be individual for each scattering type. In this paper, we discuss two models of the particles that cause a monopole scattering of sound. These are the spherical particle, whose properties are close to those of a gas bubble in the liquid, and the planar (disk-shaped) particle, whose bases oscillate without deformation.

Consider the scattering of an acoustic wave by a spherical particle whose radius R is small in terms of wavelength. We represent the particle as a gas-filled space enclosed in a shell whose mass per unit area is m. For harmonic oscillations at the circular frequency ω, the amplitude $R_s(r)$ of the pressure of the scattered acoustic wave $P(t) = P_0\exp(i\omega t)$ can be written as

$$P_s(r) = \chi(R/r)\exp(-ikr)P_0, \tag{1}$$

where r is the distance from the particle center to the observation point; k is the wave number; and χ and P_0 are the amplitudes of the scattered and incident waves, respectively. To calculate χ, we use the boundary conditions at the surface of the particle and the gas law inside it (see, e.g., [5, 6]). The only difference between the description of the particle under study and that of a gas bubble is the additional term in the relationship between the pressure P_g in gas and the pressure P_l in liquid:

$$P_g = P_l - \omega^2 m\xi, \tag{2}$$

where ξ is the amplitude of oscillations of the particle's boundary. As a result, we obtain the following expression for the amplitude of the scattered wave:

$$\begin{aligned}\chi = {} & [(\omega_0^2/\omega^2) - 1 - (m/R) \\ & + i(kR + (4\nu/\omega R^2) + \omega_0^2\sigma/\omega^2)]^{-1},\end{aligned} \tag{3}$$

where $\omega_0 = (1/R)(3\gamma P_{\mathrm{st}}/\rho)^{1/2}$; P_{st} is the static pressure in the particle; σ is the internal loss factor; γ is the adiabatic index of gas in the particle; and ρ and ν are the density of liquid and its kinematic viscosity coefficient, respectively. Exact values of ω_0 and σ with allowance for heat-transfer processes and surface tension, which can be regarded in this case as elasticity of the particle's surface, are given in [6]. An expression for the amplitude χ of the wave scattered by a particle with an elastic mass shell of a nonzero thickness is obtained in [7].

The quantity χ depends on the frequency ω in a resonance manner, and the position of the resonance ($\omega = \omega_r$) on the frequency axis is determined by the condition

$$\omega_0^2/\omega_r^2 = 1 + m/\rho R \tag{4}$$

and depends on the added mass of the liquid $4\pi\rho R^3$, as well as on the mass of the boundary $4\pi m R^2$. To retrieve the parameters of the particle from the scattered field according to Eq. (1), one must measure the product $R\chi$ and, if the particle radius R is somehow determined, for example from the float-up velocity as in [10], then ω_0 and σ can be found from condition (4) of the resonance and from its Q factor at $m = 0$. Otherwise (R is unknown and $m \neq 0$), $R\chi$ must additionally be measured at other points, for example, far from the resonance at low frequencies, where

$$\chi(\omega \longrightarrow 0) = (\omega^2/\omega_0^2)[1 - i(4\omega\upsilon/\omega_0^2 R^2) + \sigma]. \tag{5}$$

In this situation, it may be useful to transform χ to the function $W(\omega, R_{\text{ef}})$ by the formula

$$W = R\chi[R_{\text{ef}} + R\chi\exp(-ikR_{\text{ef}})], \tag{6}$$

where R_{ef} can be defined arbitrarily. Formulas (3) and (6) yield the following expression for W (kR_{ef} is small):

$$W = \left\{(R_{\text{ef}}/R)\left[\frac{\omega_0^2}{\omega^2} - 1 - \frac{m}{\rho R} + i\left(\frac{4\nu}{\omega R^2} + \frac{\omega_0^2}{\omega^2}\sigma\right)\right] + 1\right\}^{-1}. \tag{7}$$

It can be seen that function W has lost its emission loss coefficient kR for all R_{ef} while retaining the resonance dependence on ω, but not for all R_{ef}. The position of the resonance ω_{ef} on the frequency axis is now given by the formula

$$\omega_0^2/\omega_{\text{ef}}^2 = 1 + m/\rho R - R/R_{\text{ef}}, \tag{8}$$

which is valid when

$$R/R_{\text{ef}} \geq (1 + m/\rho R). \tag{9}$$

The quantity $R_{\text{ef}} = R/(1 + m/\rho R)$ gives an infinite ω_{ef} and transforms Eq. (7) to the expression

$$W = (\omega^2/\omega_r^2)[1 - i(4\omega\nu/\omega_0^2 R^2 + \sigma)], \tag{10}$$

which is proportional to χ from Eq. (5) but now is valid for the entire range of frequency ω. At $m = 0$, this behavior of the function W in the vicinity of the resonance of the amplitude χ of the scattered wave determines the particle radius R. At $m \neq 0$ and $R_{\text{ef}} = R$, Eq. (7) takes the form

$$W = (\rho R/m)\{(\omega_i^2/\omega^2) - 1 + i[(4\nu\rho/Rm) + (\omega_i^2/\omega^2)\sigma]\}^{-1}, \tag{11}$$

where $\omega_i^2 = 3\gamma P_{\text{st}}/Rm$ is the eigenfrequency in the absence of liquid.

Let us show how function $W(\omega, R_{\text{ef}})$ can be used to calculate the parameters of the particle. Let us assume that, from the field scattered by the particle, using formula (1), the resonance frequency ω_r and the values of the product $R\chi$ are determined at the frequencies ω_1 and ω_2, for example to the left and to the right of the resonance frequency ω_r, which are close enough to the coefficient σ to be constant. By substituting these values of $R\chi$ into Eq. (6) for W and setting its real part equal to ReW given by Eq. (10), where the frequency ω must be taken equal to ω_1 or ω_2, we obtain $R_{\text{ef}} = R_1$ and $R_{\text{ef}} = R_2$, which must be equal and satisfy equality (9), i.e.,

$$R/R_1 = 1 + m/\rho R = \omega_0^2/\omega_r^2. \tag{12}$$

Also, Im$W(\omega_1, R_1) = A_1$ and Im$W(\omega_2, R_1) = A_2$ must be equal to the imaginary part of Eq. (10) at the corresponding frequency. With formula (12), we obtain the equations

$$\begin{aligned} A_1 &= -(\omega_1^2/\omega_r^2)[(4\omega_1\nu R_1/\omega_r^2 R^3) + \sigma]; \\ A_2 &= -(\omega_2^2/\omega_r^2)[(4\omega_2\nu R_1/\omega_r^2 R^3) + \sigma], \end{aligned} \tag{13}$$

which yield R and σ in the form

$$\begin{aligned} R &= \left[\frac{4\nu R_1\omega_1^2\omega_2^2(\omega_1 - \omega_2)}{\omega_r^4(\omega_1^2 A_2 - \omega_2^2 A_1)}\right]^{1/3}; \\ \sigma &= \frac{\omega_r^2(\omega_2^3 A_1 - \omega_1^3 A_2)}{\omega_1^2\omega_2^2(\omega_1 - \omega_2)}. \end{aligned} \tag{14}$$

Equality (12) can be used to calculate ω_0 and m. Setting $m = \nu = \sigma = 0$ and $R = R^*$ in Eq. (3) produces expression (12) for R_χ^* from [7], while the above procedure yields the value R^*, which is equal to R_1 rather than R. In the case we study, it is the viscosity of the liquid that allowed us to separate R and R_1.

Thus, the transformation of the product $R\chi$ according to Eq. (6) eliminates the radiation loss while retaining, in general, the resonance frequency behavior of the function W. At $R_{\text{ef}} = R$, function W describes the oscillations of the particle without the liquid, because the added mass of the liquid disappears. At $R_{\text{ef}} = R/(1 + m/\rho R)$, the resonance frequency behavior of W changes to the quadratic behavior of its real part, which is equal to unity at the resonant frequency ($\omega = \omega_r$) for any R_{ef}.

Let us focus on the following significant drawback of the above model. Let the parameters ω_0 and R be found from Eqs. (12) and (14). Then, the pressure P_{st} may be calculated from the definition of ω_0 (see comments to Eq. (3)), but this pressure may differ from the actual pressure in the particle even with allowance for the elasticity of its surface. For example, it may be much lower than the external static pressure. In this case, the model can be improved so as to introduce an additional parameter affecting the frequency ω_0. To this end, consider the monopole scattering of sound on a disk-shaped particle. Let the particle be planar (its thickness be much less than the longitudinal dimension), arbitrarily shaped in the longitudinal plane, and filled with gas of volume V. Let, at a certain point of the particle, two aligned holes be cut in its plane surfaces to connect the internal and external spaces, and two pistons of radius a and mass M be inserted into these holes and be capable of oscillating in antiphase with the same amplitude ξ without deformation. The walls of the particle are also presumed to preserve their shape.

Two components can be distinguished in the field scattered from this particle. One component is attributed to the scattering of sound from a perfectly rigid particle and is equal to the monopole component of the expansion of the incident field P_0 into spherical functions. Therefore, its amplitude is proportional to k^2b^2 (b is the particle size) [8] and is small. The dominant contribution to the scattering is produced by the particle compressibility through the displacement of the pistons in the holes. To describe this process, we introduce a rigid boundary in the particle symmetry plane, which allows us to reduce the problem to oscillations of a circular rigid piston in a rigid screen (see [9]). The acoustic field (here, the scattered field P_s) produced at an arbitrary point in space due to the displacement ξ of the piston is given by the formula

$$P_s(r) = -(\omega^2\rho\xi/2\pi)\int\limits_S[\exp(-ikr')/r']dS, \qquad (15)$$

where the integration is performed over the piston surface S; $r' = |\mathbf{r} - \mathbf{r}_s|$; and $\mathbf{r}$ and $\mathbf{r}_s$ are the vectors originating from the center of the piston and ending at the observation point and at the center of the piston's surface element ds, respectively. Far from the piston, at $r^2 \gg a^2$, Eq. (15) yields

$$P_s(r) = -\omega^2\rho\xi a^2\exp(-ikr)/2r. \qquad (16)$$

The comparison of expressions (16) and (1) gives the relationship

$$\chi RP_0 = -\omega^2\rho a^2\xi/2, \qquad (17)$$

where R is as yet unknown and will be found.

Consider the oscillations of the piston: they are described by Newton's equation

$$-M\omega^2\xi = SP_g - \int\limits_s P_s(\mathbf{r}_s)dS - SP_0. \qquad (18)$$

Here, the integration is also performed over the piston surface S, and the vector $\mathbf{r}_s$ goes from the center of the piston to the element ds. The gas pressure P_g in the particle is related to ξ through the gas law with an allowance for losses σ (oscillations of the two pistons must be taken into consideration):

$$P_g = -(8\gamma SP_{\mathrm{st}}/V)(1 + i\sigma)\xi. \qquad (19)$$

The third term on the right-hand side of Eq. (18) describes the action of the field P_0 unperturbed by the particle on the piston; the second term is the response of the liquid to the oscillations of the piston, which is also calculated in [9]:

$$\int\limits_s P_s(\mathbf{r}_s)dS = -\omega^2\rho(8/3)a^3[1 - (3\pi/16)ika]\xi. \qquad (20)$$

The first term on the right-hand side of Eq. (20) is proportional to the added mass of the liquid

$$M_c = (8/3)a^3\rho, \qquad (21)$$

associated with piston oscillations, and the second term, with the energy loss coefficient due to the acoustic emission. By substituting Eqs. (19) and (20) into Eq. (18), we obtain the equation for the piston displacement

$$\begin{aligned}\xi = -(3\pi P_0/8\omega^2 a\rho)\{&(\omega_0^2/\omega^2) - 1 - (M/M)_c \\ &+ i[(3\pi/16)ka + (\omega_0^2/\omega^2)\sigma]\}^{-1},\end{aligned} \qquad (22)$$

where ω_0 is given by the formula

$$\omega_0 = (8\gamma S^2P_{\mathrm{st}}/VM_c)^{1/2}. \qquad (23)$$

Taking the radius R from Eqs. (1) and (17) to be equal to

$$R = (3\pi/16)a \qquad (24)$$

and substituting ξ from Eq. (22) into Eq. (17), we obtain the following expression for the scattering amplitude:

$$\begin{aligned}\chi = \{&(\omega_0^2/\omega^2) - 1 - (M/M_c) \\ &+ i[kr + (4\nu/\omega R^2) + (\omega_0^2/\omega^2)\sigma]\}^{-1}.\end{aligned} \qquad (25)$$

This expression includes the loss coefficient $4\nu/\omega R^2$ due to the radial oscillations of the liquid. The following reasoning can be advanced in favor of this description. At the radius R given by Eq. (24), χ given by Eq. (25) coincides with expression (3), including the loss coefficient kR due to the acoustic emission. Furthermore, the added mass appears to be close to the added mass of a pulsating sphere; therefore, the energy loss due to the tangential component of the potential velocity of liquid particles at the boundary $|\mathbf{r}| = R$ is small; i.e., the planar particle oscillates as the spherical one. The energy loss due to the vortex component of the velocity of the liquid near the piston is considered to be included into the coefficient σ. If the particle volume is represented as $V = 4\pi R^3\alpha/3$, formula (23) yields the expression $\omega_0 = (2/R)\sqrt{3\gamma P_{\text{st}}/\alpha\rho}$, which contains an additional parameter α. The latter can be defined, with the help of the procedure mentioned above, from the known γ and P_{st}.

Unlike the scattering cross-section, which is determined by the magnitude of the scattering amplitude, to obtain the scattering function itself the phase must be known, which imposes more stringent requirements on the accuracy of measuring the field scattered by the particle. The measurement methods realized experimentally—for example, the one proposed in [10], which measures the acoustic field during its several periods—cannot actually be used for this purpose. In this case, the diagnostics of the particle placed at the center of a spherical resonator seems to be methodically promising. Then, it is necessary to measure the coefficient of reflection of a spherically converging acoustic wave from the particle. For a gas bubble, the reflection coefficient is determined in [5] using boundary conditions on the bubble. For a particle of an arbitrary shape, this method can hardly be used. We calculate this quantity by a somewhat different method.

Let a unit-amplitude spherically converging pressure wave $(R/r)\exp(ikr)$ be incident on the particle; the reflected wave will have the form $\beta(R/r)\exp(-ikr)$, where β is the reflection coefficient. For $r^2 \gg R^2$ and $(kr)^2 \ll 1$, the total field can be written in two ways:

$$\begin{aligned}&(R/r)[\exp(ikr) + \beta\exp(-ikr)]\\ &\approx 2ikR + (R/r)(1+\beta)\exp(-ikr).\end{aligned} \tag{26}$$

According to Eq. (1), the second term on the right-hand side of Eq. (26) can only describe the scattered field produced by the incident field uniform in r and given by the first term; i.e., $2ikR\chi(R/r)\exp(-ikr) = (R/r)(1 + \beta)\exp(-ikr)$, which yields the relationship between β and χ:

$$\beta = -1 + 2ikR\chi. \tag{27}$$

Interestingly, for a bubble at a frequency $\omega = \omega_r$, which corresponds to the resonance in χ described by Eqs. (3) or (25), we obtain the expression for β:

$$\beta = -1 + 2kR/[kR + (4\nu/\omega_r R^2) + (\omega_0^2/\omega_r^2)\sigma], \tag{28}$$

which, under the condition

$$kR = (4\nu/\omega_r R^2) + (\omega_0^2/\omega_r^2)\sigma, \tag{29}$$

yields a zero β and a total absorption of the acoustic field incident on the particle. For an air bubble, using data on σ borrowed from [6], we obtain in this case a radius of 0.5 cm.

Finally, let us estimate the velocity of sound in water containing phytoplankton under the assumption that the individual particles can be modeled by a circular gas-filled disk with the following parameters: the disk radius is $b = 25$ μm, the disk thickness is $d = 10$ μm, the radius of the pistons is $a = 5$ μm, and the gas volume is $V = 2 \times 10^4$ μm^3. With these parameters, Eq. (24) gives the radius as $R = 3$ μm; the eigenfrequency expressed from Eq. (23) in terms of the radius and volume V is given by the formula

$$f_0 = 2(\gamma R P_{\text{st}}/\pi\rho V)^{1/2} = 1.6 \times 10^5\ \text{Hz}, \tag{30}$$

where $\gamma = 1.4$ and $P_{\text{st}} = 10^5$ Pa. In [3], where the particle parameters were close to those chosen above, the volume particle content in water was about 10^{-4}. Let the volume gas content in the particle be 0.1, which provides an approximately zero particle buoyancy. The rest of the volume is occupied by the disk walls; i.e., the volume gas content in the water is 10^{-5}. The number of particles n per unit volume is $10^{-5}/V = 0.5 \times 10^3$ (1/cm^3).

The average wave number k_m of the acoustic field in the liquid containing monopole scattering particles is given by the formula [11]

$$k_m^2 = k^2 + 4\pi R\chi n, \tag{31}$$

which yields the following relative variation in the velocity of sound $\Delta = (c_m - c)/c$:

$$\Delta = -(Rnc^2/2\pi(f_r^2 - f^2)). \tag{32}$$

Here, c_m and c are the velocities of sound in the mixture and the pure liquid, respectively; f is the frequency of sound; and χ is taken from Eq. (25) at $M = 0$ and is sufficiently far away in frequency f from the resonant frequency f_r, where the imaginary part may be neglected. By substituting $c = 1.5 \times 10^3$ m/s, $f = 3 \times 10^5$ Hz, and the above values for R, n, and f_r into Eq. (32), we obtain $\Delta = 8.3 \times 10^{-3}$, which satisfactorily agrees with the data reported in [3]. For the sake of comparison, we provide the estimates of the sound-velocity variation in water containing gas bubbles with the same volume content of 10^{-5} but with two different radii determined by the following conditions: (i) the area of the pistons equals the bubble surface area, i.e., $2\pi a^2 = 4\pi R_1^2$, which yields $R_1 = 3.5$ μm, $n_1 = 0.54 \times 10^3$ (1/cm^3), and $f_{r1} = 0.9 \times 10^6$ Hz; and (ii) the gas volume in the particle equals the bubble volume. In this case, $R_2 = 16$ μm, $f_{r2} = 2 \times 10^5$ Hz, and the particle concentration remains the same (equal to the particle concentration n). Then, Eq. (32) at $f = 3 \times 10^5$ Hz yields a negative value $\Delta_1 = -0.6 \times 10^{-3}$ in the first case and a positive value $\Delta_2 = 6 \times 10^{-2}$ that is too high in the second case. These estimates allow us to assume that the effect of the sound velocity increase observed in sea water containing plankton, at least at frequencies above 100 kHz, can be attributed to the monopole scattering of sound by individual plankton particles, which can be modeled by the particle considered above.

ACKNOWLEDGMENTS

I am grateful to D.A. Selivanskiĭ for encouragement during the period of performing this work and for useful discussions. This work was supported by the Russian Foundation for Basic Research, project no. 03-05-64993.

REFERENCES

1. A. C. Lavery, T. K. Stanton, D. E. McGehee, and D. Chu, J. Acoust. Soc. Am. **111**, 1197 (2002).
2. I. N. Didenkulov, A. B. Ezerskiĭ, and D. A. Selivanovskiĭ, Akust. Zh. **49**, 425 (2003) [Acoust. Phys. **49**, 361 (2003)].
3. B. M. Sandler, D. A. Selivanovskiĭ, and P. A. Stunzhas, Akust. Zh. **39**, 144 (1993) [Acoust. Phys. **39**, 73 (1993)].
4. B. M. Sandler, D. A. Selivanovskiĭ, and P. A. Stunzhas, Akust. Zh. **39**, 724 (1993) [Acoust. Phys. **39**, 380 (1993)].
5. M. A. Isakovich, *General Acoutics* (Nauka, Moscow, 1973) [in Russian].
6. Ch. Devin, Jr., J. Acoust. Soc. Am. **31**, 1654 (1959).
7. V. N. Alekseev and S. A. Rybak, Akust. Zh. **45**, 603 (1999) [Acoust. Phys. **45**, 535 (1999)].
8. E. Skudrzyk, *The Foundations of Acoustics* (Springer, Wien, 1971; Mir, Moscow, 1976), Vol. 2.
9. J. W. Strutt (Lord Rayleigh), *The Theory of Sound*, 2nd ed. (Macmillan, London, 1896; GITTL, Moscow, 1955), Vol. 2.
10. V. V. Bredikhin, N. I. Vasilinenko, Yu. A. Kobelev, and A. I. Potapov, Akust. Zh. **41**, 390 (1995) [Acoust. Phys. **41**, 339 (1995)].
11. P. M. Morse and H. Feshbach, *Methods of Theoretical Physics* (McGraw-Hill, New York, 1953; Inostrannaya Literatura, Moscow, 1960), Vol. 2.

Translated by A. Khzmalyan

Acoustical Physics, Vol. 50, No. 6, 2004, pp. 704–716. Translated from Akusticheskiĭ Zhurnal, Vol. 50, No. 6, 2004, pp. 813–826.
Original Russian Text Copyright © 2004 by Lebedev, Salin.

Effects of Localization of the Areas of Sound Scattering by Surface Wind Waves

A. V. Lebedev and B. M. Salin
Institute of Applied Physics, Russian Academy of Sciences,
ul. Ul’yanova 46, Nizhni Novgorod, 603950 Russia
e-mail: swan@hydro.appl.sci-nnov.ru; salin@hydro.appl.sci-nnov.ru

Received October 27, 2003

Abstract—Experimental studies of the scattering of a monochromatic sound signal by a rough sea surface are carried out. The signal is produced by a point source in a shallow-water basin. The measurements are performed with the use of horizontal and vertical linear receiving arrays. The experimental data are compared with the estimates obtained on the basis of the model developed by the authors for resonant sound scattering by surface roughness. A satisfactory agreement between the experiments and the calculations is achieved. It is shown that the scattered signal is formed within small surface areas, whose sizes have the same order of magnitude as the first Fresnel zone with respect to the source and the receiving system. *© 2004 MAIK “Nauka/Interperiodica”.*

A number of publications ([1–3], for instance) consider the amplitude and phase fluctuations that accompany the propagation of low-frequency (up to 300–400 Hz) sound waves in the sea. Such fluctuations can be caused by various phenomena: the sound scattering by the wavy surface or by moving volume inhomogeneities, the influence of turbulence and internal waves, the interference produced by the motion of the sound source and the receiver, and so on. A review of publications on acoustic fluctuations in a shallow sea can be found in [4], where a general approach is developed for the case of several-mode sound propagation, with the modes interacting due to random processes in the medium. The directivity of the sound scattering by surface waves is well known and thoroughly studied [1–3]. We should also mention the recent publication [5], in which the scattering characteristics are studied for the case of a directional sound source.

The present paper presents the experimental data on the characteristics of the fluctuations caused by surface waves on short shallow-water acoustic paths with tonal sound sources. In the experiments, the sound wavelength λ was comparable to the length Λ of surface gravity waves. The measurements were performed in the Baltic Sea and on the Sankhar Lake (Vladimirskaya oblast, Russia). The transmitted frequencies corresponded to a large number of propagating modes: $10\lambda \lesssim H$, where H is the depth of the basin. The signals were received by linear horizontal (in the sea and lake experiments) and vertical (in the lake experiment) antenna arrays. Simultaneously with the acoustic measurements on the lake, the spectrum of the surface waves was also measured.

In this paper, we quantitatively compare the measured and calculated fluctuations of the sound signals. It is shown that, with monopole (omnidirectional) sound transmission with the wavelengths $\lambda \sim \Lambda$, the scattering of sound by the wavy surface is substantially contributed to by localized areas of the surface. The centers of such areas correspond to the conditions of resonant scattering, and their sizes are determined by the size of the first Fresnel zone with respect to the positions of the sound source and the receiver.

The paper has the following structure. In Section 1, the conditions of resonant scattering and a model for calculating the scattered signals are considered. Section 2 presents the experimental data for short propagation paths in the Baltic Sea and on the Sankhar Lake. The results obtained and the validity domain of the calculation model are discussed in Section 3. The formulas used in the calculations are presented in Appendix A.

1. CALCULATION OF THE LEVELS OF RESONANT SOUND SCATTERING BY SURFACE WAVES

The conditions of the Bragg or combination scattering can be written as follows [1]:

$$\mathbf{k}_s = \mathbf{k}_i \pm \boldsymbol{\kappa}, \quad (1)$$

where $\mathbf{k}_s$ and $\mathbf{k}_i$ are the horizontal projections of the wave vectors in the scattered and incident waves and $\boldsymbol{\kappa}$ is the wave vector of the surface roughness ($\kappa = 2\pi/\Lambda$). Figure 1 shows the layout of scattering for positive Doppler frequencies of the scattered signal: $\mathbf{k}_s = \mathbf{k}_i + \boldsymbol{\kappa}$.

Suppose that low grazing angles are responsible for resonant scattering [1], so that the absolute values of the horizontal projections are equal to each other: $k_i = k_s =$

$k = 2\pi/\lambda$. In this case, the angles θ_i, θ_s, and ϕ (Fig. 1) are related by the following equalities:

$$\phi = \frac{\pi}{2}\operatorname{sgn}\theta_s^{(+)} + \frac{\theta_s^{(+)} + \theta_s^{(-)}}{2}, \quad \theta_i^{(\pm)} = \theta_s^{(\mp)}, \qquad (2)$$

$$\xi = \left|\sin\left(\frac{\theta_s^{(+)} - \theta_s^{(-)}}{2}\right)\right|, \qquad (3)$$

where $\xi = \frac{\kappa}{2k} = \frac{\lambda}{2\Lambda}$. The quantities $\theta_{s,i}^{(+)}$ and $\theta_{s,i}^{(-)}$ correspond to scattering with positive and negative Doppler shifts, respectively. The range of angles ϕ in which the conditions of resonant scattering can be met is determined by the expression

$$\phi = \pm(\pi/2 \pm \arcsin\xi). \qquad (4)$$

This angular sector is shadowed in Fig. 1. Thus, if the transmitted frequency increases (the value of ξ decreases), condition (1) is satisfied for vectors $\boldsymbol{\kappa}$ that are close to the normal SO. Evidently, the actual values of angles $\theta_{i,s}$ and ϕ should satisfy the inequalities

$$2k > \kappa \ \text{ or } \ \Lambda > \lambda/2. \qquad (5)$$

It can be shown that the areas of resonant scattering (A and B in Fig. 1) belong to the arcs of circles of radius R, which pass through the transmission and reception points:

$$R = \frac{|\mathrm{SO}|}{4\xi\sqrt{1-\xi^2}}. \qquad (6)$$

Both at high frequencies, when $\lambda \ll \Lambda$, and at low frequencies, when $\lambda/2 \sim \Lambda$, radius (6) of the circles tends to infinity. However, the positions of the areas that are responsible for resonant scattering (Eq. (1)) are different. At high frequencies ($\xi \ll 1$), these areas lie on the arcs that are close to the line connecting the source and the receiver. At low frequencies ($\xi \sim 1$), the areas of resonant scattering lie on the arcs that are most distant from the SO line (see Fig. 1).

It is shown in Appendix A that the sizes of the regions A and B that are responsible for the resonant scattering are determined by the sizes of the Fresnel zones. With multimode propagation, the relative intensity of resonant scattering is given by Eq. (A8). This intensity is governed by expression (A9') for low grazing angles that correspond to the total internal reflection from the bottom if the surface wave is a plane one.

Note that, in the first approximation of the perturbation theory (Eq. (A1)), the scattered intensity (Eq. (A9)) is proportional to the squared Rayleigh parameter: $\mathcal{R} = \mathcal{R}_0\sin\chi_1$, where $\mathcal{R}_0 = 2k\sqrt{\langle\eta^2\rangle}$, $\langle\eta^2\rangle$ is the squared surface deviation, and χ_1 is the grazing angle of the incident plane sound wave. Equation (A9) is obtained in the first approximation of the small-perturbation theory [1]. In this case, the problem is considered in relation to the scattering of a cylindrical wave generated by a localized omnidirectional sound source. Within the scattering area, the spatial structure of the surface roughness is supposed to be coherent, and condition (1) is met. Then, the area S will be limited by the Fresnel sizes with respect to the positions of the source and the receiver (see also Section 3), and the scattered intensity will be proportional to the squared value of S, because the contributions of different roughness elements are coherently combined.

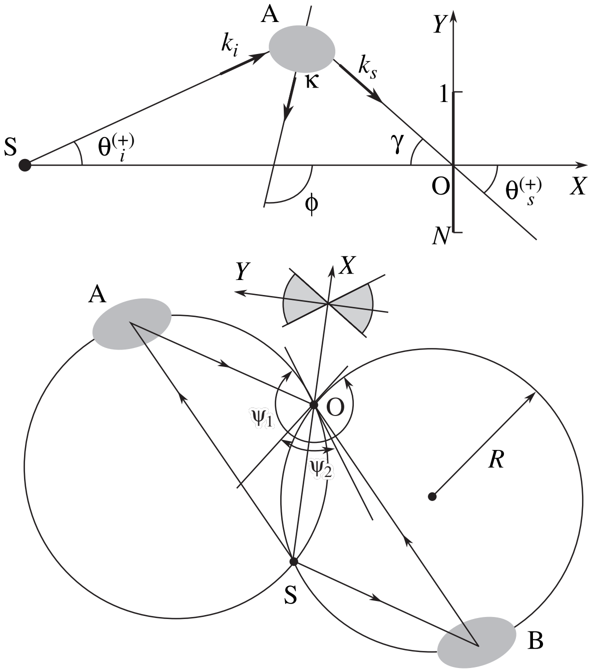

Fig. 1. Layout of the resonant scattering of sound by a wavy surface: S is the sound source, and O is the center of the vertical linear antenna array consisting of N hydrophones. Gray ellipses lying on the circular arcs schematically indicate possible positions of the surface areas responsible for the resonant scattering. The sectors of angles $\Psi_{1,2}$ indicate the possible directions of arrival of the scattered signals for low ($\lambda/2 \sim \Lambda$) and high ($\lambda \ll \Lambda$) frequencies, respectively. The dashed angular sector corresponds to possible directions of the wave vector κ.

The derivation of Eq. (A9) is somewhat tedious. Therefore, let us obtain an expression similar to Eq. (A9) from energy considerations. Equation (A2) defines the field produced by a monopole sound source with a capacity Q in the waveguide. By averaging the squared sound pressure over the coordinates of the source and the receiver (over the interference structure of the waveguide), we arrive at the following estimate:

$$I_0(r) = I_{00}\frac{2\chi_*}{rH}, \qquad (7)$$

where r is the distance between the source and the receiver (|SO| in Fig. 1), H is the waveguide thickness, χ_* is the capture angle for the rays leaving the area of excitation of the sound waves, $I_{00} = \left(\frac{\omega\rho Q}{4\pi}\right)^2$, ω is the transmitted frequency, and ρ is the density of water. The quantity I_{00}/R^2 corresponds to the intensity of the sound field produced by a monopole source in an infinite homogeneous space.

With a perfectly reflecting bottom, the capture angle is $\chi_* = \pi/2$, and Eq. (7) coincides with Eq. (5.53) of [1] if there is no loss in the sound propagation. Equation (7) can be readily obtained from formulas presented in Section 5.6 of [1] for the averaged sound intensity in shallow water. In doing so, one should assume that the number of reflections of the attenuated rays with $\chi > \chi_*$ is so large that they contribute nothing to the received signal.

The range dependence of intensity (7) implies that there is no sound attenuation for the rays corresponding to $\chi \le \chi_*$ and that the sound speed is constant in depth (the isovelocity Pekeris waveguide without bottom absorption). Equation (7) is valid for a great number of propagating modes, that is, for sufficiently short distances at which the attenuation and decay of higher modes can be neglected [1].

In the case of large-scale surface waves, the reflection coefficient is $|\mathcal{V}| = 1 - 2k^2\langle\eta^2\rangle\sin^2\chi$, where $\langle\eta^2\rangle$ is the squared surface deviation from the mean level [1]. The distance between consecutive reflections is $L \ge 2H/\tan\chi_*$. Thus, the distance between the source and the receiver should be sufficiently short for the relation $|\mathcal{V}|^N \simeq 1$ to be valid, where $N = |\mathrm{SO}|/L$. Hence, the following restriction on the distance SO must be imposed:

$$\frac{|\mathrm{SO}|}{H} < \frac{\cos\chi_*}{k^2\langle\eta^2\rangle\sin^2\chi_*}. \tag{8}$$

The experimental data discussed below satisfy inequality (8).

With a coherent summation of the contributions within the scattering area S, the time-averaged intensity I_s of the scattered signal is proportional to the squared surface deviation $\langle\eta^2\rangle$ multiplied by the squared area S and by $k^4\sin^2\chi_1\sin^2\chi_2$. The quantity I_s is also proportional to the intensity produced by the source in region A (Fig. 1). In view of Eq. (7) for the field decay, the integration over grazing angles $\chi_{1,2}$ leads to the expression

$$I_s = I_{00}\langle\eta^2\rangle\frac{k^4S^2}{16\pi^2H^2|\mathrm{SA}||\mathrm{AO}|}(2\chi_* - \sin 2\chi_*)^2. \tag{9}$$

Intensity (7) produced by the source at the reception point is $I_0 = \dfrac{2I_{00}\chi_*}{|\mathrm{SO}|H}$. The power spectral density I_s of the scattered field normalized to I_0 is given by the expression

$$\frac{I_s(\Omega)}{I_0} = \mathcal{P}(\Omega)f(\chi_*)\frac{\pi^2S^2|\mathrm{SO}|}{2\lambda^4H|\mathrm{SA}||\mathrm{AO}|}, \tag{10}$$

where $\mathcal{P}(\Omega)$ is the power spectral density of the surface waves at the frequency Ω, $f(\chi_*) = (2\chi_* - \sin 2\chi_*)^2/2\chi_*$.

If condition (1) of resonant scattering is satisfied for regions A or B (Fig. 1), the value of S is determined by the Fresnel sizes and is equal to $\sqrt{\lambda^2 \cdot |\mathrm{SA}| \cdot |\mathrm{AO}|}$. This expression is satisfied to the accuracy of a constant factor that is unity in its order of magnitude and the accounts for the orientation of region A relative to the source-to-receiver direction (see Appendix A). By substituting the area in Eq. (10) by the product of the Fresnel sizes, we arrive at expression (A9').

The assumptions accepted in deriving Eq. (10) have simple physical meaning. The independence of the results on distances |SA| and |AO| is caused, first, by the geometry of the wave front and, second, by the coherent nature of scattering: $I_s(\Omega) \propto S^2$. The dependence on the ratio $|\mathrm{SO}|/H$ is governed by the cylindrical symmetry of the wave front and by normalizing to the intensity of the incident wave at the reception point. In deriving Eqs. (10) and (A9), the sound attenuation was neglected. The monotone increase in the scattering level as a function of distance will be limited by the propagation loss and the loss due to the reflections from the bottom and the rough surface (see inequality (8)).

The experimental data presented below lead to a conclusion that the assumption on the coherent nature of sound scattering by wind waves is not as absurd as it seems at the first glance. In Section 3, we will return to considering the validity limits of the theoretical model proposed here.

2. RESULTS OF MEASUREMENTS

As we have mentioned in the Introduction, the acoustic measurements were carried out in the Baltic Sea and in a deep-water lake. In the lake experiment, the sound-signal reception was accompanied by measuring the hydrographic parameters: the wind speed and direction, the vertical displacements of the lake surface, the temperature distributions in depth, and the variations of the temperature field [6]. Therefore, in calculating the level of fluctuations caused by the waves on the lake surface, we used the measured power spectrum $\mathcal{P}(\Omega)$ of surface waves. This spectrum was not measured in the sea experiment. In analyzing the experimental records obtained in the sea, we used a model spectral function $\mathcal{P}(\Omega)$ in the Pierson–Moskowitz form [7]:

$$\mathcal{P}(\Omega) = \alpha g^{-3}V^5\left(\frac{g}{\Omega V}\right)^5\exp\left(-0.74\left(\frac{g}{\Omega V}\right)^4\right), \tag{11}$$

where $\alpha = 0.0041$, Ω is the cyclic frequency of surface roughness, V is the wind speed (in m/s), and g is the acceleration of gravity.

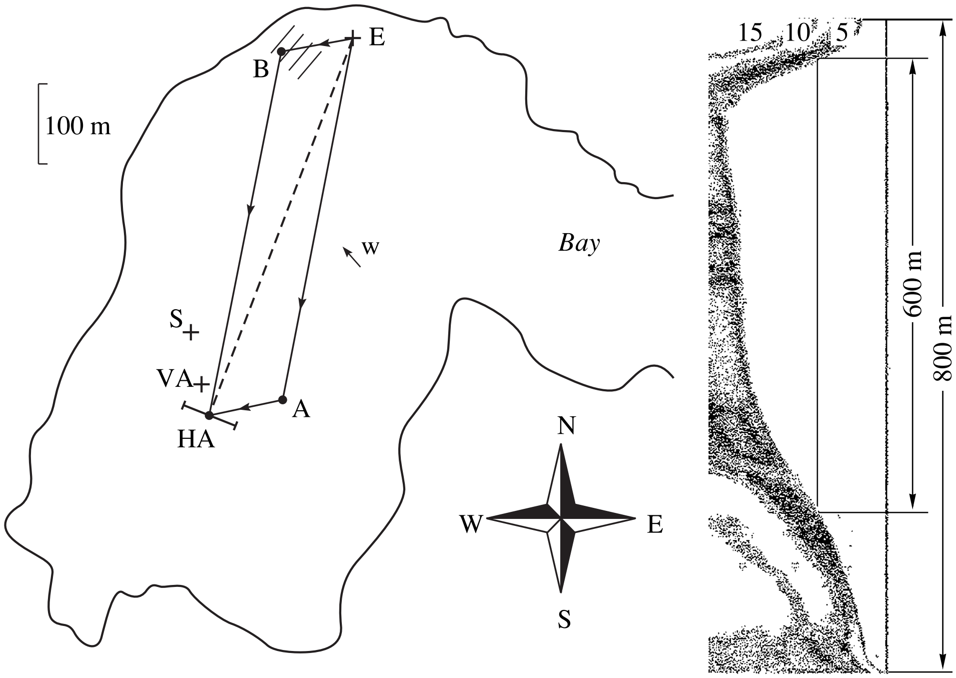

Fig. 2. Layout of the experiment on the Sankhar Lake. Symbol E denotes the position of the source placed at a depth of 9 m, 1 m above the bottom. Abbreviations VA and HA correspond to the vertical and horizontal antenna arrays, and S labels the sensor of surface waves. The resonant scattering areas are labeled by symbols A and B. The arrow labeled as w shows the direction of the southeast wind at the time of acoustic measurements.

2.1. Measurements on the Sankhar Lake

The Sankhar Lake is in the Vladimirskaya oblast of Russia. It is a rather deep-water lake, which was formed at the site of a karstic dip. The deep-water part of the lake has a size of 800 × 500 m, with a depth of 10–15 m. The maximal length of the lake, with allowance for a bay with a mean depth of 3–5 m, is 1.5 km. Figure 2 presents the map of the lake with approximate positions of the measuring systems. On the right, an echo-sounder record is presented, which was obtained in passing along the propagation path.

To obtain the values of surface displacements and their spectral levels, the measurements were performed with the use of a capacitance sensor (S in Fig. 2) that was fixed to the lake bottom. Sensor S was placed at a distance of about 50 m from the acoustic antenna arrays. The power spectral density of surface waves is presented in Fig. 3. The measurements of June 17, 1998 were performed during the day, with a stable southeast wind whose speed was 2.5 m/s and whose direction was constant during the recording time. The wind speed was measured at a height of 3 m above the lake surface.

The wind-wave spectrum (Fig. 3) measured at the Sankhar Lake differs from that of developed surface waves for an open sea (Eq. (11)). The specificity of the lake surface waves consists in the presence of spectral components with frequencies lower than g/V. Such components are caused by the finiteness of the basin and by the existence of low-frequency resonances in large-scale gravity waves (surface seiches), whose lengths are comparable with the characteristic size of the lake [6]. The measured spectral density of the surface displacements is adequately described by the dependence [8] $\mathcal{P}(\Omega) = \beta g^2\Omega^{-5}$ with $\beta = 0.0123$ (the dotted curve in Fig. 3). Such a dependence is valid for the equilibrium frequency band: $\Omega_{\max} \ll \Omega \ll \sqrt[4]{4g^3/\sigma} \simeq 15\ \mathrm{s}^{-1}$, where $\Omega_{\max} \sim g/V$ is the frequency corresponding to the maximum in the spectral density and σ is the coefficient of surface tension.

The spectral maximum “I” in Fig. 3 is shifted towards higher frequencies in comparison with Eq. (11), and the maximum “II” appears at the frequency corresponding to the synchronism between waves and wind. Such a spectrum shape has been observed earlier [8] and is well known for the case of short fetches. The difference between the measured and expected spectral levels in the domain of saturation can be attributed to a weak decrease in the value of β for shorter fetches. The experimental data [8] indicate that the value of β is doubled as the dimensionless fetch $\mathcal{L} = Lg/V^2$ decreases by a factor of 500. The value $\beta = 0.0123$ corresponds to $\mathcal{L} \sim 10^5$. In the experiments at hand, $\mathcal{L} \sim 10^2$.

The sound signals generated by the tonal source were received by horizontal and vertical antenna arrays, each of which consisted of 64 hydrophones. The length of both arrays was $L_a = 12$ m. The horizontal array was mounted at a depth of 7.5 m with the first hydrophone at 30 cm from the bottom. The distance between the

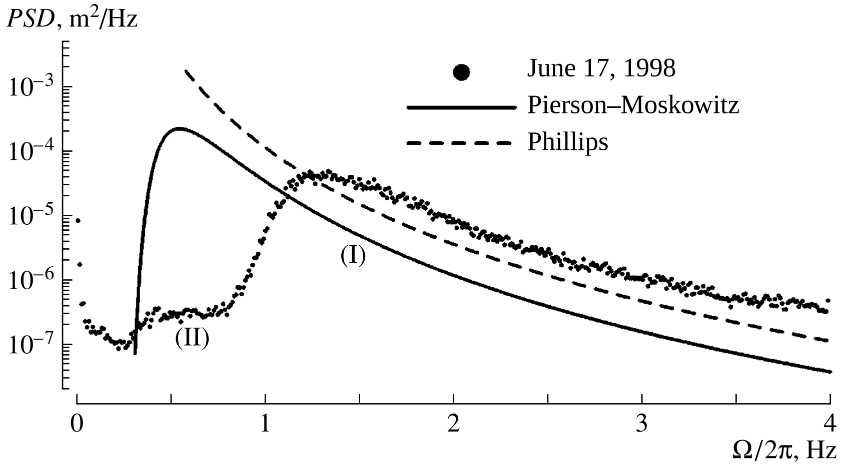

Fig. 3. Power spectral density of surface displacements. The dots indicate the experimental data for the lake measurements. The level of the instrumental noise (analog-to-digital converter and signal amplifier) is 10^{-8} m^2/Hz. The model spectrum (the solid curve) is calculated according to Eq. (11) for a wind speed $V = 2.5$ m/s. The dashed curve corresponds to the equilibrium spectrum.

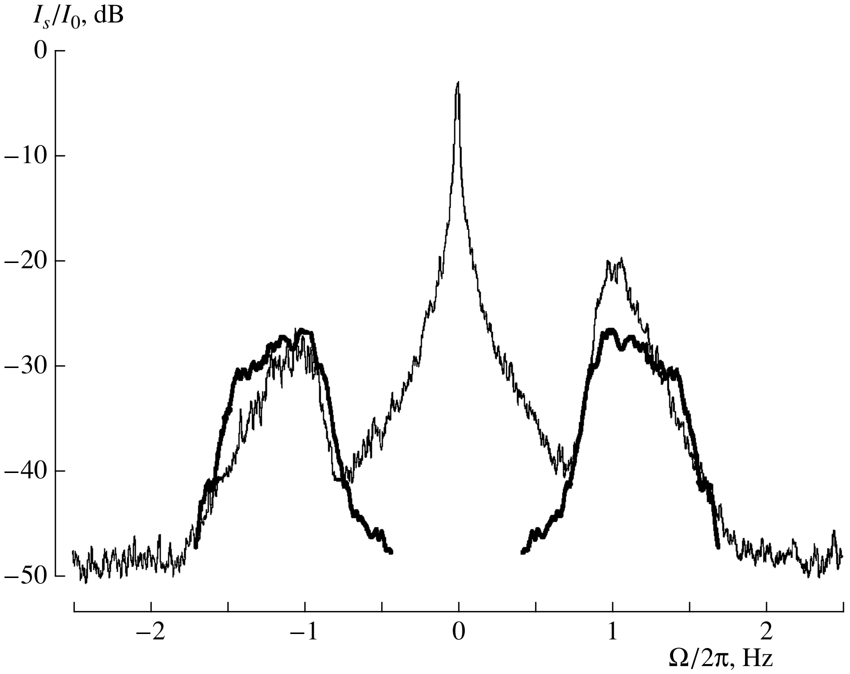

Fig. 4. Spectrum of the sound signal obtained by incoherent averaging over the 64 hydrophones of the horizontal array (omnidirectional reception). The calculated spectrum is shown by the thick curve.

arrays and the source was |SO| = 450 m. The mean lake depth was $H = 15$ m along the propagation path. The signals received by each hydrophone were heterodyned (at the frequency of transmission) and digitally filtered. The filter passband was 8 Hz, which allowed us to receive scattered signals with frequencies $|\Omega/2\pi| \le 4$ Hz. The experiment at the Sankhar Lake is described in more detail in [6, 9].

Figure 4 shows the spectra of the sound signals received by the hydrophones of the horizontal array for a transmission frequency of 1480.4 Hz. These data are obtained by incoherent summation over the hydrophones: such a method corresponds to an omnidirectional reception. By comparing the plots of Figs. 3 and 4, one can see that the spectrum of sound fluctuations is narrower than that of wind waves. The narrowing of the fluctuation spectrum relative to the surface spectrum has been mentioned by many researchers [10]. This phenomenon can be explained in terms of the resonant scattering. On the one hand, condition (1) cannot be sat-

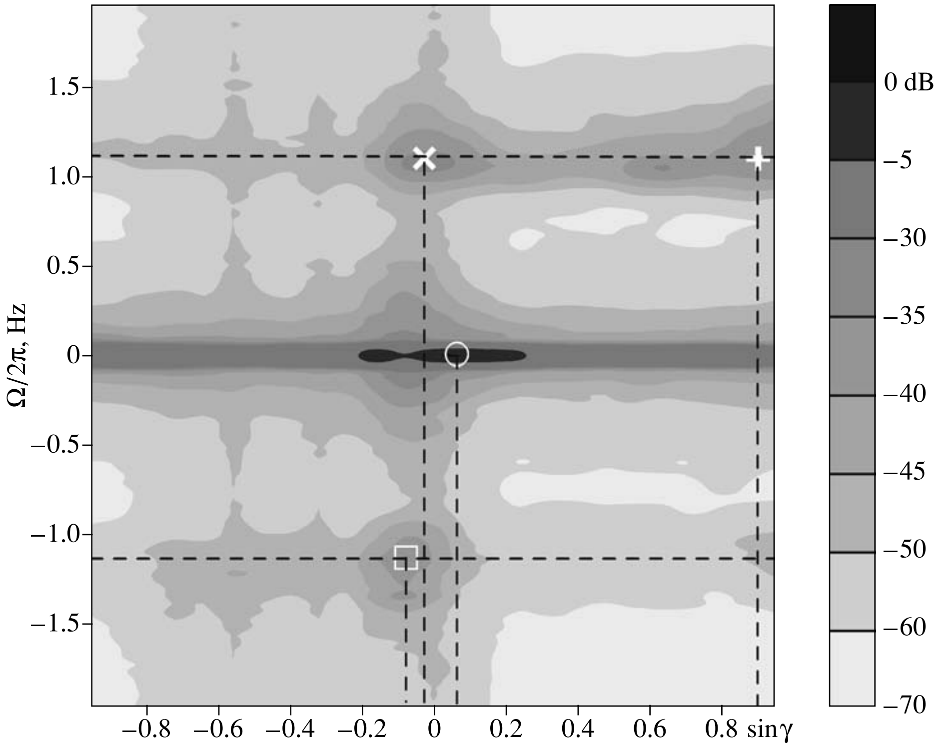

Fig. 5. Frequency-angular spectrum of the sound signal received by the horizontal array (averaged over 24 signal realizations). The circled area corresponds to the source position. Other marked areas correspond to scattering by surface waves.

isfied for frequencies of surface waves that are higher than 1.8 Hz ($\xi > 1$). On the other hand, the shores of the lake limit the allowable values of the angles θ_i and θ_s and additionally reduce the frequency band within which the scattering of type (1) can be observed.

Figure 5 shows the frequency-angular spectrum of the sound signal with a carrier frequency of 1480 Hz. Here, the domains that correspond to the source ($\Omega = 0$, $\gamma_0 \simeq 5°$) and to the scattering by the surface roughness are accentuated. Table 1 summarizes the measured angles θ_s of scattering and the angles θ_i and ϕ calculated according to Eq. (2). The domains labeled as "+" and "□" in Fig. 5 correspond to regions A and B in Fig. 2, respectively. The experimental value $\xi = \sin\left(\frac{\theta_s^{(+)} - \theta_s^{(-)}}{2}\right) = 0.57$ agrees well with the estimate $\xi \simeq 0.6$ (Table 1).

It is worth mentioning that the direction of the wave vector κ of the surface wave nearly coincided with the wind direction in the experiment: there was a stable wind from the south east (Fig. 2). Maxima labeled by symbols "×" and "□" in Fig. 2 correspond to region B that is close to the lake shore, opposite the bay (this region is indicated by dashes in Fig. 2). These maxima are more pronounced than those labeled by "+." The latter fact can be explained by the length of the fetch, which is greater for region B than for region A with south-east winds. The maximum "×" corresponds to the bearing θ_s that is close to that of the maximum "□," but with opposite sign of the Doppler frequency shift. The maximum "×" in the spatial-angular spectrum seems to be caused by the reflection of the surface wave from the nearby shore (Fig. 2, Table 1).

The sum of the levels for the signals scattered in the domains indicated in Fig. 4 is close to the levels of the modulation components with omnidirectional reception (Fig. 4). Hence, it is *local* areas of the lake surface that are responsible for the scattering by the rough surface.

Let us compare the measured levels of the modulation components (Fig. 4) with the estimates of Appendix A.

Table 1. Angles $\theta_s = -\gamma$ correspond to the maxima of the frequency-angular spectrum (Fig. 5). The quantities ϕ and θ_i are calculated according to Eq. (2). The angle θ_i for the maximum labeled as "×" is calculated with Eq. (3) at $\xi \simeq 0.6$, which corresponds to the maximum in the power spectrum of surface waves at the frequency $\Omega/2\pi \simeq 1.1$ Hz (Figs. 3 and 5) and to dispersion relation (A5). The experiments are performed for a small Rayleigh parameter: $\mathcal{R}_0 \simeq 9.3 \times 10^{-3}$ (the value of η^2 is obtained by integrating the measured power spectrum presented in Fig. 3)

Scattering area in Fig. 5	Angle θ_s, deg	Angle θ_i, deg	Angle ϕ, deg
"+" ($\Omega > 0$)	–59	+10	–114.5
"□" ($\Omega < 0$)	+10	–59	–114.5
"×" ($\Omega > 0$)	+6	–59.4	+57.3

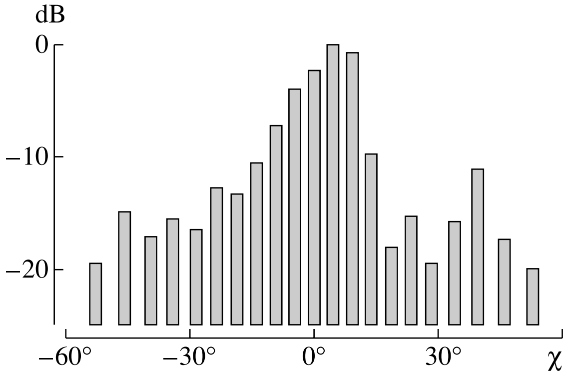

Fig. 6. Angular spectrum of the sound signal received by the vertical array. The signals are incoherently averaged over five frequencies of transmission around 1.5 kHz: 1459, 1470, 1480, 1491, and 1502 Hz.

First of all, note that propagating modes with low grazing angles correspond to the experimental conditions. The angular spectrum of the sound signal received by the vertical array is shown in Fig. 6. According to this figure, 90% of the energy comes from directions $|\chi| \leq 35°$. Such values for the angle agree with the estimate of the critical angle χ_* for a sandy lake bottom with c_b = 1800 m/s: $\chi_* = \arccos(c/c_b) \simeq 34°$.

The calculation of the modulation components illustrated by Fig. 4 was carried out according to Eq. (A9') with $\chi_* = 35°$, H = 15 m, and $|SO|$ = 450 m, under the assumption that the angular spectrum of wind waves is narrow. The measured power spectrum $\mathcal{P}(\Omega)$ of wind waves (Fig. 3) was used in the calculations. The estimates obtained from the formulas of Appendix A agree well with the measurements.

Note the difference in the levels of the modulation components for the frequencies $\Omega > 0$ and $\Omega < 0$. This difference seems to be caused by the difference in the amplitudes of the surface oscillations in the vicinity of the scattering areas of the lake (Fig. 5). It is clear that local features in the surface spectrum can be governed by the closure of the basin and by the influence of the lake shores. It is advantageous to analyze the spectra of acoustic fluctuations caused by sea surface waves.

2.2. Measurements in the Baltic Sea

For sound sources, bottom-moored tonal transducers with frequencies of 200–400 Hz and acoustic power of 0.1–1 kW were used in the sea experiments. The direct and scattered signals were received by a linear horizontal antenna array consisting of 32–64 hydrophones spaced at 3 m (the maximal length of the arrays used was 200 m). The arrays were stationary mounted at levels that were 1/3 to 1/2 of the sea depth. The main objective of experimenting in the Baltic Sea was to estimate the ultimate capability of the coherent signal processing [9]. Therefore, weather conditions with the lowest sea states were chosen. Table 2 presents the description of the sea propagation paths on which the acoustic measurements were performed. The data presented in Table 2 demonstrate the variability of wind speeds during experimentation.

Figure 7 shows the frequency-angular spectra that were used to determine the areas responsible for the resonant scattering by the surface roughness. In the sea experiment, the scattering patches are more clearly localized than in the lake (compare with the data of Fig. 5). There are no maxima produced by reflections of surface waves from the shores, and two domains of increased scattering levels exist in the spectrum. Positive and negative Doppler shifts correspond to these two domains. In Fig. 7, the arrows indicate the positions of the max-

Table 2. Experimental conditions on fixed propagation paths in the Baltic Sea. The expected values of $\left|\theta_s^{(+)} - \theta_s^{(-)}\right|$ are calculated according to Eq. (3) for the value of Λ that corresponds to the frequency of the maximum in the power spectrum of surface waves and to dispersion relation (A5). The maximal value of the Rayleigh parameter corresponds to path 1: $\mathcal{R}_0$ = 0.11 (the value of $\langle\eta^2\rangle$ is obtained by integrating Eq. (11))

Ordinal number	(1)	(2)	(3)	(4)	(5)
Date of measurements	Sep. 9, 1990	Aug. 23, 2001	Sep. 15, 1998	Aug. 26, 2001	Sep. 13, 1990
Path length, km / Mean depth, m	1.5 / 80	3 / 60	8 / 60	27 / 53	10 / 80
Transmitted frequency, Hz / Number of hydrophones	206.1 / 64	246 / 48	420.17 / 32	246 / 48	237.5 / 64
V, m/s	5–8	1–4	3–5	2–6	3–4
Frequency of modulation maximum $\Omega_{\max}/2\pi$, Hz	±0.18	±0.24	±0.315	±0.33	±0.4
Value of $\xi(\Omega_{\max})$	0.07	0.11	0.11	0.2	0.32
$\left\|\theta_s^{(+)} - \theta_s^{(-)}\right\|$ measured / expected	8.4° / 8.5°	14.3° / 13°	14.3° / 13°	18.4° / 24.2°	–

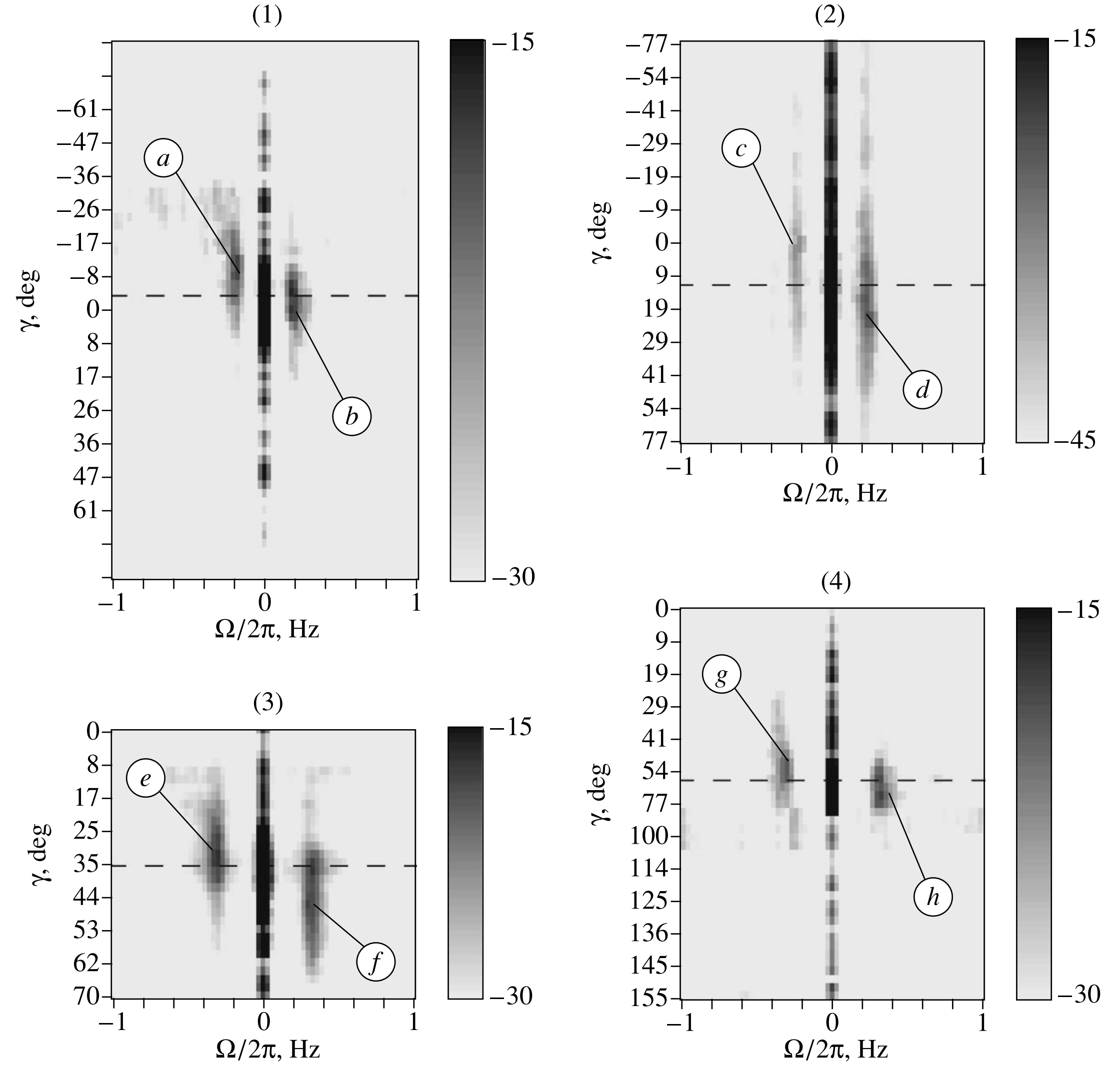

Fig. 7. Frequency-angular spectrum of fluctuations in the Baltic Sea. The brightness scale indicates the power spectral density of the sound signal in decibels. The horizontal dashed lines indicate the angular positions of the sound source relative to the normal to the horizontal linear array. The arrows indicate the positions of the maxima in the power spectrum of the scattered signal.

ima of the fluctuation level. The measured values of the scattering angles are presented in Table 3.

According to Table 3, the wind direction was nearly perpendicular to the acoustic propagation path. Such an orientation corresponds to the layouts of measurements 1–4. The values of ξ (Table 2) correspond to a narrow angular sector (record no. 4) of the directions of vector κ, in which the conditions of resonant scattering are met. Record no. 5 was obtained at low sea state, when the direction of surface waves noticeably differed

Table 3. Positions and amplitudes of maxima in the frequency-angular spectra (Fig. 7)

	Marked domains							
	a	*b*	*c*	*d*	*e*	*f*	*g*	*h*
γ_0	–4.2°		+11.7°		+34.8°		+58.6°	
γ_s	–10.5°	–2.1°	+4.7°	+19°	+32.3°	+46.6°	+50.8°	+69.2°
$\theta_s = -(\gamma_s - \gamma_0)$	–6.3°	+2.1°	–7°	+7.3°	–2.5°	+11.8°	–7.8°	+10.6°
ϕ	+87.9°		+90.2°		+94.7°		+91.4°	
I_s/I_0, dB	–24°	–23°	–37°	–29°	–22°	–22°	–27°	–26°

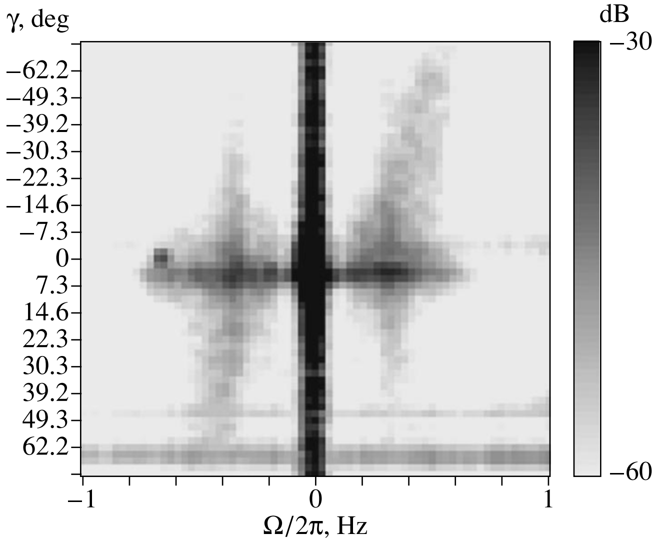

Fig. 8. Frequency angular spectrum of the sound signal on path 5 (Table 2). The modulation components with frequencies of wind waves are spread, and the localization of the scattering areas on the wavy surface cannot be observed.

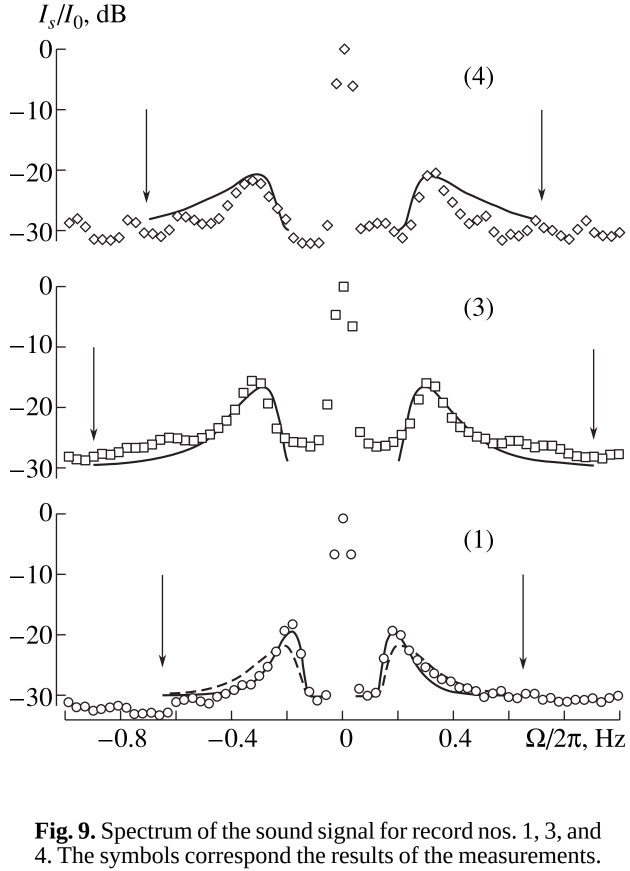

Fig. 9. Spectrum of the sound signal for record nos. 1, 3, and 4. The symbols correspond the results of the measurements. The solid and dashed curves correspond to the calculations by Eqs. (A9) and (A9'), respectively. The function $\mathcal{P}(\Omega)$ was specified by Eq. (11). The wind speed V was 6.5, 4.1, and 3.9 m/s for record nos. 1, 3, and 4, respectively. The arrows show the frequencies starting from which condition (1) of resonant scattering is violated.

from the normal to the acoustic propagation path. In this case, according to Fig. 8, the scattered signal manifests itself as fuzzy and asymmetrical domains of increased signal level in the band of surface-wave frequencies.

Suppose that, just as in the lake, the bottom of the Baltic Sea leads to a decay of modes with grazing angles higher than $\chi_* \sim 30°–40°$. Let us compare the measured scattering levels with the theoretical estimates of Appendix A. Figure 9 shows the spectra $I_s(\Omega)$ of the fluctuations for record nos. 1, 3, and 4. The spectra are obtained by incoherently averaging the signals received by the hydrophones of the horizontal array with the normalization to I_0. In the sea experiments, the hydrological parameters were not measured. Therefore, the spectrum of surface waves was defined by the model dependence (11). The wind speed changed over a wide range (Table 2), and the value of V appearing in Eq. (11) was specified so that the frequency of the maximum in the power spectrum corresponded to the experimental data.

The sector of angles ϕ that allow for condition (1) to be met is narrow. Therefore, let us estimate the fluctuation levels for a spatial spectrum of form $\delta(\phi - \pi/2)$ with $\chi_* = 35°$. In the experiment, the level of noise in the receiving channel was –30 dB relative to the value of I_0. To make the data more illustrative, to the calculated values of I_s/I_0 (Fig. 9) we added a value of 0.001 that corresponded to the instrumental noise.

According Fig. 9, a satisfactory agreement exists between the levels measured in the experiment and calculated by Eqs. (A9) and (A9'). This agreement persists for different distances between the source and the receiver, at different depths, and at different sound frequencies. It is worth mentioning that, as the distance between the sound source and the receiving system increases (record nos. 1, 3, and 4), the calculated and measured scattering levels begin to differ from each other at modulation frequencies that are higher than the frequency $\Omega_{\max}$ corresponding to the maximum in the power spectrum of surface waves.

3. DISCUSSION OF THE RESULTS

Let us discuss the data obtained. The acoustic measurements in the lake and in the Baltic Sea, together with the calculations performed, show that the signal of a concentrated source is scattered by local areas of the surface to produce the sound fluctuation at the receiver. This conclusion is true when the frequencies are low and the lengths of the surface and acoustic waves are comparable. The sizes of the scattering surface areas are determined by the sizes of the first Fresnel zones with respect to the source and the receiving system. The calculated levels of the fluctuations proved to be close to those measured in both the lake and the sea.

There are no experimental data for long propagation paths and high wind speeds. That is why we cannot determine the validity limits for the proposed method of estimating the levels of fluctuations caused by coherent sound scattering by a wavy surface. According to the data of Section 1, the functional dependences (A9) of the fluctuation levels can be obtained by using the energy considerations while taking into account the character of the field decay in the waveguide and the fact that the scattering area is limited by the Fresnel sizes. Estimation of the integral in Eq. (A6) by the stationary phase method implies that the spectral components of $\mathcal{P}(\Omega)$ are produced by a regular spatial distribution of surface displacements. Note that record nos. 3 and 4 are obtained in similar weather conditions (Table 2) and with similar wind directions (Table 3). At the same time, Fig. 9 shows that, for record no. 4, the estimated scattering levels are 5–10 dB higher than the measured levels for the frequencies $\Omega > \Omega_{\max}$. The decrease in the measured scattering level, in comparison with the estimate (A9) for the angular surface spectrum of the form $\delta(\phi - \phi_0)$, can be explained, first, by the broadening of the spectrum at the frequencies $\Omega > \Omega_{\max}$ [11, 12] and, second, by the degradation of the surface coherence for large sizes of the scattering area.

Because measurements 3 and 4 were performed under similar weather conditions, one can assume that the angular distributions of vectors κ weakly differ in these two cases. According to Fig. 9, the experimental data of record no. 3 agree with the calculations in the entire band of the surface-wave frequencies. The decrease in the level of fluctuations under the influence of the broadened angular spectrum at $\Omega > \Omega_{\max}$ depends on the distance |SO| due to the factor $\mathcal{C} = \frac{l_1 l_2}{\lambda\sqrt{r_0 r_s(r_0, \theta_0)}}$ in Eq. (A8). The value of $\mathcal{C}$ is close to unity (compare the solid and dotted curves in Fig. 9) and weakly depends on the coordinates of the stationary-phase point (hence, on the angle ϕ as well). Therefore, for record no. 4, the disagreement between the calculation and the experiment can be hardly explained by the broadening of the angular surface spectrum at the frequencies $\Omega > \Omega_{\max}$.

Let us estimate the size of the scattering surface area relative to the length of the surface wave: $n = D/\Lambda(\Omega_{\max})$. For the Baltic experiment, the sizes D of the Fresnel zones are $D_1 \sim 75$, $D_3 \sim 120$, and $D_4 \sim 290$ m for paths 1, 3, and 4, respectively. The values of n are $n_1 \sim 1.6$, $n_3 \sim 8$, and $n_4 \sim 20$ for these paths. The values of n_1 and n_3 are rather small, which, presumably, accounts for the highly localized scattering areas in Fig. 7 and for the good agreement between the measured and calculated levels of fluctuations (Fig. 9). The value $n_* \sim$ 10–20 seems to be a characteristic length of the train of surface waves. If $n > n_*$, the spatial distribution of the deviations of the surface S in Eq. (10) becomes irregular, and the coherence of the secondary sources responsible for the scattering decreases. The maximal distance |SO| between the source and the receiver at which the scattering is coherent is $\max|\mathrm{SO}| \simeq n_*^2 \Lambda^2(\Omega_{\max})/\lambda$.

Equations (A9) and (A9') can be used with minimal information on the experimental conditions, namely, the transmitted frequency, the distance from the source to the receiver, the mean depth along the propagation path, and the angle of total internal reflection by the bottom.

It is advantageous to analyze experimental data on shallow-sea sound propagation for broader ranges of the speed and direction of wind, the transmitted frequency, the distance |SO|, and the angle χ_*. Such an analysis would allow one to determine the scale of spatial coherence for surface waves and to establish the validity limits for Eqs. (A9) and (A9').

ACKNOWLEDGMENTS

This work was supported by the CRDF, project no. RPO-1346. We are grateful to J.N. Kemarskaya for assistance in processing the data of the acoustic measurements and to V.V. Bredikhin and A.V. Tsiberov for assistance in performing the experiment and in the primary processing of the experimental data.

APPENDIX A.
POSITIONS AND SIZES OF RESONANT SCATTERING AREAS

The Rayleigh parameters were small in the experiments. Therefore, one can use the small-perturbation method. According to this method, the distribution of the secondary dipole sources that are caused by the small-scale surface roughness can be related to the height of the surface waves in the following way [1]:

$$p_s(r, \theta, z, t)\big|_{z=0} = -\frac{\partial p_0(r, \theta, z, t)}{\partial z}\bigg|_{z=0} \eta(r, \theta, t). \quad \text{(A1)}$$

Here, (r, θ, z) are the distance, direction, and depth in a cylindrical coordinate system with the z axis passing through the sound source; $p_0(\cdot)$ is the distribution of sound pressure generated by the source; and $\eta(\cdot)$ is the distribution of surface roughness, which, being averaged over time, yields $\overline{\eta(r, \theta, t)}^t = 0$. Thus, $z = 0$ is the unperturbed surface. The quantity $\eta(r, \theta, t)$ is supposed to be a stationary uniform process.

Let us consider a monopole source with capacity Q. The pressure field generated by this source can be represented in the form of a series [13]:

$$\begin{aligned} & p_0(r, \theta, z, t) \\ & = \frac{-i\omega\rho Q}{4}\left[\sum_{m=0}^{\infty} H_0^{(1)}(\kappa_m r)\psi_m(z)\psi_m(z_0)\right]\exp(-i\omega t), \end{aligned} \quad \text{(A2)}$$

where ω is the frequency of transmission, ρ is the water density, and $H_0^{(1)}(\cdot)$ is the Hankel function of the zeroth order (an isotropic monopole radiation) and of the first kind. The use of the Hankel function corresponds to the omnidirectional monopole source and satisfies the Zommerfeld radiation condition (below, we omit the index "1" in the Hankel function). In Eq. (A2), κ_m denotes the horizontal projection of the wave vector corresponding to the mth mode for the waveguide with the pressure distribution $\psi_m(z)$ in depth. The basis $\psi_m(z)$ is supposed to be orthonormalized, and the functions $\psi_m(z)$ themselves satisfy the boundary conditions and the differential equation $\psi''_m(z) + (\omega^2/c^2(z) - \kappa_m^2)\psi(z) = 0$, where $c(z)$ is the sound speed profile. The horizon z_0 corresponds to the depth of the source.

To calculate the pressure field generated by the distributed dipole sources (A1), we use Green's function for the power source. As a result, the field of the sources (Eq. (A1)) is represented as an integral of the convolution type:

$$\begin{aligned} &p_s(R, z, t) \\ &= \frac{\omega\rho Q}{16}\exp(-i\omega t) \\ &\times\int_0^{\infty}\int_0^{2\pi}\sum_{m,n=0}^{\infty}[H_0(\kappa_m r)H_0(\kappa_n r_s(r, \theta)) \\ &\times\psi'_m(0)\psi_m(z_0)\psi_n(z)\psi'_n(0)\eta(r, \theta, t)]rdrd\theta, \end{aligned} \tag{A3}$$

where $r_s(r, \theta) = \sqrt{R^2 + r^2 - 2Rr\cos\theta}$ and R is the source-to-receiver distance (|SO| in Fig. 1).

It is the squared field characteristic, namely, the scattered intensity $I_s = \overline{|p_s|^2}^t$ that must to be found. The surface roughness is a statistically uniform and stationary. Therefore, by changing to the power spectral density and supposing the spatial distribution to be regular at each frequency Ω of the surface wave, we arrive at the following expression for $\hat{I}_s(\Omega)$:

$$\begin{aligned} \hat{I}_s(\Omega) &= \left(\frac{\omega\rho Q}{16}\right)^2 \\ &\times\mathcal{P}(\Omega)\int_0^{\infty}rdr\int_0^{\infty}\tilde{r}d\tilde{r}\int_0^{2\pi}d\theta\int_0^{2\pi}d\tilde{\theta}\int_0^{2\pi}d\phi\sum_{m,n=0}^{\infty}\sum_{lq=0}^{\infty}H_0(\kappa_m r) \\ &\times H_0(\kappa_n r_s(r, \theta))H_0^*(\kappa_l\tilde{r})H_0^*(\kappa_q\tilde{r}_s(\tilde{r}, \tilde{\theta})) \\ &\times\mathcal{A}(\Omega, \phi)\exp[i\kappa(r\cos(\theta - \phi) - \tilde{r}\cos(\tilde{\theta} - \phi))] \\ &\times\psi'_m(0)\psi_m(z_0)\psi_n(z)\psi'_n(0)\psi'_l(0)\psi_l(z_0)\psi_q(z)\psi'_q(0). \end{aligned} \tag{A4}$$

Here, $(\cdot)^*$ denotes complex conjugation, $\hat{I}_s(\Omega)$ is the power spectral density of scattering, Ω is the modulation frequency (the frequency of wind waves, $\Omega \ll \omega$), $\mathcal{P}(\Omega)$ is the power spectral density of wind waves, and $\mathcal{A}(\Omega, \phi)$ is the angular spectrum of surface waves with the normalization $\int_0^{2\pi}\mathcal{A}(\Omega, \phi)d\phi = 1$ for all frequencies Ω. The wave number of the surface waves, $\kappa = 2\pi/\Lambda$, is determined by the dispersion relation for gravity waves. In deep water ($\Lambda \ll H$, where H is the depth), we have [14]

$$\kappa = \Omega^2/g, \tag{A5}$$

where g is the acceleration of gravity.

The Hankel function of the first order has a weak logarithmic singularity, which makes a small contribution to the quantity I_s in integration (below, it will be shown that this statement is true when the conditions of resonant scattering are met). Let us assume that the main contribution to integral (A4) comes from areas that are far from the source and the receiver. Then, one can replace the Hankel function by its asymptotic expansion [15]: $H_0(x) \simeq \sqrt{2/\pi x}\exp(+i(x - \pi/4))$, $x \gg 1$.

To specify the model for the waveguide, we use the Pekeris waveguide [1, 13]. At long distances from the source in such a waveguide, the wave numbers $\kappa_m/k > c/c_b$ (where c_b is the sound speed in the bottom) correspond to undamped modes (or to weakly attenuated modes if the loss in the bottom is present). Let us perform averaging over the interference structure. Such an approach is justified if many modes propagate in the waveguide. Then, to calculate the functions $\psi'_m(0)$, we specify the functions $\psi_m(z)$ as $\psi_m(z) \simeq \sqrt{2/H}\sin\zeta_m z$, $\zeta_m = \pi(2m + 1)/2H$, which correspond to a waveguide with an acoustically stiff bottom. Equation (A4) can be represented as follows:

$$\begin{aligned} \frac{\hat{I}_s(\Omega)}{I_0} &= \frac{8\pi^2R^3}{\lambda^4H\chi_*}\mathcal{P}(\Omega)\int_0^{\chi_*}d\chi_1\int_0^{\chi_*}d\chi_2\int_0^{2\pi}d\phi \\ &\times\Bigg\{\sin^2\chi_1\sin^2\chi_2\mathcal{A}(\Omega, \phi) \\ &\times\left|\int_0^{+\infty}\varepsilon d\varepsilon\int_{-\pi}^{+\pi}d\theta\frac{\exp(i\mu\mathcal{S}(\varepsilon, \theta))}{\varepsilon^{1/2}\sqrt[4]{1 + \varepsilon^2 - 2\varepsilon\cos\theta}}\right|^2\Bigg\}, \end{aligned} \tag{A6}$$

where $\mu = k_0R \gg 1$ and $\varepsilon = r/R$. Upon averaging over the interference structure, the intensity of the unperturbed field produced by the source will be $I_0 = \dfrac{\omega^2\rho^2Q^2}{8\pi^2RH}\chi_*$. The phase function $\mathcal{S}(\varepsilon, \theta)$ in the integral of Eq. (A6) is determined by the following expression ($\xi = \lambda/2\Lambda$): $\mathcal{S}(\varepsilon, \theta) = \varepsilon(\cos\chi_1 + 2\xi\cos(\theta - \phi)) + \cos\chi_2\sqrt{1 + \varepsilon^2 - 2\varepsilon\cos\theta}$.

Let us estimate integral (A6) with the use of the stationary phase method [13] by assuming that $\mu \gg 1$. It can be shown that the position of the point of the stationary phase is determined by the conditions of resonant (Bragg) scattering. Let us determine the centers $(\varepsilon_0, \theta_0)$ of the regions that are responsible for resonant scattering together with their sizes (l_1, l_2):

$$\frac{\partial\mathcal{S}}{\partial\varepsilon} = \cos\chi_1 + 2\xi\cos(\theta_0 - \phi) + \frac{(\varepsilon_0 - \cos\theta_0)\cos\chi_2}{\sqrt{1 + \varepsilon_0^2 - 2\varepsilon_0\cos\theta_0}} = 0,$$

$$\frac{1}{\varepsilon}\frac{\partial\mathcal{S}}{\partial\theta} = -2\xi\sin(\theta_0 - \phi) + \frac{\cos\chi_2\sin\theta_0}{\sqrt{1 + \varepsilon_0^2 - 2\varepsilon_0\cos\theta_0}} = 0.$$

In the vicinity of the point $(\varepsilon_0, \theta_0)$, the phase variations are determined by the quadratic form: $\mathcal{S}(\varepsilon, \theta) - \mathcal{S}(\varepsilon_0, \theta_0) = a_{11}x^2 + 2a_{12}xy + a_{22}y^2 = \frac{\partial^2\mathcal{S}}{\partial\varepsilon^2}x^2 + 2\frac{1}{\varepsilon_0}\frac{\partial^2\mathcal{S}}{\partial\theta\partial\varepsilon}xy + \frac{1}{\varepsilon_0^2}\frac{\partial^2\mathcal{S}}{\partial\theta^2}y^2$, where $x = \varepsilon - \varepsilon_0$ and $y = \varepsilon_0(\theta - \theta_0)$. The quantities a_{ij} are given by the expressions

$$a_{11} = \frac{\sin^2\theta_0\cos\chi_2}{(1 + \varepsilon_0^2 - 2\varepsilon_0\cos\theta_0)^{3/2}},$$

$$a_{12} = -\frac{(\varepsilon^2 - \cos\theta_0)\cos\chi_2\sin\theta_0}{(1 + \varepsilon_0^2 - 2\varepsilon_0\cos\theta_0)^{3/2}},$$

$$a_{22} = -\frac{2\xi\cos(\theta_0 - \phi)}{\varepsilon_0} + \frac{\cos\chi_2(2\cos\theta_0(1 + \varepsilon_0^2) - (3 + \cos2\theta_0)\varepsilon_0)}{2\varepsilon_0(1 + \varepsilon_0^2 - 2\varepsilon_0\cos\theta_0)^{3/2}}.$$

After rotating the coordinate system through an angle α that is defined as $\tan2\alpha = -2a_{12}/(a_{22} - a_{11})$, the quadratic form $\|a_{ij}\|$ becomes diagonal, so that $\mathcal{S}(\varepsilon, \theta) - \mathcal{S}(\varepsilon_0, \theta_0) = \tilde{a}_{11}\tilde{x}^2 + \tilde{a}_{22}\tilde{y}^2$ and $\tilde{a}_{11} = a_{11}\cos^2\alpha + a_{12}\sin2\alpha + a_{22}\sin^2\alpha$, $\tilde{a}_{22} = a_{11}\sin^2\alpha - a_{12}\sin2\alpha + a_{22}\cos^2\alpha$. If the points of stationary phase exist ($\varepsilon_0 > 1$, $\mathrm{Im}(\theta_0) = 0$), the equal phase lines are ellipses in the vicinity of $(\varepsilon_0, \theta_0)$. The semiaxes of the ellipses are determined from the condition that the phase changes by π: $l_1 = \sqrt{\lambda R/2\tilde{a}_{11}}$, $l_2 = \sqrt{\lambda R/2\tilde{a}_{22}}$. The quantity $\sqrt{\lambda R}$ is equal to the size of the first Fresnel zone with respect to the source, and the integral can be calculated as

$$\left|\int_{-\infty}^{+\infty}\exp(i\mu\tilde{a}_{jj}\tau^2)d\tau\right| = \sqrt{\frac{\pi}{\mu\tilde{a}_{jj}}} = \frac{l_j}{R}. \quad \text{(A7)}$$

Thus, the resonant scattering by surface roughness occurs within spatially localized surface areas with sizes that are determined by the first Fresnel zones. After simple transformations in light of Eq. (A7), integral (A6) takes the form

$$\frac{\hat{I}_s(\Omega)}{I_0} = \frac{8\pi^2}{\lambda^4 RH\chi_*}\mathcal{P}(\Omega) \times \int_0^{\chi_*}d\chi_1\int_0^{\chi_*}d\chi_2\int_0^{2\pi}\frac{\mathcal{A}(\Omega, \phi)l_1^2l_2^2\sin^2\chi_1\sin^2\chi_2}{\varepsilon_0\sqrt{1 + \varepsilon_0^2 - 2\varepsilon_0\cos\theta_0}}d\phi. \quad \text{(A8)}$$

If the capture angle of the waveguide is small, $\chi_* \ll 1$, the trigonometric functions in integral (A8) can be replaced with their asymptotic expansions with a small argument: $\cos\chi_1 \simeq 1$, $\cos\chi_2 \simeq 1$, $\sin\chi_1 \simeq \chi_1$, and $\sin\chi_2 \simeq \chi_2$. Then, Eq. (A8) can be integrated over the grazing angles $\chi_{1,\,2}$. To calculate the integral over ϕ, one should specify the angular spectrum of surface waves. Many models [1, 7, 8] exist for the angular distribution $\mathcal{A}(\Omega, \phi)$. Near the maximum of the power spectrum, the spatial spectrum is narrow, with a pronounced maximum in the direction of the wind [11, 12]. For the sake of simplicity, let us assume the surface spectrum to be infinitely narrow, so that $\mathcal{A}(\Omega, \phi) = \delta(\phi - \phi_0)$, and the wind direction ϕ_0 to be such as will allow for the existence of the stationary-phase point (the conditions of resonant scattering are met). Then, Eq. (A8) is simplified ($r_0 = R\varepsilon_0$, $r_s(r_0, \theta_0) = R\sqrt{1 + \varepsilon_0^2 - 2\varepsilon_0\cos\theta_0}$):

$$\frac{\hat{I}_s(\Omega)}{I_0} = \frac{\pi^2Rf(\chi_*)}{2\lambda^2H}\frac{l_1^2l_2^2}{\lambda^2r_0r_s(r_0, \theta_0)}\mathcal{P}(\Omega), \quad \text{(A9)}$$

where $f(\chi) = (2\chi - \sin2\chi)^2/\chi \simeq 16\chi^5/9$. It can be shown that the quantity $\mathcal{C} = \frac{l_1l_2}{\lambda\sqrt{r_0r_s(r_0, \theta_0)}}$ is close to unity, and significant deviations from unity occur if the resonant scattering areas are near the source or the receiver. Evidently, such situations cannot be described by Eq. (A8), because this equation is obtained by using the high-frequency asymptotic form of the Hankel functions (κ_mr_0, $\kappa_mr_s \gg 1$). Therefore, Eq. (A9) can be simplified:

$$\frac{\hat{I}_s(\Omega)}{I_0} \simeq \frac{\pi^2Rf(\chi_*)}{2\lambda^2H}\mathcal{P}(\Omega) \approx \left.\frac{8\pi^2R\chi_*^5\mathcal{P}(\Omega)}{9\lambda^2H}\right|_{\chi_* \ll 1}. \quad \text{(A9')}$$

REFERENCES

1. L. M. Brekhovskikh and Yu. P. Lysanov, *Fundamentals of Ocean Acoustics* (Gidrometeoizdat, Leningrad, 1982; Springer, New York, 1991).
2. S. M. Flatte, R. Dasen, W. H. Munk, K. M. Watson, and F. Zachariasen, *Sound Transmission through a Fluctuating Ocean*, Ed. by S. Flatte (Cambridge Univ. Press, New York, 1979; Mir, Moscow, 1982).
3. *Ocean Acoustics*, Ed. by J. A. DeSanto (Springer, Berlin, 1979).
4. E. Yu. Gorodetskaya, A. I. Malekhanov, A. G. Sazontov, and N. K. Vdovicheva, in *The Formation of Acoustic Fields in Oceanic Waveguides*, Ed. by V. A. Zverev (Inst. Prikl. Fiz. Ross. Akad. Nauk, Nizhni Novgorod, 1998), Vol. 1 [in Russian].
5. C. S. Hayek, I. W. Schurman, J. H. Sweeney, and C. A. Boyles, J. Acoust. Soc. Am. **105**, 2129 (1999).
6. V. V. Bredikhin, A. V. Lebedev, and B. M. Salin, Preprint No. 490, IPF RAN (Inst. of Applied Physics, Russian Academy of Sciences, Nizhni Novgorod, 1999).
7. M. M. Zaslavskiĭ and A. S. Monin, in *Physics of the Ocean*, Ed. by V. M. Kamenkovich and A. S. Monin (Nauka, Moscow, 1978), Vol. 2, p. 146 [in Russian].
8. O. M. Phillips, *Dynamics of the Upper Ocean* (Cambridge Univ. Press, Cambridge, 1966; Gidrometeoizdat, Leningrad, 1980).
9. V. A. Zverev, P. I. Korotin, A. L. Matveev, *et al.*, Akust. Zh. **47**, 227 (2001) [Acoust. Phys. **47**, 184 (2001)].
10. L. M. Brekhovskikh and Yu. P. Lysanov, in *Physics of the Ocean*, Ed. by V. M. Kamenkovich and A. S. Monin (Nauka, Moscow, 1978), Vol. 2, p. 49 [in Russian].
11. Sheng-Chang Wen, Pei-Fang Guo, and Da-Cuo Zhang, J. Oceanogr. **49**, 131 (1993).
12. Sheng-Chang Wen, Pei-Fang Guo, Da-Cuo Zhang, *et al.*, J. Oceanogr. **49**, 149 (1993).
13. L. M. Brekhovshikh, *Waves in Layered Media*, 2nd ed. (Nauka, Moscow, 1973; Academic, New York, 1980).
14. L. D. Landau and E. M. Lifshitz, *Course of Theoretical Physics*, Vol. 6: *Fluid Mechanics*, 4th ed. (Nauka, Moscow, 1988; Pergamon, New York, 1987).
15. G. A. Korn and T. M. Korn, *Mathematical Handbook for Scientists and Engineers*, 2nd ed. (McGraw-Hill, New York, 1968; Nauka, Moscow, 1984).

Translated by E. Kopyl

Acoustical Physics, Vol. 50, No. 6, 2004, pp. 717–720. Translated from Akusticheskiĭ Zhurnal, Vol. 50, No. 6, 2004, pp.827–830.
Original Russian Text Copyright © 2004 by Maĭzel’.

The Total Acoustic Impedance of a Prolate Spheroid Performing Transverse Oscillatory Movements

A. B. Maĭzel’
Krylov Shipbuilding Research Institute, Russian Academy of Sciences,
Moskovskoe sh. 44, St. Petersburg, 196158 Russia
e-mail: krylov@krylov.spb.ru

Received January 22, 2004

Abstract—Using the theory of spheroidal wave functions, the total acoustic impedance is determined for a prolate spheroid performing transverse translational and rotational oscillatory movements. Expressions for the radiation resistance, the added mass, and the added moment of inertia are derived. It is shown that, in the low-frequency approximation, this mass and moment of inertia reach limiting values identical to hydrodynamic ones. The components of the total acoustic impedance are calculated for spheroids of different relative thicknesses at an arbitrary frequency. © *2004 MAIK “Nauka/Interperiodica”.*

In solving the problems of sound radiation by bodies of spheroidal shape, it is necessary to determine their radiation resistances and the added liquid masses. It is of interest to compare these quantities with the results of solving a similar classical problem for an oscillating sphere. The present paper is devoted to the determination of the radiation resistance, the added mass, and the added moment of inertia of a prolate spheroid performing transverse oscillatory movements by means of determining its total acoustic impedance. Let us denote the longitudinal axis of the spheroid by z and consider harmonic translational movements of the spheroid along the x axis and its rotational movements about the y axis (Fig. 1). In this paper, the dependence of the oscillatory processes on time t is assumed to have the form $\exp(-j\omega t)$, where ω is the angular frequency.

Expressions for the total acoustic impedance of a spheroid performing oscillations along the x axis with a linear velocity V_x or rotations about the y axis with an angular velocity ω_y, Z_x, or Z_y have the form [1]

$$Z_x = \frac{F_x}{V_x} = R_x - j\omega M_x,$$
$$Z_y = \frac{M_y}{\omega_y} = R_y - j\omega I_y, \qquad (1)$$

respectively. Here, F_x and M_y are the driving force and moment with which the spheroid acts on the liquid when the two aforementioned types of oscillatory motion take place, R_x and R_y are the respective radiation resistances, M_x is the added mass of the liquid in the case of translational oscillations of the spheroid, and I_y is the added moment of inertia of the liquid mass in the case of rotational movement.

The driving force and moment can be determined by integrating the pressures produced in the liquid by the oscillating spheroid (denote this pressure by p_x) or by the rotating spheroid (p_y) over the spheroid surface:

$$F_x = \int_s p_x \cos(n, x)\,ds,$$
$$M_y = -\int_s p_y[\cos(n, z)x - \cos(n, x)z]\,ds. \qquad (2)$$

Here, **n** is the outer normal to the spheroid surface; the direction cosines are given by the formulas

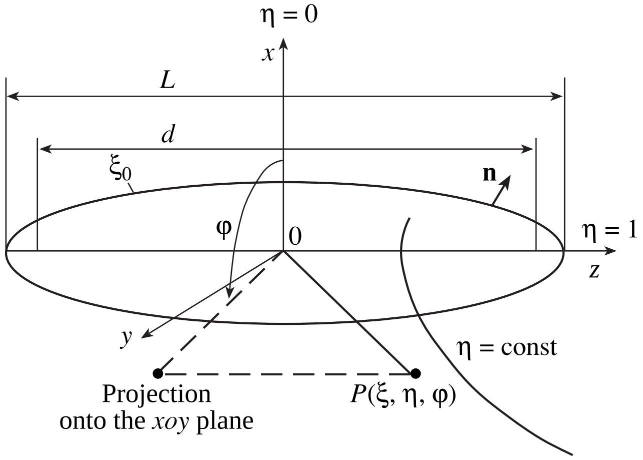

Fig. 1. Geometry of the problem and the prolate spheroidal coordinate system.

1063-7710/04/5006-0717$26.00 © 2004 MAIK “Nauka/Interperiodica”

$$\cos(n, x) = \xi\sqrt{\frac{1-\eta^2}{\xi^2-\eta^2}}\cos\varphi,$$

$$\cos(n, z) = \eta\sqrt{\frac{\xi^2-1}{\xi^2-\eta^2}}; \qquad (3)$$

$$ds = \frac{d^2}{4}\sqrt{(\xi^2-1)(\xi^2-\eta^2)}\,d\eta\, d\varphi;$$

ξ, η, φ are the prolate spheroid coordinates [1]; and d is the focus spacing of the spheroid (Fig. 1).

The pressures produced by the spheroid performing oscillatory movements can be sought in the form of a series:

$$p_{x,y} = \sum_{n=1}^{\infty} P_{x,y} R_{1\text{n}}^{(3)}(h, \xi) S_{1\text{n}}(h, \eta)\cos\varphi, \qquad (4)$$

that satisfies the radiation condition at infinity. In Eq. (4), $R_{1\text{n}}^{(3)}(h, \xi)$ are the prolate radial spheroidal functions of the third kind, $S_{1\text{n}}(h, \eta)$ are the prolate angular spheroidal functions, $h = kd/2$ is the wave size of the spheroid, and k is the wave number of sound in the liquid. This approach is conventionally used in solving similar problems (see, e.g., [2]). The unknown coefficients $P_{x,y}$ can be determined from the boundary condition at the spheroid surface:

$$V_\text{n} = \frac{1}{jk\rho c}\frac{\partial p}{\partial n} = \frac{1}{jk\rho c}\frac{1}{g_\xi}\frac{\partial p}{\partial \xi}, \quad \xi = \xi_0, \qquad (5)$$

where V_n is the normal component of the velocity amplitude, ρ is the density of the liquid, c is the velocity of sound in it, and g_ξ is the metric tensor element expressed as [1]

$$g_\xi = \frac{d}{2}\sqrt{\frac{\xi^2-\eta^2}{\xi^2-1}}.$$

The normal velocity component V_n is related to the velocity V_x by the formula

$$V_\text{n} = V_x\cos(n, x).$$

When the spheroid performs rotational oscillations about the y axis, the linear velocity of the points of its surface along the x axis is

$$V_x = \omega_y z = \omega_y\frac{d}{2}\xi_0\eta.$$

The presence of the factor $\cos\varphi$ in the direction cosine $\cos(n, x)$ given by Eq. (3) corresponds to the geometry of the problem under study and dictates the choice of precisely this type of dependence on φ in Eq. (4).

Let us substitute the latter formulas and Eqs. (3) and (4) into boundary condition (5), multiply its both sides by the function $S_{1k}(h, \eta)$, and integrate them over η from –1 to +1. Then, using the orthogonality property of the prolate angular spheroidal functions [1],

$$\int_{-1}^{+1} S_{mn}(h, \eta) S_{mk}(h, \eta)\, d\eta = \begin{cases} N_{mn}(h), & k = n \\ 0, & k \neq n, \end{cases}$$

we determine the coefficients $P_{x,y}$ from expansion (4) for both translational and rotational movements of the spheroid. After performing the aforementioned procedures, we arrive at the following results:

$$p_x = V_x\frac{4}{3}jh\rho c\frac{\xi_0}{\sqrt{\xi_0^2-1}}\cos\varphi$$

$$\times\sum_{n=1,3,\dots}^{\infty}\frac{d_0^{1n}(h) R_{1\text{n}}^{(3)}(h, \xi) S_{1\text{n}}(h, \eta)}{N_{1\text{n}}(h) R_{1\text{n}}^{(3)'}(h, \xi_0)},$$

$$p_y = \omega_y\frac{2}{5}jh\rho c\frac{d\xi_0^2}{\sqrt{\xi_0^2-1}}\cos\varphi \qquad (6)$$

$$\times\sum_{n=2,4,\dots}^{\infty}\frac{d_1^{1n}(h) R_{1\text{n}}^{(3)}(h, \xi) S_{1\text{n}}(h, \eta)}{N_{1\text{n}}(h) R_{1\text{n}}^{(3)'}(h, \xi_0)}.$$

Here, $d_0^{1n}(h)$ and $d_1^{1n}(h)$ are the expansion coefficients for the prolate angular spheroidal function expansions in terms of the associated Legendre functions [1].

Now, substituting expressions (6) into Eqs. (1)–(3), we obtain the desired expressions for the total acoustic impedance:

$$Z_x = \frac{2\pi}{9}j\omega\rho\xi_0^2 d^3\sum_{n=1,3,\dots}^{\infty}\frac{[d_1^{1n}(h)]^2 R_{1\text{n}}^{(3)}(h, \xi_0)}{N_{1\text{n}}(h) R_{1\text{n}}^{(3)'}(h, \xi_0)} \qquad (7)$$

for an oscillating spheroid and

$$Z_y = \frac{\pi}{50}j\omega\rho\xi_0^2 d^5\sum_{n=2,4,\dots}^{\infty}\frac{[d_0^{1n}(h)]^2 R_{1\text{n}}^{(3)}(h, \xi_0)}{N_{1\text{n}}(h) R_{1\text{n}}^{(3)'}(h, \xi_0)}$$

for a rotating spheroid.

The radiation resistances and the added mass and moment of inertia can be derived from these series either analytically (in the low-frequency approximation) or by numerical calculation (for an arbitrary frequency). Assuming that the wave size of the spheroid

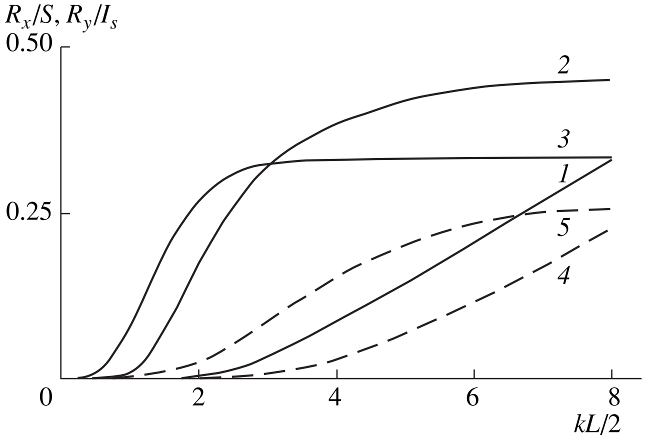

Fig. 2. Radiation resistance of a spheroid as a function of its wave half-length: (*1*) an oscillating spheroid, R_x/S, $\xi_0 = 1.01$; (*2*) an oscillating spheroid, R_x/S, $\xi_0 = 1.1$; (*3*) an oscillating sphere, R_x/S; (*4*) a spheroid performing rotational oscillatory movements, R_y/I_s, $\xi_0 = 1.01$; and (*5*) a spheroid performing rotational oscillatory movements, R_y/I_s, $\xi_0 = 1.1$.

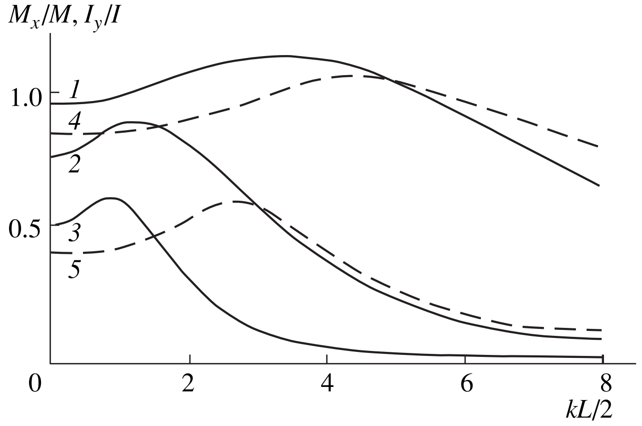

Fig. 3. Added mass and moment of inertia of a spheroid as functions of its wave half-length: (*1*) an oscillating spheroid, M_x/M, $\xi_0 = 1.01$; (*2*) an oscillating spheroid, M_x/M, $\xi_0 = 1.1$; (*3*) an oscillating sphere, M_x/M; (*4*) a spheroid performing rotational oscillatory movements, I_y/I, $\xi_0 = 1.01$; and (*5*) a spheroid performing rotational oscillatory movements, I_y/I, $\xi_0 = 1.1$.

tends to zero, from Eq. (7) with the use of [1, 3], we obtain

$$\begin{aligned} \lim_{h\to 0} Z_x &= \frac{\pi}{6} j\omega\rho\xi_0^2 d^3 \frac{Q_1^1(\xi_0)}{Q_1^{1'}(\xi_0)} = -j\omega\lambda_{11}, \\ \lim_{h\to 0} Z_y &= \frac{\pi}{120} j\omega\rho\xi_0^2 d^5 \frac{Q_2^1(\xi_0)}{Q_2^{1'}(\xi_0)} = -j\omega\lambda_{55}, \end{aligned} \tag{8}$$

where $Q_1^1(\xi_0)$ and $Q_2^1(\xi_0)$ are the associated Legendre functions of the second kind; λ_{11} is the added mass of the liquid in the case of a uniform motion of the spheroid along the x axis, which is widely used in hydrodynamics [3]; and λ_{55} is a similar added moment of inertia of the liquid mass in the case of a uniform rotation of the spheroid about the y axis [3]. From Eq. (8) one can see that, in the low-frequency limit, acoustics and hydrodynamics yield identical descriptions for the added masses of a spheroid performing oscillatory movements while its radiation resistances tend to zero.

In the higher frequency region, the radiation resistance, the added mass, and the added moment of inertia of the spheroid can be determined by calculating the real and imaginary parts of Eq. (7) and comparing them with Eq. (1). However, unlike the hydrodynamic approximation, owing to the use of the spheroidal wave functions these quantities should depend on frequency and should take into account the wave motion of the liquid. The calculations were performed using the tables of spheroidal wave functions [4–6]. The results of the calculations were normalized as follows:

(i) R_x, by the spheroid surface area S calculated as

$$S = \frac{\pi d^2}{2}\sqrt{\xi_0^2 - 1}\left(\sqrt{\xi_0^2 - 1} + \xi_0^2 \arcsin\frac{1}{\xi_0}\right);$$

(ii) R_y, by the moment of inertia of the spheroid surface area with respect to the y axis, which is equal to

$$\begin{aligned} I_s = \frac{\pi d^4}{64}\sqrt{\xi_0^2 - 1}\Big[&\xi_0^2(\xi_0^4 + 5\xi_0^2 - 4)\arcsin\frac{1}{\xi_0} \\ &- \sqrt{\xi_0^2 - 1}(\xi_0^4 - 5\xi_0^2 + 2)\Big]; \end{aligned}$$

(iii) M_x, by the mass of the floating spheroid whose density is equal to the density of the liquid,

$$M = \frac{\pi}{6}\rho d^3 \xi_0(\xi_0^2 - 1);$$

(iv) I_y, by the moment of inertia of the floating spheroid with respect to the y axis,

$$I = \frac{\pi}{120}\rho d^5 \xi_0(\xi_0^2 - 1)(2\xi_0^2 - 1).$$

Figures 2 and 3 show the calculated components of the total acoustic impedance for two spheroids of different relative thickness as functions of the wave half-length of the spheroid $kL/2$, where L is the spheroid length. The first spheroid is characterized by $\xi_0 = 1.01$ (a length-to-width ratio of 7.12), and the second spheroid, by $\xi_0 = 1.1$ (a length-to-width ratio of 2.40). For comparison, the same figures show the data from similar calculations for an oscillating sphere as a function of its wave radius (in the case of rotational oscillatory movements of the sphere, the radiation resistance and the added moment of inertia are equal to zero). Using the plots shown in Figs. 2 and 3, it is possible, from a given wave size of a spheroid, to determine the radiation resistance of the latter and its added mass or moment of inertia.

REFERENCES

1. E. Skudrzyk, *The Foundations of Acoustics. Basic Mathematics and Basic Acoustics* (Springer, New York, 1971; Mir, Moscow, 1976), Vol. 2.
2. Z. Ye and E. Hoskinson, J. Acoust. Soc. Am. **103**, 822 (1998).
3. N. E. Kochin, I. A. Kibel’, and N. V. Roze, *Theoretical Hydromechanics* (Gostekhizdat, Leningrad, 1948), Part 1 [in Russian].
4. C. Flammer, *Spheroidal Wave Functions* (Stanford Univ. Press, Stanford, 1957; Vychisl. Tsentr Akad. Nauk SSSR, Moscow, 1962), CIV.
5. *Tables of Spheroidal Wave Functions and Their First Derivatives*, Ed. by V. I. Krylov (Nauka i Tekhnika, Minsk, 1976), Vol. 1 [in Russian].
6. *Spheroidal Wave Functions*, Ed. by J. A. Stratton, P. M. Morse, L. J. Chu, *et al.* (Technology Press of MIT and Wiley, New York, 1956), XIV.

Translated by E. Golyamina

Acoustical Physics, Vol. 50, No. 6, 2004, pp. 721–724. Translated from Akusticheskiĭ Zhurnal, Vol. 50, No. 6, 2004, pp. 831–835.
Original Russian Text Copyright © 2004 by Pushkina.

Nonlinear Wave Interactions in Porous Media Filled with a Quantum Fluid

N. I. Pushkina
Research Computing Center, Moscow State University, Vorob'evy gory, Moscow, 119992 Russia
e-mail: N.Pushkina@mererand.com

Received January 28, 2004

Abstract—The problem of the nonlinear interaction between the fourth sound and an acoustic wave propagating in a porous medium filled with superfluid helium is solved. Based on the Landau equations of quantum fluid dynamics and on the Biot theory of mechanical waves in a porous medium, nonlinear wave equations are derived for studying the aforementioned interaction. An expression is obtained for the vertex that determines the excitation of an acoustic wave by two waves of the fourth sound. The possibility of an experimental observation of this process is estimated. *© 2004 MAIK "Nauka/Interperiodica".*

Fluid-filled porous media are the object of intensive studies, both experimental and theoretical. This is explained not only by the scientific interest in revealing the physical properties of these complex systems but also by the technological significance of such media. In studying the dynamics of a porous medium, the use of superfluid helium as a liquid for filling the pores proves to be rather effective (see, e.g., [1–5]). If the transverse size of the capillaries of a porous medium is comparable to the mean free path of excitations or is smaller than it, a situation is realized in which, in the course of wave propagation in helium, the normal component of the superfluid is decelerated and becomes stationary with respect to the solid component of the porous medium. This is the well-known effect of fourth sound in superfluid helium (see, e.g., [6, 7]). According to the Biot theory [8–10] of the acoustics of fluid-filled porous solids, such media are characterized by the presence of two independent oscillation branches: the so-called fast and slow compressional waves. While the slow wave often represents a strongly attenuated relaxation oscillation with the solid and liquid components moving in antiphase, the fast wave is, in essence, a common sound wave with the solid and liquid components moving almost in phase. In [11] it was shown that, in the context of a porous medium, the fourth sound in liquid helium is equivalent to the slow wave of the Biot theory, which in this case is not a strongly damped wave but an essentially undamped wave, because it only includes the motion of the superfluid component containing no excitation gas. Various problems of linear wave propagation, including the propagation of the fourth sound, in porous media filled with superfluid helium are also considered in [12]. The velocity of the slow wave (the fourth sound) c_1 in a disordered porous medium differs from the velocity of the fourth sound in a straight capillary u_1 (which, at sufficiently low temperatures, is equal to the velocity of the first sound in helium to a fair degree of accuracy): $c_1 \approx u_1/\alpha^{1/2}$, where α is the structure constant from the Biot theory. This constant takes into account the complex geometry of a porous medium with nonstraight channels (pores), which considerably changes the acoustic path. The slow and fast oscillation branches of a porous medium are independent in the linear approximation. When the wave intensities are sufficiently high, nonlinear interactions between these two branches may manifest themselves.

The purpose of the present study is to consider the nonlinear interaction between the slow wave (fourth sound) and the fast (acoustic) wave in a porous medium filled with a superfluid. Until now, no such studies have been carried out. Meanwhile, nonlinear wave interactions may provide valuable information on the parameters of the medium that govern these processes and on the properties of the excitations and physical phenomena that underlie the interactions of interest. In addition, by taking into account the nonlinear phenomena, one gains a better insight into the phenomena observed in experiments with waves of relatively high intensities.

To solve the problem of nonlinear wave interaction in a porous medium filled with a quantum fluid, let us use the superfluid helium II equations [13] together with the Biot theory of mechanical waves in porous media [8–10]. The nonlinear equations of a superfluid in application to narrow capillaries can be represented in the form

$$\begin{gathered}\frac{\partial \rho}{\partial t} + \operatorname{div}\mathbf{j} = 0,\\ \frac{\partial \mathbf{v}_s}{\partial t} + \nabla\left(\frac{v_s^2}{2} + \mu\right) = 0, \qquad (1)\\ \frac{\partial(\rho s)}{\partial t} + \operatorname{div}(\rho s \mathbf{u}) = 0.\end{gathered}$$

Here, ρ is the density of helium; $\mathbf{j}$ is the density of the mass flux density of the liquid; ρ_s and $\mathbf{v}_s$ are the density and velocity of the superfluid component; μ is the chemical potential; s is the entropy per unit mass; and $\mathbf{u}$ is the velocity of the normal component of superfluid helium, which in the given case coincides with the velocity of the capillary wall, i.e., with the velocity of the solid phase of the porous medium. For the differential of the chemical potential μ, the following relation is valid [13]:

$$d\mu = -s\,dT + \frac{1}{\rho}dP - \frac{\rho_n}{\rho}(\mathbf{u}-\mathbf{v}_s)d(\mathbf{u}-\mathbf{v}_s),$$

where P is the pressure in the superfluid and ρ_n is the density of the normal component. Therefore, the second equation of system (1), correct to the quadratic nonlinearity in the velocities, can be represented in the form

$$\frac{\partial \mathbf{v}_s}{\partial t} + \frac{1}{\rho}\nabla P - s\nabla T + \frac{1}{2}\nabla v_s^2 - \frac{\rho_n}{2\rho}\nabla(\mathbf{u}-\mathbf{v}_s)^2 = 0.$$

Note that, according to [14], in a fourth sound wave in He^4 the relative amplitude of the temperature oscillations is much smaller than the relative amplitude of the pressure oscillations:

$$T'/T_0 = \kappa P'/P_0,$$

where T_0 and P_0 are equilibrium values of temperature and pressure and the coefficient is $\kappa \sim -10^{-4}$ at $T \approx 1.5$K. Therefore, in the problem under consideration, we can ignore the temperature oscillations. Moreover, it is known that, at sufficiently low temperatures, the density of the normal component is much smaller than the density of the superfluid component. For example, already at $T = 1.5$K, we have $\rho_n \approx 0.1\rho_s$. Hence, with reasonable accuracy, we can assume that $\rho_s \approx \rho$ ($\rho = \rho_n + \rho_s$). In this case, we can ignore the last equation of system (1), which is the equation of entropy conservation, the entropy transfer being associated with normal motion. Below, the velocity of the superfluid component $\mathbf{v}_s$ is everywhere denoted as $\mathbf{v}$.

Equation (1) is written for the case of a straight channel. For a disordered porous medium, the equations should be modified according to the Biot theory [8], taking into account the geometry of the pores. The Biot equations complemented with nonlinear terms have the form

$$\begin{gathered}\rho_{11}\frac{\partial v}{\partial t} + \frac{1}{2}\rho_{11}\frac{\partial v^2}{\partial x} + \rho_{12}\frac{\partial u}{\partial t} + \frac{1}{2}\rho_{12}\frac{\partial u^2}{\partial x} = -m\frac{\partial P}{\partial x}, \\ \rho_{22}\frac{\partial u}{\partial t} + \frac{1}{2}\rho_{22}\frac{\partial u^2}{\partial x} + \rho_{12}\frac{\partial v}{\partial t} + \frac{1}{2}\rho_{12}\frac{\partial v^2}{\partial x} \\ = \frac{\partial \sigma_{xx}}{\partial x} - (1-m)\frac{\partial P}{\partial x}.\end{gathered} \tag{2}$$

Equations (2) are represented in one-dimensional form, because such a consideration is sufficient for revealing the essential features of the nonlinear interactions discussed below. In these equations, v and $u - x$ are the x components of the particle velocities of the liquid and solid phases; m is the porosity of the medium;

$$\begin{gathered}\rho_{11} = \alpha m\rho, \quad \rho_{12} = -(\alpha-1)m\rho, \\ \rho_{22} = (1-m)\rho_m + (\alpha-1)m\rho,\end{gathered} \tag{3}$$

where ρ_m is the density of the solid phase and α is the structure constant; σ_{xx} is the effective stress in the porous medium; in the linear approximation [15],

$$\sigma_{xx}^l = \left(k + \frac{4}{3}\tilde{\mu}\right)U_{xx} + \frac{k}{k_s}P_l, \tag{4}$$

where k and k_s are the bulk moduli of the frame and its constituent grains, respectively; $\tilde{\mu}$ is the shear modulus of the frame; U_{xx} is the frame strain tensor; and P_l is the linear part of pressure in the liquid, which is determined by the relations [16]

$$\begin{gathered}P_l = G^{-1}\xi - F\,\mathrm{div}\mathbf{U}, \\ G = \frac{1-m}{k_s} + \frac{m}{k_f} - \frac{k}{k_s^2}, \quad F = \left(1 - \frac{k}{k_s}\right)G^{-1}, \\ \xi = m\,\mathrm{div}(\mathbf{U}-\mathbf{V}).\end{gathered} \tag{5}$$

Here, k_f is the bulk modulus of the liquid phase, $\mathbf{V}$ is the displacement of the liquid, $\mathbf{U}$ is the displacement of the frame, and ξ is the liquid volume flowing into the volume element of the medium or out of it. Note that, in reality, the bulk modulus of liquid helium k_f is much smaller than the bulk modulus of the solid phase k_s. Therefore, in the case under consideration, $G \approx m/k_s$, provided that m is not too close to zero. In relation (5), it is convenient to change from the variables ξ and $\mathbf{U}$ to the variables $\delta\rho$ and $\delta\rho_m$:

$$P_l = G^{-1}\left(\frac{m}{\rho}\delta\rho + \frac{\nu}{\rho_m}\delta\rho_m\right), \tag{6}$$

where $\nu = 1 - m - k/k_s$. Equation (2) does not involve the Biot frequency correlation function taking into account the viscous loss due to the relative motion of phases, because the superfluid component of the quantum fluid has no viscosity. Generally speaking, if the density of the normal component is not neglected, the absorption of the fourth sound is caused by the viscous mechanisms of dissipation and by heat conduction. However (see, e.g., [17]), the contribution of heat conduction is vanishingly small compared to the viscous loss, and the main mechanism of viscous absorption is the slip of the normal component relative to the walls of the channels. The value of the absorption coefficient for the fourth sound is virtually zero at sufficiently low temperatures $T < 1.2$–1.5 K [17]. The absorption of a wave propagating in the solid phase because of the friction inside the frame and other possible mechanisms can theoretically be described by replacing the bulk moduli and the shear moduli of the frame by operators describing the inelastic response of the solid component of the porous medium [16, 18]. Below, it is noted that the absorption inside the frame has virtually no effect on the development of the nonlinear interactions discussed in this paper.

The first equation of system (2) corresponds to the second equation of system (1). Equation (2) should be complemented with continuity equations for the liquid and solid phases:

$$\begin{gathered}\frac{\partial}{\partial t}m\rho + \frac{\partial}{\partial x}m\rho v = 0,\\ \frac{\partial}{\partial t}(1-m)\rho_m + \frac{\partial}{\partial x}(1-m)\rho_m u = 0.\end{gathered} \tag{7}$$

The first of these equations, written for an ordinary liquid, corresponds to the first equation of system (1) for the superfluid with allowance for the fact that, at the temperatures under consideration, $\rho_s \approx \rho$ (as was noted above).

Taking into account the nonlinear terms up to the quadratic ones in systems of equations (2) and (7), we reduce these equations to the form

$$\begin{gathered}\frac{\partial^2\rho}{\partial t^2} - \frac{u_1^2}{\alpha}\frac{\partial^2\rho}{\partial x^2} - \frac{\alpha-1}{\alpha}\frac{\rho}{\rho_m}\frac{\partial^2\rho_m}{\partial t^2} - \frac{\nu}{m}\frac{\rho}{\rho_m}\frac{u_1^2}{\alpha}\frac{\partial^2\rho_m}{\partial x^2}\\
= -\frac{\alpha-1}{\alpha}\frac{\rho}{\rho_m^2}\frac{\partial}{\partial t}\left(\delta\rho_m\frac{\partial\rho_m}{\partial t}\right) + \frac{\alpha-1}{\alpha}\frac{\rho}{\rho_m}\frac{\partial}{\partial t}\left(u\frac{\partial\rho_m}{\partial x}\right)\\
+ \rho\frac{\partial^2 v^2}{\partial x^2} - \frac{\alpha-1}{\alpha}\frac{\partial}{\partial x}\left(\delta\rho\frac{\partial u}{\partial t}\right) - \frac{1}{2}\frac{\alpha-1}{\alpha}\rho\frac{\partial^2 u^2}{\partial x^2} + \frac{1}{\alpha}\frac{\partial^2 P_n}{\partial x^2},\\
\frac{\partial^2\rho_m}{\partial t^2}\left[1 + (\alpha-1)\frac{m}{1-m}\frac{\rho}{\rho_m}\right] - c_2^2\frac{\partial^2\rho_m}{\partial x^2}\\
-(\alpha-1)\frac{m}{1-m}\frac{\partial^2\rho}{\partial t^2} - \frac{\nu}{1-m}u_1^2\frac{\partial^2\rho}{\partial x^2}\\
= (\alpha-1)\frac{m}{1-m}\frac{\partial}{\partial t}\left(v\frac{\partial\rho}{\partial x}\right) - (\alpha-1)\frac{m}{1-m}\frac{1}{\rho}\frac{\partial}{\partial t}\left(\delta\rho\frac{\partial\rho}{\partial t}\right)\\
-(\alpha-1)\frac{m}{1-m}\frac{\rho}{\rho_m}\frac{\partial}{\partial t}\left(u\frac{\partial\rho_m}{\partial x}\right)\\
+(\alpha-1)\frac{m}{1-m}\frac{\rho}{\rho_m^2}\frac{\partial}{\partial t}\left(\delta\rho_m\frac{\partial\rho_m}{\partial t}\right)\\
+(\alpha-1)\frac{m}{1-m}\frac{\partial}{\partial x}\left(\delta\rho\frac{\partial u}{\partial t}\right) - (\alpha-1)\frac{m}{1-m}\frac{\partial^2}{\partial x\partial t}(\delta\rho v)\\
-(\alpha-1)\frac{m}{1-m}\rho\frac{\partial^2 v^2}{\partial x^2}\\
+\rho_m\left[1 + \frac{1}{2}(\alpha-1)\frac{m}{1-m}\frac{\rho}{\rho_m}\right]\frac{\partial^2 u^2}{\partial x^2}\\
+\frac{\nu}{1-m}\frac{\partial^2 P_n}{\partial x^2} - \frac{1}{1-m}\frac{\partial^2\sigma_{xx}^n}{\partial x^2}.\end{gathered} \tag{8}$$

Here, the nonlinear terms are present on the right-hand sides of the equations; c_2 is the velocity of the sound branch; the nonlinear parts of pressure P_n and stress tensor σ_{xx}^n are the subsequent quadratic terms of expansions for Eqs. (6) and (4), respectively.

Before solving the nonlinear problem, let us continue to the normal oscillations Θ (the slow wave) and Φ (the sound branch) in the respective linear equations:

$$\begin{gathered}\delta\rho = \Theta - \frac{\alpha-1}{\alpha}\frac{\rho}{\rho_m}\Phi,\\ \delta\rho_m = -\frac{m\alpha}{1-m}\left(\frac{\alpha-1}{\alpha} + \frac{\nu}{m}\right)\frac{c_1^2}{c_2^2}\Theta + \Phi.\end{gathered} \tag{9}$$

Consider the nonlinear interaction of three waves: two waves of the fourth sound, (Ω_1, q_1) and (Ω_2, q_2), and the fast compressional wave (the acoustic wave) (ω, k), for which the relations $\omega = \Omega_1 + \Omega_2$ and $\mathbf{k} = \mathbf{q}_1 + \mathbf{q}_2$ are valid. The fourth sound velocity c_1 is much smaller than the acoustic wave velocity c_2, and, correct to the velocity ratio c_1/c_2, we have $\Omega_1 \approx \Omega_2 \approx \omega/2$; $k = q_1 - q_2 \ll q_1, q_2$ (the case of interaction along a straight line; the wave (Ω_2, q_2) is an inverse wave). We seek the solution to the system of nonlinear equations (8) in the form of a sum of three waves:

$$\begin{gathered}\delta\rho = \frac{1}{2}\sum_{j=1,2}\Theta_j e^{i(\mathbf{q}_j\mathbf{r} - \Omega_j t)}\\
-\frac{1}{2}\left(\frac{\alpha-1}{\alpha}\frac{\rho}{\rho_m} + \lambda\right)\Phi e^{i(\mathbf{kr} - \omega t)} + \text{c.c.},\\
\delta\rho_m = \frac{1}{2}\sum_{j=1,2}\left[-\frac{m\alpha}{1-m}\left(\frac{\alpha-1}{\alpha} + \frac{\nu}{m}\right)\frac{c_1^2}{c_2^2} + \epsilon_j\right]\\
\times\Theta_j e^{i(\mathbf{q}_j\mathbf{r} - \Omega_j t)} + \frac{1}{2}\Phi e^{i(\mathbf{kr} - \omega t)} + \text{c.c.}\end{gathered} \tag{10}$$

Here, λ and ϵ_j are nonlinear corrections to linear relations (9). We assume that the amplitudes of waves slowly vary along the propagation direction because of nonlinearity. Consider, for example, the nonlinear excitation of a sound wave Φ by two sufficiently intense waves of the fourth sound, Θ_1 and Θ_2. Substituting relations (10) and the corresponding expressions for the velocities v and u, we perform some algebraic transformations and eliminate the nonlinear corrections λ and

ϵ_j from the equations. As a result, we obtain an equation for the amplitude of the sound wave Φ:

$$\frac{d\Phi}{dx} = -\frac{i}{4kc_2^2}\left[N(\alpha-1)\frac{m}{1-m}+M\right], \tag{11}$$

where N and M are the respective right-hand sides of Eq. (8), into which the normal coordinates are substituted. It should be noted that the problem under consideration involves small parameters c_1/c_2 and ρ/ρ_m ($\rho \approx 0.1$ g/cm^3 and ρ_m exceeds 1 g/cm^3). Taking these parameters into account and analyzing the right-hand sides of nonlinear system (8), we find that the maximal contribution to the interaction of interest is made by the second term from M:

$$-\frac{\alpha-1}{\rho}\frac{m}{1-m}\frac{\partial}{\partial t}\left(\delta\rho\frac{\partial\rho}{\partial t}\right).$$

Finally, Eq. (11) takes the form

$$c_2\frac{d|\Phi|}{dx} \approx \frac{\omega}{4\rho}\frac{m}{1-m}(\alpha-1)|\Theta_1||\Theta_2|. \tag{12}$$

Thus, the effective vertex (the third-order anharmonicity) that determines the interaction under consideration is equal to

$$A \sim \frac{\omega}{4\rho}\frac{m}{1-m}(\alpha-1). \tag{13}$$

Let us estimate the possibility of an experimental observation of this nonlinear process. For example, let us determine the order of magnitude of the distance l at which the acoustic wave can be amplified to observable magnitude. For this purpose, we use the numbers that are realistic for an experiment with a porous medium allowing the propagation of both the fourth sound and a fast compressional wave: $\omega = 2 \times 2\pi \times 10^5$ s^{-1}, $c_2 = 4 \times 10^5$ cm/s, $\alpha \approx 2$, and $m = 0.3$, $\rho = 0.1$ g/cm^3. The intensity of the acoustic wave and the fourth sound can be represented in order of magnitude by the formulas:

$$I_1 \sim \rho m c_1^3\left(\frac{\delta\rho}{\rho}\right)^2, \quad I_2 \sim \rho_m(1-m)c_2^3\left(\frac{\delta\rho_m}{\rho_m}\right)^2.$$

Then, taking into account Eq. (12), for the intensity of the amplified fast compressional wave at a distance l we obtain the expression

$$I_2 \sim \frac{c_2\omega^2}{16\rho_m c_1^6}\frac{(\alpha-1)^2}{1-m}I_1^2 l^2.$$

If $I_1 \approx 10^{-2}$–10^{-3} W/cm^2, we have $I_2 \times 10^{-5}$–10^{-6} W/cm^2 at a distance $l \sim 10$ cm, which is a real value for an experiment. Equation (12) ignores the sound absorption because, for the frequency under consideration, it is fairly small: according to [2], the absorption of transverse waves (even at higher frequencies), which is much stronger than the absorption of longitudinal sound waves, is very small at low temperatures. Note that the effective interaction vertex (13) strongly depends on the quantity ($\alpha - 1$), i.e., on $\rho_{12} = -(\alpha - 1)\rho m$; the quantity ρ_{12} describes the inertial action (unlike the viscous one) of the liquid on the solid when the latter is accelerated relative to the former and vice versa. The structure constant α is a purely geometrical quantity and does not depend on the densities of the liquid and solid phases. Thus, we can conclude that the nonlinear interaction under consideration strongly depends on the geometry of the pores. In addition, it should be noted that the fourth sound in porous media is often studied using unconsolidated molding powders, which do not possess the elastic properties necessary for sustaining the acoustic mode. Therefore, the consideration presented in this paper refers to consolidated elastic media, in which, in addition to the slow wave, the fast compressional wave, i.e., the common acoustic wave, can propagate.

ACKNOWLEDGMENTS

This work was supported by the Russian Foundation for Basic Research, project no. 01-02-17039.

REFERENCES

1. J. D. Reppy, J. Low Temp. Phys. **87** (3/4), 205 (1992).
2. K. Warner and J. R. Beamish, Phys. Rev. B **50**, 15896 (1994).
3. D. L. Johnson, D. L. Hemmick, and H. Kojima, J. Appl. Phys. **76** (1), 104 (1994).
4. S. I. Kiselev, V. V. Khmelenko, D. A. Geller, *et al.*, J. Low Temp. Phys. **119** (3/4), 357 (2000).
5. E. A. Popov, A. A. Pelmenev, and E. B. Gordon, J. Low Temp. Phys. **119** (3/4), 367 (2000).
6. I. M. Khalatnikov, *The Theory of Superfluidity* (Nauka, Moscow, 1971) [in Russian].
7. I. Rudnick, in *Proceedings of the Enrico Fermi Summer School, Course LXIII* (Academic, New York, 1976), p. 112.
8. M. A. Biot, J. Acoust. Soc. Am. **28**, 168 (1956).
9. M. A. Biot, J. Acoust. Soc. Am. **28**, 179 (1956).
10. M. A. Biot, J. Acoust. Soc. Am. **34**, 1254 (1962).
11. D. L. Johnson, Appl. Phys. Lett. **37**, 1065 (1980).
12. Sh. E. Kekutiya and N. D. Chkhaidze, Fiz. Nizk. Temp. **28**, 1115 (2002) [Low Temp. Phys. **28**, 795 (2002)].
13. L. D. Landau and E. M. Lifshitz, *Course of Theoretical Physics*, Vol. 6: *Fluid Mechanics*, 4th ed. (Nauka, Moscow, 1988; Pergamon, New York, 1987).
14. B. N. Esel'son, N. E. Dyumin, É. Ya. Rudavskiĭ, and I. A. Serbin, Zh. Éksp. Teor. Fiz. **51**, 1064 (1966) [Sov. Phys. JETP **24**, 711 (1967)].
15. V. G. Bykov and V. N. Nikolaevskiĭ, Akust. Zh. **36**, 606 (1990) [Sov. Phys. Acoust. **36**, 342 (1990)].
16. R. D. Stoll, in *Ocean Seismo-Acoustics. Low Frequency Underwater Acoustics* (Plenum, New York, 1986).
17. N. E. Dyumin and É. Ya. Rudavskiĭ, Fiz. Nizk. Temp. **1**, 521 (1975) [Sov. J. Low Temp. Phys. **1**, 255 (1975)].
18. R. D. Stoll and G. M. Bryan, J. Acoust. Soc. Am. **47**, 1440 (1970).

Translated by E. Golyamina

Acoustical Physics, Vol. 50, No. 6, 2004, pp. 725–731. Translated from Akusticheskiĭ Zhurnal, Vol. 50, No. 6, 2004, pp. 836–843.
Original Russian Text Copyright © 2004 by Rudenko, Robsman.

Nonlinear Processes in Media with an Acoustic Hysteresis and the Problems of Dynamic Interaction between Piles and Earth Foundation

O. V. Rudenko* and V. A. Robsman**

* *Physical Faculty, Moscow State University, Vorob'evy gory, Moscow, 119992 Russia*
e-mail: rudenko@acs366.phys.msu.ru
** *Research Institute of Transport Construction, ul. Kol'skaya 1, Moscow, 129329 Russia*
e-mail: nat-ana-sv@yandex.ru

Received June 16, 2004

Abstract—Evolution of a pulsed disturbance in a nonlinear medium whose properties irreversibly vary in the course of wave propagation is studied. Equations describing the propagation process are obtained. It is demonstrated that the waveform distortion and the dynamics of the field and energy characteristics of a signal noticeably differ from those observed in conventional nonlinear media. New nonlinear equations describing a pulse in a medium with relaxation of its nonlinear properties are derived. A finite "delay time" for irreversible processes is introduced in the defining equation. The shape of a pulse reflected from the boundary between an ordinary medium and a nonlinear hereditary medium is calculated. It is demonstrated that, in the case of a fixed relation between the peak pressure in the incident pulse and the ratio of linear impedances of the two media, a total transmission of the trailing edge of the pulse into the compressed medium occurs. Possible applications of the results to topical construction problems are discussed. *© 2004 MAIK "Nauka/Interperiodica".*

1. INTRODUCTION

Nonlinear-acoustics methods have been used in construction for testing materials, structures, and buildings since the early 1980s. The physical foundations of these methods [1], as applied to objects of industrial and civil engineering, are described in [2–4]. By now, the testing of tens of bridges, transport trestleworks, thermal power plants, underground structures, and architectural–historical monuments in Russian and foreign cities has been carried out.

It is necessary to note that the strong nonlinearity connected with the presence of structural inhomogeneities in the medium and of internal defects in some cases has manifested itself under a sudden external action (as in the case of testing buildings in the region of the Spitak earthquake) or as a result of the natural deterioration of a structure (as in the case of testing the state of the basement brickwork of architectural–historical monuments). In other cases, in laboratory and bench tests, an analogous situation was created on purpose by loading the models of structures up to the critical fracture stresses.

In addition, nonlinear phenomena were observed in the technological testing of construction works, for example, in the case of manufacturing and assembling various types of piles and their impact tests.

This problem became most urgent in constructing trestles for the third Moscow transport ring, where the majority of piers were pile grillages constructed of drilled-filling piles. These piles had a length of 40–50 m and a diameter of up to 1.5 m. However, industrial piles (in contrast to drilled-filling piles) have much smaller dimensions and require the application of impact or vibration loads for their mounting.

A drilled-filling pile is manufactured directly at a construction site by performing several sequential operations: borehole drilling, mounting of a reinforcing cage, concreting, testing of the concrete shaft for homogeneity, and impact testing of the force interaction of the pile and the soil.

The appearance of various defects, such as partial caving of a borehole, changes in its geometric dimensions, and inhomogeneity of the concrete because of the time intervals between the stages of borehole concreting is possible in the course of pile manufacture. Therefore, pile testing is conducted to evaluate the pile bearing strength. Both the values of compression stress at the contact of the pile butt-end with the soil and the quality of adherence of the concrete shaft of a pile with soil along its lateral surface are determined.

Taking into account the relatively large diameters of drilled-filling piles and their length, it is inexpedient to perform static loading of a pile being tested by increasing the external force load and measuring the deformation until the critical value, since this requires the construction of a special cumbersome structure, the installation of anchor piles, and prolonged testing. Instead, a method of impact testing called TNO is widely used in

1063-7710/04/5006-0725$26.00 © 2004 MAIK "Nauka/Interperiodica"

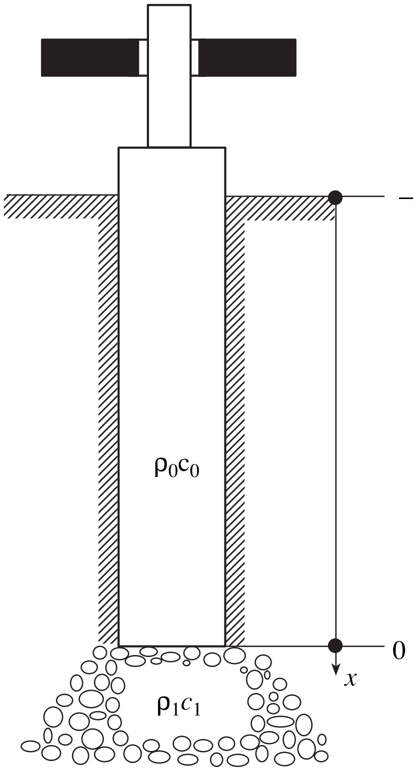

Fig. 1.

Russia and abroad to evaluate the bearing capability of large drilled-filling piles [5, 6].

The essence of the TNO method lies in periodic impact loading of the upper (open) end of a pile by dropping a load along a lead bar. The impact excites a pressure pulse in the pile (Fig. 1).

A wave propagates downwards and is partially reflected from the lower pile end–soil boundary, producing an irreversible displacement both as the result of soil consolidation and due to the "slippage" of the compressed lateral surface. Recording this displacement as a function of the height of the load fall, load mass, and number of impact loadings, it is possible to evaluate the bearing capability of a pile by the compression stress in the pile end–soil region.

In the case of impact testing by the TNO method, acceleration sensors and strain gauges are installed at the upper end and adjoining lateral surface of a pile. The parameters of signals reflected from the lower end–soil boundary and the inhomogeneities within the concrete are recorded. The mathematical model used for processing the results is based on a linear wave equation for the pulse propagation in a pile. In the numerical algorithm, a pile is replaced by a series of discrete viscoelastic elements. The boundary with the soil is also simulated by a concentrated element, which, however, permits nonlinear elastoplastic behavior.

Despite the wide application of the TNO method, which is connected with its convenience for builders, its shortcomings are evident. These include both the mathematical model describing the waves in a pile (the equations must be nonlinear) and the nonlinear pile foundation–soil system (it must be treated as a distributed system). It is clear that the formulation of new engineering and computer solutions goes beyond the framework of this paper. However, in considering a specific problem we examine here more general problems, which may be important for some applied problems, as well as for the physics of nonlinear waves.

2. PULSED SIGNAL IN A MEDIUM WITH HYSTERESIS

Up to now, the foundations of the theory of nonlinear wave propagation in media with hysteresis of the stress–strain dependence have been insufficiently developed because of the difficulties of solving the corresponding problems. This is also true for nonlinear acoustics of hysteretic media [7].

Therefore, it is necessary to develop a theory of wave propagation in media with irreversible deformations depending on the history of the loading and unloading processes. It is necessary to note that the problem of pile interaction with the soil foundation is not the only one in which hysteresis should be taken into account. Similar problems arise in road building, in the case of vibration compression of the roadbed foundation before laying asphalt surfacing and in testing bridges that have been in service for a long time (which leads to the appearance of a great number of defects and to the sag of span structures). Naturally, the solution of the "hysteresis" problems covers important problems of seismic engineering and seismoacoustics.

A model of a hysteretic medium used below for describing a nonlinear pulsed signal is illustrated in Fig. 2. In the course of the pressure growth, the density of the medium changes as follows:

$$\rho' = \frac{p'}{c_1^2}\left(1 - \frac{\varepsilon}{c_1^2\rho_1}p'\right), \quad \frac{\partial p'}{\partial t} > 0. \tag{1}$$

Here, ε is the nonlinear parameter of the medium and ρ_1 and c_1 are the initial values of the soil density and the sound velocity in soil, respectively. In the process of unloading, the increments of density ρ' and pressure p' are related by a linear dependence, but the properties of the medium are altered by the previous loading process and determined by the maximum load applied, p'_m [8]:

$$\rho' = \frac{p'}{c_1^2}\left(1 - \frac{2\varepsilon}{c_1^2\rho_1}p'_m\right) + \frac{\varepsilon p'^2_m}{c_1^4\rho_1}, \quad \frac{\partial p'}{\partial t} < 0. \tag{2}$$

At $p' = p'_m$, Eqs. (1) and (2) yield coinciding values. As follows from Eq. (2), a residual deformation $\rho'_{\text{res}} = \varepsilon p'^2_m/(c_1^4\rho_1)$ arises in the medium after unloading.

We assume that the physical nonlinearity of the medium that is present in defining equations (1) and (2) is greater than the geometric nonlinearity of the equations of motion [9], which can be linearized in this case and reduced to a single equation:

$$\frac{\partial^2 p'}{\partial x^2} = \frac{\partial^2 \rho'}{\partial t^2}. \qquad (3)$$

Let a wave propagate along the x axis, which coincides in Fig. 1 with the pile axis. Assuming the nonlinearity to be weak and using the method of a slowly changing profile [10], we obtain from Eqs. (3) and (1) an equation for the growing part of a pressure wave:

$$\frac{\partial p'}{\partial x} = \frac{\varepsilon}{c_1^3\rho_1} p' \frac{\partial p'}{\partial \tau}, \quad \frac{\partial p'}{\partial \tau} > 0. \qquad (4)$$

Analogously, we obtain for a discharge wave

$$\frac{\partial p'}{\partial x} = \frac{\varepsilon}{c_1^3\rho_1} p'_m(x) \frac{\partial p'}{\partial \tau}, \quad \frac{\partial p'}{\partial \tau} < 0. \qquad (5)$$

Solutions to these equations have the forms

$$p' = \Phi_1\left(\tau + \frac{\varepsilon}{c_1^3\rho_1} p' x\right), \quad \frac{\partial p'}{\partial \tau} > 0, \qquad (6)$$

$$p' = \Phi_2\left(\tau + \frac{\varepsilon}{c_1^3\rho_1}\int_0^x p'_m(x')dx'\right), \quad \frac{\partial p'}{\partial \tau} < 0. \qquad (7)$$

Here, Φ_1 and Φ_2 are arbitrary functions of their arguments. The solutions given by Eqs. (6) and (7) should be sewed combined at the point $\tau_m(x)$, where the pressure reaches its maximum value $p'(x, \tau_m) = p'_m(x)$ and the derivative $\partial p'/\partial\tau$ changes its sign.

Let us consider the simplest model of a pulse in the form of a symmetric single disturbance of a triangular shape (the curve corresponding to $x = 0$ in Fig. 3). The specific form of the functions Φ_1 and Φ_2 is determined according to the condition at the boundary $x = 0$. In the case of the pulse under consideration, the solutions given by Eqs. (6) and (7) take on the forms

$$\frac{p'}{p'_0} = \frac{\tau}{T}\frac{1}{1 - \dfrac{\varepsilon p'_0 x}{c_1^3\rho_1 T}}, \quad \frac{p'}{p'_0} = 1 - \frac{\tau}{T} - \frac{\varepsilon p'_0}{c_1^3\rho_1 T}\int_0^x \frac{p'_m(x')}{p'_0}dx', \qquad (8)$$

respectively. Equating functions (8) at the point of the maximum, we obtain several equations for two unknown functions $\tau_m(x)$ and $p'_m(x)$. The equations are reduced to a solvable differential equation of the first order. Taking into account the boundary conditions, we obtain the following from this equation:

$$\frac{p'_m(x)}{p'_0} = \frac{1}{2} = \text{const}, \quad \frac{\tau_m(x)}{T} = \frac{1}{2}\left(1 - \frac{x}{x_s}\right). \qquad (9)$$

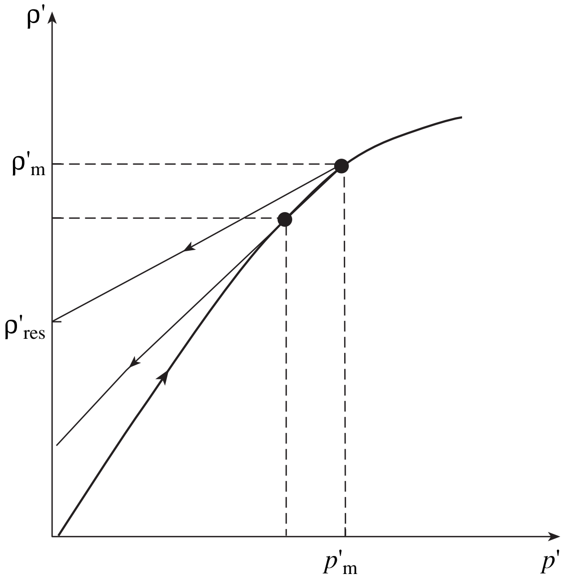

Fig. 2.

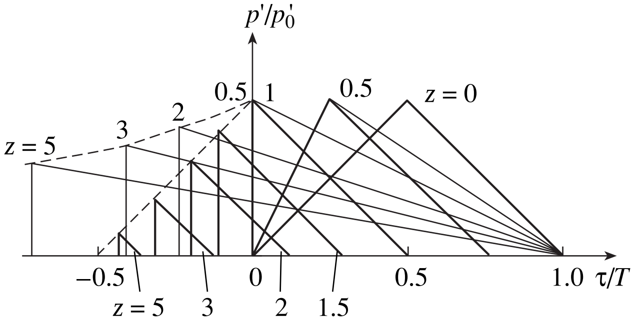

Fig. 3.

Here and below,

$$x_s = \frac{c_1^3\rho_1 T}{\varepsilon p'_0} \qquad (10)$$

is the characteristic nonlinear length or the distance of shock formation [10].

In Fig. 3, z denotes the distance normalized by length (10): $z = x/x_s$. It is necessary to note that the result given by Eq. (9) is valid within the range of distances $0 < x < x_s$, i.e., before the shock formation at the wave front.

In the region $x > x_s$, it is necessary to use the equation of the wave-front motion in the moving coordinate system, which is known from the theory of weak shock waves (for example, see [11]):

$$\frac{d\tau_m(x)}{dx} = -\frac{\varepsilon}{2c_1^3\rho_1} p'_m(x). \qquad (11)$$

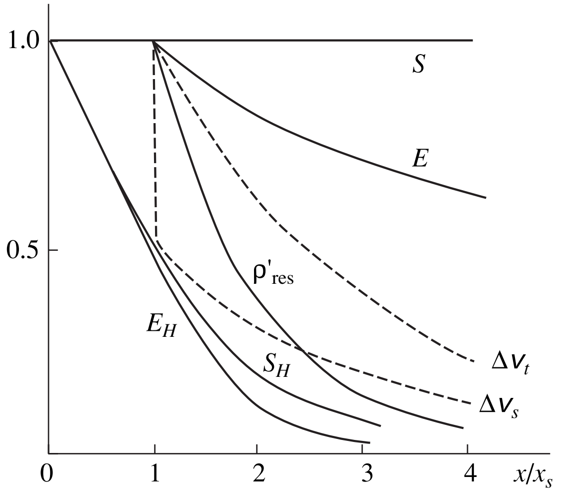

Fig. 4.

Now, we set $p' = p'_m(x)$ and $\tau = \tau_m(x)$ in the second of Eqs. (8), differentiate the resulting expression with respect to x, and use Eq. (11) to eliminate one of the variables. Solving the equation obtained in this way together with the evident conditions of joining with Eqs. (9) at $x = x_s$, we obtain an extension of Eqs. (9) to the region $x > x_s$:

$$\frac{p'_m(x)}{p'_0} = \frac{1}{2}\exp\left(-\frac{x-x_s}{2x_s}\right),$$
$$\frac{\tau_m(x)}{T} = -\frac{1}{2}\left[1-\exp\left(-\frac{x-x_s}{2x_s}\right)\right]. \tag{12}$$

One can see that, at large distances $x \gg x_s$, the peak pressure at the front of a shock wave decreases and tends to zero. However, in this case, the front “stops”: it cannot move forward farther than by $\tau_m(\infty) = -0.5$. This is the essential difference in the pulse behavior in a hysteretic medium from common “nonlinear spreading” [10, 11] leading to unrestricted growth of the pulse length in a permanent area (i.e., momentum). As is demonstrated below (Fig. 4), there are many other differences in this pulse behavior from the known results for a nonlinear pulse in a medium with an algebraic equation of state (without “hereditary” properties).

All characteristics of a pulsed signal in Fig. 4 are normalized to their peak values at $x = 0$.

Curves S and S_H illustrate the dependence of the pulse area

$$S \sim \int_{-\infty}^{\infty} p'(x,\tau)d\tau$$

on the distance traveled in the ordinary and hysteretic media. While in an ordinary medium the momentum remains constant and S = const both before and after the shock formation, in a hysteretic medium, S_H starts to decrease immediately even at arbitrarily small distances x.

The pulse energy

$$E \sim \int_{-\infty}^{\infty} p'^2(x,\tau)d\tau$$

in an ordinary medium remains constant in the region before the shock formation and then decreases because of the nonlinear wave attenuation. In a hysteretic medium, E_H starts to decrease immediately, since the energy is spent for the generation of residual deformations (curve $\rho'_{res}(x)$ in Fig. 4) and, after the shock formation, also for dissipation.

The velocity of propagation of the trailing edge of a wave is equal to

$$v_t = c_1\left[1+\frac{\varepsilon}{2}\frac{p'_0}{c_1^2\rho_1}Q(x)\right],$$

where $Q = 1$ at $x < x_s$ and $Q = \exp(-(x-x_s)/2x_s)$ at $x > x_s$. It exceeds the sound velocity c_1, since the trailing edge propagates in the medium already compressed by the loading wave, and it is constant up to the shock formation (in the region $x < x_s$). At distances $x > x_s$, the velocity v_t decreases asymptotically, tending to the sound velocity c_1.

The velocity of the leading edge v_s coincides with v_t at $x < x_s$, but after the shock formation its velocity drops down stepwise and then starts to decrease according to the law

$$v_s = c_1\left[1+\frac{\varepsilon}{4}\frac{p'_0}{c_1^2\rho_1}\exp\left(-\frac{x-x_s}{2x_s}\right)\right].$$

Since $v_s < v_t$, the trailing edge tends to catch up with the leading edge, and the pulse tends to “collapse.” Normalized increments of the propagation velocity of the leading and trailing edges are shown by the dashed curves Δv_s and Δv_t in Fig. 4.

3. SIGNAL IN A MEDIUM WITH A RELAXING NONLINEARITY

As is known, soil is sensitive to deformation rate and has rheological properties [12]. The processes of motion, partial fracture of grains, and formation of microflows of fluid in pores occur with certain characteristic times, which, generally speaking, may differ from the length of the pulsed signal. In contrast to the Mandel’shtam–Leontovich acoustic relaxation [10, 13], here, the internal processes in the medium are not only delayed but also irreversible. Moreover, they are evidently nonlinear.

Relaxation may be significant for both increasing and decreasing pressures. However, below we consider a simplified model in which only the unloading wave is assumed to be the relaxing. Thus, we refine the results of Section 2.

Let the front have a very small length, within which internal processes are “frozen” and the unloading follows the same path (*1*) (the curve in Fig. 2) as the loading of the medium. On the contrary, a very slow unloading follows a direct line *2* (the thin line in Fig. 2). In the intermediate region of deformation rates, it is possible to write down the dynamic relation

$$\frac{d\rho'}{dt} + \frac{\rho'}{T_R} = \frac{d}{dt}\rho'_{\text{fast}}(p') + \frac{1}{T_R}\rho'_{\text{slow}}(p'), \qquad (13)$$

where T_R is the characteristic relaxation time. Here, the dependence $\rho'_{\text{fast}}(p')$ is given by Eq. (1) and $\rho'_{\text{slow}}(p')$, by Eq. (2). The following defining equation can be obtained from Eq. (13):

$$\rho' = \frac{p'}{c_1^2} - \frac{\varepsilon}{c_1^4\rho_1}p'^2 + \frac{\varepsilon}{c_1^4\rho_1}\frac{1}{T_R}\int_{t_m}^{t}[p'(x,t') - p'_m(x)]^2\exp\left(-\frac{t-t'}{T_R}\right)dt'. \qquad (14)$$

Substituting Eq. (14) into Eq. (3) and using the method of a slowly changing profile, we arrive at an integro-differential equation

$$\frac{\partial p'}{\partial x} - \frac{\varepsilon}{c_1^3\rho_1}p'\frac{\partial p'}{\partial\tau} = -\frac{\varepsilon}{2c_1^3\rho_1}\frac{1}{T_R}\frac{\partial}{\partial\tau}\int_{\tau_m(x)}^{\tau}[p'(x,\tau') - p'_m(x)]^2\exp\left(-\frac{\tau-\tau'}{T_R}\right)d\tau'. \qquad (15)$$

As is well known [10], in the case of an exponential kernel equations of the type of Eq. (15) are reduced to differential equations of the form

$$\frac{\partial}{\partial\tau}\left[\frac{\partial p'}{\partial x} - \frac{\varepsilon}{c_1^3\rho_1}p'\frac{\partial p'}{\partial\tau}\right] + \frac{1}{T_R}\left[\frac{\partial p'}{\partial x} - \frac{\varepsilon}{c_1^3\rho_1}p'\frac{\partial p'}{\partial\tau}\right] = -\frac{\varepsilon}{2c_1^3\rho_1 T_R}\frac{\partial}{\partial\tau}[p' - p'_m(x)]^2. \qquad (16)$$

Equation (16) differs from the well-known equation of evolution [10] for an ordinary relaxing medium in its right-hand side, which now is nonlinear.

To make the form of subsequent expressions more convenient, we proceed to the dimensionless variables

$$z = \frac{x}{x_S}, \quad \theta = \frac{\tau}{T}, \quad P = \frac{p'}{p'_0}, \qquad (17)$$

where the nonlinear distance x_S is given by Eq. (10). Equation (16) in terms of the variables given by Eqs. (17) takes on the form

$$\frac{\partial}{\partial\theta}\left[\frac{\partial P}{\partial z} - P\frac{\partial P}{\partial\theta}\right] + \frac{T}{T_R}\left[\frac{\partial P}{\partial z} - P_m(z)\frac{\partial P}{\partial\theta}\right] = 0. \qquad (18)$$

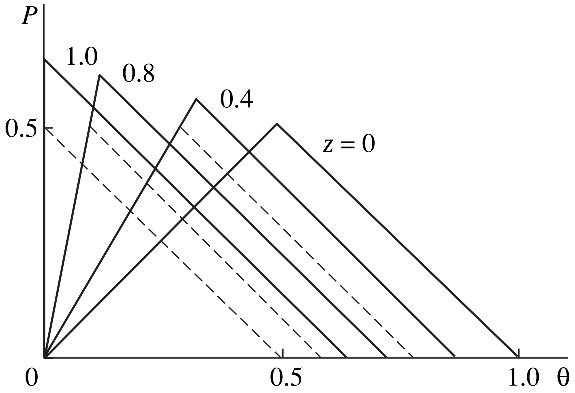

Fig. 5.

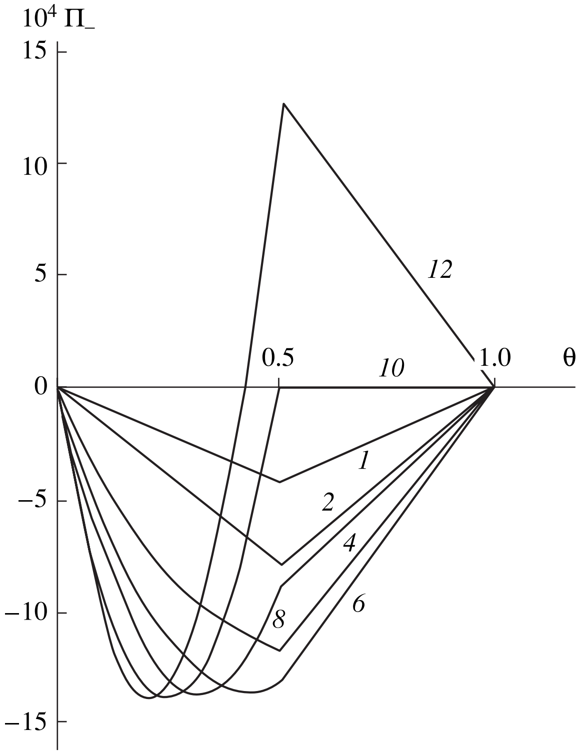

Fig. 6.

In the limiting case of small relaxation times ($T/T_R \gg 1$) (a “strong” manifestation of hysteresis), Eq. (18) is simplified:

$$\frac{\partial P}{\partial z} - P_m(z)\frac{\partial P}{\partial\theta} = \frac{T_R}{2T}\frac{\partial^2}{\partial\theta^2}[P - P_m(z)]^2. \qquad (19)$$

In the other limiting case, of large relaxation times ($T/T_R \ll 1$), the general equation (18) is also simplified:

$$\frac{\partial P}{\partial z} - P\frac{\partial P}{\partial\theta} = -\frac{T}{2T_R}[P^2 - 2P_m(z)P]. \qquad (20)$$

Now it is possible to calculate the pulse shape. To do this, it is necessary to solve Eq. (18) (or its simplified versions (19) and (20)) for an arbitrary function $P_m(z)$ and then to join the solution at the profile point $P = P_m(z)$, $\theta = \theta_m(z)$ with the solution to Eq. (4), which describes the leading edge of the pulse, by simultaneously determining the functions $P_m(z)$ and $\theta_m(z)$ from the conditions of joining. For $T_R \longrightarrow 0$, this procedure was performed in Section 2. However, taking into account the finiteness of the relaxation time makes it much more difficult.

Equations (18) and (19) have an exact solution in the form of a function linear in time:

$$P = 1 - \theta - \frac{z}{2} - 2\frac{T_R}{T}\left(1 - \frac{z}{2}\right)\ln\left(1 - \frac{z}{2}\right), \tag{21}$$

which describes the trailing edge of the pulsed signal. Joining Eq. (21) with the leading edge given by the first formula of Eqs. (8), $P = \theta/(1 - z)$, we determine the parameters

$$\begin{aligned} P_m(z) &= \frac{1}{2} - \frac{T_R}{T}\ln\left(1 - \frac{z}{2}\right), \\ \theta_m(z) &= \frac{1}{2}(1 - z) - \frac{T_R}{T}(1 - z)\ln\left(1 - \frac{z}{2}\right). \end{aligned} \tag{22}$$

The nonlinear transformation of the signal in the region before the shock formation is represented in Fig. 5 for the ratio of the relaxation time to the pulse length $T_R/T = 0.2$. The solid curves refer to the wave profiles at the distances $z = 0$, 0.4, 0.8, and 1. The trailing edge in the absence of delay ($T_R = 0$) is shown by dashed curves for comparison. One can see that the delay leads to a "spreading" of the signal and to a certain increase in its maximum. Correspondingly, the momentum and wave energy decrease more slowly.

4. INTERACTION OF THE PULSE WITH THE BOUNDARY

Let us now consider the reflection of a pulsed signal from the pile–soil boundary (Fig. 1). Taking into account only the physical nonlinearity of soil and equating the acoustic pressures and velocities in the media on both sides of the boundary $x = 0$, we obtain the relation between the pressures in the incident p'_+ and reflected p'_- pulses:

$$\Delta(p'_+ - p'_-) = (p'_+ + p'_-)\left[1 - \frac{2\varepsilon}{c_1^2\rho_1}(p'_+ + p'_-)\right]. \tag{23}$$

The derivation scheme for Eq. (23) is standard. However, in this case, Eq. (1) is used, which is nonlinear, and valid only for a rising front ($\partial p'/\partial t > 0$). Here, $\Delta = \rho_1 c_1/\rho_0 c_0$ is the ratio of linear impedances.

Assuming that

$$p'_- = -\left(\frac{1-\Delta}{1+\Delta}\right)p'_+ + \frac{\eta}{1+\Delta}p'_+$$

in Eq. (23), we arrive at a parametric relation between p'_+ and p'_-:

$$\begin{aligned} \Pi_- \equiv \frac{2\varepsilon}{c_1^2\rho_1}p'_- &= \frac{(1+\Delta)\eta[\eta - (1-\Delta)]}{(\eta + 2\Delta)^2}, \\ \Pi_+ \equiv \frac{2\varepsilon}{c_1^2\rho_1}p'_+ &= \frac{(1+\Delta)^2\eta}{(\eta + 2\Delta)^2}. \end{aligned} \tag{24}$$

The profile of the reflected pulse is shown in Fig. 6 for $\Delta = 0.9$. The shape of the incident pulse is assumed to be triangular in time, as before. Its leading edge is $\Pi_+ = 2\Pi_m\theta$; $\Pi_m = (2\varepsilon/c_1^2\rho_1)p'_m$, $0 < \theta < 0.5$. The curves in Fig. 6 correspond to different values of the parameter $10^2\Pi_m = 1$, 2, 4, 6, 8, 10, and 12, which are indicated near the respective curves. For the dimensionless time within $0 < \theta < 0.5$, the pulse was constructed with the help of solution (24). For $0.5 < \theta < 1$, according to equation of state (2), the unloading occurred by a linear law.

In the case of small values of $10^2\Pi_m$, the profile of the reflected pulse repeats the shape of the incident pulse and, since $\Delta = 0.9 < 1$ (the reflection occurs from a less "dense" medium), its polarity changes. As the parameter $10^2\Pi_m$ increases, a nonlinear distortion of the reflected signal occurs because of the soil compression. When this parameter is equal to ten, the difference in the impedances of the two media is compensated by the nonlinear compression and the boundary becomes completely "transparent" for the trailing edge. Within the range of dimensionless time values $0.5 < \theta < 1$, the reflection is absent (see Fig. 6). In the case of even greater peak values of pressure $10^2\Pi_m$, at a certain time moment soil becomes denser than the pile, and a part of the reflected pulse acquires the same (positive) polarity as the signal incident on the boundary.

The "self-clarification" phenomenon described above must be observed at relatively small peak pressures in media with large values of acoustic nonlinearity ε and with the ratio Δ slightly below unity.

In the process of pile testing, the ratio $\Delta = \rho_1 c_1/\rho_0 c_0$ can be measured experimentally by detecting the reflected pulse at the free (upper) end of the pile in the linear mode (i.e., at small p'_m corresponding to small heights of load dropping).

Proceeding to measurements in the nonlinear mode, it is possible to observe the process of small deepening of the pile at each impact because of the irreversible compression of the medium.

The pile displacement at an arbitrary value of Δ can be estimated as

$$\delta = \alpha d\left(\frac{2\Delta}{1+\Delta}\right)^2 \frac{\varepsilon}{c_1^4\rho_1^2} p_m'^2. \tag{25}$$

Here, d is the pile diameter and α is a constant of order unity. The peak pressure in the pulse excited in the pile is estimated according to the formula [14]

$$p_m' = \frac{E}{c_0}\sqrt{\frac{gh}{2}},$$

where E is the Young modulus of the pile material and h is the height of the load dropping. As can be readily demonstrated, at a height on the order of 1 m, the particle velocity and the maximum pressure in the pile are about 5 m/s and 10^8 Pa. In the case of a pile diameter of about 50–80 cm, the downward displacement at an impact must be about 1 cm. Simultaneous measurements of the reflected pulse and the irreversible displacement of the pile at different heights h of load dropping form an array of experimental data sufficient for a qualitative solution of the inverse problem, i.e., for the evaluation of the soil properties under the pile and its bearing strength. This problem is a purely engineering one. Its analysis and the development of recommendations for builders goes beyond the framework of this study.

5. CONCLUSIONS

Thus, we have studied the propagation of a pulsed disturbance in a nonlinear medium whose properties irreversibly vary after the wave propagation. Equations describing the process of nonlinear propagation are derived. It is demonstrated that, in contrast to an ordinary nonlinear medium, the momentum and energy decrease even in the region where the shock front is not yet formed, because the compression of the medium occurs under the effect of the leading edge. The pulsed signal becomes shorter and is strongly attenuated. The leading edge, in the coordinates accompanying the wave, is shifted forward to only a finite distance.

New nonlinear equations describing a pulse in a medium with relaxation of its nonlinear and irreversible properties are obtained. The presence of a finite delay time in the defining equation leads to signal "spreading" and to a deceleration of the dissipative process.

The shape of the pulse reflected from the boundary between an ordinary medium and a nonlinear hereditary medium is calculated. It is demonstrated that, in the case of a fixed relation between the peak pressure in the incident pulse and the ratio of nonlinear impedances of the two media, a total transmission of the trailing edge of the pulse into the compressed medium occurs.

Possible applications of the results to some problems of transport engineering are discussed.

ACKNOWLEDGMENTS

This work was supported in part by a grant of the Russian Academy of Sciences, the Program in Support of Leading Scientific Schools, and the TsNIIS.

REFERENCES

1. O. V. Rudenko, Russ. J. Nondestr. Test. **29** (8), 583 (1993).
2. V. A. Robsman, Akust. Zh. **37**, 1038 (1991) [Sov. Phys. Acoust. **37**, 541 (1991)].
3. V. A. Robsman, Akust. Zh. **39**, 333 (1993) [Acoust. Phys. **39**, 176 (1993)].
4. V. A. Robsman, Akust. Zh. **38**, 129 (1992) [Sov. Phys. Acoust. **38**, 66 (1992)].
5. *TNO Report—TNO-DLT Dynamic Load Testing Signal Matching, Users Manual* (1985–1996).
6. P. Middendorp and F. J. Reiding, in *Proceedings of Third International Conference on the Application of Stress Wave Theory to Piles* (Ottawa, 1988).
7. L. A. Ostrovsky and P. A. Johnson, Riv. Nuovo Cimento **24** (7), 1 (2001).
8. Yu. N. Rabotnov, *Elements of Hereditary Mechanics of Solids* (Nauka, Moscow, 1977) [in Russian].
9. C. A. Hedberg and O. V. Rudenko, J. Acoust. Soc. Am. **110**, 2340 (2001).
10. O. V. Rudenko and S. I. Soluyan, *Theoretical Foundations of Nonlinear Acoustics* (Nauka, Moscow, 1975; Plenum, New York, 1977).
11. S. N. Gurbatov and O. V. Rudenko, *Nonlinear Acoustics as a Collection of Problems* (Mosk. Gos. Univ., Moscow, 1990) [in Russian].
12. W. K. Nowacki, *Zagadnienia Falowe w Teorii Plastycznosci* (Panstwowe Wydawnictwo Naukowe, Warszawa, 1974; Mir, Moscow, 1978).
13. L. D. Landau and E. M. Lifshitz, *Course of Theoretical Physics*, Vol. 6: *Fluid Mechanics*, 3rd ed. (Nauka, Moscow, 1986; Pergamon, New York, 1987).
14. Ya. G. Panovko, *Introduction to the Theory of Mechanical Impact* (Nauka, Moscow, 1977) [in Russian].

Translated by M. Lyamshev

Acoustical Physics, Vol. 50, No. 6, 2004, pp. 732–741. Translated from Akusticheskiĭ Zhurnal, Vol. 50, No. 6, 2004, pp. 844–854.
Original Russian Text Copyright © 2004 by O. Tarasenko, S. Tarasenko, Yurchenko.

Localization of a Transverse Elastic Wave in a Semibounded Acoustic Superlattice of Ferrimagnetic and Superconducting Layers: 2. Effect of a Nonmagnetic Coating

O. S. Tarasenko, S. V. Tarasenko, and V. M. Yurchenko
Galkin Physicotechnical Institute, National Academy of Sciences of Ukraine,
Donetsk, ul. R. Lyuksemburg 72, 83114 Ukraine
e-mail: tarasen@host.dipt.donetsk.ua

Received August 20, 2003

Abstract—For a semibounded fine-layered magnetic superlattice of the ferrimagnet–superconductor type, it is shown that the continuous acoustic contact of its outer surface with an elastically isotropic perfect diamagnet gives rise to several specific features of the propagation and localization of a shear bulk magnetoelastic wave. *© 2004 MAIK “Nauka/Interperiodica”.*

Earlier [1], it was shown that, in an acoustically continuous semibounded ($x > 0$) fine-grained superlattice consisting of tangentially magnetized layers of easy-axis (the *OZ* axis) two-sublattice (with sublattice magnetizations $M_{1,2}$) ferrimagnet [2] (medium 1 with a shear modulus μ_1 and a density ρ_1) and a perfect superconductor (medium 2 with a shear modulus μ_2 and a density ρ_2), the conditions of the formation of a shear elastic wave with a wave vector $\mathbf{u} \parallel OZ$ strongly depend on the mutual orientation of the vectors $\mathbf{L} = \mathbf{M}_1 - \mathbf{M}_2$ [2] ($\mathbf{L} \parallel OZ$) in the neighboring ferrimagnetic layers that form the elementary period of the superlattice. In [1], two types of equilibrium magnetic configurations are considered: configuration *A*, in which the equilibrium directions of vectors **L** are parallel to each other for any pair of neighboring tangentially magnetized ferrimagnetic layers separated by a superconducting interlayer, and configuration *B*, in which the equilibrium directions of **L** are antiparallel. For such a geometry, the only structure allowing the propagation of a shear elastic wave is $\mathbf{n} \perp OZ \parallel \mathbf{u}$ (**n** is the normal to the interface). In addition, the superconducting medium is assumed to be a perfect diamagnet. Then, in the case of a fine-layered superlattice, we have

$$k_{\parallel 1} d_1 \ll 1; \quad k_{\parallel 2} d_2 \ll 1, \tag{1}$$

where $k_{\parallel 1}$ and $k_{\parallel 2}$ are the normal components of the wave vector of a normal shear elastic wave in media 1 and 2, respectively. The propagating shear SH wave is a one-partial excitation, even with allowance for the magnetoelastic and magnetodipole interactions. Criterion (1) requires that, in each of the layers forming the elementary period of the superlattice, the inhomogeneity of the field of elastic displacements along the normal to the interface between the media must be much smaller than the inverse thickness of the corresponding layer. This makes it possible to study the dynamics of the superlattice in the framework of the effective media method without restricting the consideration to only the long-wave limit of the partial oscillation spectrum [3–5]. On this basis, the propagation of shear elastic waves along a slip boundary between two half-spaces was studied in [1], where one half-space ($x > 0$) was assumed to be occupied by a semibounded two-component magnetic superlattice of the easy-axis ferrimagnet–superconductor type and the second half-space, by an elastically isotropic perfect superconductor (with a shear modulus μ_* and a density ρ_*). Calculations showed that the equilibrium magnetic configurations *A* and *B* of the aforementioned superlattice are noticeably different from the viewpoint of the dynamics of a shear elastic wave. In the case of the equilibrium magnetic configuration *A*, already in the long-wave limit a “macroscopic” acoustic gyrotropy is formed in the superlattice (when $k \in XY$ and $\mathbf{n} \perp OZ \parallel \mathbf{u}$, the effective elastic moduli averaged over the elementary period of the superlattice $D_A = d_1 + d_2$ satisfy the relation $\bar{c}_{45} = -\bar{c}_{54} \neq 0$). In the case of configuration *B*, when $k \in XY$ and $\mathbf{n} \perp OZ \parallel \mathbf{u}$, the effective elastic moduli averaged over the elementary period of the superlattice $D_B = 2(d_1 + d_2)$ satisfy the relation $\bar{c}_{45} = \bar{c}_{54} = 0$ despite the fact that each individual ferrimagnetic layer of the superlattice retains its gyrotropic properties.

It is of interest to answer the following question: how much is the elastic dynamics of a magnetic superlattice with equilibrium magnetic configuration *A* or *B* influenced by the presence of a slip boundary between the semibounded magnetic superlattice ($x \geq 0$) and a perfect superconductor ($x < 0$)?

In light of this, the purpose of this study is, in terms of the effective medium method, to analyze the gyrotropy-induced features of the propagation and the localization of an elastic *SH* wave traveling along the surface of a semibounded acoustic fine-layered superlattice of the easy ferrimagnet–perfect superconductor type, whose outer surface has a rigid acoustic contact with a perfect superconductor.

BASIC RELATIONS

As in [1], we assume that the magnetic superlattice under study is a system of equidistant easy-axis (the *OZ* axis) ferrimagnetic layers (medium 1) each of thickness d_1, which are acoustically coupled via identical superconducting layers of a perfect superconductor (medium 2) each with a thickness d_2 (following [1], we assume that, in the superconductor, the London penetration depth λ satisfies the relation $2\lambda \ll d_2$). The normal n to the interface between the layers coincides with the *OX* axis. In this case, a shear surface acoustic wave (SAW) of the *SH*-wave type can propagate near the surface of the easy-axis ferromagnet only when its elastic displacement vector is $\mathbf{u} \parallel OZ$ and its wave vector lies in the *XY* plane, i.e., when $\mathbf{n} \perp \mathbf{u} \parallel \mathbf{L} \perp \mathbf{k}_\perp$. We assume that, at the interlayer boundaries of the acoustically continuous magnetic superlattice under consideration, the following elastic boundary conditions (where $N = 0$, 1, …, ξ is the running coordinate along the boundary between the magnetic (medium 1) and nonmagnetic (medium 2) layers of the superlattice) [6]

$$u_i^{(1)} = u_i^{(2)}; \quad \xi = d_1 + N(d_1 + d_2), N(d_1 + d_2); \tag{2}$$

$$\begin{gathered} \sigma_{ik}^{(1)} n_k^{(1)} = \sigma_{ik}^{(2)} n_k^{(2)}; \\ \xi = d_1 + N(d_1 + d_2), N(d_1 + d_2) \end{gathered} \tag{3}$$

and electrodynamic boundary conditions (where $\mathbf{B}$ is the magnetic induction vector)

$$Bn = 0 \quad \xi = d_1 + N(d_1 + d_2), N(d_1 + d_2) \tag{4}$$

are satisfied. Under condition (1), the propagation of an *SH* wave with $\mathbf{u} \parallel OZ$, $k \in XY$, and $\mathbf{n} \parallel OX$ can be described in terms of the effective medium method by the effective elastic moduli $\bar{c}_{55}$, $\bar{c}_{44}$, $\bar{c}_{45}$, and $\bar{c}_{54}$, which are calculated in [1] for the equilibrium magnetic configurations of both *A* (I.22) and *B* (I.23) types.[1] These elastic moduli relate the elastic stress ($\langle\sigma_4\rangle$, $\langle\sigma_5\rangle$) and strain ($\langle u_4\rangle$, $\langle u_5\rangle$) tensor components averaged over the elementary period of the superlattice:

$$\begin{aligned} \langle\sigma_5\rangle &= \bar{c}_{55}\langle u_5\rangle + i\bar{c}_{54}\langle u_4\rangle; \\ \langle\sigma_4\rangle &= \bar{c}_{44}\langle u_4\rangle - i\bar{c}_{45}\langle u_5\rangle. \end{aligned} \tag{5}$$

If we set $\mu_1 = \mu_2 = \mu$ and $\rho_1 = \rho_2 = \rho$, we obtain

$$\begin{gathered} \bar{c}_{55}/\mu = c_\parallel = \frac{(\omega_{1+}^2 - \omega^2)(\omega_{1-}^2 - \omega^2)}{(\omega_{2+}^2 - \omega^2)(\omega_{2-}^2 - \omega^2)}; \\ \bar{c}_{44}/\mu = c_\perp = \frac{(\omega_{4+}^2 - \omega^2)(\omega_{4-}^2 - \omega^2)}{(\omega_{2+}^2 - \omega^2)(\omega_{2-}^2 - \omega^2)}; \\ \bar{c}_{45}/\mu = -\bar{c}_{54}/\mu = c_* = \frac{\nu\omega_E\omega_{me}^2\omega f_1}{(\omega_{2+}^2 - \omega^2)(\omega_{2-}^2 - \omega^2)}; \\ f_1 = d_1/(d_1 + d_2); \quad f_2 = d_2/(d_1 + d_2) \end{gathered} \tag{6}$$

for configuration *A* and

$$\begin{gathered} \bar{c}_{55}/\mu = c_\parallel = \frac{(\omega_{1+}^2 - \omega^2)(\omega_{1-}^2 - \omega^2)}{(\omega_{2+}^2 - \omega^2)(\omega_{2-}^2 - \omega^2)}; \\ \bar{c}_{44}/\mu = c_\parallel = \frac{(\omega_{3+}^2 - \omega^2)(\omega_{3-}^2 - \omega^2)}{(\omega_{1+}^2 - \omega^2)(\omega_{1-}^2 - \omega^2)}; \\ \bar{c}_{45} = \bar{c}_{54} = 0 \end{gathered} \tag{7}$$

for configuration *B*. In Eq. (6), we introduced the following notations: $\omega_{1\pm}$ are the positive roots of the equation $(\omega_0^2 + \omega_{me}^2 - \omega^2)(\omega_0^2 - \omega^2) - \nu^2\omega_E^2\omega^2 = 0$ biquadratic in ω, $\omega_{2\pm}$ are the positive roots of the equation $(\omega_0^2 + \omega_{me}^2 - \omega^2)(\omega_0^2 + f_1\omega_{me}^2 - \omega^2) - \nu^2\omega_E^2\omega^2 = 0$ biquadratic in ω, and $\omega_{4\pm}^2$ are the positive roots of the equation $(\omega_0^2 + \omega_{me}^2 - \omega^2)(\omega_0^2 - \omega^2) - \nu^2\omega_E^2\omega^2 + f_1 f_2\omega_{me}^4 = 0$ biquadratic in ω. In addition, for any $k_\perp$, the following relation is satisfied: $\omega_{1-} < \omega_{4-} < \omega_{2-} < \omega_{4+} < \omega_{1+} < \omega_{2+}$. In Eq. (7), $\omega_{3\pm}$ are the positive roots of the equation $(\omega_0^2 - \omega^2)(\omega_0^2 + f_2\omega_{me}^2 - \omega^2) - \nu^2\omega_E^2\omega^2 = 0$ biquadratic in ω. In addition, for any $k_\perp$ and $f_1 < f_2$, the relation $\omega_{3-} < \omega_{1-} < \omega_{2-} < \omega_{3+} < \omega_{1+} < \omega_{2+}$ is satisfied, while for $f_1 > f_2$, the relation $\omega_{3-} < \omega_{1-} < \omega_{3+} < \omega_{2-} < \omega_{1+} < \omega_{2+}$ is valid.

From Eq. (5) it follows that a shear *SH* wave propagating in the superlattice under study is a one-partial excitation in both configurations *A* and *B*:

$$\langle u_z\rangle = A\exp(ik_\parallel x)\exp(ik_\perp y - i\omega t). \tag{8}$$

For $k_\parallel^2 > 0$, we obtain a propagating bulk (trigonometric) elastic *SH* wave, while for $k_\parallel^2 < 0$, only a hyperbolic shear elastic wave satisfying the condition

$$\langle u_z\rangle \longrightarrow 0 \text{ at } x \longrightarrow \infty \tag{9}$$

can propagate along the surface of the semibounded magnetic superlattice under study ($x \geq 0$).

---

[1] In what follows, we refer to formulas from the first section of paper [1] by using two numbers. For example, a reference to formula (22) from paper [1] is given as (I.22).

SHEAR ELASTIC WAVE IN A SEMIBOUNDED MAGNETIC SUPERLATTICE WITH A SUPERCONDUCTING COATING

Let the outer surface of the effective medium under study $x \geq 0$ and the outer surface of a perfect elastically isotropic superconductor $x < 0$ (with a density ρ_* and a shear modulus μ_*; the superscript "<" indicates the quantities belonging to the lower half-space) have a continuous acoustic contact at $x = 0$:

$$\langle\sigma_{xi}\rangle = \sigma_{xi}^{<};\quad \langle u_i\rangle = u_i^{<};\quad x = 0. \tag{10}$$

Then, calculations with Eqs. (5)–(8) show that the formation of a shear SAW with

$$\langle u_i\rangle(x \longrightarrow \infty) \longrightarrow 0,\quad u_i^{<}(x \longrightarrow -\infty) \longrightarrow 0 \tag{11}$$

at the acoustically continuous boundary between the two media is possible for the equilibrium magnetic configuration *A* (the *A*–*S* structure):

$$\begin{gathered} k_\perp^2 = \omega^2[(c_\perp - c_\parallel\alpha^2)s_t^2]^{-1}; \\ \alpha \equiv \frac{c_*\sigma - aq}{c_\parallel},\quad \sigma \equiv \frac{k_\perp}{|k_\perp|}; \\ c_\parallel = \frac{(\omega_{1+}^2-\omega^2)(\omega_{1-}^2-\omega^2)}{(\omega_{2+}^2-\omega^2)(\omega_{2-}^2-\omega^2)}; \\ c_\perp = \frac{(\omega_{4+}^2-\omega^2)(\omega_{4-}^2-\omega^2)}{(\omega_{2+}^2-\omega^2)(\omega_{2-}^2-\omega^2)}; \\ c_* = \frac{\nu\omega_E\omega_{me}^2\omega f_1}{(\omega_{2+}^2-\omega^2)(\omega_{2-}^2-\omega^2)}, \end{gathered} \tag{12}$$

and for the equilibrium magnetic configuration *B* (the *B*–*S* structure):

$$\begin{gathered} k_\perp^2 = \omega^2[(c_\perp - c_\parallel\alpha^2)s_t^2]^{-1}; \\ \alpha \equiv -aq\frac{(\omega_{2+}^2-\omega^2)(\omega_{2-}^2-\omega^2)}{(\omega_{1+}^2-\omega^2)(\omega_{1-}^2-\omega^2)}; \\ c_\parallel = \frac{(\omega_{1+}^2-\omega^2)(\omega_{1-}^2-\omega^2)}{(\omega_{2+}^2-\omega^2)(\omega_{2-}^2-\omega^2)}; \\ c_\perp = \frac{(\omega_{3+}^2-\omega^2)(\omega_{3-}^2-\omega^2)}{(\omega_{1+}^2-\omega^2)(\omega_{1-}^2-\omega^2)}. \end{gathered} \tag{13}$$

In both cases, we have $q^2 \equiv 1 - \omega^2/(s_*^2k_\perp^2) > 0$ and $s_*^2 \equiv \mu_*/\rho_*$; $a \equiv \mu_*/\mu$ $(s_* > s_t)$.

Applying a formal passage to the limit $a \longrightarrow 0$ (a slip boundary) to Eq. (12), we obtain formula (I.30).

From the comparison of Eqs. (12) and (13), it follows that the most important distinctive feature of the spectrum of a collective shear SAW in the magnetic superlattice with configuration *B* (Eq. (13)) is the reciprocity of the spectrum with respect to the inversion of the propagation direction $\omega(k_\perp) = \omega(-k_\perp)$, despite the fact that each individual magnetic layer of the superlattice possesses an acoustic gyrotropy in the given geometry. The shear SAW given by Eq. (13) has two branches: the low-frequency branch (we denote its dispersion law as $\Omega_{B-}(k_\perp)$) and the high-frequency one (with a dispersion law $\Omega_{B+}(k_\perp)$). In addition, we have $\omega_{B+} < \Omega_{B+}(k_\perp) < \omega_{2+}$ and $\omega_{B0} < \Omega_{B-}(k_\perp) < \omega_{2-}$. Here, $\omega_{B\pm}(k_\perp)$, $\omega_{B0}(k_\perp)$ $(\omega_{B-}(k_\perp) < \omega_{B0}(k_\perp) < \omega_{B+}(k_\perp))$ are the characteristic frequencies determined from Eq. (13) by the condition $\alpha = 0$ (see also [1]). In the case of $f_1 < f_2$, both branches have long-wave (at $q = 0$) and short-wave boundaries ($\omega = \omega_{2-}$; $k_\perp = k_{*B}$ for $\Omega_{B-}(k_\perp)$ and $\omega = \omega_{2+}$; $k_\perp = k_{**}$ for $\Omega_{B+}(k_\perp)$) of the spectrum, which allows us, according to the terminology used in polariton dynamics [7], to consider such a surface elastic *SH* wave as a virtual shear SAW or a shear SAW of the second type (see also [1]). The spectrum of the low-frequency branch $\Omega_{B-}(k_\perp)$ strongly depends on the relative thicknesses of the magnetic and nonmagnetic layers: d_1/d_2. When $d_1/d_2 \longrightarrow 1$, the wave number corresponding to the short-wave boundary of the spectrum $\Omega_{B-}(k_\perp)$ unboundedly increases; i.e., when $d_1 > d_2$, this branch transforms to a SAW of the first type (see also [1]). As the wave number $k_\perp$ increases, its dispersion curve asymptotically tends to the frequency $\Omega_{B-}(\infty)$, the equation for which, with allowance for the notation introduced in Eq. (13), can be represented as

$$-a = c_\parallel\sqrt{\frac{c_\perp}{c_\parallel}}. \tag{14}$$

When $f_1 \longrightarrow 0.5$ (or $f_2 \longrightarrow 0.5$), we have $\Omega_{B-}(\infty) \longrightarrow \omega_{2-} = \omega_{3+}$. Here and below, the trend to the limit $k_\perp \longrightarrow \infty$ is understood as the elastostatic limit $\omega/(s_tk_\perp) \ll 1$ of the elastodynamics equations, which agrees with condition (1).

As for the second branch of the shear SAW spectrum $\Omega_{B+}(k_\perp)$, it remains within the frequency interval $(\omega_{B+}, \omega_{2+})$ and has both long-wave and short-wave boundaries in its spectrum; i.e., it is a virtual SAW of the second type.

In the case of the *SH*-type SAW formed near the acoustically continuous boundary ($x = 0$) between the superconducting medium and the superlattice with a collinear ordering of the equilibrium magnetic moments of the neighboring ferromagnetic layers (configuration *A*), its dispersion law, according to Eq. (12), remains nonreciprocal with respect to the inversion of the propagation direction for $a \neq 0$ as well: $\omega(k_\perp) \neq \omega(-k_\perp)$. At $\sigma = 1$, it has two branches, namely, the high-frequency branch $\tilde{\Omega}_{A+}(k_\perp)$ and the low-frequency branch $\tilde{\Omega}_{A-}(k_\perp)$ $(\tilde{\Omega}_{A-}(k_\perp) < \tilde{\Omega}_{A+}(k_\perp))$, while at $\sigma = -1$, it has one branch

$\tilde{\Omega}_{A0}(k_\perp)$. Under a formal passage to the limit $a \longrightarrow 0$, their dispersion curves transform to the respective expressions from [1] (see (I.30)) for the spectrum of a shear SAW propagating along a mechanically free surface of a semibounded acoustic magnetic superlattice: $\tilde{\Omega}_{A\pm}(k_\perp) \longrightarrow \Omega_{A\pm}(k_\perp)$ and $\tilde{\Omega}_{A0}(k_\perp) \longrightarrow \Omega_{A0}(k_\perp)$. From Eqs. (12) and (13), it follows that the presence of a nonmagnetic coating ($a \neq 0$) provides the possibility for the formation of short-wave spectrum boundaries in the branches of the shear SAW under consideration; i.e., it provides the possibility for the transformation of SAW-I to SAW-II. This is related to the fact that, for certain a, ω, and $k_\perp$, the following equation may be satisfied:

$$\sigma\nu\omega_E\omega\omega_{me}^2 f_1 - aq(\omega_{2+}^2 - \omega^2)(\omega_{2-}^2 - \omega^2) = 0. \quad (15)$$

From the analysis of Eq. (15), it follows that, in the case of $\sigma = 1$ and any $a \geq 1$, this equation always has two roots $\omega_{+\pm}$ ($\omega_{+-} < \omega_{2-} < \omega_{2+} < \omega_{++}$); however, if $\sigma = -1$, the existence of positive roots $\omega_{-\pm}$ ($\omega_{2-} < \omega_{-\pm} < \omega_{2+}$) is possible only when $0.25aq(\omega_{2+}^2 - \omega_{2-}^2)^2 > \nu\omega_E\omega_{me}^2 f_1\omega_*$ ($\omega_*^2 \equiv 0.5(\omega_{2+}^2 + \omega_{2-}^2)$). Otherwise, for $\sigma = -1$, Eq. (15) will have no positive roots. In particular this means that, for $a \neq 0$ and $\sigma = 1$, the dispersion curve of the high-frequency ($\tilde{\Omega}_{A+}(k_\perp)$) branch of spectrum (12), as in the case of $a = 0$ (I.3), satisfies the condition $\tilde{\Omega}_{A+}(k_\perp) > \omega_{1+}(k_\perp)$, but now, for any $a > 1$ and f_1/f_2, it has not only the long-wave spectrum boundary but also the short-wave spectrum boundary, whose frequency is $\omega = \omega_{++}$; the corresponding wave number is determined from Eq. (12) by the relation $\tilde{\Omega}_{A+}(k_\perp) = \omega_{A+}$ ($\omega > \omega_{2+}$). For the low-frequency branch of the spectrum of the *SH* wave under study ($\omega_{A-}(k_\perp)$), in the case of $\sigma = 1$ and $a \neq 0$, from Eqs. (12) and (15) it follows that the character of its dispersion curve $\tilde{\Omega}_{A-}(k_\perp)$ strongly depends on the relation between ω_{+-} and ω_{4-}, ω_{1-} ($\omega_{1-} < \omega_{4-}$). The condition for the formation of a short-wave boundary of this branch is the relation $\omega_{1-} < \omega_{+-} < \omega_{4-}$. In this case, the SAW branch under consideration corresponds to the virtual shear SAW. However, if $\omega_{+-} > \omega_{4-}$, the dispersion curve $\omega_{A-}(k_\perp)$ corresponds to SAW-I and, as the wave number $k_\perp$ increases, it asymptotically tends to the frequency $\tilde{\Omega}_{A-}(\infty)$, which, in the elastostatic limit, is determined from the relation

$$c_* - a = c_\parallel\sqrt{\frac{c_\perp}{c_\parallel}}. \quad (16)$$

If $\omega_{1-} > \omega_{+-}$, from Eqs. (12) and (15) we obtain that the dispersion curve $\tilde{\Omega}_{A-}(k_\perp)$ corresponds to a SAW of type I.

As for the dispersion law of a SAW (12) in the case of $\sigma = -1$ and $a \neq 0$ ($\tilde{\Omega}_{A0}(k_\perp)$), an analysis shows that the corresponding dispersion curve satisfies the condition $\tilde{\Omega}_{A0}(k_\perp) > \omega_{1-}$ for all allowed $k_\perp$ and that this curve possesses a long-wave spectrum boundary determined from Eq. (12) by the condition $q = 0$. Starting from the line $q = 0$, as the wave number $k_\perp$ increases, the dispersion curve under consideration tends to the frequency $\tilde{\Omega}_{A0}(\infty)$ for $\sigma = -1$, which, in the elastostatic limit $\omega/(s_t k_\perp) \longrightarrow 0$ ($q \longrightarrow 1$) with allowance for the notation introduced in Eq. (6), is determined by the relation

$$c_* + a = -c_\parallel\sqrt{\frac{c_\perp}{c_\parallel}}. \quad (17)$$

From Eqs. (16) and (17), it follows that, when $d_1 > d_2$, in the case of $\mu_1 = \mu_2 = \mu_*$, we have

$$\tilde{\Omega}_{A-}(\infty)$$

$$= (\omega_0^2 + \omega_{me}^2 a/(1+a) + 0.25\nu^2\omega_E^2)^{1/2} - 0.5\nu\omega_E,$$

$$\tilde{\Omega}_{A0}(\infty)$$

$$= (\omega_0^2 + \omega_{me}^2 a/(1+a) + 0.25\nu^2\omega_E^2)^{1/2} + 0.5\nu\omega_E; \quad (18)$$

in the case of $\mu_1 = \mu_2 = \mu_*$, we have

$$\tilde{\Omega}_{A-}(\infty)$$

$$= (\omega_0^2 + 0.5\omega_{me}^2 + 0.25\nu^2\omega_E^2)^{1/2} - 0.5\nu\omega_E,$$

$$\tilde{\Omega}_{A-}(\infty)$$

$$= (\omega_0^2 + 0.5\omega_{me}^2 + 0.25\nu^2\omega_E^2)^{1/2} + 0.5\nu\omega_E.$$

If, in Eqs. (18), we formally pass to the limit $a \longrightarrow 0$ (a slip boundary), we obtain $\tilde{\Omega}_{A0}(\infty) \longrightarrow \Omega_{A0}(\infty)$ and $\tilde{\Omega}_{A-}(\infty) \longrightarrow \Omega_{A-}(\infty)$, where $\Omega_{A0}(\infty)$ and $\Omega_{A-}(\infty)$ are determined by relations (I.31) and (I.32), respectively [1].

Until now, we studied the conditions of the localization of a shear elastic wave near the surface of an acoustic magnetic superlattice whose outer boundary has continuous acoustic contact with a perfect superconducting half-space. It is of interest to study the features of the formation of localized acoustic excitations of the *SH*-wave type in the case of an unbounded magnetic superlattice (with configuration *A* or *B*) containing a "defect" superconducting layer (*S*) introduced into it. In the following section, we consider the structures of the *A*–*S*–*A* and *B*–*S*–*B* types.

CONDITIONS OF THE FORMATION OF A SLIT *SH* WAVE

We assume that the superconducting medium is a perfect, elastically isotropic superconductor with a shear modulus μ_* and density ρ_* and that it has the form of an infinite strip of thickness $2d$ ($-d < x < d$). If the elastic boundary conditions on both surfaces of this layer ($x = \pm d$) correspond to a slip boundary (I.29), then, in the long-wave limit (1), the conditions of the formation of a shear elastic SAW in this structure will be the same as in the case [1] of a slip boundary between a semibounded magnetic superlattice and a semibounded perfect superconductor (I.30) for both $x > d$ and $x < -d$.

However, if the slip condition ($\sigma_{zx} = 0$) is satisfied at one boundary of the superconducting layer (e.g., at $x = d$), while a continuous acoustic contact (10) occurs at the other boundary (at $x = -d$), then, in the long-wave limit (1), the conditions of localization of an elastic *SH* wave in a semibounded superlattice of the ferrimagnet–superconductor type for $x > d$ will coincide with (I.30), while the dispersion law of a shear elastic *SH* wave in a semibounded superlattice of the ferrimagnet–superconductor type for $x < -d$ will be determined, depending on the magnetic configuration (*A* or *B*), by relations (12) or (13) with allowance for the substitution $a \longrightarrow aq\tanh(qk_\perp 2d)$ (an acoustic contact of a semibounded magnetic superlattice ($x < -d$) and a superconducting layer of thickness $2d$, whose outer surface ($x = d$) is mechanically free).

In both cases, the structure of the field of the **z** component of the elastic displacement vector **u** in the shear SAW formed in a semibounded superlattice is determined with allowance for the magnetic configuration by relations (8), (9) and (12), (13), and the formation of a shear SAW localized near the surface of the superconducting defect ($-d < x < d$) occurs in each half-space independently (for $x > d$ $k_\parallel \longrightarrow i\alpha k_\perp$, and for $x < -d$ $k_\parallel \longrightarrow -i\alpha k_\perp$, ($\alpha > 0$)).

A qualitatively different situation takes place in the case of a rigid contact of both surfaces of the superconducting defect layer of thickness $2d$ with the surrounding acoustic magnetic superlattice, i.e., in the case in which elastic boundary conditions (10) are satisfied at $x = \pm d$. Now, although as before we have $\mathbf{n} \parallel OX$, $\mathbf{u} \parallel OZ$, and $k \in XY$ and, for both $x > d$ and $x < -d$, the spatial structure of u_z of the elastic *SH* wave is determined by the relations similar to Eqs. (8) and (9), the localization of the shear elastic wave near the superconducting defect ($-d < x < d$) does not occur independently in each of the half-spaces. Such a wave is called a slit SAW of the *SH* type. Depending on the magnetic configuration of the superlattice, the corresponding dispersion equation for the spectrum of this shear slit wave, with allowance for the notation introduced for $c_\parallel$, $c_\perp$, and c_* in Eqs. (12) and (13), can be represented in the form ($\alpha^2 \equiv [c_\perp - \omega^2/(s_t^2 k_\perp^2)]/c_\parallel$):

$$\begin{gathered}(\beta_1 + \beta_2)\tilde{k}_\parallel \cot(\tilde{k}_\parallel d) = \tilde{k}_\parallel^2 - \beta_1\beta_2;\\ \tilde{k}_\parallel^2 \equiv \omega^2/s_*^2 - k_\perp^2;\end{gathered} \tag{19}$$

$$\beta_1 \equiv (\alpha c_\parallel + c_*\sigma)/a; \quad \beta_2 \equiv (\alpha c_\parallel - c_*\sigma)/a$$

for the *A*–*S*–*A* configuration and

$$(\alpha c_\parallel + aq\tanh(qk_\perp d))(\alpha c_\parallel + aq\coth(qk_\perp d)) = 0 \tag{20}$$

for the *B*–*S*–*B* configuration ($q^2 k_\perp^2 \equiv -\tilde{k}_\parallel^2$).

From the comparison of Eqs. (19) and (20), it follows that, as in the case of the SAW of the *SH* type considered above and described by Eqs. (12) and (13), the formation of the shear slit wave essentially depends on the magnetic configuration of the acoustic superlattice surrounding the superconducting defect ($-d < x < d$). In the case of the magnetic configuration corresponding to an acoustically nongyrotropic medium (*B*–*S*–*B*), from Eq. (20) it follows that the necessary condition for the formation of a shear slit SAW is that the following inequalities be simultaneously satisfied:

$$\alpha^2 > 0, \quad c_\parallel < 0. \tag{21}$$

Then, for preset ω and $k_\parallel$, from Eq. (20) it follows that the number of branches in the slit *SH* wave with dispersion law (20) depends on the thickness of the superconducting defect layer $2d$, which separates two semibounded acoustic magnetic superlattices. This number is equal to two when

$$|\alpha c_\parallel| > a/(dk_\perp) \tag{22}$$

and to one in the opposite case.

As for the necessary conditions for the formation of a slit wave in the case when both sides of the superconducting layer ($x = \pm d$) have a continuous acoustic contact with a semibounded acoustic magnetic superlattice with configuration *A*–*S*–*A*, from Eq. (19) it follows that, for those ω and $k_\perp$ at which conditions

$$\alpha^2 > 0, \quad \alpha c_\parallel > 0 \tag{23}$$

are simultaneously satisfied, the spectrum of the slit *SH* wave has only one branch, and the following relations should simultaneously be satisfied for this purpose:

$$|\alpha^2 c_\parallel^2 - c_*^2| d > \alpha a |c_\parallel|; \quad \alpha^2 c_\parallel^2 < c_*^2. \tag{24}$$

If we have

$$\alpha^2 > 0, \quad \alpha c_\parallel < 0, \tag{25}$$

then the spectrum of the slit *SH* wave (19) will have two branches on the condition that the following relations are simultaneously satisfied:

$$\left|\alpha^2 c_{\|}^2 - c_*^2\right| d < \alpha a |c_{\|}|; \quad \alpha^2 c_{\|}^2 > c_*^2. \qquad (26)$$

In the case of $\alpha^2 c_{\|}^2 < c_*^2$, the spectrum of the elastic *SH* wave (19) localized near the superconducting layer ($-d < x < d$) will also have only one branch in the region of ω and $k_\perp$ determined by conditions (25).

In the limit $d \longrightarrow \infty$ (the thickness $2d$ of the introduced superconducting layer unboundedly increases), the expression for the spectrum of the slit *SH* wave (19) transforms to Eq. (12), and Eq. (20) transforms to Eq. (13), i.e., to the expressions for the spectrum of a shear SAW traveling along the acoustically continuous boundary between two half-spaces, namely, the magnetic superlattice and the superconductor.

Now, let us consider the relationship between the conditions for the existence of a slit *SH* wave localized near the surface of the acoustic magnetic superlattice under study and the conditions of the reflection of a bulk elastic wave with the same polarization that is incident on the surface of the introduced superconducting layer ($x = d$) from the depth of the magnetic superlattice ($\mathbf{u} \parallel OZ$, $k \in XY$, $x \geq 0$).

REFLECTION OF A BULK ELASTIC *SH* WAVE FROM THE SURFACE OF A MAGNET–SUPERCONDUCTOR ACOUSTIC SUPERLATTICE

Calculations show that, in terms of the effective medium method, for an acoustically continuous boundary ($x = 0$) between two half-spaces (10) occupied by the magnetic superlattice under study ($x > 0$) and the superconductor ($x < 0$), the reflection coefficient R of a bulk transverse *SH* wave polarized perpendicularly to the plane of incidence ($\mathbf{u} \parallel OZ$, $k \in XY$) and incident from the magnetic superlattice on its surface, depending on the equilibrium magnetic configuration (*A* or *B*) of the superlattice, with allowance for Eqs. (12) and (13), can be represented as follows ($k_{\|}^2 > 0$, $\tilde{k}_{\|}^2 \equiv -q^2 k_\perp^2 > 0$):

$$R = \frac{c_{\|}k_{\|} - (a\tilde{k}_{\|} - ic_*\sigma k_\perp)}{c_{\|}k_{\|} + (a\tilde{k}_{\|} - ic_*\sigma k_\perp)} \text{ for the } A\text{–}S \text{ structure,} \quad (27)$$

where

$$c_{\|} = \frac{(\omega_{1+}^2 - \omega^2)(\omega_{1-}^2 - \omega^2)}{(\omega_{2+}^2 - \omega^2)(\omega_{2-}^2 - \omega^2)};$$

$$c_\perp = \frac{(\omega_{4+}^2 - \omega^2)(\omega_{4-}^2 - \omega^2)}{(\omega_{2+}^2 - \omega^2)(\omega_{2-}^2 - \omega^2)};$$

$$c_* = \frac{\nu\omega_E\omega_{me}^2\omega f_1}{(\omega_{2+}^2 - \omega^2)(\omega_{2-}^2 - \omega^2)},$$

and

$$R = \frac{c_{\|}k_{\|} - a\tilde{k}_{\|}}{c_{\|}k_{\|} + a\tilde{k}_{\|}} \text{ for the } B\text{–}S \text{ structure,} \quad (28)$$

where

$$c_{\|} = \frac{(\omega_{1+}^2 - \omega^2)(\omega_{1-}^2 - \omega^2)}{(\omega_{2+}^2 - \omega^2)(\omega_{2-}^2 - \omega^2)};$$

$$c_{\|} = \frac{(\omega_{3+}^2 - \omega^2)(\omega_{3-}^2 - \omega^2)}{(\omega_{1+}^2 - \omega^2)(\omega_{1-}^2 - \omega^2)}.$$

With allowance for the substitutions $k_{\|} \longrightarrow i\alpha k_\perp$ and $\tilde{k}_{\|} \longrightarrow -iqk_\perp$, the reflection coefficient R given by Eqs. (27) and (28) has a pole on the ω–$k_\perp$ plane, and this pole corresponds to the dispersion law determined above for the *SH* SAW (Eqs. (12), (13)) propagating in these geometries along the acoustically continuous ($a \neq 0$) boundary between the magnetic superlattice and the superconductor with $\mathbf{n} \parallel OX$; $\mathbf{u} \parallel OZ$, and $\mathbf{k}_\perp \parallel OY$.

In particular, from Eqs. (27) and (28) it follows that, if the boundary $x = 0$ between the two half-spaces (the magnetic superlattice and the superconductor) is a slip boundary (for this purpose, in Eqs. (27) and (28) we formally pass to the limit $a \longrightarrow 0$), we obtain $R = 1$ for configuration *B* at any angle of incidence of the shear bulk elastic wave on the surface of the superlattice, while, for the superlattice with magnetic configuration *A*, the bulk elastic wave will experience a total internal reflection at all angles of incidence: $|R| = 1$. In this case, the reflected bulk *SH* wave will acquire an additional gyrotropy-induced phase shift $R = \exp(i\phi)$ with respect to the incident wave (see [1]).

Because of the gyrotropy effect $c_* \neq 0$, for those ω and $k_\perp$ for which $\tilde{k}_{\|}^2 > 0$, in the case of $a \neq 0$ a total transmission of the bulk *SH* wave with $\mathbf{u} \parallel OZ$ through the acoustically continuous interface of the *A*–*S* structure is impossible. In this case, both transmitted and reflected shear bulk waves will have phase shifts relative to the bulk elastic *SH* wave incident on the surface of the superlattice. At the same time, for the *B*–*S* structure (Eq. (28)), at $a \neq 0$, a total transmission of the shear bulk elastic wave incident from the depth of the superlattice on its surface is possible: $R = 0$. As for the values of ω and $k_\perp$ at which the inequality $\tilde{k}_{\|}^2 < 0$ is valid, for them the interaction of the bulk *SH* wave incident on the interface at $a \neq 0$ is also characterized by a total internal reflection $|R| = 1$, and the reflected wave acquires an additional phase shift ϕ for both equilibrium magnetic configurations *A* and *B*. For preset values of the frequency ω and wave number $k_\perp$, the quantity ϕ in the case of configuration *A* is nonreciprocal with respect to the substitution $k_\perp \longrightarrow -k_\perp$ and, at $a \neq 0$, is determined from Eq. (27) by not only the gyrotropic properties of the superlattice but also the relative values of the acoustic parameters of the contacting media:

$$\tan(\phi/2) = \frac{\sigma\nu\omega_E\omega\omega_{me}^2 f_1 - aq(\omega_{2+}^2 - \omega^2)(\omega_{2-}^2 - \omega^2)}{(\omega_{2+}^2 - \omega^2)(\omega_{2-}^2 - \omega^2)}. \qquad (29)$$

As a result, at $\omega = \omega_{+\pm}$ and $\sigma = 1$ or at $\omega = \omega_{-\pm}$ and $\sigma = -1$, we have $\phi = 0$ and, in Eq. (27), $R = 1$.

The presence of the "macroscopic" gyrotropy effect for a superlattice with equilibrium magnetic configuration A leads to the situation in which, at the acoustically continuous boundary between two identical semibounded magnetic superlattices ($\mathbf{n} \parallel OX$), the coefficient of reflection of a bulk elastic SH wave with $\mathbf{u} \parallel OZ$ and $k \in XY$ is nonzero if the easy magnetization directions at $x > 0$ and $x < 0$ are anticollinear. Following the notation introduced in Eqs. (27) and (28), this structure can be represented as A–$\bar{A}$. Calculations show that, in this case, unlike Eqs. (27) and (28), we obtain

$$R = \frac{2ic_*\sigma k_\perp}{c_\parallel k_\parallel - ic_*\sigma k_\perp} \text{ for the } A\text{–}\bar{A} \text{ structure.} \qquad (30)$$

Note that, with allowance for the substitution $k_\parallel \longrightarrow i\alpha k_\perp$, Eq. (30) suggests the possibility of the formation of a specific shear SAW at the boundary $x = 0$. According to the general theory of wave processes [5], the dispersion law of this wave is determined by the pole of reflection coefficient (30) and, as one can easily verify, coincides with relation (I.30) for the spectrum of an SH SAW traveling along a slip boundary between two half-spaces, one of which is occupied by a perfect superconductor and the second, by a magnetic superlattice with configuration A.

The gyrotropy-induced extra features of the reflection of a bulk elastic SH wave from the boundary between the magnetic superlattice and a superconductor arise in a structure formed as a magnetic sandwich of the magnetic superlattice–superconductor–magnetic superlattice type (A–S–A or B–S–B), i.e., in the cases in which the formation of a slit shear SH wave (Eqs. (19), (20)) takes place. As in the case of Eqs. (19) and (20), we assume that we have an unbounded superlattice of the easy-axis ferrimagnet (medium 1)–perfect superconductor (medium 2) type, into which an elastically isotropic, perfectly superconducting layer of thickness $2d$ ($-d < x < d$) is introduced. We assume that this three-layer structure is acoustically continuous (Eqs. (2)–(4)). Then, in the framework of the effective medium method (1), for a shear bulk elastic wave with $\mathbf{u} \parallel OZ$ and $k \in XY$ that is incident in the upper half-space on the boundary between the magnetic superlattice and the superconducting layer $x = d$, the reflection coefficient V can be represented as

$$V = \frac{V_{32} + V_{21}(1 + V_{23} + V_{32})\exp(i4\tilde{k}_\parallel d)}{1 - V_{23}V_{21}\exp(i4\tilde{k}_\parallel d)}, \qquad (31)$$

where

$$V_{23} = \frac{-(c_\parallel k_\parallel - ic_*\sigma k_\perp) + a\tilde{k}_\parallel}{c_\parallel k_\parallel - ic_*\sigma k_\perp + a\tilde{k}_\parallel},$$

$$V_{21} = \frac{-(c_\parallel k_\parallel + ic_*\sigma k_\perp) + a\tilde{k}_\parallel}{c_\parallel k_\parallel + ic_*\sigma k_\perp + a\tilde{k}_\parallel}, \qquad (32)$$

$$V_{32} = \frac{c_\parallel k_\parallel + ic_*\sigma k_\perp - a\tilde{k}_\parallel}{c_\parallel k_\parallel - ic_*\sigma k_\perp + a\tilde{k}_\parallel} \text{ for the } A\text{–}S\text{–}A \text{ structure and}$$

$$V_{23} = V_{21} = -V_{32} = \frac{-c_\parallel k_\parallel + a\tilde{k}_\parallel}{c_\parallel k_\parallel + a\tilde{k}_\parallel} \qquad (33)$$

for the B–S–B structure.

Here, according to the notation used in [5], V_{ij} denotes the coefficient of reflection of a one-partial bulk SH wave incident from medium i on the boundary between media i and j; index 3 refers to the medium in the region $x > d$, index 2, to the layer ($-d < x < d$), and index 1, to the medium in the region $x < -d$.

When $d \longrightarrow \infty$, the expression for V given by Eqs. (31)–(33) coincides with the expression for the coefficient of reflection of a shear elastic SH wave, $V \longrightarrow R$, in the case of an acoustically continuous boundary between the magnetic superlattice and a semibounded superconductor in both configuration A (Eq. (27)) and configuration B (Eq. (28)). With allowance for the substitution $k_\parallel \longrightarrow \pm i\alpha k_\perp$ ($ik_\parallel \longrightarrow -\alpha k_\perp$) for $x > d$ and $ik_\parallel \longrightarrow \alpha k_\perp$ for $x < -d$, the poles of reflection coefficient (31)–(33) on the $\omega - k_\perp$ plane coincide with the spectrum determined above for the slit SH wave localized near the superconducting layer introduced in magnetic superlattice in the case of configuration A (Eq. (19)) or in the case of configuration B (Eq. (20)).

Analyzing the magnitude of reflection coefficient V (31)–(33), one can see that, in addition to the situation in which the superconducting layer is a half-wave one, i.e., $2\tilde{k}_\parallel d = m\pi$, where $m = 1, 2\ldots$ ($\tilde{k}_\parallel^2 > 0$), the total transmission ($|V| = 0$) of an elastic SH wave through the structure under study is also possible on the condition that

$$V_{32} = 0. \qquad (34)$$

In this case, the reflection coefficient V_{32} should be calculated with allowance for the magnetic configuration of the superlattice (32)–(33). For preset ω and $k_\perp$, a bulk elastic SH wave ($\tilde{k}_\parallel^2 > 0$) should be formed in the superconducting layer $-d < x < d$. For the A–S–A structure, condition (34) cannot be satisfied.

If the acoustic properties of the magnetic superlattice are such that the latter is nongyrotropic (configuration B), we have $V_{23} = V_{21} = -V_{32}$. As a consequence, at $k_\parallel \longrightarrow 0$ we obtain the following dependence: if

$V_{32} \longrightarrow -1$, we have $V \longrightarrow \pm 1$, which corresponds to the impossibility of the propagation of a bulk homogeneous elastic *SH* wave along the surface of the introduced superconducting layer $x = \pm d$ for both the *A–S–A* and *B–S–B* structures.

In the case of a magnetic nongyrotropic superlattice, the behavior of the coefficient of reflection of a shear bulk wave V_{32} (medium 2 is an elastically isotropic diamagnet and medium 3, a fine-layered acoustic magnetic superlattice) as a function of the angle of incidence is illustrated in Figs. 1–3. These figures, for a fixed frequency of the incident bulk *SH* wave ω, present the scalar surface impedances of both contacting media $Z_{2,3}$ versus $k_\perp$ ($V_{32} = (Z_2 - Z_3)/(Z_2 + Z_3)$ [5]) for the three most typical situations. For medium 3, $Z_3 \equiv \mu|c_\parallel|k_\parallel$ ($k_\parallel^2 > 0$), and for medium 2, $Z_2 \equiv \mu_* \tilde{k}_\parallel$ ($\tilde{k}_\parallel^2 > 0$). As a result, at a given $k_\perp$ the points at which $Z_2(k_\perp) = Z_3(k_\perp)$ (points $a_\pm$) in Figs. 1, 2 correspond to the reflectionless (Eq. (34)) transmission of a bulk *SH* wave from medium 3 to medium 2 (and in the opposite direction). The total internal reflection of the *SH* wave (with $k_\parallel^2 > 0$) incident on the interface from medium 3 ($|V_{32}| = 1$) is realized for those values of $k_\perp$ for which $\tilde{k}_\parallel^2 < 0$. The case of a partial transmission of the incident *SH* wave with $k_\parallel^2 > 0$ from medium 3 to medium 2 ($|V_{32}| < 1$) takes place when $\tilde{k}_\parallel^2 > 0$ and $Z_2 \neq Z_3$. At $Z_3 = 0$, we have $V_{32} = 1$, while at $Z_2 = 0$, $V_{32} = -1$.

From Eqs. (31)–(33), it follows that a bulk elastic *SH* wave reflected from the superconducting layer is shifted in phase ψ ($\tan\psi = \mathrm{Im}V/\mathrm{Re}V$) with respect to the incident wave. In the particular case of $c_\parallel = \infty$, at any wave number $k_\perp$, for the incident elastic *SH* wave we have $|V| = 1$ and $\psi = 0$. However, if $c_\parallel = 0$, from Eqs. (31)–(33) it follows that, for any $k_\perp$, $V = -1$.

Irrespective of the equilibrium magnetic configuration of the superlattice into which the "defect" layer is introduced (*A–S–A* or *B–S–B*), for the coefficient of reflection *V* of a bulk elastic *SH* wave incident from the depth of the superlattice on the surface of the superconducting layer ($-d < x < d$), we obtain $V \longrightarrow 0$ as $d \longrightarrow 0$.

Under the conditions of total internal reflection, i.e., when in Eqs. (27), (28), (31)–(33) $|R| = 1$ and $\phi \neq 0$, a beam of shear elastic waves incident from the depth of the ferrimagnet–superconductor superlattice on its surface acquires not only a phase shift ϕ at reflection but also experiences a longitudinal displacement $\Delta \equiv -\partial\phi/\partial k_\perp$ along the interface (the Schoch effect) [5]. For equilibrium magnetic configuration *B* and a full acoustic contact at the boundary between the semibounded superlattice and a semibounded superconductor (the *B–S* structure), the expression for Δ with allowance for the notation used in Eq. (13) can be represented as

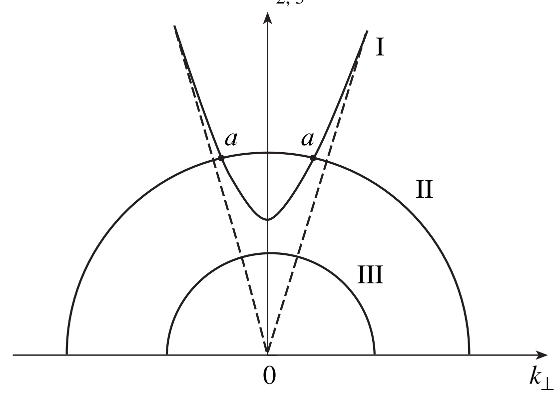

Fig. 1. Surface impedances of a semibounded superlattice of the easy-axis ferrimagnet–perfect superconductor type Z_3 and a semibounded nonmagnetic medium Z_2 versus $k_\perp$ for $c_\parallel > 0$ and $c_\perp < 0$: (I) $Z_3(k_\perp)$, (II) $Z_2(k_\perp)$ ($\mu_*/\mu > \sqrt{c_\parallel}\, s_*/s$), and (III) $Z_2(k_\perp)$ ($\mu_*/\mu < \sqrt{c_\parallel}\, s_*/s$).

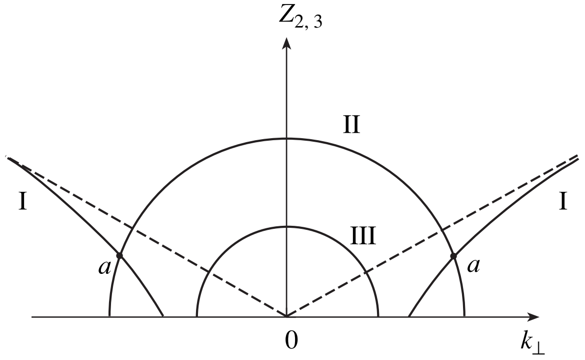

Fig. 2. Surface impedance of a semibounded superlattice of the easy-axis ferrimagnet–perfect superconductor type Z_3 and a semibounded nonmagnetic medium Z_2 versus $k_\perp$ ($c_\parallel < 0$; $c_\perp > 0$): (I) $Z_3(k_\perp)$, (II) $Z_2(k_\perp)$ ($c_\perp > (s_*/s)^2$), and (III) $Z_2(k_\perp)$ ($c_\perp < (s_*/s)^2$).

$$\Delta = \frac{-2k_\parallel}{k_\parallel^2 + \kappa^2 k_\perp^2}\left[\kappa + \frac{\kappa k_\perp^2 c_\perp}{c_\parallel k_\parallel^2} + \frac{a\omega^2}{c_\parallel s_*^2 q k_\perp^2}\right]; \qquad (35)$$

$$\kappa \equiv \frac{-aq}{c_\parallel}; \quad k_\parallel^2 > 0; \quad k_\parallel^2 = \left(\frac{\omega^2}{s_t^2} - c_\perp k_\perp^2\right)\frac{1}{c_\parallel}.$$

As for the equilibrium magnetic configuration *A*, in [1] it was shown that in this case, because of the gyrotropy, the Schoch effect is also possible for a slip boundary (see (I.38)). In the presence of a coating with $a \neq 0$, the expression for the longitudinal displacement Δ with

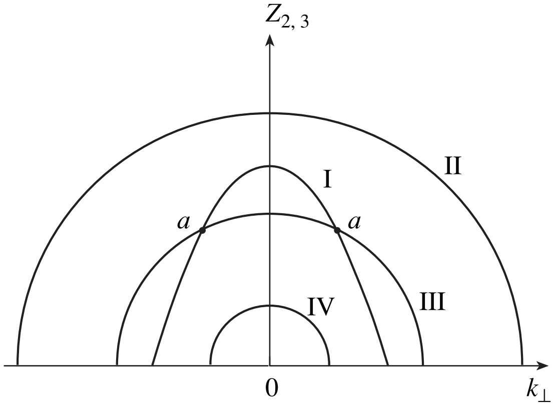

Fig. 3. Surface impedance of a semibounded superlattice of the easy-axis ferrimagnet–perfect superconductor type Z_3 and a semibounded nonmagnetic medium Z_2 versus $k_\perp$ for $c_\parallel > 0$ and $c_\perp > 0$: (I) $Z_3(k_\perp)$, (II) $Z_2(k_\perp)$ ($\mu_*/\mu > s_*\sqrt{c_\parallel}/s$ and $c_\perp > (s_*/s)^2$), (III) $Z_2(k_\perp)$ ($\mu_*/\mu < s_*\sqrt{c_\perp}/s$ and $c_\perp > (s_*/s)^2$), and (IV) $Z_2(k_\perp)$ ($c_\perp < (s_*/s)^2$, $\mu_*/\mu < s_*\sqrt{c_\perp}/s$).

allowance for the notation from Eq. (12) structurally coincides with Eq. (35) on the condition that

$$\kappa \equiv \frac{-aq + c_*\sigma}{c_\parallel}. \tag{36}$$

Compared to Eq. (35) (a nongyrotropic superlattice of the magnetic–superconductor type), gyrotropic medium (36) is characterized by the following extra feature of the effect: for preset values of ω and $|k_\perp|$, the magnitude and sign of the longitudinal displacement of the reflected acoustic beam Δ prove to be nonreciprocal with respect to the change of sign of the wave vector projection onto the propagation direction of the incident *SH* wave; i.e., $\Delta(k_\perp) \neq \Delta(-k_\perp)$.

In this case, as in [1], the following dependence takes place: if the medium in which the incident *SH* wave propagates possesses no acoustic gyrotropy (configuration *B*), under the conditions of a total internal reflection the beam of reflected bulk *SH* waves will have a negative longitudinal displacement Δ. If the medium in which the incident shear bulk wave propagates is acoustically gyrotropic (configuration *A*), under the conditions of a total internal reflection the beam of reflected bulk *SH* waves may have a negative longitudinal displacement along the outer surface of the superlattice.

CONCLUSIONS

Thus, in this paper, on the basis of a simultaneous consideration of the magnetoelastic and magnetodipole interactions and in terms of the effective medium method, we studied the characteristic features of the propagation of a shear elastic wave in a semibounded acoustic superlattice of the easy-axis ferrimagnet–superconductor type whose surface has a continuous acoustic contact with a perfect superconducting layer (half-space). The analysis was performed for the cases of the parallel (configuration *A*) and antiparallel (configuration *B*) orientations of the equilibrium magnetic moments of the tangentially magnetized neighboring ferrimagnetic layers of the superlattice. Although, in the Voigt geometry, an unbounded ferrimagnetic medium possesses a gyrotropy, in the case of the magnetic superlattice with the same geometry of the elastic wave propagation the first of the aforementioned configurations possesses a “macroscopic” acoustic gyrotropy (configuration *A*), while the second (configuration *B*) is nongyrotropic. Calculations show that, for a preset frequency and wave number, the necessary conditions for the SH wave localization near the surface of the magnetic acoustic superlattice under study also noticeably vary depending on the type of the equilibrium magnetic configuration. In particular, unlike the case of a slip boundary (see [1]), the presence of an acoustically continuous coating (a perfect superconductor) on the outer surface of a semibounded magnetic superlattice with equilibrium magnetic configuration *B* provides the possibility for the following:

(i) the formation of a shear SAW. Depending on the relative thickness of the magnetic and superconducting layers forming the superlattice period, the corresponding dispersion curve may have or not have a short-wave end point of the spectrum;

(ii) the realization of the effect of total internal reflection for a shear bulk wave incident from the depth of the magnetic superlattice on its surface. In this case, the reflected bulk *SH* wave is shifted in phase with respect to the incident wave;

(iii) the formation of the Schoch effect under the conditions of total internal reflection for a beam of shear bulk *SH* waves incident from the depth of the magnetic superlattice on its surface; and

(iv) the absence of a homogeneous bulk *SH* wave slipping along the surface of the magnetic superlattice.

As for the magnetic superlattice with configuration *A*, the presence of gyrotropy in the case of an acoustically continuous interface between the semibounded superlattice and the superconductor half-space leads to the following distinctive features, with respect to the case of a slip boundary (see [1]):

(i) the possible formation of a short-wave boundary of the spectrum in the dispersion curve of a shear SAW of the first type, i.e., the possible transformation of a SAW of the first type into a SAW of the second type (a virtual SAW). However, its spectrum remains nonreciprocal with respect to the inversion of the propagation direction and consists of three branches;

(ii) part of the spectrum branches of the shear SAW formed may possess a dispersion already in the elastostatic limit.

If a superconducting layer (*S*) is introduced into the magnetic superlattice under study with configuration *A* or *B*, the formation of a propagating slit elastic *SH* wave is possible near this layer, while the spectrum of this wave remains reciprocal with respect to the inversion of the propagation direction for both types of the equilibrium magnetic configuration of the superlattice. The number of branches in such a slit wave with preset values of frequency ω and wave number $k_\perp$ may vary depending on the thickness of the "defect" superconducting layer introduced in the magnetic superlattice. For all two- and three-component layered structures considered in this paper, we studied the relation between the conditions of the formation of slit *SH* waves and the characteristic features of the reflection of a bulk shear elastic wave incident from the depth of the superlattice on its outer surface.

We have shown that, not only in the case of a slip boundary (see [1]) but also in the case of a continuous acoustic contact at the interface between a semibounded magnetic superlattice and a semibounded perfect superconductor, the following dependences take place:

(i) If, for a given frequency, the bulk *SH* wave incident from the depth of the superlattice on its surface undergoes a total internal reflection and the medium in which this wave propagates is acoustically gyrotropic, the reflected beam of bulk shear waves will experience a negative longitudinal displacement (Δ) along the surface of the superlattice ($\Delta < 0$);

(ii) If, for a given frequency, the bulk shear wave incident from the depth of the superlattice on its surface undergoes a total internal reflection and the medium in which this wave propagates is acoustically nongyrotropic, the reflected beam of bulk *SH* waves will experience a positive longitudinal displacement (Δ) along the surface of the superlattice ($\Delta > 0$).

The influence of an inhomogeneous exchange interaction and finite dimensions of a real magnetic superlattice on the effects considered in this paper will be the subject of a further study.

ACKNOWLEDGMENTS

One of the authors (S.V.T.) is grateful to I.E. Dikshteĭn for supporting the idea of this study and for useful discussions.

REFERENCES

1. O. S. Tarasenko, S. V. Tarasenko, and V. M. Yurchenko, Akust. Zh. **50**, 700 (2004) [Acoust. Phys. **50**, 602 (2004)].
2. B. A. Ivanov and A. L. Sukstanskiĭ, Zh. Éksp. Teor. Fiz. **84** (1), 370 (1983) [Sov. Phys. JETP **57**, 214 (1983)].
3. S. M. Rytov, Akust. Zh. **2**, 72 (1956) [Sov. Phys. Acoust. **2**, 68 (1956)].
4. M. G. Cottam and D. R. Tilley, *Introduction to Surface and Superlattice Excitations* (Cambridge Univ. Press, Cambridge, 1989).
5. L. M. Brekhovskikh, *Waves in Layered Media*, 2nd ed. (Nauka, Moscow, 1973; Academic, New York, 1980).
6. V. I. Al'shits, A. S. Gorkunova, and A. L. Shuvalov, Zh. Éksp. Teor. Fiz. **110**, 924 (1996) [JETP **83**, 509 (1996)].
7. *Surface Polaritons: Electromagnetic Waves at Surfaces and Interfaces*, Ed. by V. M. Agranovich and D. L. Mills (North-Holland, Amsterdam, 1982; Nauka, Moscow, 1985).

Translated by E. Golyamina

Acoustical Physics, Vol. 50, No. 6, 2004, pp. 742–750. Translated from Akusticheskiĭ Zhurnal, Vol. 50, No. 6, 2004, pp. 855–864.
Original Russian Text Copyright © 2004 by Tyutekin.

Circumferential Normal Modes in an Empty Elastic Cylinder

V. V. Tyutekin
Andreev Acoustics Institute, Russian Academy of Sciences, ul. Shvernika 4, Moscow, 117036 Russia
e-mail: Tyutekin@akin.ru

Received May 18, 2004

Abstract—The so-called circumferential normal modes propagating in an empty elastic cylinder are considered. A dispersion equation for the wave numbers of these waves, an equation for the critical frequencies, and expressions for the eigenfunctions of such a waveguide are derived. Solutions to these equations are obtained by numerical methods for different values of the parameter *d* representing the relative thickness of the cylinder. An analysis of the solutions is performed, and the main properties of the dispersion curves are described, including those for the low-frequency waves of the new type, which correspond to the branches in the form of open loops. Individual normal modes are identified on the basis of the calculations and subsequent analysis of eigenfunctions. *© 2004 MAIK "Nauka/Interperiodica".*

The waveguide properties of cylindrical elastic bodies are of considerable scientific interest. In the literature, one can find a great number of publications concerned with this subject, including studies of bodies in the form of thick-walled cylindrical shells [1–3]. For the most part, these publications deal with waves in which the elastic fields are periodic functions of the polar angle θ; i.e., in the general case, the solutions are proportional to the factor exp($in\theta$), where n is an integer. Some papers [4–6] consider the asymptotic solutions for waves propagating in the direction of the angular coordinate; in this case, the quantity n is $n = \nu$, where ν plays the role of the angular wave number and, in the general case, is a noninteger. Such waves are taken into account, in particular, in solving the problems of diffraction by cylindrical obstacles [7, 8]. Exact solutions for these waves were obtained in the previous publication [9] devoted to the waveguide properties of a plane ring-shaped plate with flexural waves propagating in it.

The present paper considers the properties of circumferential normal modes propagating in an empty elastic cylinder of infinite length (the wave front is parallel to the z axis).

Let us preset the geometric dimensions of such a cylinder as follows: $r = a$ is the outer boundary, $r = br$ is the inner boundary, and $2L = a - b$ is the thickness of the waveguide.

To solve the problem, we introduce a scalar potential $\varphi(r, \theta)$ and (since the problem is two-dimensional) a single component of the vector potential $\psi_Z(r, \theta) \equiv \psi(r, \theta)$. These functions should satisfy the Helmholtz equations

$$\Delta\varphi(r, \theta) + k_l^2\varphi(r, \theta) = 0, \qquad (1)$$

$$\Delta\psi(r, 0) + k_t^2\psi(r, 0) = 0, \qquad (2)$$

where $\Delta = \frac{\partial^2}{\partial r^2} + \frac{1}{r}\frac{\partial}{\partial r} + \frac{1}{r^2}\frac{\partial^2}{\partial\theta^2}$; k_l is the longitudinal wave number, $k_l^2 = \frac{\rho\omega^2}{\lambda + 2\mu}$; k_t is the shear wave number, $k_t^2 = \frac{\rho\omega^2}{\mu}$; λ and μ are the Lame coefficients; ρ is the density; and ω is the circular frequency.

For boundary conditions, we use the absence of stress on the cylinder surfaces:

$$\sigma_{rr} = 0, \quad \sigma_{r\theta} = 0; \text{ at } r = a, b, \qquad (3)$$

where σ_{rr} and $\sigma_{r\theta}$ are the normal and tangential stresses, respectively.

These quantities can be expressed via the potentials φ and ψ (see, e.g., [1]):

$$\sigma_{rr} = -k_l^2\varphi + 2\mu\left(\frac{\partial^2\varphi}{\partial r^2} + \frac{1}{r}\frac{\partial^2\psi}{\partial r\partial\theta} - \frac{1}{r^2}\frac{\partial\psi}{\partial\theta}\right), \qquad (4)$$

$$\sigma_{r\theta} = \mu\left(\frac{2}{r}\frac{\partial^2\varphi}{\partial r\partial\theta} - \frac{2}{r^2}\frac{\partial\varphi}{\partial\theta} + \frac{1}{r^2}\frac{\partial^2\psi}{\partial\theta^2} - \frac{\partial^2\psi}{\partial r^2} - \frac{1}{r}\frac{\partial\psi}{\partial r}\right). \qquad (5)$$

According to the statement of the problem, we seek the solution to the set of equations (1), (2) in the form of elastic waves travelling in the direction of the angle θ:

$$\varphi(r, \theta) = \Phi(r)\exp(i\nu\theta), \qquad (6)$$

$$\psi(r, \theta) = \Psi(r)\exp(i\nu\theta). \qquad (7)$$

1063-7710/04/5006-0742$26.00 © 2004 MAIK "Nauka/Interperiodica"

Substituting Eqs. (6) and (7) into Eqs. (1) and (2), we obtain a set of equations for determining the amplitudes of normal modes:

$$\Delta\Phi + \left(k_l^2 - \frac{\nu^2}{r^2}\right)\Phi = 0, \tag{8}$$

$$\Delta\Psi + \left(k_t^2 - \frac{\nu^2}{r^2}\right)\Psi = 0. \tag{9}$$

Equations (4) and (5), with allowance for Eqs. (6) and (7), can be represented as

$$\frac{\sigma_{rr}}{2\mu} = \frac{d^2\Phi}{dr^2} - \frac{\lambda}{2\mu}k_l^2\Phi + i\nu\frac{d}{dr}\left(\frac{\Psi}{r}\right), \tag{10}$$

$$\frac{\sigma_{r\theta}}{2\mu} = -\frac{d^2\Psi}{dr^2} - \frac{1}{2}k_t^2\Psi + i\nu\frac{d}{dr}\left(\frac{\Phi}{r}\right). \tag{11}$$

The solutions to the set of equations (8), (9) have the form

$$\Phi_\nu(r) = AJ_\nu(k_l r) + BY_\nu(k_l r), \tag{12}$$

$$\Psi_\nu(r) = CJ_\nu(k_l r) + DY_\nu(k_l r), \tag{13}$$

where J_ν and Y_ν are the Bessel and Neumann functions, respectively, and A, B, C, and D are arbitrary constants. Let us introduce the following dimensionless parameters: $x = k_t r$, $y = k_l r$, and $\alpha = \frac{k_l}{k_t} = \frac{y}{x}$, where the latter can be expressed via the Poisson ratio σ: $\sigma = \sqrt{\frac{1-2\sigma}{2(1-\sigma)}}$. Note that, in the following treatment, we use the value $\sigma = 0.25$, which yields $\alpha \approx 0.58$. With allowance for this expression and after some cumbersome transformations, Eqs. (10) and (11) take the form

$$\frac{\sigma_{rr}}{2\mu k_t^2} = L_1(x)\Phi_\nu(\alpha x) + T_1(x)\Psi_\nu(x), \tag{14}$$

$$\frac{\sigma_{r\theta}}{2\mu k_t^2} = L_2(x)\Phi_\nu(\alpha x) + T_2(x)\Psi_\nu(x), \tag{15}$$

where the operators L and T are determined by the formulas

$$L_1(x) = -\frac{\alpha}{x}\frac{d}{dx} + \left[\frac{\nu(\alpha - 1 + \nu)}{x^2} - \frac{1}{2}\right];$$

$$T_1(x) = \frac{i\nu}{x}\left(\frac{d}{dx} - \frac{1}{x}\right);$$

$$L_2(x) = \frac{i\nu}{x}\left[\alpha\frac{d}{dx} - \frac{(\alpha-1)\nu + 1}{x}\right];$$

$$T_2(x) = \frac{1}{x}\frac{d}{dx} - \left(\frac{\nu^2}{x^2} - \frac{1}{2}\right).$$

It should be noted that, at $\alpha = 1$ (which is a physically unrealizable case), we have $L_1 = -T_2$ and $L_2 = T_1$.

Substituting expressions (12) and (13) into Eqs. (14) and (15), we finally obtain

$$\begin{aligned}\frac{\sigma_{rr}}{2\mu k_t^2} = {} & AL_1(x)J_\nu(\alpha x) + BL_1(x)Y_\nu(\alpha x) \\ & + CT_1(x)J_\nu(x) + DT_1(x)Y_\nu(x),\end{aligned} \tag{16}$$

$$\begin{aligned}\frac{\sigma_{r\theta}}{2\mu k_t^2} = {} & AL_2(x)J_\nu(\alpha x) + BL_2(x)Y_\nu(\alpha x) \\ & + CT_2(x)J_\nu(x) + DT_2(x)Y_\nu(x).\end{aligned} \tag{17}$$

Introducing the notation $x_a = k_t a$ and $x_b = k_t b$ and applying boundary conditions (3), we obtain a homogeneous set of algebraic equations for determining the quantities A, B, C, and D:

$$\begin{aligned}& AL_1(x_a)J_\nu(\alpha x_a) + BL_1(x_a)Y_\nu(\alpha x_a) \\ & + CT_1(x_a)J_\nu(x_a) + DT_1(x_a)Y_\nu(x_a) = 0,\end{aligned} \tag{18}$$

$$\begin{aligned}& AL_2(x_a)J_\nu(\alpha x_a) + BL_2(x_a)Y_\nu(\alpha x_a) \\ & + CT_2(x_a)J_\nu(x_a) + DT_2(x_a)Y_\nu(x_a) = 0,\end{aligned} \tag{19}$$

$$\begin{aligned}& AL_1(x_b)J_\nu(\alpha x_b) + BL_1(x_b)Y_\nu(\alpha x_b) \\ & + CT_1(x_b)J_\nu(x_b) + DT_1(x_b)Y_\nu(x_b) = 0,\end{aligned} \tag{20}$$

$$\begin{aligned}& AL_2(x_b)J_\nu(\alpha x_b) + BL_2(x_b)Y_\nu(\alpha x_b) \\ & + CT_2(x_b)J_\nu(x_b) + DT_2(x_b)Y_\nu(x_b) = 0.\end{aligned} \tag{21}$$

The dispersion equation for the unknown wave number ν is obtained as usual, by equating the determinant of set (18)–(21) to zero:

$$\Delta(\nu) = \begin{vmatrix} L_1(x_a)J_\nu(\alpha x_a) & L_1(x_a)Y_\nu(\alpha x_a) & T_1(x_a)J_\nu(x_a) & T_1(x_a)Y_\nu(x_a) \\ L_2(x_a)J_\nu(\alpha x_a) & L_2(x_a)Y_\nu(\alpha x_a) & T_2(x_a)J_\nu(x_a) & T_2(x_a)Y_\nu(x_a) \\ L_1(x_b)J_\nu(\alpha x_b) & L_1(x_b)Y_\nu(\alpha x_b) & T_1(x_b)J_\nu(x_b) & T_1(x_b)Y_\nu(x_b) \\ L_2(x_b)J_\nu(\alpha x_b) & L_2(x_b)Y_\nu(\alpha x_b) & T_2(x_b)J_\nu(x_b) & T_2(x_b)Y_\nu(x_b) \end{vmatrix} = 0. \tag{22}$$

The equation $\Delta(\nu) = 0$ has many roots $\nu = \nu_n(x_a, x_b)$, where the subscript n determines different branches of the solution to the characteristic equation. For the purpose of their identification and also for testing the validity of boundary conditions (18)–(21), we assume that the roots $\nu = \nu_n(x_a, x_b)$ are calculated and determine the eigenfunctions (modes of vibration) of the waveguide under study. We use the first three equations of set (18)–(21) (the fourth equation is their linear combination). Setting $A = 1$ (without loss of generality), we obtain a set of equations for determining the remaining coefficients, which depend on both ν_n and n:

$$\begin{aligned} &BL_1(x_a)Y_\nu(\alpha x_a) + CT_1(x_a)J_\nu(x_a) \\ &+ DT_1(x_a)Y_\nu(x_a) = -L_1(x_a)J_\nu(\alpha x_a), \end{aligned} \tag{23}$$

$$\begin{aligned} &BL_2(x_a)Y_\nu(\alpha x_a) + CT_2(x_a)J_\nu(x_a) \\ &+ DT_2(x_a)Y_\nu(x_a) = -L_2(x_a)J_\nu(\alpha x_a), \end{aligned} \tag{24}$$

$$\begin{aligned} &BL_1(x_b)Y_\nu(\alpha x_b) + CT_1(x_b)J_\nu(x_b) \\ &+ DT_1(x_b)Y_\nu(x_b) = -L_1(x_b)J_\nu(\alpha x_b). \end{aligned} \tag{25}$$

The solution to set (23)–(25) can be represented in the form

$$B_n = \frac{\Delta_B(\nu_n)}{\Delta(\nu_n)}, \quad C_n = \frac{\Delta_C(\nu_n)}{\Delta(\nu_n)}, \quad D_n = \frac{\Delta_D(\nu_n)}{\Delta(\nu_n)}, \tag{26}$$

where

$$\Delta(\nu_n) = -\begin{vmatrix} L_1(x_a,\nu_n)Y_\nu(\alpha x_a) & T_1(x_a,\nu_n)J_\nu(x_a) & T_1(x_a,\nu_n)Y_\nu(x_a) \\ L_2(x_a,\nu_n)Y_\nu(\alpha x_a) & T_2(x_a,\nu_n)J_\nu(x_a) & T_2(x_a,\nu_n)Y_\nu(x_a) \\ L_1(x_b,\nu_n)Y_\nu(\alpha x_b) & T_1(x_b,\nu_n)J_\nu(x_b) & T_1(x_b,\nu_n)Y_\nu(x_b) \end{vmatrix},$$

$$\Delta_B(\nu_n) = -\begin{vmatrix} L_1(x_a,\nu_n)J_\nu(\alpha x_a) & T_1(x_a,\nu_n)J_\nu(x_a) & T_1(x_a,\nu_n)Y_\nu(x_a) \\ L_2(x_a,\nu_n)J_\nu(\alpha x_a) & T_2(x_a,\nu_n)J_\nu(x_a) & T_2(x_a,\nu_n)Y_\nu(x_a) \\ L_1(x_b,\nu_n)J_\nu(\alpha x_b) & T_1(x_b,\nu_n)J_\nu(x_b) & T_1(x_b,\nu_n)Y_\nu(x_b) \end{vmatrix},$$

$$\Delta_C(\nu_n) = -\begin{vmatrix} L_1(x_a,\nu_n)Y_\nu(\alpha x_a) & L_1(x_a,\nu_n)J_\nu(\alpha x_a) & T_1(x_a,\nu_n)Y_\nu(x_a) \\ L_2(x_a,\nu_n)Y_\nu(\alpha x_a) & L_2(x_a,\nu_n)J_\nu(\alpha x_a) & T_2(x_a,\nu_n)Y_\nu(x_a) \\ L_1(x_b,\nu_n)Y_\nu(\alpha x_b) & L_1(x_b,\nu_n)J_\nu(\alpha x_b) & T_1(x_b,\nu_n)Y_\nu(x_b) \end{vmatrix},$$

$$\Delta_D(\nu_n) = -\begin{vmatrix} L_1(x_a,\nu_n)Y_\nu(\alpha x_a) & T_1(x_a,\nu_n)J_\nu(x_a) & L_1(x_a,\nu_n)J_\nu(\alpha x_a) \\ L_2(x_a,\nu_n)Y_\nu(\alpha x_a) & T_2(x_a,\nu_n)J_\nu(x_a) & L_2(x_a,\nu_n)J_\nu(\alpha x_a) \\ L_1(x_b,\nu_n)Y_\nu(\alpha x_b) & T_1(x_b,\nu_n)J_\nu(x_b) & L_1(x_b,\nu_n)J_\nu(\alpha x_b) \end{vmatrix}.$$

With the coefficients obtained above, the eigenfunctions of the waveguide for stresses can be represented as

$$\begin{aligned} \frac{\sigma_{rr}}{2\mu k_t^2} &= L_1(x)J_{\nu_n}(\alpha x) + B_nL_1(x)Y_{\nu_n}(\alpha x) \\ &+ C_nT_1(x)J_{\nu_n}(x) + D_nT_1(x)Y_{\nu_n}(x), \end{aligned} \tag{27}$$

$$\begin{aligned} \frac{\sigma_{r\theta}}{2\mu k_t^2} &= L_2(x)J_{\nu_n}(\alpha x) + B_nL_2(x)Y_{\nu_n}(\alpha x) \\ &+ C_nT_2(x)J_{\nu_n}(x) + D_nT_2(x)Y_{\nu_n}(x). \end{aligned} \tag{28}$$

The eigenfunctions for the radial u_r and angular u_θ displacements can be determined via the scalar and vector potentials:

$$u_r = \frac{\partial\varphi}{\partial r} + \frac{1}{r}\frac{\partial\psi}{\partial\theta}, \quad u_\theta = \frac{1}{r}\frac{\partial\varphi}{\partial\theta} - \frac{\partial\psi}{\partial r}. \tag{29}$$

Introducing the operators $R_1 = \frac{d}{dx}$ and $R_2(\nu) = \frac{i\nu}{x}$, we represent displacements (29) corresponding to the root ν_n of characteristic equation (22) in the form

$$\frac{u_r}{k_t} = R_1\Phi_{\nu_n}(\alpha x) + R_2(\nu_n)\Psi_{\nu_n}(x), \tag{30}$$

$$\frac{u_\theta}{k_t} = R_2(\nu_n)\Phi_{\nu_n}(\alpha x) - R_1\Psi_{\nu_n}x, \tag{31}$$

where

$$\Phi_{\nu_n}(\alpha x) = J_{\nu_n}(\alpha x) + B_nY_{\nu_n}(\alpha x),$$

$$\Psi_{\nu_n}(x) = C_nJ_{\nu_n}(x) + D_nY_{\nu_n}(x).$$

Before discussing the results of the calculations, it is necessary to make some comments concerning their representation. Above, it was noted that the desired

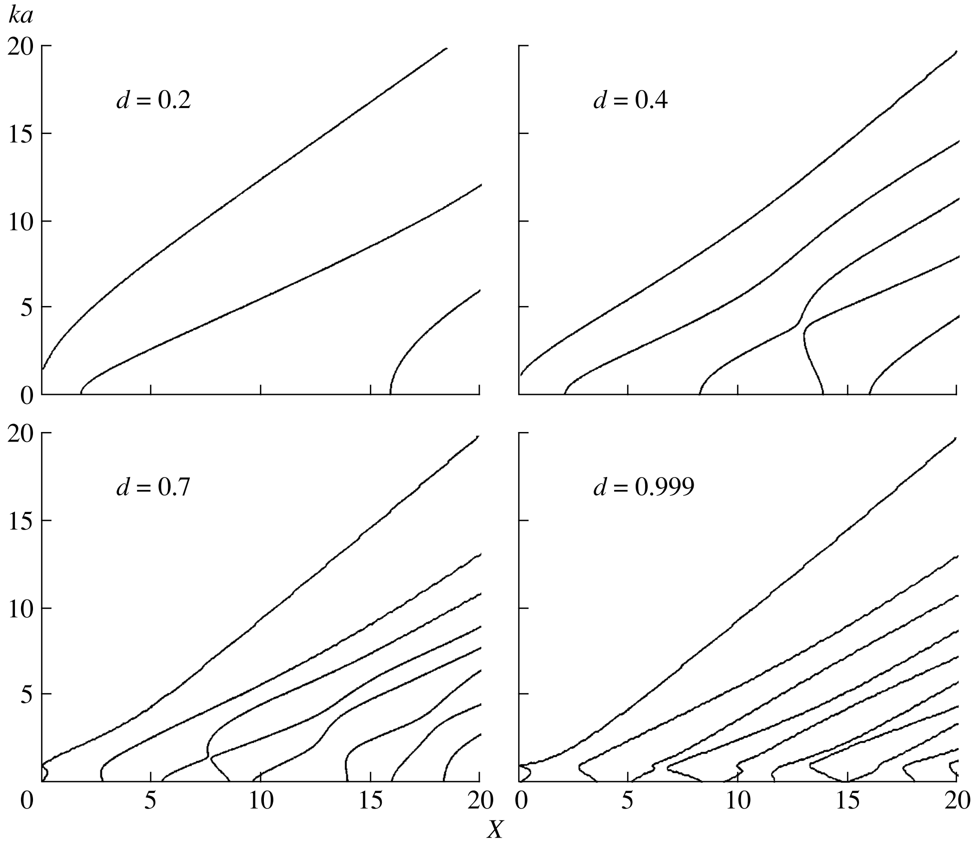

Fig. 1. Dispersion curves for the circumferential normal modes in an empty elastic cylinder; $X = k_t a$.

quantity ν plays the role of the wave number involved in the expression for the phase of the normal mode: $\varphi = \nu\theta$. As in the previous paper [9], this expression can be transformed as $\varphi = \frac{\nu}{r} r\theta = k_r S$, where $k_r = \frac{\nu}{r}$ is the "linear" wave number and $S = r\theta$ is the arc length traveled by the wave. Choosing this form of the result representation, we set $r = a$ for the sake of definiteness; i.e., we consider the wave number corresponding to the outer boundary of the empty cylinder. Then, in the equations given above, the unknown quantity ν can be replaced by $\nu = ka$ (the subscript of k is omitted). The arguments involved in the equations given above can be represented in the form $x_a = k_t a$ and $x_b = k_t(1 - d)$, where $d = \frac{L}{R_0}$ is the dimensionless thickness of the cylinder. The velocity of wave propagation c also depends on the radius. Choosing the quantity $X = k_t a$ as the main argument, we represent the desired dimensionless velocity in the form $C = \frac{c}{c_t} = \frac{k_t a}{\nu} = \frac{X}{ka}$, where c_t is the velocity of shear waves in the medium.

To solve Eq. (22) for the unknown quantity $\nu = ka$ as a function of the dimensionless frequency $X = k_t a$ for different values of the dimensionless thickness of the cylinder d, a special computer program was used.

Figure 1 shows the results of calculations for different values of d. The plot is typical of all values of the parameter $0 < d < 1$. One can see three groups of dispersion curves: (a) single branches ($n = 0$) that begin at zero frequency and have the value $\nu = 1$ at this point; (b) single branches ($n = 0'$) in the form of open loops lying in the immediate vicinity of the origin of coordinates (the latter branches are shown in more detail in Fig. 2 for some of the values of the parameter d: branches corresponding to the waves with $n = 0'$ lie in the region $ka \leq 1$, and waves with $n = 0$ are partially represented in the region $ka \geq 1$; similar branches were also obtained for normal modes in [9]); and (c) an infinite number of branches corresponding to the higher-order normal modes, as in any waveguide (the number of these waves increases with increasing d).

Figure 3 shows the plots for the dimensionless phase velocity $C = \frac{c}{c_t}$ of the wave with $n = 0$ for certain values of d. One can see that, near the origin of coordinates, this velocity is proportional to the frequency. When d is large, the velocity as a function of frequency exhibits maxima and, then, at $X \longrightarrow \infty$, tends to a constant value

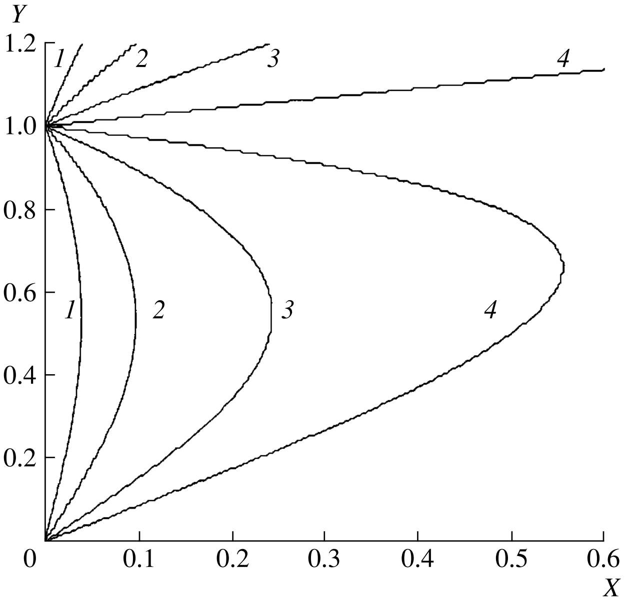

Fig. 2. Low-frequency half-closed loops; $Y = ka$ and d = (*1*) 0.2, (*2*) 0.4, (*3*) 0.7, and (*4*) 0.9.

of $C_\infty \simeq 0.933$, which does not depend on the parameter d. When d is small, such maxima are absent and the velocity tends to the same constant C_∞ but at much higher frequencies. In its physical meaning, the velocity $C = C_\infty$ is close to the Rayleigh wave velocity.

To identify different branches of the dispersion curves, eigenfunctions were calculated for the displacements u_r and u_θ and for the stresses σ_{rr} and $\sigma_{r\theta}$ by using formulas (28)–(31) with different values of the parameter d at certain frequencies. The aforementioned quantities were normalized to their maximal values, and the dimensionless coordinate x was given in the form $x = \frac{r}{a} - \frac{a+b}{2a}$, so that the origin of coordinates corresponded to the median surface of the cylinder and the quantity x varied within $-\frac{d}{2} \le x \le \frac{d}{2}$. In all subsequent plots the factor i is omitted in the quantities u_θ and $\sigma_{r\theta}$.

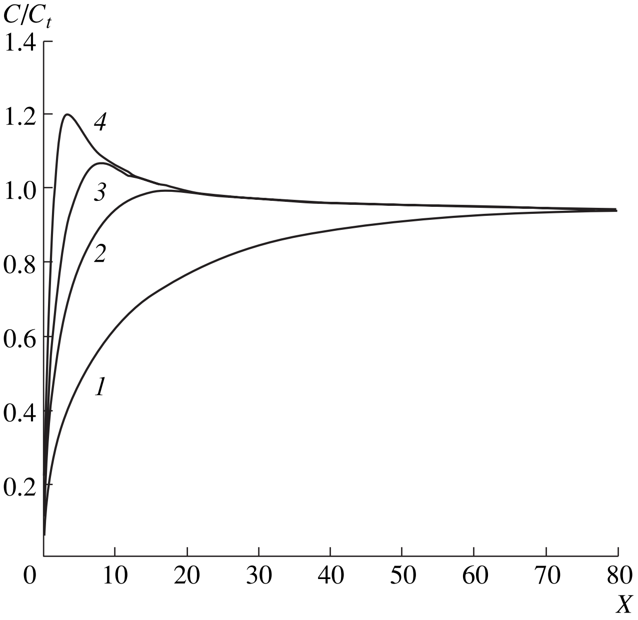

Fig. 3. Phase velocities of normal modes with $n = 0$; d = (*1*) 0.1, (*2*) 0.3, (*3*) 0.5, and (*4*) 0.9.

Figure 4 shows the plots for $d = 0.9$ (other parameters are indicated in the figure caption). One can see that, at low frequencies (Fig. 3a), the radial displacement u_r is almost independent of the radius; i.e., a quasi-flexural wave propagates in the body. In this case, the angular displacement u_θ and the stresses σ_{rr} and σ_{r2} are maximal near the inner surface of the cylinder and decrease toward the outer surface. Other cases (Figs. 3b–3d) correspond to the transformation of the eigenmodes with increasing frequency, which consists of the sequential displacement of all quantities toward the outer surface and their concentration near it.

Figure 5 shows similar data for $d = 0.1$. The behavior of the quantities under consideration is approximately the same as for $d = 0.9$, except that the maximal stress values initially occur at the median surface of the cylinder ($x = 0$), and that the concentration of displacements and stresses near the outer surface occurs at a much higher frequency.

Figure 6 represents (for $d = 0.9$) the eigenfunctions for the normal modes with $n = 0'$, which are described by open loops (Fig. 2). One can see that, independently

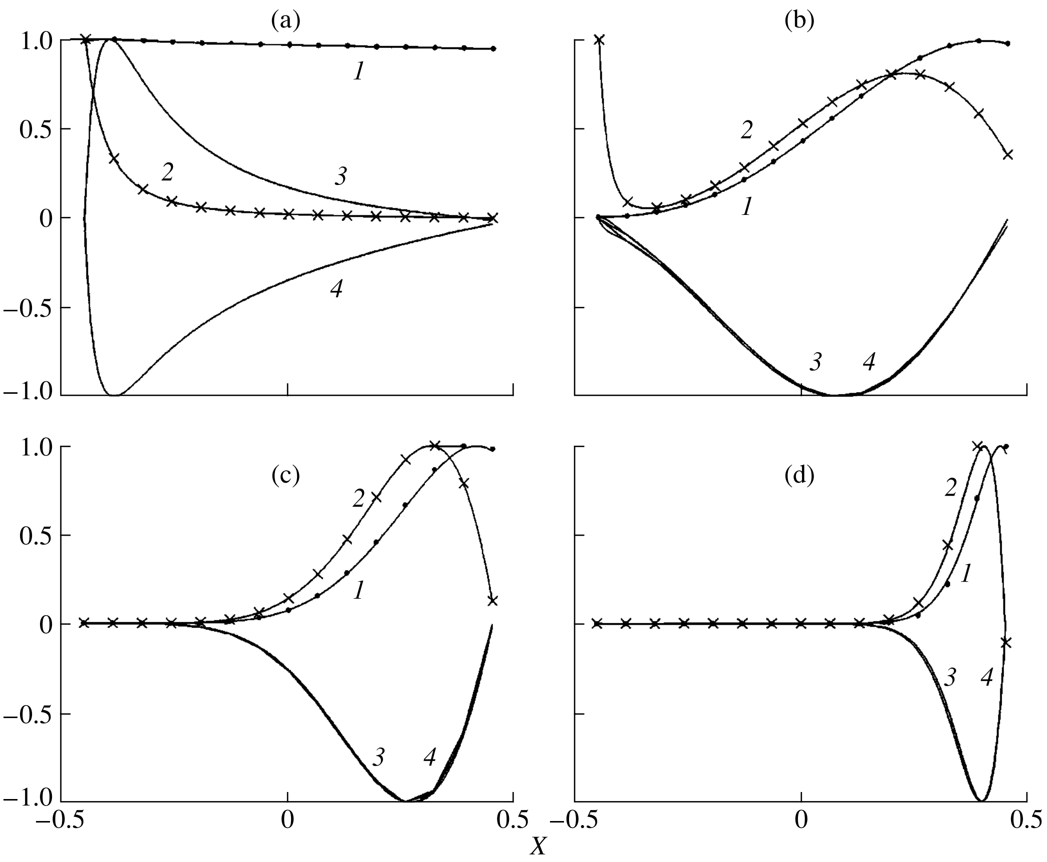

Fig. 4. Eigenfunctions for a normal mode with $n = 0$ at $d = 0.9$: (*1*) displacement u_r, (*2*) displacement u_θ, (*3*) stress σ_{rr}, and (*4*) stress $\sigma_{r\theta}$; X = (a) 0.5, (b) 5, (c) 10, and (d) 32.

of frequency, all the functions differ little from each other and from the corresponding functions for the waves with $n = 0$ (Fig. 1a), except that the displacement u_r changes its phase for the opposite one. Cases (a) and (c) correspond to the lower half of the loop, and cases (b) and (d), to the upper half.

The data shown in Figs. 2 and 6 suggest the following basic qualitative conclusions about the properties of low-frequency waves with $n = 0'$:

(i) these waves have two different phase velocity values at the same frequency (except for the frequency at which the upper and lower branches merge);

(ii) the group velocity determined by the formula $c_g = \frac{d\omega}{dk} = c_t\frac{dX}{dY}$ is negative for the upper (descending) branch and positive for the lower (ascending) branch;

(iii) the waves are of quasi-flexural nature, with a concentration of stresses near the inner surface of the cylindrical body.

From Fig. 1, one can see that normal modes of higher orders ($n \geq 1$) originate at $\nu_n = 0$. The quantities describing the corresponding normal mode field do not depend on the polar angle θ. At the instant of origination of each of these waves, the wave front has the form of a circle coaxial with the waveguide boundaries $r = a$ and $r = b$. In this case, the displacements are expressed via cylindrical functions of zero order. In plane waveguides, the process of normal mode origination is analogous to that considered above: the wave front is parallel to the plane waveguide boundary.

As in the plane waveguides, critical frequencies (the frequencies of wave origination) exist in the cylinder under study. The equation for the critical frequencies can be easily obtained from Eq. (22) by setting $\nu = \nu_n = 0$. Then, the operators $L_{1,2}(x)$ and $T_{1,2}(x)$ have the form

$$L_1(x) = -\left(\frac{\alpha}{x}\frac{d}{dx} + \frac{1}{2}\right); \quad L_2(x) = T_1(x) = 0;$$

$$T_2(x) = \frac{1}{x}\frac{d}{dx} + \frac{1}{2},$$

and Eq. (22) takes the form

$$\begin{vmatrix} J(\alpha x_a) & Y(\alpha x_a) \\ J(\alpha x_b) & Y(\alpha x_b) \end{vmatrix} \begin{vmatrix} I(x_a) & K(x_a) \\ I(x_b) & K(x_b) \end{vmatrix} = 0, \qquad (32)$$

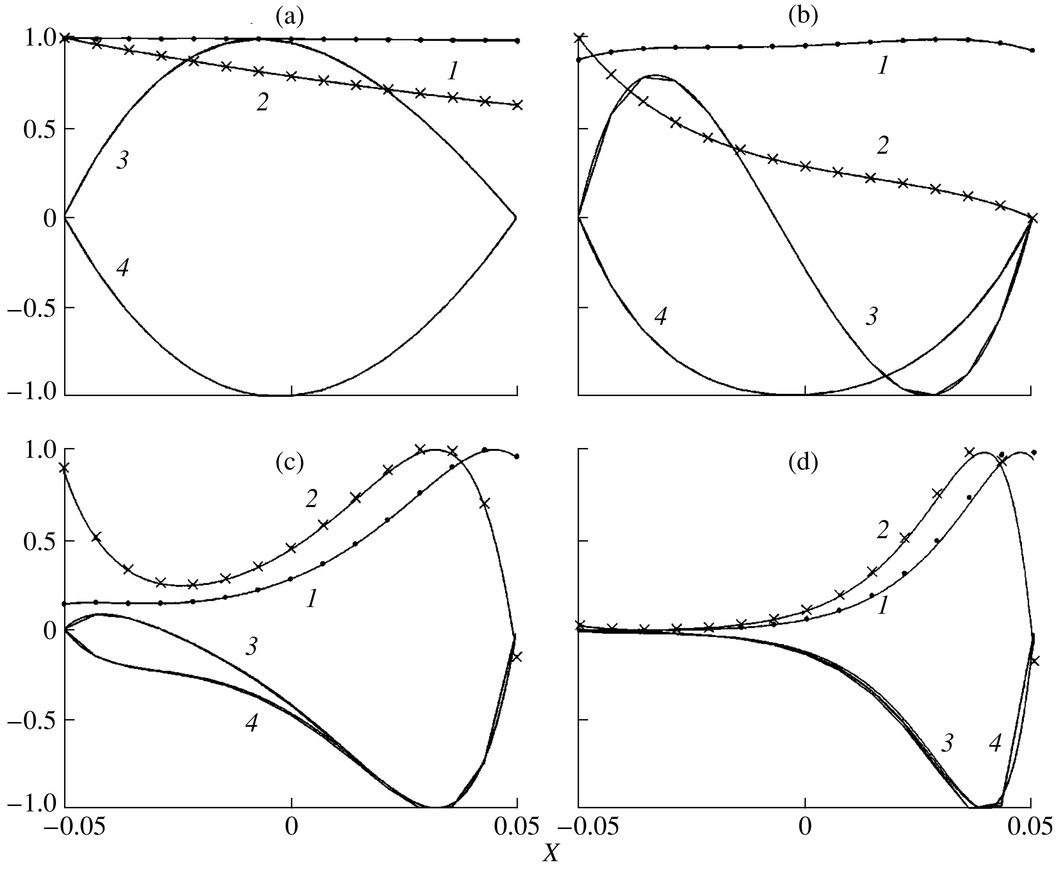

Fig. 5. The same as in Fig. 4 but for $d = 0.1$; X = (a) 0.5, (b) 30, (c) 90, and (d) 148.

where additional notations are introduced:

$$J(x) = \frac{\alpha}{x}J_1(x) - \frac{1}{2}J_0(x);$$

$$Y(x) = \frac{\alpha}{x}Y_1(x) - \frac{1}{2}Y_0(x);$$

$$I(x) = -\frac{1}{x}J_1(x) + \frac{1}{2}J_0(x);$$

$$K(x) = -\frac{1}{x}Y_1(x) + \frac{1}{2}Y_0(x).$$

Thus, as one would expect, the equation for the critical frequencies consists of two independent equations, the first of which refers to the waves originating as longitudinal, and the second to the waves originating as transverse.

Figure 7 shows the dimensionless wave numbers $\frac{k}{k_t}$ for the first four modes (n = 1–4) at $d = 0.9$. According to Eq. (32), $n = 1$ and $n = 4$ correspond to the modes originating as longitudinal, and $n = 2$ and $n = 3$ to the modes originating as transverse. It is essential that, when the wave size of the cylinder tends to infinity, the velocity of all the normal modes tends to that of transverse waves, which testifies that they belong to the quasi-Lamb wave type. The difference between them and the Lamb waves of an elastic layer consists, in particular, in that the mode with $n = 1$ originates as a transverse wave in the case of the Lamb waves and as a longitudinal wave in the case under study.

Figure 8 represents the eigenmodes of the displacements for n = 1–4 at a high dimensionless frequency $X = 80$. Here, only positive values of the x coordinate are used, because, for $x < 0$, both displacements and forces are fairly small at this frequency, and all fields concentrate near the outer surface of the cylinder. From this figure, one can see that the number of a mode (as in plane waveguides) corresponds to the number of intersections of the corresponding curves with the x axis.

The results obtained above can be used for studying the characteristics of circumferential normal modes of a shear-longitudinal type in a ring-shaped thin plate (such a problem for flexural waves was solved in [9]). For this purpose, it is necessary to replace the elastic modulus of a plane wave $\lambda + 2\mu$ by the longitudinal elastic modulus

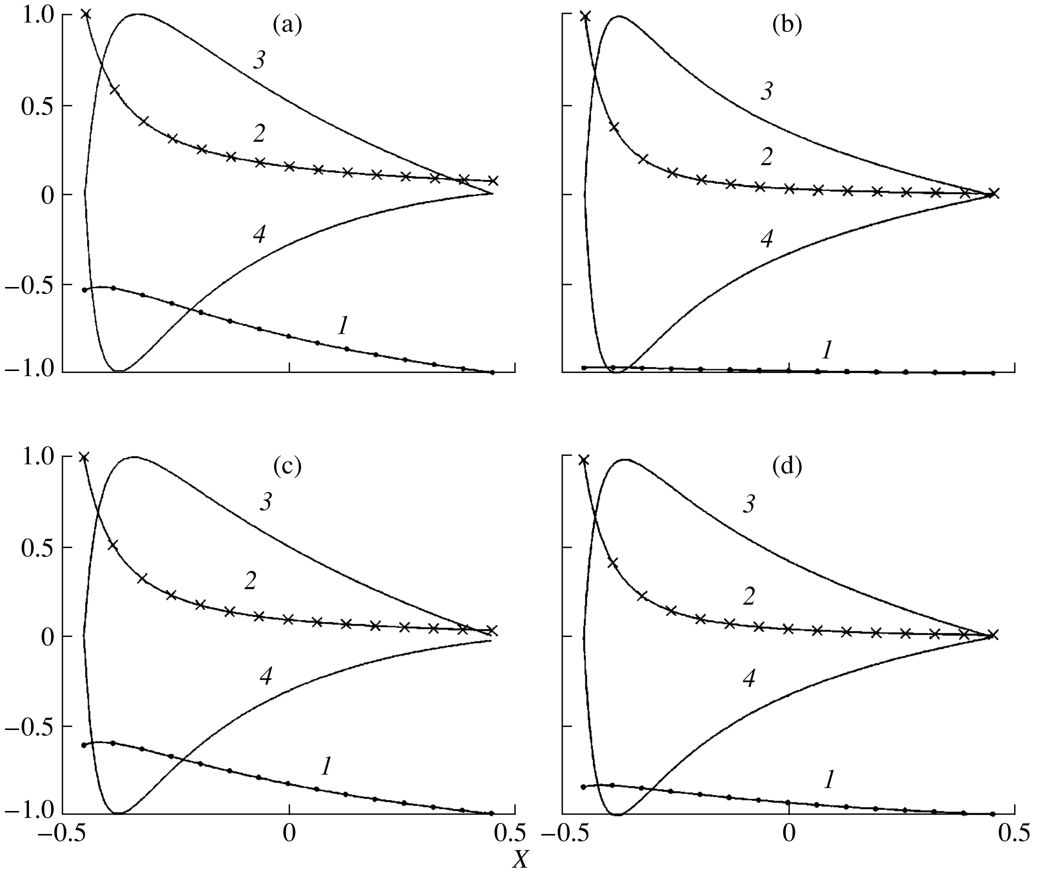

Fig. 6. Eigenfunctions for the normal mode with $n = 0'$ at $d = 0.9$; X = (a) 0.5, (b) 5, (c) 10, and (d) 32.

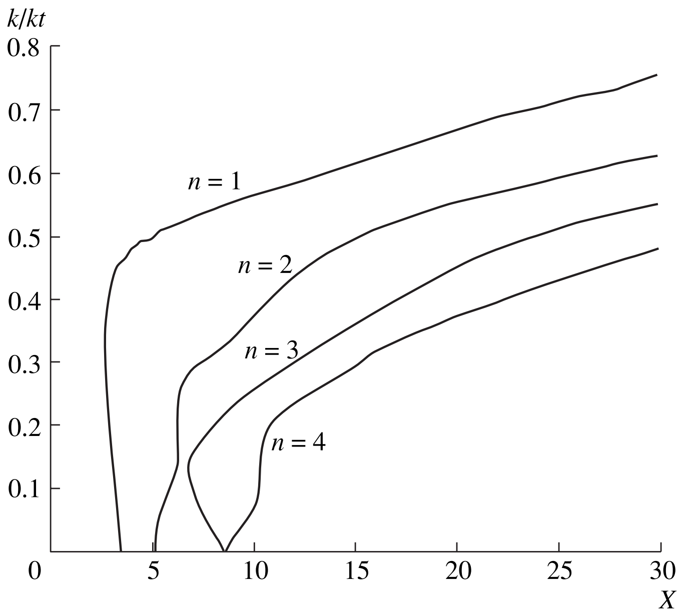

Fig. 7. Frequency characteristics of the dimensionless wave numbers for $n \geq 1$ ($d = 0.9$).

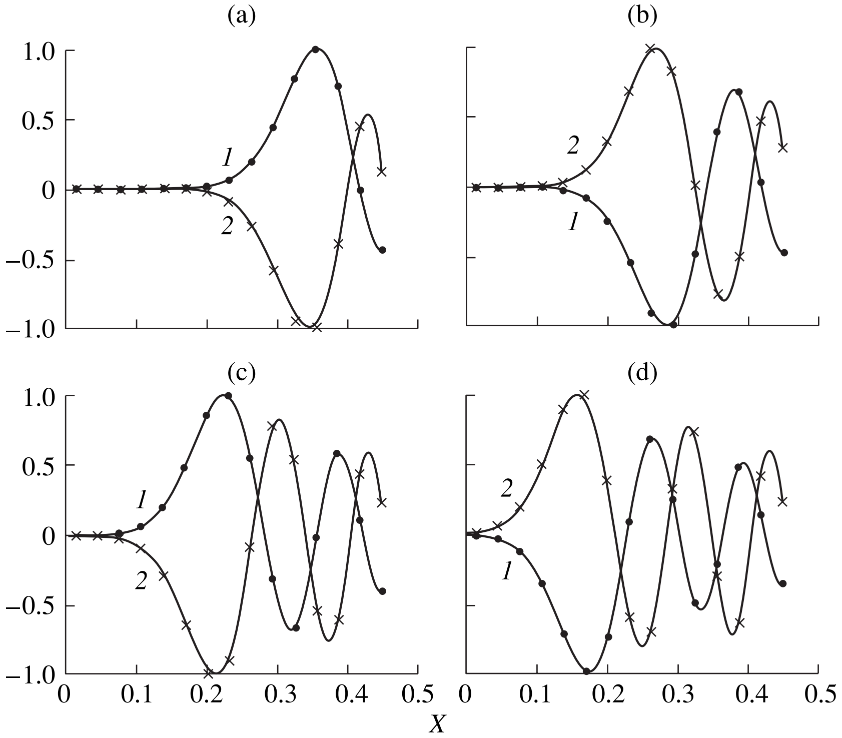

Fig. 8. Displacement eigenfunctions for normal modes with $n \geq 1$; $d = 0.9$, $X = 80$, and $n =$ (a) 1, (b) 2, (c) 3, and (d) 4.

of a plate $E_p = \frac{E}{1-\sigma^2}$ and to represent the factor α in the form $\alpha = \frac{k_p}{k_t} = \sqrt{\frac{1-\sigma}{2}}$. For the value $\sigma = 0.25$ used in the calculations, this factor is $\alpha \cong 0.612$.

In closing, it should be noted that the normal modes studied in this paper can be considered as helical waves propagating in an empty elastic cylinder at an angle $\vartheta = \frac{\pi}{2}$ to its axis. For helical waves with other values of this angle, the aforementioned wave numbers of circumferential waves can be determined as "critical wave numbers" (by analogy with critical frequencies).

REFERENCES

1. *Physical Acoustics. Principles and Methods*, Ed. by W. P. Mason (Academic, New York, 1964; Mir, Moscow, 1966), Vol. 1, Part A.
2. Kumar Ram, Acustica **27** (6), 317 (1972).
3. A. A. Kleshchev, Akust. Zh. **50**, 86 (2004) [Acoust. Phys. **50**, 74 (2004)].
4. L. M. Brekhovskikh, Akust. Zh. **13**, 541 (1960) [Sov. Phys. Acoust. **13**, 462 (1960)].
5. I. A. Viktorov, *Acoustic Surface Waves in Solids* (Nauka, Moscow, 1981), p. 215 [in Russian].
6. E. V. Golubeva, Akust. Zh. **32**, 385 (1986) [Sov. Phys. Acoust. **32**, 238 (1986)].
7. G. Vboulis, S. A. Paipetis, and P. S. Theocaris, J. Sound Vibr. **35** (4), 521 (1974).
8. E. L. Shenderov, *Radiation and Scattering of Sound* (Sudostroenie, Leningrad, 1989), p. 301 [in Russian].
9. V. V. Tyutekin, Akust. Zh. **49**, 843 (2003) [Acoust. Phys. **49**, 721 (2003)].

Translated by E. Golyamina